The synthesis of boron enriched core-shell nanoparticles for neutron capture therapy.
&
The synthesis and biological impact of model plastic nanoparticles.

Brad John Coward

Doctor of Philosophy

Aston University

September 2024

Abstract

Nanoparticles, with their unique properties at the nanoscale, have garnered significant interest. Their potential in medicine, catalysis, and other fields is tremendous. However, it is crucial to acknowledge the potential detrimental effects of nanoparticles, particularly plastic nanoparticles and the largely unknown effect on human health through plastic degradation in the environment.

This thesis is structured around two pivotal research topics. The first explores the synthesis of nanoparticles for a groundbreaking purpose - treating glioblastomas with a new radiotherapy, neutron capture therapy. The second topic delves into the environmental impact of plastic waste, particularly its breakdown and the toxicity of plastic nanoparticles to cell lines.

Within the first two research chapters [chapters 3 and 4], a deep study on the synthesis of iron-boron core and gold shell (FeB-Au) nanoparticles for neutron capture therapy. Patients diagnosed with GBM have a very short life expectancy, with 17.7 % of patients having a survival rate of one year. Two essential methods were trialled to synthesise the trimetallic nanoparticles: non-aqueous conditions using redox-transmetalation and aqueous conditions using reverse micelles. When using an Fe^{3+} salt ($FeCl_3$) in non-aqeuous conditions led to a significant incorporation of boron into the core when compared to using an Fe^{2+} salt ($FeCl_2$), with a B/Fe atomic ratio of 0.92 compared to 0.32, respectively. Redox-transmetalation helped overcome the lattice mismatch between the Fe-B core and Au shell, with Fe being used as the reducing agent for gold, which promotes seeding at the surface of the core. From this method, high importance around the temperature drop of the core solution to minimise homonucleation of the gold and promote hetronucleation was essential for forming a gold shell and partial core-shell nanoparticles were formed. The reverse micelle method was not reproducible compared to the literature and was ineffective at forming core-shell nanoparticles. It was challenging to confirm whether there was micelle stability which led to a significant challenge in forming a shell around the core material. There was no clear core-shell structure formation using reverse micelles and the method proved to be less effective compared to the redox-transmetalation method. Within the plastic nanoparticle toxicity test [chapter 5], different common petroleum-based waste plastics [PS, PMMA, PE, PP] were synthesised and used for cell testing on MRC-5 cells. Several analysis techniques (EDX, XRF, XPS TGA, XRD, FTIR), were used to compare raw polystyrene and a polystyrene coffee lid to identify the differences and additives in processed commercial coffee lids. In this case, it was found that the coffee lid had $CaCO_3$ and TiO_2 added as a colourant and TiO_2 as an antimicrobial. The average sizes of all plastic nanoparticle solutions (PS, PMMA, PP, PE, PS coffee lid) were between 50-200 nm at high concentrations between 2×10^{12} and 2×10^{14} particles per ml. It was found that the coffee lid was highly toxic towards MRC-5 cells, with cell viability of less than 10 %. However, the concerning information found in this chapter was that all the plastics indicate that DNA damage is caused by double-strand breaks in the DNA and a delay in the cells progressing through the cell cycle due to damage being caused.

Keywords:

Core-shell, neutron capture therapy, glioblastomas, nanoparticles, plastic pollution, DNA damage, cell toxicity, cell viability, boron incorporation.

Dedication

I want to thank my supervisors, Dr Jiawei Wang and Dr Boris Kysela, for the support they offered during my PhD. It has allowed me to develop numerous skills and process development techniques while pursuing different scientific avenues. Their knowledge and experience have inspired me to drive for better and more exciting results to get to the bottom of questions and progress science forward. It has been a hard, long three years, but none of this would have been possible without their support and encouragement.

I want to thank Professor Paul Topham, who stepped in and took over supervision in the last few months of my PhD and gave me advice and best practice on how a thesis should look. Even though he was out of the office during the summer, he still found time to give me feedback.

I want to thank everyone in the EPS department for their support in making the progress required on the project. From the support to order the desired chemicals and equipment, Dr Val Franklin in ensuring everything is done correctly and all documents are in place, James Hammerton in support of booking and using analytical equipment. All their support made for a much more enjoyable research project.

I want to thank Dr David Nagel for his support on the biology side of the project and for giving the advice and knowledge transfer to become a better cell biologist while testing plastic nanoparticles for their toxicity. Not only academically but for the general chats, laughs and mentorship to make the three years enjoyable and keep my sanity high. Having his support is something I will not forget.

I would also like to thank all the other PhD students whom I have been able to collaborate with and make these three years enjoyable and exciting, from going out for a post-work drink to learning more about your research. It was all a great part of this journey.

Finally, I want to thank my family and partner for their incredible support during this process. It was a gruelling three years, and when the times got tough, they were always there to pick me up and push me forward to keep persisting, as there was always light at the end of the tunnel.

Contents

List of Abbreviations

Å - Angstrom
AV - Anexin V
BF - Bright Field
BPA - Bisphenol A
BrdU - Bromodeoxyuridine
BSE - Back Scattered Electrons
C.L - Coffee Lid
CBB - Cellulose-based bioplastic
CCP - Cubic Close Packed
CMC - Critical Micelle Concentration
CP - Cacumen Platycladi
CTAB - Cetrimonium bromide
DLS - Dynamic Light Scattering
DMEM - Dulbecco's Modified Eagle's medium
DNA - Deoxyribonucleic acid
DO - Dissolved Oxygen
E.A - Early Apoptosis
EDS - Energy Dispersive X-ray Spectroscopy
EDX - Energy Dispersive X-ray
EELS - Electron Energy Loss Spectroscopy
EM - Electron Microscope
E° - Standard Electrode Potential
Eq - Equation
ETD - Everhart-Thornley Detector
FC - Flow Cytometry
FP - Fundamental Parameters
FTIR - Fourier-transform Infrared Spectroscopy
GBM - Glioblastoma
HAADF - High-Angle Annular Dark-Field
HCP - Hexagonal Close Packed
HV - High Vacuum
ICP-OES - Inductively Coupled Plasma Optical Emission Spectroscopy
L.A - Late Apoptosis
LET - Linear energy transfer
MRI - Magnetic Resonance Imaging
NCT - Neutron Capture Therapy
NFCM - Nano Flow Cytometry
nm - Nanometre
NMR - Nuclear Magnetic Resonance
PBS - Phosphate-buffered saline
PDI - Polydispersity Index
PE - Polyethylene
PET - Polyethylene terephthalate
PHBV - Polyhydroxybutyrate-valerate
PI - Propidium Iodide
PLA - Polylactide
PMMA - Polymethyl methacrylate
PP - Polyproylene
ppm - Parts Per Million
PS - Polystyrene
PU - Polyurethane
PVP - Poly(vinyl pyrrolidone)
RCF - Relative Centrifugal Force
ROS - Reactive Oxygen Species
S.S NMR - Solid-State NMR
SE - Secondary Electrons
SEM - Scanning electron microscopy
STEM - Scanning Transmission Electron Microscopy
TEM - Transmission Electron Microscopy
TGA - Thermogravimetric analysis
UV-Vis - Ultraviolet-Visible Spectroscopy
W - Water to Stabiliser molar ratio
WDXRF - Wavelength-Dispersive X-ray Fluorescence
XPS - X-ray photoelectron spectroscopy
XRD - X-ray Diffraction
XRF - X-ray Fluorescence
WWF - World Wildlife Foundation
ΔE - Electrochemical Potential

List of Tables

List of Figures

Chapter 1 – Introduction

1.1 Introduction

Nanoparticles have the potential to be both a panacea and a bane for society. The use of nanoparticles in medicine is ever expanding with nano antibiotics being used due to the surface area to volume ratio and the rapid release of medicine into the body *(Arora et al. 2020)*. Silver-gold alloyed nanoparticles have shown anticancer and antimicrobial activity which can directly target the surface of human breast cancer cells (MCF-7) *(Roopan et al. 2014)*, *(de Oliveira Gonçalves et al. 2020).* Antibody drug conjugates have been used in medicine by using the targeting properties of monoclonal antibodies which are attached to a cytotoxic drug nanoparticle that is delivered directly to the diseased tissue *(Tsuchikama et al. 2024)*. However, nanoparticles can also be the bane to society. Single use plastic production reached 390 metric tonnes in 2021 *(Plastics Europe, 2022)* and a major concern is that only 9 % of these plastics are recycled correctly *(MacLeod et al. 2021)*.This leads to a serious concern about plastic pollution and the inevitable breakdown in micro and nanoplastics and the damage caused to human health. Polypropolyne and polyethylene terephthalate with sizes between 100-600nm and 100-200nm respectively did not have a cytotoxic effect towards Caco-2 and HepG2 but caused DNA damage which the long term effects are unknown *(Roursgaard et al. 2022).* A further study on the impact of nanoparticles on human health is required to delve into these areas further.

Within this thesis, the research has been split into two different topics. The first two research chapters, (chapters 3 + 4) are focused on the synthesis of trimetallic nanoparticles of Fe-B@Au to tackle the cornering glioblastoma (GBM). The research concentrates on how nanoparticles are used effectively for a positive use to benefit human life. However, the second topic of research (chapter 5) focuses on the negative impact of nanoplastics and the damage they cause to the environment and the effects caused to organisms. Both the positive and negative impacts of nanoparticles are studied to understand how nanoparticles can be used effectively but also detrimentally.

1.1.1 Glioblastomas

GBMs are the most common central nervous system (CNS) tumours; patients diagnosed with GBM have a very short life expectancy, with 17.7 % of patients having a survival rate of one year *(Delgado-López et al. 2016)*. The median survival rate is only 15 months, and in elderly patients, even worse, 8.5 months on average *(De Souza et al. 2022)*. The severity of GBM is reinforced as the survival rate of 5 years is limited to 5 %. These GBM are aggressive, and the low survival rate is due to some key characteristics. One is radio-resistance; chemotherapy is ineffective; another is the tumours high proliferation rate and diffuse infiltration capacity whereby the tumour disperses by integrating into healthy brain tissue which are initially undetectable *(De Souza et al. 2022), (Seker-Polat et al. 2022).*

For the above reasons, there is undoubtedly a need to investigate and research further a treatment method for these GBM to increase the survival rate and reduce the number of deaths. Since current treatment options, such as chemotherapy and surgical resection, are ineffective *(Jin et al. 2022)*, a novel method is required to overcome the current shortcomings. One underdeveloped method that could efficiently kill the tumour without affecting the healthy cells around it is neutron capture therapy (NCT).

1.1.2 Neutron capture therapy

NCT is a method that received a lot of early research attention during the 90s as a possible cancer treatment *(Hawthorne. 1993)*, *(Coderre et al. 1999)* but did not advance and make it through the necessary trials to be an approved treatment used in today's medical field due to poor neutron penetration in deeply seated tumours, difficulty in producing the particles for NCT and the accumulation of them within the tumour *(Dymova et al. 2020)*. However, interest has spiked again as a possible effective treatment for a range of different cancers. This is because of develpments in small footprint accelerator based neutron sources, improvement in nanoparticle synthesis techniques, advancements in targeting peptides and antibodies to help deliver the boron to the tumour and advancement in treatment planning software to optimise treatment delivery *(Jin et al. 2022)*. NCT works by having a neutron absorber such as the isotope ^{10}boron, which has a large neutron capture cross-sectional area of 3838 barns (1 barn = 10^{-24} cm^2), when compared to one of the most abundant isotope in mammal tissue, ^{16}oxygen, which makes 65 % of the human body, has a neutron capture cross-sectional area of 0.00019 barns *(Issa et al. 2013)*. NCT works by firing a neutron beam at a neutron absorber isotope, such as ^{10}boron, which absorbs the thermalised neutrons (neutrons in thermal equilibrium with surrounding medium). Upon neutron capture, the ^{10}boron becomes excited to the ^{11}boron isotope, leading to two simultaneous fission reactions as seen in equations 1.1 and 1.2 *(Issa et al. 2013)*.

$$^{10}B + n_{th} \rightarrow \; ^{11}B = \; ^{4}He^{2+} + \; ^{7}Li^{3+} + 2.79\ MeV \qquad \text{Eq 1.1}$$

$$^{10}B + n_{th} \rightarrow \; ^{11}B = \; ^{4}He^{2+} + \; ^{7}Li^{3+} + E_{\gamma} + 2.79\ MeV \qquad \text{Eq 1.2}$$

The excited ^{11}boron isotope splits producing two high energy ions, He^{2+}alpha particles and a Li^{3+} ion. The alpha particles deliver a toxic radiation dose to kill the GBM cells. The one significant advantage of NCT is that the path length of the alpha particles is shorter than the path length of biological tissue, meaning none of the toxic doses of radiation can spread to the healthy surrounding tissue, making it a very targeted approach to killing the cancerous cells directly *(Dai et al. 2022)*. There have been advancements whereby the neutron absorber isotopes can be delivered via targeting peptides and payload linkers which help deliver the treatment to the desired areas *(Sgouros et al. 2020)*. As GBM being notoriously difficult to access due to integrating into healthy brain tissue, ^{10}B particles accompanied by a targeting peptide or payload linker, would be invaluable to tackle these resistant tumours There are other possible routes for NCT, such as using gadolinium^{155} or gadolinium^{157}, which have a much higher neutron capture cross-sectional area but take a more complicated route to produce the toxic radiation dose to kill the cancerous cells. The essential advantage of using boron is that it is non-toxic and non-radioactive compared to other isotopes available for this process *(Issa et al. 2013).*

1.1.3 The NCT nanoparticle

The critical issue is producing particles with a high enough boron^{10} content, as only 20 % of naturally occurring boron is boron^{10}, and the other 80 % is boron^{11}. Furthermore, the particles must be smaller than 50 nm to effectively permeate across the blood-brain barrier (BBB) to reach the GBM *(Ohta et al. 2020)*. One route for synthesising the necessary particles is using the borohydride (BH_4^-), such as sodium borohydride, as a reducing agent and as a source of boron for the nanoparticles *(Issa et al. 2013)*. The current synthesis routes to produce transition metal–boron alloy nanoparticles require further optimisation to increase the boron content of the alloy. Mixing pattern, concentrations of both the iron salt and borohydride source, addition rates, and pH can all affect the boron content *(Corrias et al. 1993)*, *(Egami, 1984)*, *(Schaefer et al. 2008), (Yang et al. 2019)*. By mixing a transition metal salt with sodium borohydride either via aqueous synthesis or non-aqueous synthesis, the boron content can be as high as 40 % and sizes smaller than 50 nm, meaning the particles can pass through the BBB. However, the standard boron-containing reducing agents would only contain 20 % boron^{10}. If the process were to be effective in producing the alloy particle, further advancements are required to synthesise an enriched boron^{10} borohydride reducing agent so that the alloys contain 40 % boron^{10}, which is a significant amount for NCT *(Issa et al. 2013)*.

A method for synthesising the particles for neutron capture therapy is using a borohydride reducing agent, such as sodium borohydride, as a reducing agent and source of boron. By reducing a metal salt, such as iron chloride, with sodium borohydride an alloyed core containing both iron and boron can be synthesised *(Corrias et al. 1993)*.The transition metal, such as iron, nickel and cobalt would offer the additional properties of making the particles magnetic, meaning purification in the downstream processing is easier by using magnets to separate monometallic gold from the core-shell particles. One issue with producing an alloyed particle of Fe-B for NCT is that oxidation will occur and disrupt the alloy. This poses a great threat when thinking about NCT as a potential novel therapy for cancer. If administered into the body, the effects that the iron or iron oxide-boron nanoparticles have on the cells due to high cytotoxicity would be more damaging to normal cells before being implemented against the tumours *(Malhotra et al. 2020)*.

To overcome this issue an inert shell layer, such as gold, over the Fe-B alloy would stabilise the core from oxidation leading to an effective core-shell particle for NCT. Gold has low toxicity towards human cells, making it safe to use in the body without any adverse effects *(Saqr et al. 2021), (Y. Li et al. 2019)*. A gold shell will maintain the magnetic properties and the boron content required for an effective dose for NCT. The synthesis of core-shell iron-gold particles has already been successfully carried out for medical use, such as MRI scans *(Iancu et al. 2020)*. Due to golds high fluorescence, the gold can be visualised and quantified within specific body areas based on concentration density *(Tarkistani et al. 2021)*.

1.2 Thesis structure

1.2.1 Iron-boron core gold shell nanoparticle synthesis for glioblastomas.

The first two research chapters (chapters 3 + 4) will focus on synthesising the trimetallic nanoparticles of Fe-B@Au. These chapters will combine two sets of methodology. (1) producing an iron-boron alloy core and (2) adding a gold shell to ensure the particle is stabilised and inert, ready for biological testing and NCT. The project aims to optimise previous research to incorporate as much boron as possible, using borohydride as a reducing agent and boron source for the nanoparticle's core. This will provide a baseline, allowing subsequent investigation to be carried out to further increase the content of boron[10]. The second step of the project focuses on implementing existing work on Fe@Au core-shell nanoparticles to coat this iron-boron core and produce a new trimetallic nanoparticle. The advantage of such a nanoparticle is that it incorporates the properties of all three metals, becoming an effective particle which can be used for NCT and drastically increase GBM patient survival. The boron can deliver a toxic dose of radiation, the iron provides magnetic properties to help collect and move the particles around, and gold has very distinguished optical properties and makes the particles inert. After the successful synthesis of the particle, trials can begin on the functionalisation of the gold shell towards the biological side of the project. The gold layer is pivotal as the targeting peptide that attaches to the gold layer via a S-H bond, which has a high affinity to gold, would help deliver the particles to attach to the GBM *(Xue et al. 2014)*.

1.2.2 Synthesis and biological testing of model plastic nanoparticles

The final research chapter (chapter 5) will look at the negative impact of nanoplastics and the effects on cells and the environment. The damage nanoplastics cause is a crucial piece of research due to the rise in plastic waste found in all environments, from rainforests to marine life *(Guzmán et al. 2022), (Nielsen et al. 2020), (Rubio et al. 2020)*. The final research chapter focuses on the effects these plastics have on the MRC-5 cell line, which was originally derived from lung cells. The biological research carried out within chapter 5 will focus predominately on cell toxicity along with DNA damage to analyse and understand how the accumulation of nanoplastics could be damaging to all life forms. Four common waste plastics have been tested: polystyrene (PS), polyethylene (PE), polypropylene (PP) and Polymethyl methacrylate (PMMA), to get a broad range of results from plastic pollution *(Plastics Europe, 2022)*. Over time, plastic waste breaks down into micron and nanoparticles. Plastics have already been found in the food chain through marine life *(Gigault et al. 2016)* and many studies have been undertaken on the toxicity of some of these plastic pollutants *(Soo et al. 2018), (Guzmán et al. 2022), (Rubio et al. 2020)*.

It has been found that not only the plastic micron and nanoparticles are of concern; many processed plastics contain additives to make the plastic more suitable for its intended use. For instance, in the case of coffee cup lids, plasticisers like phthalates or phthalic acid esters are often added to increase flexibility, making the plastic more suitable for its purpose *(Chen et al. 2021)*. These phthalic acid esters have been found in popular drinks plastic bottles such as, lemonade, cola and mineral water in Turkey *(Ustun et al. 2015)*. A range of inorganic materials have also been found in plastics. A study in China found plastics such as polyethylene, polypropylene, polystyrene, polyamide and polyvinyl chloride contained Cd, Cr, Pb, Ag, Cu, Sb, Hg, Fe and Mn which was found at different soil sites *(Tang et al. 2010).*

A study was carried out using 50nm PS NPs on human hematopoietic cell lines *(Rubio et al. 2020).* It was found that in Raji-B and TK6 cell lines, there was an increase in reactive oxygen species (ROS) production and genotoxicity were detected suggesting toxic damage is caused due to plastics breaking down in the environment *(Rubio et al. 2020).* PET NPs of 250nm diameter were tested on RAW 264.7 macrophage cells. and showed that the plastics were easily internalised leading to effects on cell proliferation and small increases in ROS.

The chapter will build upon the research already carried out and expand on the effects of different plastics with a key set of research being carried out around plastic toxicity and DNA damage which can indicate possible long-term effects to human health, animals and marine life.

1.2.3 Thesis chapters

This thesis will be split into six chapters to give a complete overview of the research carried out over the last three years. These being:

Chapter 1 – Introduction: This chapter briefly overviews what this research is based on and the specific challenge that is being tackled.

Chapter 2 – Literature review: This gives a more detailed overview of the area of nanoparticles and NCT to understand and discuss the advantages and disadvantages of different methods. It will detail which method appears to be more effective from prior published research to achieve the goals of trimetallic nanoparticles to tackle GBM.

Chapter 3 – Redox transmetalation in non-aqueous conditions: This chapter will look at the different aspects and reaction pathways of using non-aqueous conditions to form the iron-boron core and the use of redox-transmetalation to take advantage of the reduction potential difference between the core and the shell to form a gold shell around the core. It will look at the conditions which optimise the amount of boron incorporated into the core and optimise the shell formation between two completely different lattice structures.

Chapter 4 – Reverse micelle synthesis Fe-B@Au nanoparticles: This chapter will analyse the reverse micelle method for synthesising core-shell structures and how the reaction pathway occurs in aqueous conditions. It will discuss how controlling the water-to-stabiliser ratio affects the particle size and stability. The key conditions will be analysed to optimise the amount of boron incorporated into the core.

Chapter 5 – Synthesis and biological study of plastic nanoparticles on the MRC-5 cell line: With the growing concern of plastic pollution of micro and nanoplastics entering the food chain, this chapter will look at synthesising plastic nanoparticles from common single use plastic and conducting an in-depth study on what damage is caused to cells focusing on cell toxicity and research into the DNA damage caused by the plastic. This chapter will lay the foundation for future research around DNA damage to continue to propose a mechanism for the damage being caused.

Chapter 6 – Conclusion: An overall evaluation and summary of the research carried out and an overview of the future research to be carried out to advance this research further.

References

Chen, Yuan, Abhishek Kumar, Fan Wei, Quanyin Tan, and Jinhui Li. 2021. “Science of the Total Environment Single-Use Plastics : Production , Usage , Disposal , and Adverse Impacts.” *Science of the Total Environment* 752:141772. doi: 10.1016/j.scitotenv.2020.141772.

Coderre, Jeffrey A., Gerard M. Morris, No Jan, Jeffrey A. Coderrea, and Gerard M. Morrisb. 1999. “The Radiation Biology of Boron Neutron Capture Therapy Linked References Are Available on JSTOR for This Article : The Radiation Biology of Boron Neutron Capture Therapy.” 151(1):1–18.

Corrias, A., G. Ennas, A. Musinu, G. Marongiu, and G. Paschina. 1993. “Amorphous Transition Metal-Boron Ultrafine Particles Prepared by Chemical Methods.” *Chemistry of Materials* 5(12):1722–26. doi: 10.1021/cm00036a009.

Dai, Qi, Qiyao Yang, Xiaoyan Bao, Jiejian Chen, Min Han, and Qichun Wei. 2022. “The Development of Boron Analysis and Imaging in Boron Neutron Capture Therapy (BNCT).” *Molecular Pharmaceutics* 19(2):363–77. doi: 10.1021/acs.molpharmaceut.1c00810.

Delgado-López, P. D., and E. M. Corrales-García. 2016. “Survival in Glioblastoma: A Review on the Impact of Treatment Modalities.” *Clinical and Translational Oncology* 18(11):1062–71. doi: 10.1007/s12094-016-1497-x.

Dymova, Mayya Alexandrovna, Sergey Yurjevich Taskaev, Vladimir Alexandrovich Richter, and Elena Vladimirovna Kuligina. 2020. “Boron Neutron Capture Therapy: Current Status and Future Perspectives.” *Cancer Communications* 40(9):406–21. doi: 10.1002/cac2.12089.

Egami, T. 1984. “Magnetic Amorphous Alloys: Physics and Technological Applications.” *Reports on Progress in Physics* 47(12):1601–1725. doi: 10.1088/0034-4885/47/12/002.

Gigault, Julien, Boris Pedrono, Benoît Maxit, and Alexandra Ter Halle. 2016. “Marine Plastic Litter: The Unanalyzed Nano-Fraction.” *Environmental Science: Nano* 3(2):346–50. doi: 10.1039/c6en00008h.

Guzmán, J. Cristóbal Aguilar, Katarzyna Bejtka, Marco Fontana, Eugenia Valsami Jones, Anaid Meza Villezcas, Rafael Vazquez Duhalt, and Ana G. Rodríguez Hernández. 2022. “Polyethylene Terephthalate Nanoparticles Effect on RAW 264 . 7 Macrophage Cells.” *Microplastics and Nanoplastics* 1–15. doi: 10.1186/s43591-022-00027-1.

Hawthorne, M. Frederick. 1993. “The Role of Chemistry in the Development of Boron Neutron Capture Therapy of Cancer.” *Angewandte Chemie International Edition in English* 32(7):950–84. doi: 10.1002/anie.199309501.

Iancu, Stefania D., Camelia Albu, Liviu Chiriac, Remus Moldovan, Andrei Stefancu, Vlad Moisoiu, Vasile Coman, Laszlo Szabo, Nicolae Leopold, and Zoltán Bálint. 2020. “Assessment of Gold-Coated Iron Oxide Nanoparticles as Negative T2 Contrast Agent in Small Animal MRI Studies.” *International Journal of Nanomedicine* 15:4811–24. doi: 10.2147/IJN.S253184.

Issa, F., J. A. Ioppolo, and L. M. Rendina. 2013. “Boron and Gadolinium Neutron Capture Therapy.” *Comprehensive Inorganic Chemistry II (Second Edition): From Elements to Applications* 3(9):877–900. doi: 10.1016/B978-0-08-097774-4.00335-1.

Jin, Linchun, Yang Wu, and Heike E. Daldrup-link. 2022. “Therapies and Mechanisms of Resistance.” 1–64. doi: 10.1016/j.phrs.2021.105780.Glioblastoma.

Jin, Will H., Crystal Seldon, Michael Butkus, Wolfgang Sauerwein, and Huan B. Giap. 2022. “A Review of Boron Neutron Capture Therapy: Its History and Current Challenges.” *International Journal of Particle Therapy* 9(1):71–82. doi: 10.14338/IJPT-22-00002.1.

Li, Yunqian, Udesh Dhawan, Huey-yuan Wang, Xinrui Liu, and Huan-hsuan Ku. 2019. “Theranostic Iron @ Gold Core – Shell Nanoparticles for Simultaneous Hyperthermia-Chemotherapy Upon.” 1800419:1–14. doi: 10.1002/ppsc.201800419.

MacLeod, Matthew, Hans Peter H. Arp, Mine B. Tekman, and Annika Jahnke. 2021. “The Global Threat from Plastic Pollution.” *Science* 373(6550):61–65. doi: 10.1126/science.abg5433.

Malhotra, Nemi, Jiann Shing Lee, Rhenz Alfred D. Liman, Johnsy Margotte S. Ruallo, Oliver B. Villaflore, Tzong Rong Ger, and Chung Der Hsiao. 2020. “Potential Toxicity of Iron Oxide Magnetic Nanoparticles: A Review.” *Molecules* 25(14):1–26. doi: 10.3390/molecules25143159.

Nielsen, Tobias D., Jacob Hasselbalch, Karl Holmberg, and Johannes Stripple. 2020. “Politics and the Plastic Crisis: A Review throughout the Plastic Life Cycle.” *Wiley Interdisciplinary Reviews: Energy and Environment* 9(1):1–18. doi: 10.1002/wene.360.

Ohta, Seiichi, Emi Kikuchi, Ayumu Ishijima, Takashi Azuma, Ichiro Sakuma, and Taichi Ito. 2020. “Investigating the Optimum Size of Nanoparticles for Their Delivery into the Brain Assisted by Focused Ultrasound-Induced Blood–Brain Barrier Opening.” *Scientific Reports* 10(1):1–13. doi: 10.1038/s41598-020-75253-9.

de Oliveira Gonçalves, Karina, Daniel Perez Vieira, Débora Levy, Sergio Paulo Bydlowski, and Lilia Coronato Courrol. 2020. “Uptake of Silver, Gold, and Hybrids Silver-Iron, Gold-Iron and Silver-Gold Aminolevulinic Acid Nanoparticles by MCF-7 Breast Cancer Cells.” *Photodiagnosis and Photodynamic Therapy* 32(October). doi: 10.1016/j.pdpdt.2020.102080.

Plastics Europe. 2022. “Plastics – the Facts 2022.” *Plastics Europe* (October).

Roopan, Selvaraj Mohana, Tammineni Venkata Surendra, Ganesh Elango, and Subramanian Hari Subbish Kumar. 2014. “Biosynthetic Trends and Future Aspects of Bimetallic Nanoparticles and Its Medicinal Applications.” *Applied Microbiology and Biotechnology* 98(12):5289–5300. doi: 10.1007/s00253-014-5736-1.

Roursgaard, Martin, Monika Hezareh Rothmann, Juliane Schulte, Ioanna Karadimou, Elena Marinelli, and Peter Møller. 2022. “Genotoxicity of Particles From Grinded Plastic Items in Caco-2 and HepG2 Cells.” *Frontiers in Public Health* 10(July). doi: 10.3389/fpubh.2022.906430.

Rubio, Laura, Irene Barguilla, Josefa Domenech, Ricard Marcos, and Alba Hernández. 2020. “Biological Effects, Including Oxidative Stress and Genotoxic Damage, of Polystyrene Nanoparticles in Different Human Hematopoietic Cell Lines.” *Journal of Hazardous Materials* 398(May):122900. doi: 10.1016/j.jhazmat.2020.122900.

Saqr, Ahmed Al, El-sayed Khafagy, Ahmed Alalaiwe, Mohammed F. Aldawsari, Saad M. Alshahrani, Khalid Anwer, Salman Khan, Amr S. Abu Lila, and Hany H. Arab. 2021.

"Synthesis of Gold Nanoparticles by Using Green Machinery : Characterization and In Vitro Toxicity." 1–14.

Schaefer, Zachary L., Xianglin Ke, Peter Schiffer, and Raymond E. Schaak. 2008. "Direct Solution Synthesis, Reaction Pathway Studies, and Structural Characterization of Crystalline Ni 3B Nanoparticles." *Journal of Physical Chemistry C* 112(50):19846–51. doi: 10.1021/jp8082503.

Seker-Polat, Fidan, Nareg Pinarbasi Degirmenci, Ihsan Solaroglu, and Tugba Bagci-Onder. 2022. "Tumor Cell Infiltration into the Brain in Glioblastoma: From Mechanisms to Clinical Perspectives." *Cancers* 14(2). doi: 10.3390/cancers14020443.

Sgouros, George, Lisa Bodei, Michael R. McDevitt, and Jessie R. Nedrow. 2020. "Radiopharmaceutical Therapy in Cancer: Clinical Advances and Challenges." *Nature Reviews Drug Discovery* 19(9):589–608. doi: 10.1038/s41573-020-0073-9.

Soo, Jin, Youn-joo Jung, Nam-hui Hong, Sang Hee, and June-woo Park. 2018. "Toxicological e Ff Ects of Irregularly Shaped and Spherical Microplastics in a Marine Teleost , the Sheepshead Minnow (Cyprinodon Variegatus)." *Marine Pollution Bulletin* 129(1):231–40. doi: 10.1016/j.marpolbul.2018.02.039.

de Souza, Izadora, Maria Carolina Clares Ramalho, Camila Banca Guedes, Isabeli Yumi Araújo Osawa, Linda Karolynne Seregni Monteiro, Luciana Rodrigues Gomes, and Clarissa Ribeiro Reily Rocha. 2022. "Ferroptosis Modulation: Potential Therapeutic Target for Glioblastoma Treatment." *International Journal of Molecular Sciences* 23(13). doi: 10.3390/ijms23136879.

Tang, Xianjin, Chaofeng Shen, Lei Chen, Xi Xiao, Jingyan Wu, Muhammad I. Khan, Changming Dou, and Yingxu Chen. 2010. "Inorganic and Organic Pollution in Agricultural Soil from an Emerging E-Waste Recycling Town in Taizhou Area, China." *Journal of Soils and Sediments* 10(5):895–906. doi: 10.1007/s11368-010-0252-0.

Tarkistani, Mariam Abdulaziz M., Varsha Komalla, and Veysel Kayser. 2021. "Recent Advances in the Use of Iron – Gold Hybrid Nanoparticles for Biomedical Applications."

Tsuchikama, Kyoji, Yasuaki Anami, Summer Y. Y. Ha, and Chisato M. Yamazaki. 2024. "Exploring the next Generation of Antibody–Drug Conjugates." *Nature Reviews Clinical Oncology* 21(3):203–23. doi: 10.1038/s41571-023-00850-2.

Ustun, Ihsan, Sana Sungur, and Ramazan Okur. 2015. "Determination of Phthalates Migrating from Plastic Containers into Beverages." 222–28. doi: 10.1007/s12161-014-9896-5.

Xue, Yurui, Xun Li, Hongbin Li, and Wenke Zhang. 2014. "Quantifying Thiol-Gold Interactions towards the Efficient Strength Control." *Nature Communications* 5. doi: 10.1038/ncomms5348.

Yang, Chuncheng, Mengchun Yu, Xiuling Cao, and Xiufang Bian. 2019. "Application of Amorphous Nanoparticle Fe-B Magnetic Fluid in Wastewater Treatment." *Nano* 14(9). doi: 10.1142/S1793292019501194.

Chapter 2 – Literature Review.

2.1 Introduction

Recently, nanotechnology has come to the forefront of research and development due to its multifunctional uses across many fields of science and engineering, such as chemistry / chemical engineering, biology, medicine, physics and material science. The prefix nano comes from the Greek word ‘nanos’, which means ‘dwarf’. Nano refers to things one billionth of its size *(Charles P. Poole et al. 2003)*. Many scientists have continuously developed the field of nanotechnology, but one key scientist was Richard Feynman, an American physicist known as the ‘Father of nanotechnology’, who in the mid-20th century delivered a lecture at the American Physical Society on how all books can fit in a pamphlet. Different methods were explained on how different atoms and molecules can be transformed into smaller forms using different tools *(Charles et al. 2003)*. These lectures ignited the change in the field of science. Another key scientist who added to the development of nanotechnology was Eric Drexler, who wrote a book called ‘Engines of Creation’. Within this book, Drexler explained nanotechnology in terms of the nanometric scale so that it can be defined as the application of controlling the properties of matter at the molecular level *(Sharma et al. 2019).*

Nanotechnology plays a significant role in many fields due to the change in properties at the nanoscale. For example, the melting point, fluorescence, electrical conductivity and chemical permeability are all function of the size of the particle *(Asha et al. 2020).* One common example that displays this change in properties is gold NPs optical properties as the size changes. As the particles become smaller there is a red shift in the UV-Vis spectra and as the size increases or change in shape, there may be a blue shift. The change is due to the scattering cross section of the photos with different wavelengths of light *(Jin et al. 2022)*. It allows the power to manipulate atoms or molecules to achieve predefined morphologies and sizes to obtain the properties required for the process *(Ramsden. 2016)*. There are many uses of nanoparticles, such as the role of nanoparticles in drug delivery *(Mitchell et al. 2021)*, cancer treatment *(Gavas et al. 2021)*, environmental uses for wastewater management *(Scaria, et al. 2020)* and making chemical reactions viable through nanocatalysts *(Lee et al. 2022)*.

2.2 Nanoparticles

A nanoparticle (NP) is typically defined as a particle with one dimension between 1 and 100 nanometres (nm) *(Dolai et al. 2021)*. A nanoparticle with all three dimensions in the nanoscale is known as a isodimensional NP *(Sharma et al. 2019)*. The definition of NPs changes depending on the field and material being discussed. A theoretical definition is that NPs are defined as the combination of hundreds of atoms or molecules with properties between molecular and bulk properties *(Jin et al. 2021)*. NPs can be made of the same or different atoms to form crystalline or amorphous NPs *(Ferrando et al. 2008)*. The small size leads to very different physical, chemical, and electrical properties than the bulk properties due to the surface area to volume ratio, higher particle surface binding without loss of composite ductility *(Coetzee et al. 2020)* which usually leads to NPs superior, novel properties that are not attainable in the bulk form *(Sedighi et al. 2014).* The surface area to volume ratio makes nanomaterials excellent catalysts, improving the selectivity, yield of a chemical process *(Sedighi et al. 2014)*. However, there is a critical range in particle size which the nanoparticle must be to obtain these properties. Another factor which changes down at the nanoscale is the electrical properties. Nanomaterials can increase the conductivity in ceramics but increase resistance in metals. This is because in nanomaterials, the quantum effect takes over compared to delocalised electrons in bulk material *(Mekuye et al. 2023)*. The energy bands become replaced with discrete energy states that can lead to bulk conductive materials becoming semiconductors or insulators *(Mekuye et al. 2023)*. Due to the NP size, they are subject to Brownian motion and in general will remain in suspension within a fluid. However, other factors do cause NPs to diffuse and aggregate due to size, mass and surface charge still leading to the requirement of stabilisers *(Kang et al. 2019)*. The NPs are smaller than the wavelength of visible light, meaning they cannot be seen with optical microscopes and require electron microscopes to visualise them *(Irfan. 2021)*. NPs play an influential role in our daily lives. For example, titanium dioxide NPs are a crucial component in sunscreen products that only allow visible light to pass through to the skin. At the same time, ultraviolet rays are reflected by the titanium dioxide NPs *(Vaudagna et al. 2023)*.

2.3 Synthesis routes

The synthesis routes for NPs are split into two main routes: top-down and bottom-up approaches. Top-down approaches start with large bulk material and use some form of physical method to break the particles down into NPs. This method disassembles bulk solids via mechanical methods into finer pieces until they are constituted of only a few atoms. This approach is preferred in industrial settings due to being able to process a large amount of bulk material at once *(Charitidis et al. 2014)*. Physical methods rely on mechanical tools which limits the smallest size they can reach, but they are generally highly reproducible and flexible *(Amusat et al. 2021)*.

In contrast, bottom-up processes assemble atoms/molecules. Atoms or molecules are the building blocks to produce nanoparticles, nanotubes, nanorods, thin films or layered structures. This approach is preferred in research due to having a much greater control of the size and morphology *(Ijaz et al. 2020)*. Figure 2.1 displays a simple diagram of the difference between top-down and bottom-up processes.

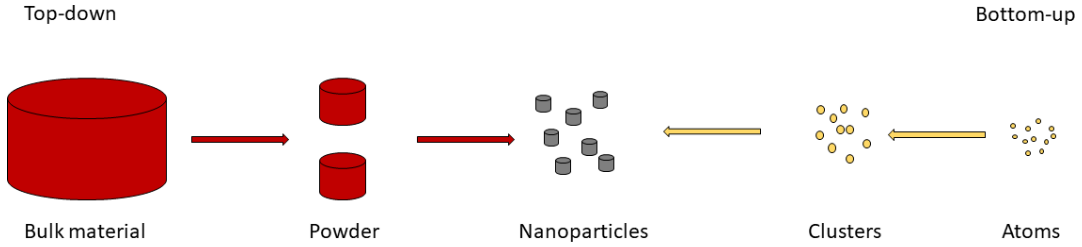

Figure 2.1: Schematic representation of the building of Nanoparticles. Adapted from *(Mazhar et al. 2017)*.

Synthesis routes for nanoparticles can further be broken down into three different methods. These are physical, chemical, and biological methods. Each process takes a different route to synthesise the NPs. In Figure 2.2, there are multiple different synthesis routes for each method. However, the critical issue with many NP synthesis methods is the cost of production. Physical methods are usually energy-intensive; chemical methods can use expensive reagents and biological methods are limited to the experimental conditions used. In addition, one challenge of these processes would be finding a feasible method to scale the processes up from a lab scale to an industrial scale process. Figure 2.2 shows a flow diagram representing only a few of the different synthesis routes available to produce NPs. The advantages and disadvantages of these methods are discussed below.

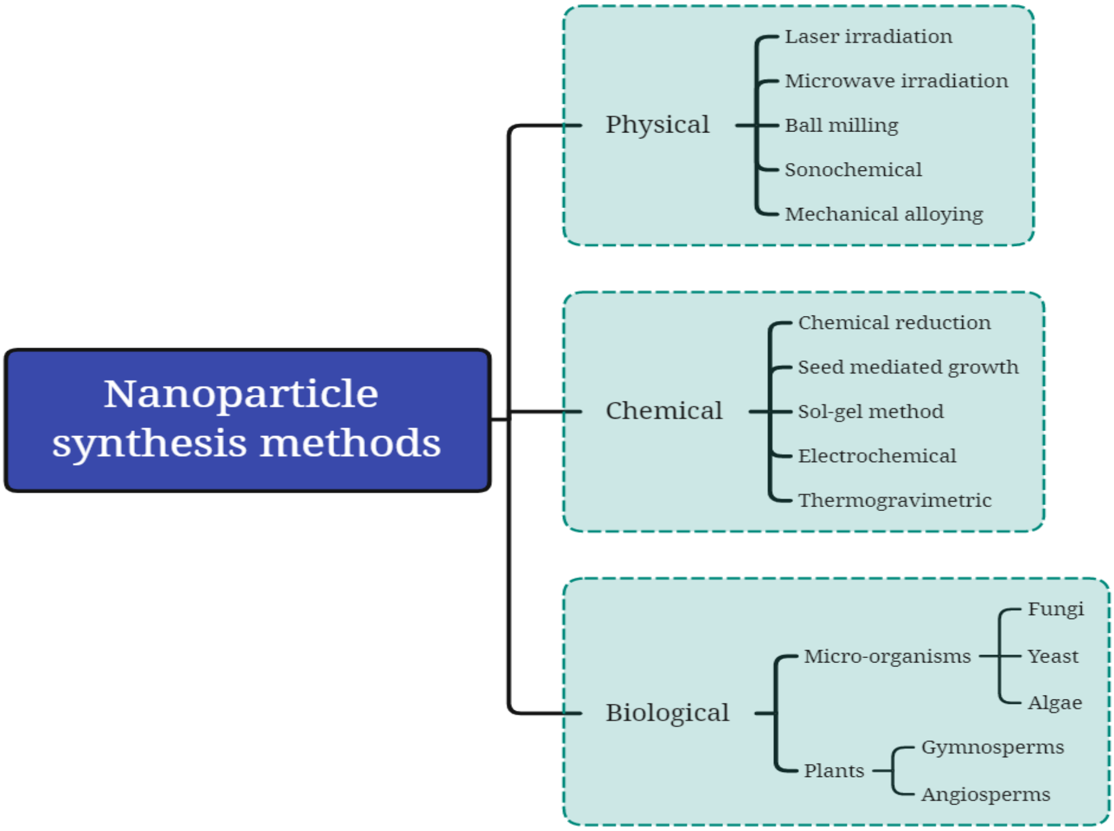

Figure 2.2: Various nanoparticle synthesis routes.

2.3.1 Physical methods

Physical methods hold certain advantages over other methods, such that there is a lower requirement for solvents or other chemicals in comparison to chemical and biological methods. In ball milling, it is possible to only require the material that needs milling. In laser irradiation requires a powerful laser to synthesise NPs. Platinum-gold (Pt-Au) bimetallic NPs have been synthesised in this way by dissolving the precursors in the necessary solvent and irradiated *(Chau et al. 2011)*, *(Fathima et al. 2021)*. Many of these physical methods lead to a large distribution in particle size, as seen in Figure 2.3. Conventional physical methods produce predominately micron-sized particles. However, the new advancements in these physical methods have produced smaller particles but still with a larger size distribution. Physical methods are usually energy intensive due to physically breaking the bulk material into smaller particles. By fine tuning the variables in laser ablation, as a more advanced top-down technique can produce small NPs from 10-200 nm *(Semaltianos. 2010)*, *(Fathima et al. 2021)*, *(Isa et al. 2022)*. However, this process can be very complicated, with several variables needing to be taken into consideration for the desired particles to be produced in the NP range, such as the wavelength, pulse duration, pulse energy, repetition rate, focal distance, scanning speed and laser fluence. All these factors require optimisation to synthesise NPs with a tighter size distribution in comparison to conventional ball milling.

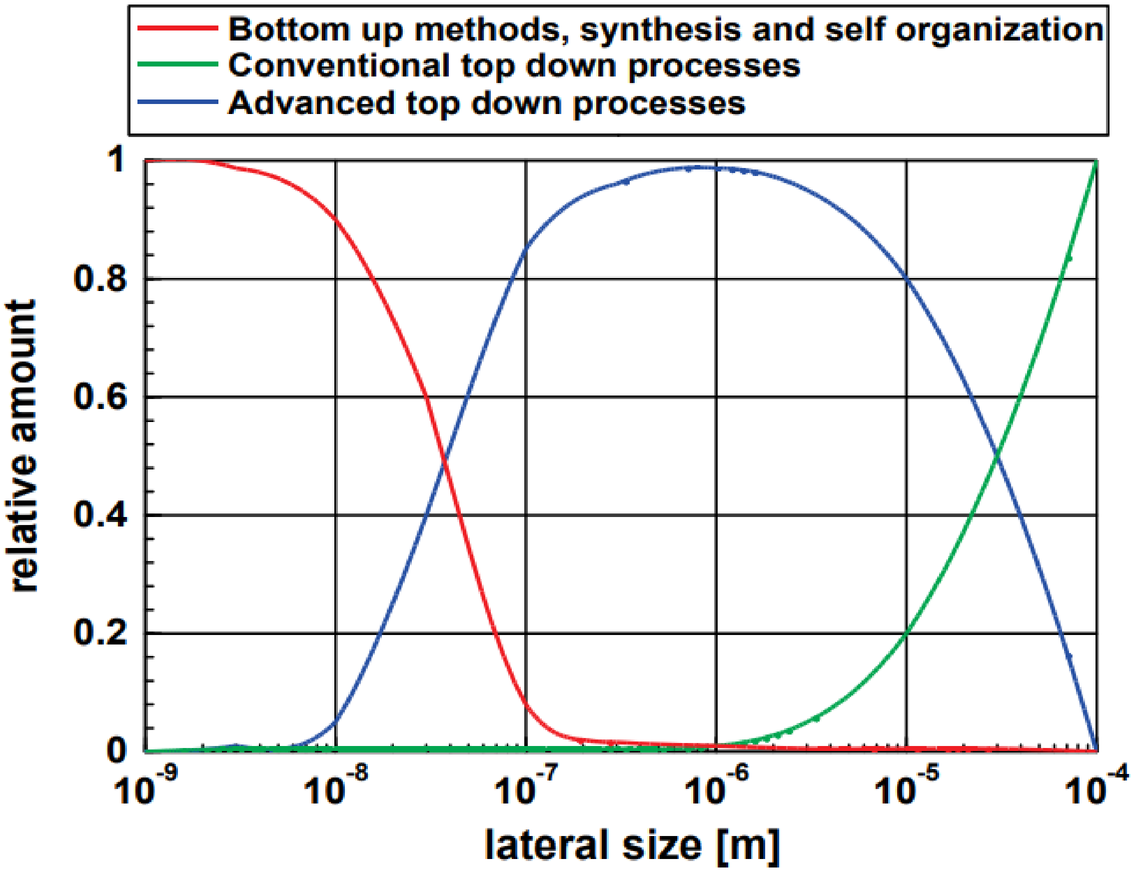

Figure 2.3: Projected lateral limits of different NP synthesis techniques *(Vollath, 2013)*.

2.3.2 Chemical methods

Chemical methods are relatively simple and can achieve a very tight size distribution in a comparatively short period. Using chemical methods to synthesise NPs is an effective method to the control size and morphology of the particle to achieve the desired properties. Chemical reduction is by far the most common technique used to synthesise NPs. Changing small variables of a process in a chemical reduction reaction leads to subtle differences in the type of NP produced *(Lee et al. 2015)*, *(Arno et al. 2020)*. These changes could be size, shape and type of nanoalloys produced. An example of a chemical method is sol-gel synthesis. The monomers are converted to colloidal suspensions, which behave as a precursor of integrated networks *(Mazhar et al. 2017)*, *(Arya et al. 2021)*. There are four steps which occur for the synthesis of NPs via sol-gel synthesis. These are hydrolysis, condensation, growth and agglomeration of the particles *(Das et al. 2013)*. Cu-Ce oxides can be produced in this way: stochiometric amounts of both metal salts with the presence of urea synthesise Cu-Ce oxides in solution and was kept at 80 °C until a gel formed. The gel was decomposed by raising the temperature to 250 °C and then calcinating above 600 °C to form the NPs *(Mazhar et al. 2017)*.

In Figure 2.3, chemical methods yield small NPs, with the average distribution being less than 10 nm with a tighter size distribution than any of the physical top-down approaches *(Noordeen et al. 2013), (Wu et al. 2011), (Daoush et al. 2015) (Kang et al. 2012)*. Chemical methods can control the size of the nanoparticle. For instance, with reverse micelle processes, changing the molar ratio of water to cetrimonium bromide (CTAB) tightly controls the size of the reverse micelle and, therefore, the size of the nanoparticle formed within it *(Kvitek et al. 2019)*, *(Elmi et al. 2022)*. One of the critical factors in the chemical reduction approach is the reducing agent chosen for the process. In Table 2.1 numerous reducing agents have advantages and disadvantages for specific processes. Each reducing agent may lead to a different-sized NP or a different morphology or structure of bimetallic NP. For example, if a mild reducing agent were used to synthesise Au-Pd NPs, the metal salt with the higher redox potential would be reduced first and form the core of the NP and then the salt with the lower redox potential would become the shell. Slow-reduction kinetics can benefit from seeding one NP on top of another to form core-shell NPs. If a stronger reducing agent, such as ascorbic acid, were used, both metal salts would be reduced simultaneously and lead to an alloyed or two monometallic distributions of the NPs *(Zhang et al. 2020)*. The reducing agent used can vastly affect the structure of bimetallic NPs.

Another example is sodium borohydride, a common strong reducing agent used to form NPs. Sodium borohydride was used in *Deraedt et al. 2014* to form monometallic Au NPs with specific reaction conditions. However, altering the reaction conditions and adjusting the pH along with other factors can lead to sodium borohydride being a source of boron to form bimetallic NPs, as shown in *(Wu et al. 2011)* and trimetallic particles in *Wang et al. 2020* where Co-Cu-B NPs were formed through using $NaBH_4$ as a source of boron to alter the properties. With a very high pH, $CoCl_2$ and $NaBH_4$ produce bimetallic Co-B NPs rather than monometallic Co NPs.

Table 2.1: Comparison of different reducing agents and metals reduced by these agents.

Reducing agent	Metals reduced	Size of nanoparticle (nm)	Reference
Sodium-Naphthylamide	B, Mo, W, Fe, Ru, Re, Au and Zn	<10	*(Schöttle et al. 2015), (Pickering et al. 2007), (Schulz-Dobric et al. 2005)*
	Pt-Ni	<21	*(Leonard et al. 2011)*
	Pt_3-Ti	<3.3	*(Saravanan et al. 2010)*
Sodium borohydride	Cu, Ag, Ni, Au, Sn	<20 15-85	*(Ansari et al. 2018), (Chee et al. 2012)* *(Noordeen et al. 2013), (Wu et al. 2011), (Daoush et al. 2015)* *(Kang et al. 2012)*
	Co-B,	<7	
	Pt-Ni	<16	
	Pd-Co	<12.51	
	Fe-Ni	10-30	
	Ni-Pd		
Sodium citrate	Au, Ag	50	*(Grys et al. 2020)*
Hydrogen	Co-Pt	18-32	*(Sui et al. 2003)*
	Ni, Co		*(Forsman et al. 2008)*
Hydrazine	Ni,	50	(Z. G. Wu, 2011)
	Cu	2-10	*(Ong et al. 2014)*
	Fe-Co-Ni	60	*(Chokprasombat et al. 2016)*
Ascorbic acid	Au-Pt-Pd	48.3	*(Chen et al. 2018)*
	Au	22-42	*(Khan et al. 2013)*
	Mn_2O_3, Ag, Cu, Co_3O_4, Fe_2O_3, MoO_2	<28.7	*(Khorasani-Motlagh et al. 2010)*

2.3.3 Biological methods

Recently, significant concerns about the environmental impacts of industrial processes, with new regulations coming in to hit carbon neutral by 2050 *(Schreyer et al. 2020)*, have led to a surge in research into biological methods to produce products in a greener way. Processes with microorganisms or leaf extract as the reducing agent and/or stabiliser led to a more environmentally friendly process with fewer by-products and a smaller energy requirement *(Bhardwaj et al. 2020)*. In previous studies, fungi, algae, bacteria, and viruses have been used to synthesise monometallic NPs using two synthesis routes via intracellular or extracellular processes *(Khatami et al. 2018), (Patil et al. 2019) (Tomar et al. 2013) (Tamuly et al. 2013)*. Microorganisms are capable of reducing metals due to reductase enzymes that help accumulate and reduce the metals and the cell removes them through chelation *(Jadoun et al. 2022)*.The metal salt reduction process occurs by the proteins and enzymes within the microorganisms *(Mohamad et al. 2013)*. Yeast was used to synthesise Au-Ag NPs via extracellular processes, producing NPs as small as 9-25 nm. Yeast extract was used as a reducing agent and stabiliser which contains carbohydrates, vitamins, and amino Acids that are able to reduce and cap the metal NPs *(Jadoun et al. 2022)*. The process was carried out at 30 °C with no toxic chemical compounds, meaning very few harmful waste products were produced *(Zheng et al. 2010)*. *Elmi et al. 2022* used yeast where selenium nanoparticles with an average size of 71.14 ± 18.17 nm are formed using biological materials.

Leaf extracts can be an effective and green way of reducing and capping NPs. Plant extracts are effective reducing agents as they contain phytochemicals and antioxidants that can reduce and cap NPs from the aromatic, ester and methyl groups present within the organic material *(Jadoun et al. 2022)*. Neem leaf has been used as a reducing and capping agent to synthesis Au-Ag NPs in successive steps. The aromatic compounds, ester linkages and methyl groups stabilised and capped the bimetallic NP with a size range of 50-100 nm *(Shankar et al. 2004)*. The leaf extract of the capsicum Chinese plant was used to form gold and silver NPs 16.76 ± 0.32 and 20.67 ± 0.26 nm, respectively *(Elmi et al. 2022)*, showing that biological reducing agents such as leaf extract can produce a tight and small size distribution while minimising the toxic waste formed. These green processes can be effective ways to synthesise NPs as the leaf extract can be the reducing and capping agent at low temperatures, meaning the process is not energy intensive, cheaper and environmentally friendly. This would be an effective method for producing the desired NPs but for the core-shell NPs for the treatment of glioblastomas a source of boron is required which is not possible using biological methods at present.

2.3.4 Comparison

When comparing chemical methods to physical methods the advantages are that the techniques used are relatively simple, economical and can achieve a tight size distribution. There is a much higher tuneability in producing the desired NP when compared to physical methods which is challenging to finetune and adjust the size and morphology for different properties.

Physical methods are effective at producing a large quantity of microparticles and NPs, as seen in Figure 2.3. The conventional mechanical methods tend to produce the wide size distribution or micro/nanoparticles, whereas advanced top-down approaches that are continually advancing are producing narrower size distributions with smaller particles being produced. *Van Devener et al. 2009* uses an advanced physical ball milling method to produce monometallic boron NPs and, in fact, synthesised NPs within the range of 35-60 nm. Whereas, when regular ball milling is used, bismuth titanate can be formed and reach a size of 535 ± 50 nm after milling for 22 hours *(Yu et al. 2021)*, which shows that depending on how advanced and the power of the physical grinding method can vastly change the size of the particle even after grinding for 22 hours. However, with the high energy requirements with most top-down approaches, chemical methods are more effective in producing NPs with a narrow size distribution with small NPs as seen from Figure 2.4 and Table 2.1. In *Yan et al. 2013*, a Gd-Au bimetallic NP is synthesised with an average size of 3.20 ± 0.35 nm with a specified morphology and smaller NP when compared to the physical ball milling method.

When comparing chemical and biological methods to physical methods one disadvantage is the scale of production in research is meagre, producing milligrams of material. The scaling up process of chemical and biological methods leads to further challenges which more research is required into the economics of scale.. *Schöttle et al. 2015* reviewed the synthesis of various monometallic NPs using sodium naphthylamide under inert conditions. There would be significant challenges in scaling up *Schöttle et al. 2015* methodology due to the inert and toxic chemicals that are required that would need disposal. Whereas with physical methods, which are energy intensive, leave little toxic by-products.

One advantage of using biological methods over chemical and physical methods is that most experiments are completed at room temperature and pressure, or very mild conditions are required to not damage or affect the microorganisms or leaf extract. In *Zhan et al. 2011*, Au-Pd NPs were synthesised using Cacumen Platycladi (CP) leaf extract to reduce and cap the bimetallic NPs, which led to an average NP size of 7.4 nm. Biological methods can be as effective as chemical methods, synthesising very small NPs in a similar range to that in Table 2.1 via chemical methods. Similarly, *Hawar et al. 2022*, used alhaji graecorum leaf extract to synthesise Ag NPs in very mild conditions of 35 °C for 15 minutes to synthesise the particles with a size distribution between 22-36 nm. These biological methods produce little harmful waste that needs disposal due to not using potent reducing agents. In many cases, the leaf extract acts as a reducing agent and a stabiliser. However, there are some cases where elevated temperatures are used. In *Song et al. 2008*, Au-Ag NPs were synthesised using Diospyros kaki leaf extract at a temperature of 90 °C, leading to a particle size in the range of 50-500 nm. The leaf extract was used as a reducing and capping agent. The large size distribution was due to the interactions between the bioorganic capping molecules bound to the gold and silver nanoparticles, which led to agglomeration. Even though the process was greener due to the organic leaf extract, additional interactions were taking place, increasing the size of the particles.

In chemical reduction methods, a strong reducing agent, such as sodium borohydride, produces either monometallic or bimetallic NPs, where another metal is used to cap and stabilise the NP, called a core-shell NP, or alloyed where there is a random or structured configuration *(Yan et al. 2013).* Likewise, the advantage of chemical methods over biological methods is that the end use of the NP can be used in high-temperature situations, such as for catalysis in fuel cells *(Wu et al. 2018)*. When biological matter is used as the capping agent for the final stabilisation of the NPs, such as microorganisms, which can be reused to synthesise more NPs, the microorganisms would be significantly affected by the high temperatures, leading to them dying and reducing the yield of NPs produced that may destabilise the NPs produced due to a reduced amount of stabiliser produced. Pd-Cu bimetallic NPs were synthesised to catalyse fuel cell reactions such as oxygen reduction reaction (ORR) *(Gholinejad et al. 2021)*. Within this process, the temperatures the catalyst are exposed to are above 250 °C. At these temperatures, the leaf extract which would have a lower boiling point that inorganic material would be affected and cause destabilisation to the NP. It could be advantageous to synthesise NPs via these biological methods and purposefully burn off the organic material to be left with a pure monometallic or bimetallic NP that can have a chemical stabiliser added afterwards, such as 1-dodecanethiol, for the stabilisation of Au particles to take advantage of both the biological synthesis with a chemical stabiliser. Biological stabilisers may be a problem for medical use as further interactions could take place in the body and slow or stop the NP from reaching the desired area of the body.

2.3.5 Selection of methods

Overall, the most effective method of NP synthesis for this research is chemical methods due to having greater control of the reaction conditions, narrow size distribution, small NPs and being able to use the desired chemicals to optimise the process for NCT.

With chemical methods being the most effective for NP synthesis, the reverse micelle is an effective and commonly used technique for synthesising NPs and nanoalloys due to the highly tuneable size of the micelle to control the size of the NPs *(Zhang et al. 2020)*. It offers very reproducible results, as shown in Figure 2.4, with very small NPs produced with various reducing agents. Even though reverse micelles use many chemicals, such as CTAB, to stabilise the micelle, the size of the monometallic or bimetallic particle can be tightly controlled by the nanometre by changing the water to CTAB molar ratio. In

Kvitek et al. 2019, Fe@Au NPs were formed whereby the water to CTAB ratio of 8 was used for the core, which led to a core size of 8 nm. To incorporate the shell, the micelle water to CTAB ratio was expanded to 12 to form a shell of 2 nm thickness. The core or shell size can be controlled by the molar ratio of water and CTAB, giving that tight control required to form particles. The CTAB is a cationic surfactant with a positively charged hydrophilic headgroup with a neutral and hydrophobic tail that repels other micelles via steric effects. The CTAB starts to cap the water to form micelles whereby if you increase the CTAB to water ratio then there is more CTAB available to stabilise the micelle leading to a smaller micelle. However, as the water to CTAB ratio increases and there is less stabiliser available to cap the water leading to larger micelles. A key variable is the critical micelle concentration (CMC) in the formation of micelles. The CMC is the lowest concentration of stabiliser required for micelle aggregation to begin and measures the thermodynamic stability of the micelles *(Goronja et al. 2016)*.

Reverse micelles can promote the seeding of two materials with large lattice mismatch by controlling the size and shape of the micelle. In *Kvitek et al. 2019*, when forming Fe core and Au shell NPs, by controlling the expansion of the micelle to incorporate a shell layer means the gold nanoseeds will be formed in close proximity to the Fe core with little space to grow forcing the seeding at the surface where there is a high energy barrier due to difference in lattice structures. Using a method that does note promote the seeding of nanoparticles with different lattice structures would lead to two distribution of the Fe and Au NPs. There are many factors that can be controlled to fine tune the variables of the particles formed. Micelles that form aggregates for having a greater amount of stabiliser than the CMC have a typical shape of often being spherical or cylindrical and bilayer in shape *(Perumal et al. 2022)*. However, the concentration of the surfactant, the temperature of the micelle solution and pH can affect the size and shape of the micelle *(Goyal et al. 2017)*. Within casein micelles, the micelle size and polydispersity decreased with an increase in temperature with a micelle size of 76.4 ± 5.3 nm at 6 °C, 77.4 ± 1.9 nm at 20 °C, and 137.3 ± 2.7 nm at 50 °C *(Beliciu et al. 2009).* The decrease in micelle size was due to the increase in temperature led to an increase in the strength of the hydrophobic bonds *(Beliciu et al. 2009)*. The temperature also affects the CMC due to an increase in temperature leading to an increase in solubility of the surfactants and ease of forming micelles further complementing the strength in hydrophobic bonds *(Abooali et al. 2023)*. The pH can affect both the size and shape of the micelle. In *Patel et al. 2014*, it was found in micelles formed using Trition X-100, that a decrease in pH using cinnamic acid favoured micelle growth at low temperatures and that the shape of the micelles changed from ellipsoidal to rod-like in acidic conditions but spherical in basic conditions. This is due to cinnamic acid at low pH becoming nonionised and hydrophobic which gets solubilised in the micelle leading to greater surfactant aggregation into micelles (*Patel et al. 2014*).

A method which is less commonly used but could be coupled with a reverse micelle process and further promote the seeding of different lattice-structured metals is redox-transmetalation *(Ban et al. 2005)*, *(Chen et al. 2009)*, which is predominately used for core-shell nanoparticle structures where the reduction potential of the core is much lower than that of the shell material. The core material is used as the reducing agent for the shell material to further increase the chances of seeding at the surface of the core even when there are significant lattice mismatches due to being reduced at the surface of the core material. This takes the advantages of both reverse micelle method and redox-transmetalation to form thin shell layers. However, the redox–transmetalation process is not at the forefront of research. It is less commonly published, which may be due to challenges to reproduce or more effective and straightforward methods to produce the desired core-shell structure.

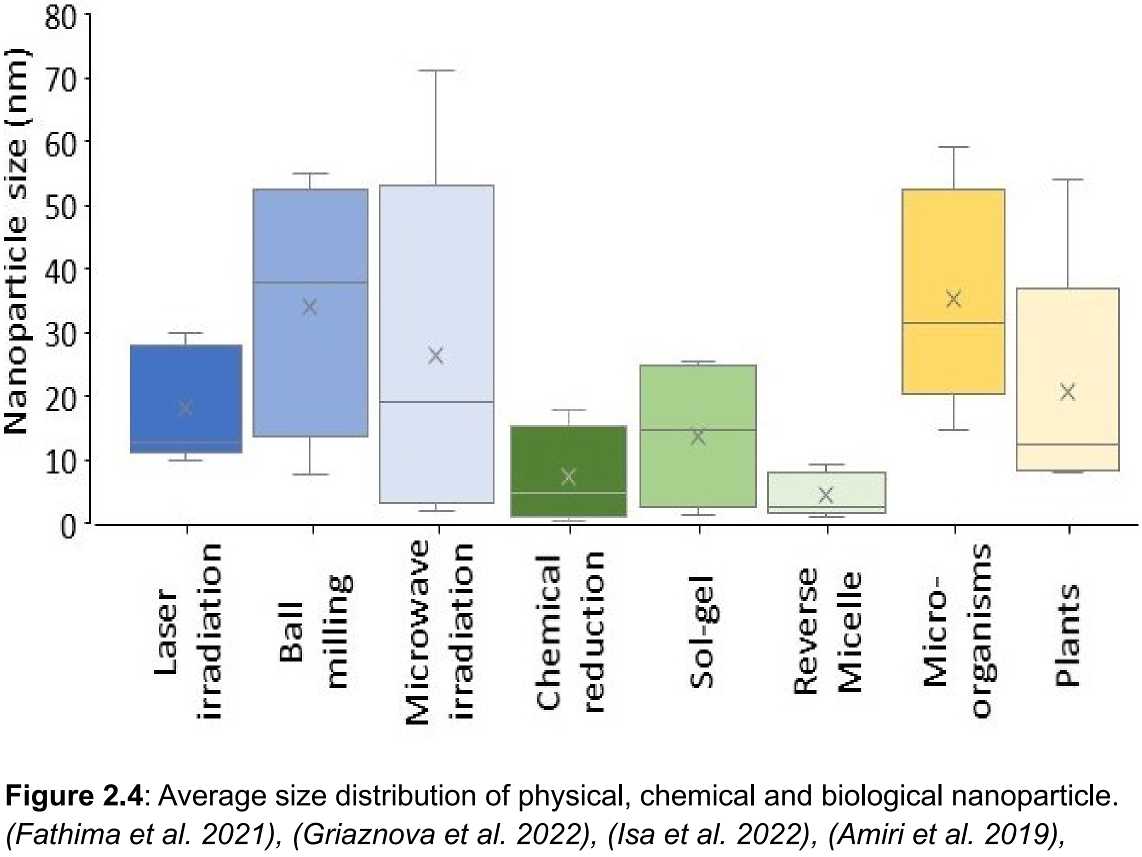

Figure 2.4: Average size distribution of physical, chemical and biological nanoparticle. *(Fathima et al. 2021), (Griaznova et al. 2022), (Isa et al. 2022), (Amiri et al. 2019), (Amusat et al. 2021), (Navidpour et al. 2020), (Joseph et al. 2015), (Kuang et al. 2019), (Lomelí-Rosales et al. 2022), (Chen et al. 2018), (Da Silva et al. 2017), (Peng et al. 2020), (Arachchige et al. 2006), (Arya et al. 2021), (Mahajan et al. 2020), (D. Chen et al. 2009), (Kvitek et al. 2019), (Shiri et al. 2019), (Bhardwaj et al. 2020), (Herman et al. 2020), (Jadoun et al. 2022), (Wang et al. 2016), (Younis et al. 2023)*

2.4 Monometallic nanoparticles

Monometallic NPs, as the name suggests, are made up of a single metal. NPs have a high surface energy due to their surface area to volume ratio and without stabilisation would lead to the NPs agglomerating aggregating leading to larger NPs that may change the properties of the *(Ansari et al. 2018)*. Copper NPs have attracted attention in research due to the low-cost production. The application areas of copper NPs include adsorbents / filters, electronic devices *(Szekeres et al. 2018)*, catalysts *(Zhu et al. 2022)* and optoelectronics *(Jhuang et al. 2021)*. During the Covid-19 pandemic, it was found by the New England Medical Journal that no viable SARS-CoV-2 were measured after 4 hours, and no viable SARS-CoV-1 were measured after 8 hours on copper surfaces in comparison to stainless steel surfaces which the virus was still present after 72 hours (Patients et al. 2020). This showing that copper NPs imbedded into different materials could lead to a highly virucidal material that can reduce the spread of disease.

2.5 Bimetallic nanoparticles

Bimetallic NPs, unlike monometallic NPs, are comprised of two different metals. The properties of the bimetallic NPs depend on the structure of the bimetallic NP, the size of the entire NP as well as the individual sizes of each metal NP and the concentration of each metal present. Advancements are taking place in synthesis routes allowing for an array of NP shapes that have been synthesised to form monometallic NPs but optimisation means that bimetallic NP structures such as cube *(Kaur et al. 2021)*, hexagonal *(Ma et al. 2022)*, disc *(Mandari et al. 2021)*, wire *(Dean et al. 2010)*, rod *(Umesh et al. 2021)* and tube *(Niu et al. 2022)* can be achieved.

Song et al. 2004 showed that predominately the size of the NPs affects the magnetic properties of the material. However, the shape of the NP us a dominating factor for the coercivity which is the ability of a ferromagnetic material to resist demagnetisation. Other shape effects on bimetallic NPs can change the particles' catalytic activity and selectivity *(Lee et al. 2006)*, optical properties *(Millstone et al. 2009)* and melting points *(Gupta et al. 2008)* due to the number of surface atoms to volume as the shape changes.. Figure 2.5 displays six main ordering patterns of bimetallic NPs. Figure 2.5A, core-shell is the most common and widely researched *(Swierzy et al. 2022)*. These types of bimetallic NPs consist of one core metal surrounded by another metal NP, similar to Figure 2.5B and C, where some mixing between the shell and core occurs but keeping an AcoreBshell structure *(Ferrando et al. 2008)*. Figure 2.5D involves subclusters that may share a mixed interface. Figure 2.5E, can take highly ordered structures or random mixing can take place and alloyed NPs in Figure 2.5F *(Arora et al. 2020), (Y. Yu et al. 2021)*.

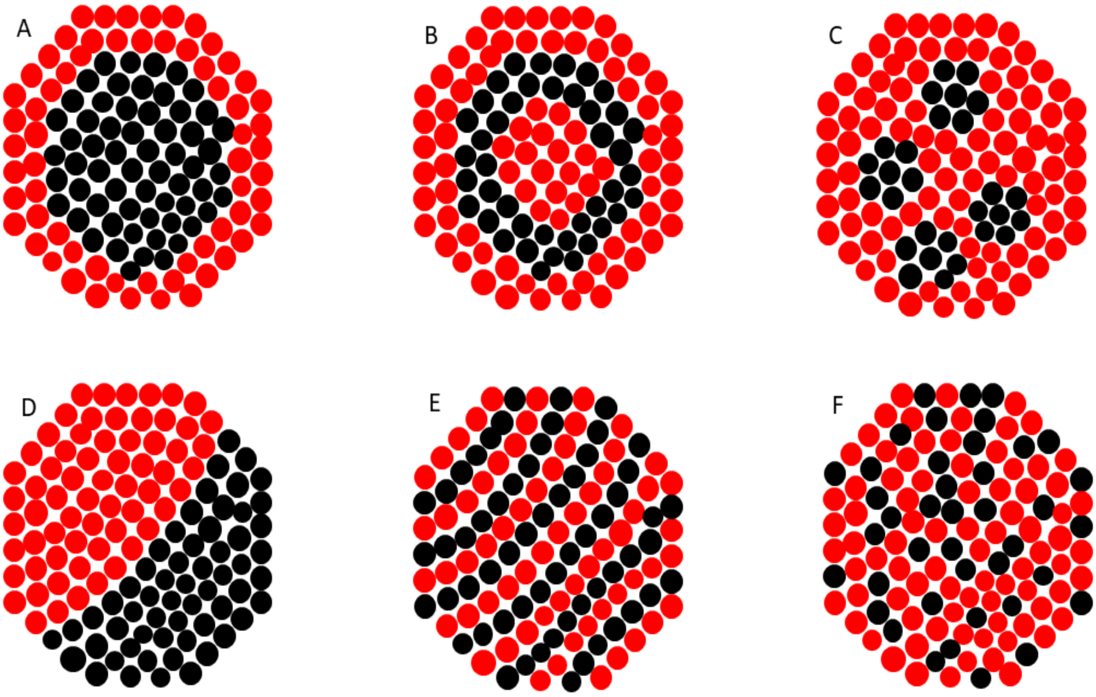

Figure 2.5: Schematic representation of bimetallic nanoparticle structures: A - core-shell, B - three shell, C - Multicore, D – subcluster, E - intermetallic, F - alloyed. Adapted from *(Ferrando et al. 2008)*.

Bimetallic NPs have characteristic mixing patterns that enhance their functionality, which monometallic NPs cannot do due to containing only a single metal *(Scala et al. 2022)*. Due to having two different metals present within the NP, the properties of both metal NP are obtained to improve upon what monometallic can do which opens up opportunities for development as bimetallic NPs show higher stability, selectivity and catalytic activity due to mixing pattern and enhancing the properties of both metal NPs *(Lim et al. 2009)*. *Paris et al. 2022* demonstrated bimetallic NPs achieving higher catalytic activity when compared to monometallic NPs, where the process was not feasible using monometallic NPs in comparison to the bimetallic NPs. The two metals present can show synergistic effects and produce properties that would not be seen in the metal NP alone, further adding to its functionality and requirement for exploration. By simply changing the metals present, the geometry and the chemical and physical properties will optimise the NPs for the required process *(Kodama et al. 2006)*.

2.6 Neutron capture therapy (NCT)

The neutron's discovery in 1932 *(Chadwick, 1932)* started a series of nuclear fission experiments. One of these is the neutron capture therapy experiments (NCT). This involved the Boron^{10} isotope *(Gilbert, 1948)*. In 1936, Gordon L. Locher suggested a concept for a new cancer treatment that involved introducing a small number of solid neutron absorbers into the regions where it was desired to liberate ionization energy *(Issa et al. 2013)*. For example, glioblastomas are very radioresistant cancerous cells, and routine cancer treatments such as chemotherapy are shown to be ineffective, which calls for different treatments to attack these cells *(Ali et al. 2020)*. It was also found that the neutron cross-sectional area in barns (1 barn = 10^{-24} cm^2) was independent of the nuclear mass but was based on the structure of the nucleus *(Barth et al. 2005)*. This means that that heavier elements, such as Fe has a neutron cross sectional area of 2.62 barns, when compared to ^{10}boron that has 3838 barns. The structure of the nucleus is key for NCT as it effects the likelihood of interactions between a neutron source and the nucleus *(Barth et al. 2005)*. The structure of the nucleus is key as the ^{11}boron isotope has a neutron cross sectional area of 0.005 showing the a makor difference between the two boron isotopes.

The NCT process is an effective cancer treatment due to the short path lengths and high linear energy transfer (LET) fission products *(Issa et al. 2013)* meaning a localised dose of radiation can be supplied to the desired area to treat cancerous cells without damaging the surrounding healthy cells. Referring to Equation 2.1 and 2.2 *(Issa et al. 2013)*, the two reactions during the NCT process where a ^{10}B isotope becomes excited to an B^{11} isotope. During the process, 94% of the ^{10}B is converted via Equation 2.2 where E_γ = 0.48 MeV and 6% of the ^{10}B is converted by Equation 2.1. A high enough dose of the ^{10}B NPs [109 atoms per cell] in radioresistant tumours will lead to the successful death of the tumour. *(Issa et al. 2013)*

$$^{10}B + n_{th} \rightarrow \ ^{11}B = \ ^{4}He^{2+} + \ ^{7}Li^{3+} + 2.79\ MeV \qquad \text{Eq 2.1}$$

$$^{10}B + n_{th} \rightarrow \ ^{11}B = \ ^{4}He^{2+} + \ ^{7}Li^{3+} + E_\gamma + 2.79\ MeV \qquad \text{Eq 2.2}$$

The boron^{10} isotope has a cross-sectional area of 3838 barns and is not radioactive and non-toxic. It works because when fired with neutrons, it becomes an excited boron^{11} that splits into high energy alpha and lithium particles with short path lengths *(Suzuki, 2020), (Dymova et al. 2020)*. Figure 2.6 show the cross-sectional area of many different isotopes that have been noted to be functional for NCT. However, not all these isotopes may be suitable for NCT; for example, Li$^+$, due to its size, is easily dispersed in the body and challenging to deliver to a specific tumour. U^{235} is also unsuitable due to the high toxicity and radioactivity *(Issa et al. 2013)*. NCT has multiple reaction routes. However, the Li^{6} and ^{10}B NCT reaction is (n, α), the most straightforward reaction with an alpha particle being released when bombarded with thermalised neutrons. Gd^{157} has a much greater neutron cross-sectional area and the highest stable isotopes of 255000 barns compared to ^{10}B 3838 barns. However, Gd^{157} has much more complex reactions which induce complex inner shell transitions that generate γ-emissions, which is why ^{10}B is of more interest to NCT.

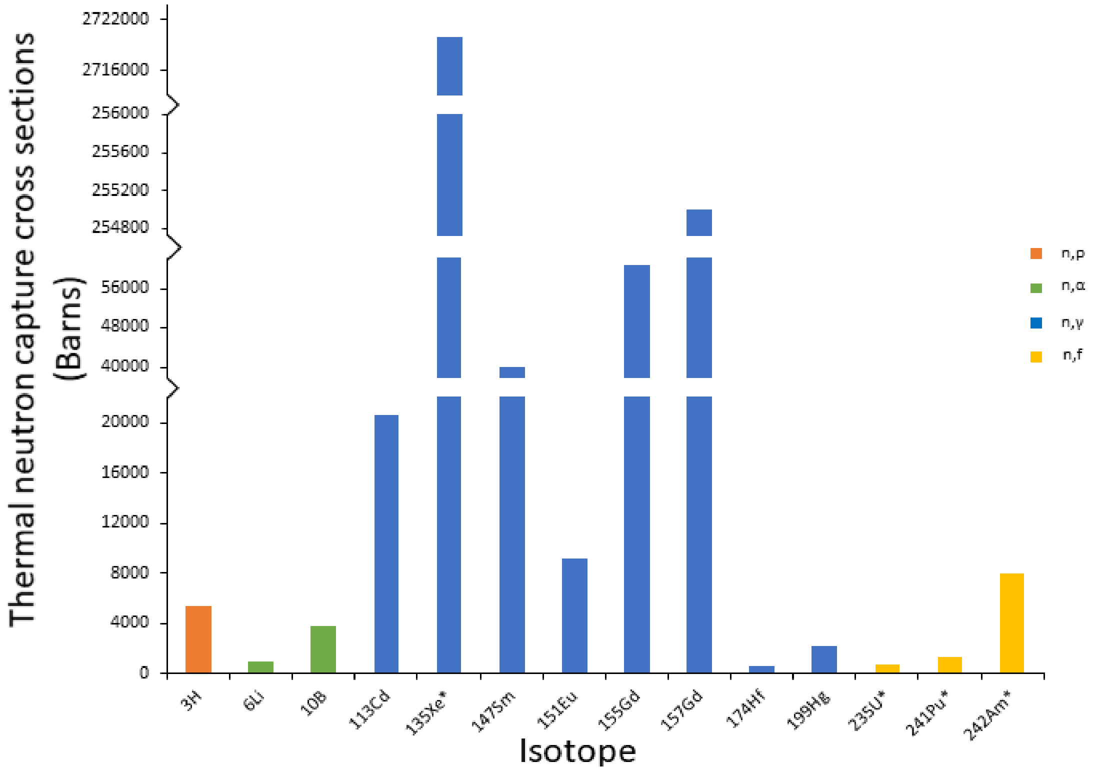

Figure 2.6: Different neutron cross-sectional areas of elements. Adapted from *(Issa et al. 2013)* (Note: 1 barn = 10^{-24} cm^{2}. * Radioactive.).

Figure 2.7 displays most abundant elements in the body compared to ^{10}boron to show the significant difference between naturally occurring elements within the body and a NCT element such as ^{10}boron. Even though such elements as H, O, C, and N have small neutron cross-sectional areas that, on their own, would be negligible, the sheer amount of these in the human body becomes a factor in NCT that needs to be taken into consideration when carrying out the treatment for the amount of radiation that would be absorbed by healthy tissues *(Issa et al. 2013)*. Figure 2.7 displays ^{10}B as a comparison to show the significant difference in neutron capture cross-sectional areas of common elements in mammals and ^{10}B. This is a crucial reason why NCT is a viable cancer treatment. There is over a 100 x difference between the highest commonly occurring mammal element in Cl and ^{10}B, which has a thermal neutron cross-sectional area of 3838.

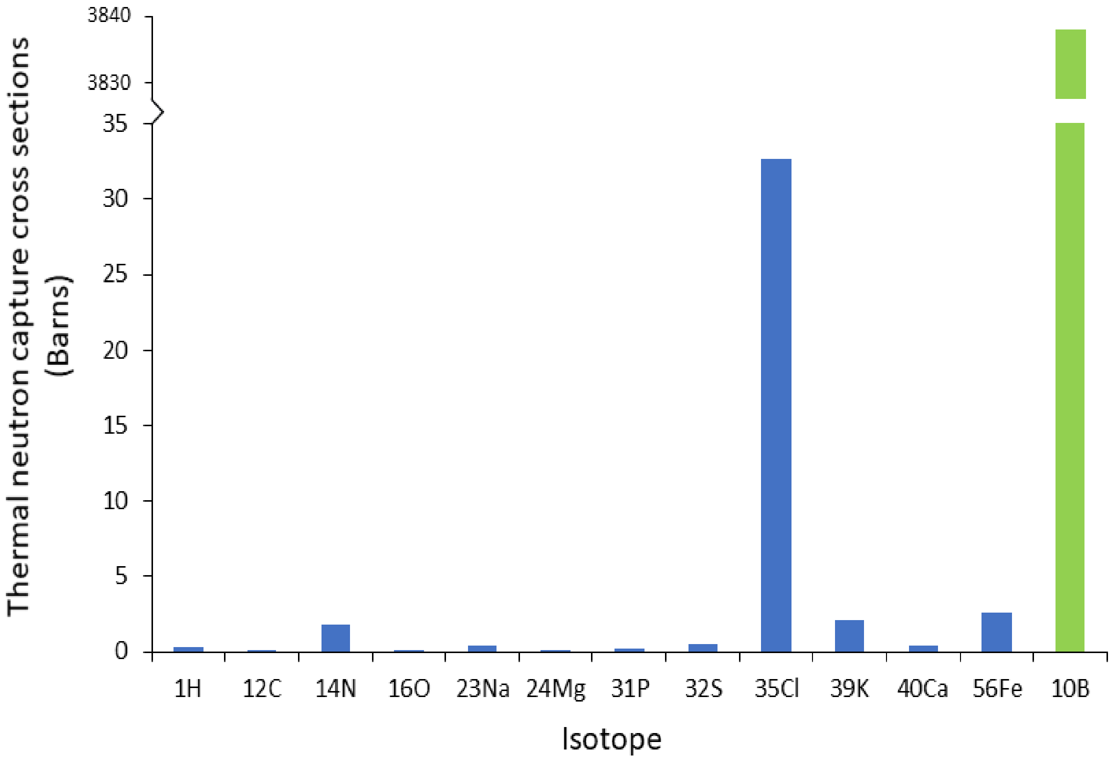

Figure 2.7: Thermal neutron capture cross sections of the elements commonly present in mammalian tissues. Adapted from *(Issa et al. 2013)*) (Note: ^{10}B is not commonly present in the body but there as a comparison).

2.7 Conclusion

Overall, it has been established that to synthesise a particle that would be effective for NCT, a neutron absorber is required to deliver the toxic dose of radiation to the cancerous cells. However, there is currently no effective way to supply to ^{10}boron to the cancerous cells. There has been a lack of research on developing these particles that can be efficiently transported to the glioblastomas. *Coward et al. 2024,* developed a methodolgy to sythesise Fe-B@Au core-shell NPs using a redox-transmetalation method by using the Fe as a sacrafical layer for the the reduction of Au^{3+} to promote the seeding of gold at the surface of the core where there is a high energy barrier due to lattice mismatches. This research needs to be devloped further to gain a complete gold shell but to increase the ^{10}B enrichment to have an effecitve particle for NCT. By choosing either redox-transmetalation or reverse micelle as the method of syntheis will give good control of the size of the NPs but also promote the seeding of gold at the surface that will inert core from oxidation. The gold is highly important in this process as targeting peptides can be added to the surface of the gold via a thiol group that can help transport the particles to the cancerous cells.

2.8 Characterisation methodology

2.8.1 SEM / EDX

Electron microscopy (EM) uses electrons rather than light to obtain an image under observation. Using electrons allows for high magnification due to a short wavelength that electrons exhibit that allowing analysis down to the nanoscale. SEM uses a focused beam of electrons to scan an area of the sample. The electron source is a gun controlled by electromagnetic optics column. The electrons interact with the sample that gives a signal characteristic to the material. Backscattered electrons (BSE) have been elastically scattered by the nucleus of the material and have a low penetration depth. BSE can give good detail on atomic number. Secondary electrons (SE) are electrons which have been knocked out of the material by the beam that creates an empty space within the shell of the nucleus giving topographic information. The penetration depth is dependent on the atomic number and the acceleration voltage used in the analysis *(Pretorius, 2010)*. STEM-in-SEM, or as Stokes put it, ‘poor man’s STEM’ *(Stokes, 2008),* uses standard SEM equipment with an additional STEM detector that is placed underneath the material. Within STEM mode there are different modes that can be selected to analyse; most commonly Bright Field (BF) and High-Angle Annular Dark field (HAADF). In BF, the analysis looks more at the topography of the material and analyses the electrons that have traversed through the material without deflection and detected by the detector underneath the material. If the material is thinner, there is less chance for the electrons to be scattered and a higher amount reach the detector. In BF, the thicker the material the brighter it appears in the analysis. In HAADF, the analysis looks at the electrons that have been scattered by the material and can indicate the difference in materials Z-number. The heavier the element the more the electrons would be scattered at higher angles and therefore appear brighter in the HAADF image.

Energy Dispersive X-ray scattering (EDX) is a technique that provides elemental composition of the material. As discussed with the secondary electrons, an electron from a higher energy orbital drops down to fill the empty vacancy which emits an x-ray that which energy is associated to a specific element *(Tendeloo et al. 2020)*. It is defined by the energy level which the vacancy occurs within, K, L, M and the energy level which the electron originated from (α), (β), (γ) *(Roomans et al. 2014)*. The interaction is dependent on the Z number of the sample. Each element has signature peaks defined by the intensity and positioning.

2.8.2 DLS

Dynamic light scattering (DLS) is a colloidal technique used to measure hydrodynamic diameter using diffusion coefficients *(Yeh et al. 1964)*. The way that particles scatter light can determine the hydrodynamic diameter of the particle which is the effective diameter of a particle when suspended in a fluid. It takes into account the surrounding solvent and how it moves through the fluid *(Gordillo-Galeano. et al. 2021)*. However, it takes into account assumptions that the particles are spherical that has the same translational diffusion coefficient as the true particle. Particles that are in suspension are in continuous interaction with surrounding liquid via Brownian motion. When a given wavelength is directed at the particles that are continuously moving in dispersion leads to the scattered light fluctuating. This fluctuation is recorded and generates a correlogram from the raw correlation against time delay. It is possible to calculate the hypothetical diameter of the particle assuming that the particles are completely spherical which diffuse at the same rate.

2.8.3 XPS

The examination was conducted by means of X-ray Photoelectron Spectroscopy (XPS). This involves irradiating a sample with X-rays of a characteristic energy causing photo electrons to be ejected with a range of energies depending on the element from which they are emitted and the chemical state of that element. The emitted electrons are then collected and transferred through apertures and focused onto an energy analyser entrance to be sorted by their energies. From this electron energy identification, XPS provides information on the elements present at a sample surface and their chemical and bonding states. Under the conditions of this analysis, XPS gives quantitative information on all elements excluding H and He at a detection limit of 0.1%.

2.8.4 UV-Vis

Ultraviolet-visible light spectroscopy (UV-Vis) is a technique that measures the difference between electrons that have been excited from the ground state and move from the highest occupied orbital to the lowest unoccupied orbital, which is known as the HOMO-LUMO gap. Due to the energy being absorbed from the UV-Vis and the wavelength of the absorption indicates the energy difference between the orbitals which is distinct to each material.

2.8.5 ICP-OES

Inductively coupled plasma optical emission spectroscopy (ICP-OES) is a technique used that can give the exact bulk elemental composition of a sample. ICP-OES takes advantage of the unique emission spectra of elements to identify and quantify them. It relies on a concentration curve to be stabilised where if done incorrectly, will lead to poor quantification. A high temperature argon plasma is used to excite the atoms in the sample which leads to the emission of a characteristic wavelength of light for each element. The intensity of the wavelength is proportional to the concentration of the element due to the concentration curve of known amounts being set up.

2.8.6 XRF

X-ray Fluorescence (XRF) uses the interaction of X-rays with a material to determine its elemental composition. Wavelength Dispersive XRF uses x-rays to that excites the electrons and removes one from the innermost orbitals. As the atom relaxes, an outer electron drops into a lower energy orbital emitting X-ray fluorescence radiation that is characteristic to an element allowing the identification of elemental composition.

2.8.7 XRD

X-ray diffraction analysis (XRD) is a technique used to determine the crystallographic structure of a material. It works by irradiating the material with incident x-rays whereby the intensities and scattering angles are measured that leave the material. The technique is used to identify what materials are present by the diffraction pattern as well as the crystallinity of the material. As each material with have a specific lattice structure, such as body centred cubic, hexagonal close packed; the regular array of atoms scatter incident x-rays through interactions with the atoms' electrons causing elastic scattering.

2.8.8 NMR

Nuclear magnetic resonance (NMR) spectroscopy is a key analytical technique used to obtain physical, chemical, electronic and structural data from the molecules due to the chemical shift of the resonance frequencies of the nuclear spins in the sample *(Palmer, 2004)*. In NMR, some nuclei have a specific nuclear spin state, that when expose to an external magnetic field observe transitions between different spin states. Proton NMR analysed the protons within the material, the different H atoms and what they are attached to. When an external magnetic field is applied the H-1 spin aligns with the magnetic field. The magnetic field strengths of the protons can then be measured and analysed to identify the bonding present. In carbon-13 NMR, the analysis identifies the different carbon atoms present depending on what the carbon is bonded to.

2.8.9 FTIR

Infrared spectroscopy probes the molecular vibrations. Functional groups can be associated with characteristic infrared absorption bands *(Berthomieu et al. 2009)*. Depending on the wavelength of light used will cause different bonds to behave differently. In the mid infrared region (functional groups between 4000 and 1500 cm^{-1}) will cause the bonds to stretch. Less than 1500 cm^{-1} is the fingerprint region where the entire molecule vibrates will cause the bonds to bend. Each molecule has its own vibration at these lower wavelengths like a fingerprint being able to identify the molecule.

2.8.10 NFCM

Flow cytometry (FC) is a technology that quickly analyses single cells or particles as they pass individually by a laser or multiple lasers in solution. FC can use visible light scatters or fluorescence scatters if the particles or cells have been tagged with a dye. It is a powerful characterisation technique that can identify particle size but also particle concentration by measuring the scatter but also the amount of times the beam was broken by a particle passing by *(Adan et al. 2016)*.

2.8.11 TGA

Thermogravimetric analysis (TGA) is a quantitative technique to analyse small amounts of sample from 1 mg to a few grams. TGA works by using a furnace to slowly heat the sample up to a desired temperature in a stable of changing flow of carrier gas. This technique can determine moisture content and identify different compounds within a mixture through different evaporation of sublimation points. A precise micro balance is used to measure the change in mass during the heating of the sample within the furnace.

References

Ali, M.Y. *et al.* (2020) ‘Radioresistance in glioblastoma and the development of radiosensitizers’, *Cancers*, 12(9), pp. 1–29. Available at: https://doi.org/10.3390/cancers12092511.

Amusat, S.O. *et al.* (2021) ‘Ball-milling synthesis of biochar and biochar–based nanocomposites and prospects for removal of emerging contaminants: A review’, *Journal of Water Process Engineering*, 41(March), p. 101993. Available at: https://doi.org/10.1016/j.jwpe.2021.101993.

Ansari, M.M., Shahid, M. and Ansari, A.S. (2018) ‘Synthesis and characterization of Cu nanoparticles by chemical reduction method’, *AIP Conference Proceedings*, 1953, pp. 24–27. Available at: https://doi.org/10.1063/1.5032341.

Arno, M.C. *et al.* (2020) ‘Exploiting the role of nanoparticle shape in enhancing hydrogel adhesive and mechanical properties’, *Nature Communications*, 11(1). Available at: https://doi.org/10.1038/s41467-020-15206-y.

Arora, N., Thangavelu, K. and Karanikolos, G.N. (2020) ‘Bimetallic Nanoparticles for Antimicrobial Applications’, *Frontiers in Chemistry*, 8(May), pp. 1–22. Available at: https://doi.org/10.3389/fchem.2020.00412.

Arya, S. *et al.* (2021) ‘Review—Influence of Processing Parameters to Control Morphology and Optical Properties of Sol-Gel Synthesized ZnO Nanoparticles’, *ECS Journal of Solid State Science and Technology*, 10(2), p. 023002. Available at: https://doi.org/10.1149/2162-8777/abe095.

Asha, A.B. and Narain, R. (2020) *Nanomaterials properties*, *Polymer Science and Nanotechnology: Fundamentals and Applications*. Elsevier Inc. Available at: https://doi.org/10.1016/B978-0-12-816806-6.00015-7.

Ban, Z. *et al.* (2005) ‘The synthesis of core-shell iron@gold nanoparticles and their characterization’, *Journal of Materials Chemistry*, 15(43), pp. 4660–4662. Available at: https://doi.org/10.1039/b504304b.

Barth, R.F. *et al.* (2005) ‘Boron neutron capture therapy of cancer: Current status and future prospects’, *Clinical Cancer Research*, 11(11), pp. 3987–4002. Available at: https://doi.org/10.1158/1078-0432.CCR-05-0035.

Bhardwaj, B. *et al.* (2020) ‘Eco-friendly greener synthesis of nanoparticles’, *Advanced Pharmaceutical Bulletin*, 10(4), pp. 566–576. Available at: https://doi.org/10.34172/apb.2020.067.

Chadwick, J. (1932) ‘The existence of a neutron’, 49(June), pp. 62–69.

Charitidis, C.A. *et al.* (2014) ‘Manufacturing nanomaterials: From research to industry’, *Manufacturing Review*, 1. Available at: https://doi.org/10.1051/mfreview/2014009.

Charles P. Poole, J. and Owens, F.J. (2003) ‘2.1.3 Face-Centered Cubic Nanoparticles’, *Introduction to nanotechnology*, pp. 12–14. Available at: https://books.google.com/books/about/Introduction_to_Nanotechnology.html?id=XfzgEoY9SNkC (Accessed: 26 November 2021).

Chau, J.L.H. *et al.* (2011) ‘Femtosecond laser synthesis of bimetallic Pt-Au nanoparticles’, *Materials Letters*, 65(4), pp. 804–807. Available at: https://doi.org/10.1016/j.matlet.2010.10.088.

Chee, S.S. and Lee, J.H. (2012) ‘Effects of process parameters in synthesizing Sn nanoparticles via chemical reduction’, *Electronic Materials Letters*, 8(1), pp. 53–58. Available at: https://doi.org/10.1007/s13391-011-0510-3.

Chen, D. *et al.* (2009) ‘Nanometre Ni and core/shell Ni/Au nanoparticles with controllable dimensions synthesized in reverse microemulsion’, *Journal of Alloys and Compounds*, 475(1–2), pp. 494–500. Available at: https://doi.org/10.1016/j.jallcom.2008.07.115.

Chen, H.Y. *et al.* (2018) ‘One-pot wet-chemical synthesis of uniform AuPtPd nanodendrites as efficient electrocatalyst for boosting hydrogen evolution and oxygen reduction reactions’, *International Journal of Hydrogen Energy*, 43(49), pp. 22187–22194. Available at: https://doi.org/10.1016/j.ijhydene.2018.10.120.

Chokprasombat, K., Pinitsoontorn, S. and Maensiri, S. (2016) ‘Effects of Ni content on nanocrystalline Fe-Co-Ni ternary alloys synthesized by a chemical reduction method’, *Journal of Magnetism and Magnetic Materials*, 405, pp. 174–180. Available at: https://doi.org/10.1016/j.jmmm.2015.12.064.

Coetzee, D. *et al.* (2020) ‘Influence of nanoparticles on thermal and electrical conductivity of composites’, *Polymers*, 12(4). Available at: https://doi.org/10.3390/POLYM12040742.

Coward, B., Wang, J. and Kysela, B. (2024) ‘Synthesis of trimetallic iron-boron core and gold shell nanoparticles for experimental cancer radiotherapy’, *Frontiers in Bioengineering and Biotechnology*, 12(September), pp. 1–7. Available at: https://doi.org/10.3389/fbioe.2024.1448081.

Daoush, W.M. and Imae, T. (2015) ‘Fabrication of PtNi bimetallic nanoparticles supported on multi-walled carbon nanotubes’, *Journal of Experimental Nanoscience*, 10(5), pp. 392–406. Available at: https://doi.org/10.1080/17458080.2013.838703.

Das, S.K. *et al.* (2013) ‘A study on biosynthesis of iron nanoparticles by Pleurotus sp.’, *Vegetable Crops Research Bulletin*, 8(1), pp. 5–19. Available at: https://doi.org/10.1016/j.jare.2015.02.007.

Dean, S.L., Stapleton, J.J. and Keating, C.D. (2010) ‘Organically modified silicas on metal nanowires’, *Langmuir*, 26(18), pp. 14861–14870. Available at: https://doi.org/10.1021/la102070c.

Deraedt, C. *et al.* (2014) ‘Sodium borohydride stabilizes very active gold nanoparticle catalysts’, *Chemical Communications*, 50(91), pp. 14194–14196. Available at: https://doi.org/10.1039/c4cc05946h.

Van Devener, B., Perez, J.P.L. and Anderson, S.L. (2009) ‘Air-stable, unoxidized, hydrocarbon-dispersible boron nanoparticles’, *Journal of Materials Research*, 24(11), pp. 3462–3464. Available at: https://doi.org/10.1557/jmr.2009.0412.

Dolai, J., Mandal, K. and Jana, N.R. (2021) ‘Nanoparticle Size Effects in Biomedical Applications’, *ACS Applied Nano Materials*, 4(7), pp. 6471–6496. Available at: https://doi.org/10.1021/acsanm.1c00987.

Dymova, M.A. *et al.* (2020) ‘Boron neutron capture therapy: Current status and future perspectives’, *Cancer Communications*, 40(9), pp. 406–421. Available at: https://doi.org/10.1002/cac2.12089.

Elmi, G.R. *et al.* (2022) ‘Recent Advances of Magnetic Gold Hybrids and Nanocomposites, and Their Potential Biological Applications’, *Magnetochemistry*, 8(4), pp. 1–18. Available at: https://doi.org/10.3390/magnetochemistry8040038.

Fathima, R. and Mujeeb, A. (2021) ‘Enhanced nonlinear and thermo optical properties of laser synthesized surfactant-free Au-Pt bimetallic nanoparticles’, *Journal of Molecular Liquids*, 343, p. 117711. Available at: https://doi.org/10.1016/j.molliq.2021.117711.

Ferrando, R., Jellinek, J. and Johnston, R.L. (2008) ‘Nanoalloys: From Theory to Applications of Alloy Clusters and Nanoparticles’, *Chemical Reviews*, 108(3), pp. 845–910. Available at: https://doi.org/10.1021/CR040090G.

Forsman, J. *et al.* (2008) ‘Production of cobalt and nickel particles by hydrogen reduction’, *Journal of Nanoparticle Research*, 10(5), pp. 745–759. Available at: https://doi.org/10.1007/s11051-007-9304-9.

Gavas, S., Quazi, S. and Karpiński, T.M. (2021) ‘Nanoparticles for Cancer Therapy: Current Progress and Challenges’, *Nanoscale Research Letters*, 16(1). Available at: https://doi.org/10.1186/s11671-021-03628-6.

Gholinejad, M. *et al.* (2021) ‘Applications of bimetallic PdCu catalysts’, *Catalysis Science and Technology*, 11(8), pp. 2652–2702. Available at: https://doi.org/10.1039/d0cy02339f.

Gilbert, C.W. (1948) ‘The disintegration of boron by slow neutrons. II’, *Mathematical Proceedings of the Cambridge Philosophical Society*, 44(3), pp. 447–452. Available at: https://doi.org/10.1017/S0305004100024440.

Grys, D.B. *et al.* (2020) ‘Citrate Coordination and Bridging of Gold Nanoparticles: The Role of Gold Adatoms in AuNP Aging’, *ACS Nano*, 14(7), pp. 8689–8696. Available at: https://doi.org/10.1021/acsnano.0c03050.

Gupta, S.K., Talati, M. and Jha, P.K. (2008) ‘Shape and Size Dependent Melting Point Temperature of Nanoparticles’, *Materials Science Forum*, 570, pp. 132–137. Available at: https://doi.org/10.4028/www.scientific.net/msf.570.132.

Hawar, S.N. *et al.* (2022) ‘Green Synthesis of Silver Nanoparticles from Alhagi graecorum Leaf Extract and Evaluation of Their Cytotoxicity and Antifungal Activity’, *Journal of Nanomaterials*, 2022. Available at: https://doi.org/10.1155/2022/1058119.

Ijaz, I. *et al.* (2020) ‘Detail review on chemical, physical and green synthesis, classification, characterizations and applications of nanoparticles’, *Green Chemistry Letters and Reviews*, 13(3), pp. 59–81. Available at: https://doi.org/10.1080/17518253.2020.1802517.

Irfan, M. (2021) ‘Study of Brownian motion and thermophoretic diffusion on non-linear mixed convection flow of Carreau nanofluid subject to variable properties’, *Surfaces and Interfaces*, 23(December 2020), p. 100926. Available at: https://doi.org/10.1016/j.surfin.2021.100926.

Isa, S.Z.M., Zainon, R. and Tamal, M. (2022) ‘State of the Art in Gold Nanoparticle Synthesisation via Pulsed Laser Ablation in Liquid and Its Characterisation for Molecular

Imaging: A Review', *Materials*, 15(3). Available at: https://doi.org/10.3390/ma15030875.

Issa, F., Ioppolo, J.A. and Rendina, L.M. (2013) 'Boron and Gadolinium Neutron Capture Therapy', *Comprehensive Inorganic Chemistry II (Second Edition): From Elements to Applications*, 3(9), pp. 877–900. Available at: https://doi.org/10.1016/B978-0-08-097774-4.00335-1.

Jadoun, S. *et al.* (2022) *Synthesis of nanoparticles using microorganisms and their applications : a review*, *Environmental Chemistry Letters*. Springer International Publishing. Available at: https://doi.org/10.1007/s10311-022-01444-7.

Jhuang, L.S., Kumar, G. and Chen, F.C. (2021) 'Localized surface plasmon resonance of copper nanoparticles improves the performance of quasi-two-dimensional perovskite light-emitting diodes', *Dyes and Pigments*, 188(February), p. 109204. Available at: https://doi.org/10.1016/j.dyepig.2021.109204.

Jin, R. and Higaki, T. (2021) 'Open questions on the transition between nanoscale and bulk properties of metals', *Communications Chemistry*, 4(1), pp. 6–9. Available at: https://doi.org/10.1038/s42004-021-00466-6.

Jin, W.H. *et al.* (2022) 'A Review of Boron Neutron Capture Therapy: Its History and Current Challenges', *International Journal of Particle Therapy*, 9(1), pp. 71–82. Available at: https://doi.org/10.14338/IJPT-22-00002.1.

Kang, H. *et al.* (2012) 'Reduction of nitrate by bimetallic Fe/Ni nanoparticles', *Environmental Technology (United Kingdom)*, 33(18), pp. 2185–2192. Available at: https://doi.org/10.1080/09593330.2012.665486.

Kang, H. *et al.* (2019) 'Stabilization of Silver and Gold Nanoparticles: Preservation and Improvement of Plasmonic Functionalities', *Chemical Reviews*, 119(1), pp. 664–699. Available at: https://doi.org/10.1021/acs.chemrev.8b00341.

Kaur, A. *et al.* (2021) 'Supported bimetallic nanoparticles as anode catalysts for direct methanol fuel cells: A review', *International Journal of Hydrogen Energy*, 46(29), pp. 15820–15849. Available at: https://doi.org/10.1016/j.ijhydene.2021.02.037.

Khan, Z. *et al.* (2013) 'Au(III)-CTAB reduction by ascorbic acid: Preparation and characterization of gold nanoparticles', *Colloids and Surfaces B: Biointerfaces*, 104, pp. 11–17. Available at: https://doi.org/10.1016/j.colsurfb.2012.11.017.

Khatami, M., Alijani, H.Q. and Sharifi, I. (2018) 'Biosynthesis of bimetallic and core-shell nanoparticles: Their biomedical applications - A review', *IET Nanobiotechnology*, 12(7), pp. 879–887. Available at: https://doi.org/10.1049/iet-nbt.2017.0308.

Khorasani-Motlagh, M., Noroozifar, M. and Shahroosvand, H. (2010) 'A new reduction route for the synthesis of nanoscale metals and metal oxides with ascorbic acid at low temperature', *Journal of the Iranian Chemical Society*, 7(2), pp. 113–122. Available at: https://doi.org/10.1007/bf03246190.

Kodama, D. *et al.* (2006) 'Chemical synthesis of sub-micrometer- to nanometer-sized magnetic FeCo dice', *Advanced Materials*, 18(23), pp. 3154–3159. Available at: https://doi.org/10.1002/adma.200601292.

Kvitek, O. *et al.* (2019) ‘Immobilization of Fe@Au superparamagnetic nanoparticles on polyethylene’, *European Polymer Journal*, 110(November 2018), pp. 56–62. Available at: https://doi.org/10.1016/j.eurpolymj.2018.10.043.

Lee, H. *et al.* (2006) ‘Morphological control of catalytically active platinum nanocrystals’, *Angewandte Chemie - International Edition*, 45(46), pp. 7824–7828. Available at: https://doi.org/10.1002/anie.200603068.

Lee, Y.L. *et al.* (2022) ‘Optimization of nano-catalysts for application in compact reformers’, *Chemical Engineering Journal*, 431(P3), p. 134299. Available at: https://doi.org/10.1016/j.cej.2021.134299.

Lee, Y.R. *et al.* (2015) ‘ZIF-8: A comparison of synthesis methods’, *Chemical Engineering Journal*, 271, pp. 276–280. Available at: https://doi.org/10.1016/j.cej.2015.02.094.

Leonard, B.M. *et al.* (2011) ‘Erratum: Facile synthesis of PtNi intermetallic nanoparticles: Influence of reducing agent and precursors on electrocatalytic activity (Chemistry of Materials (2011) 23 (1136-1146) DOI: 10.1021/cm1024876)’, *Chemistry of Materials*, 23(9), p. 2499. Available at: https://doi.org/10.1021/cm2009835.

Lim, B. *et al.* (2009) ‘Pd-Pt bimetallic nanodendrites with high activity for oxygen reduction’, *Science*, 324(5932), pp. 1302–1305. Available at: https://doi.org/10.1126/science.1170377.

Ma, W. *et al.* (2022) ‘Ag-Pd bimetallic hollow nanostructures with tunable compositions and structures for the reduction of 4-nitrophenol’, *Journal of Alloys and Compounds*, 925, p. 166689. Available at: https://doi.org/10.1016/j.jallcom.2022.166689.

Mandari, K.K., Son, N. and Kang, M. (2021) ‘Journal of Colloid and Interface Science Improved charge carrier separation of Schottky junction containing a bimetallic Cu-Pd alloy and N-Bi 2 WO 6 square-shaped discs for photocatalytic H 2 performance’, *Journal of Colloid And Interface Science*, 593, pp. 276–289. Available at: https://doi.org/10.1016/j.jcis.2021.02.127.

Mazhar, T., Shrivastava, V. and Tomar, R.S. (2017) ‘Green synthesis of bimetallic nanoparticles and its applications: A review’, *Journal of Pharmaceutical Sciences and Research*, 9(2), pp. 102–110.

Mekuye, B. and Abera, B. (2023) ‘Nanomaterials: An overview of synthesis, classification, characterization, and applications’, *Nano Select*, 4(8), pp. 486–501. Available at: https://doi.org/10.1002/nano.202300038.

Millstone, J.E. *et al.* (2009) ‘Colloidal gold and silver triangular nanoprisms’, *Small*, 5(6), pp. 646–664. Available at: https://doi.org/10.1002/smll.200801480.

Mitchell, M.J. *et al.* (2021) ‘Engineering precision nanoparticles for drug delivery’, *Nature Reviews Drug Discovery*, 20(2), pp. 101–124. Available at: https://doi.org/10.1038/s41573-020-0090-8.

Mohamad, N.A.N. *et al.* (2013) ‘A short review on the synthesis of bimetallic nanoparticles using plant extract’, *Proceedings - 2013 IEEE International Conference on Control System, Computing and Engineering, ICCSCE 2013*, pp. 334–339. Available at: https://doi.org/10.1109/ICCSCE.2013.6719985.

Niu, Y. *et al.* (2022) 'Engineering iron-group bimetallic nanotubes as efficient bifunctional oxygen electrocatalysts for flexible Zn – air batteries', *eScience*, 2(5), pp. 546–556. Available at: https://doi.org/10.1016/j.esci.2022.05.001.

Noordeen, S., Karthikeyan, K. and Parveen, M. a N. (2013) 'Synthesis of Silver Nanoparticles by using Sodium Borohydride as a Reducing Agent', *International Journal of Engineering Research and Technology*, 2(4), pp. 388–397.

Ong, H.R. *et al.* (2014) 'Synthesisof copper nanoparticles at room temperature using hydrazine in glycerol', *Applied Mechanics and Materials*, 481, pp. 21–26. Available at: https://doi.org/10.4028/www.scientific.net/AMM.481.21.

Paris, C.B. *et al.* (2022) 'Impact of the Experimental Parameters on Catalytic Activity When Preparing Polymer Protected Bimetallic Nanoparticle Catalysts on Activated Carbon'. Available at: https://doi.org/10.1021/acscatal.1c05904.

Patil, M.P. *et al.* (2019) 'Biogenic synthesis, characterization of gold nanoparticles using Lonicera japonica and their anticancer activity on HeLa cells', *Journal of Drug Delivery Science and Technology*, 51, pp. 83–90. Available at: https://doi.org/10.1016/j.jddst.2019.02.021.

Pickering, A.L. *et al.* (2007) 'Room temperature synthesis of surface-functionalised boron nanoparticles', *Chemical Communications*, 2(6), pp. 580–582. Available at: https://doi.org/10.1039/b614363f.

Ramsden, J.J. (2016) 'Nanofacture of devices', *Nanotechnology*, pp. 199–230. Available at: https://doi.org/10.1016/B978-0-323-39311-9.00014-5.

Saravanan, G. *et al.* (2010) 'Pt3Ti nanoparticles: Fine dispersion on SiO2 supports, enhanced catalytic CO oxidation, and chemical stability at elevated temperatures', *Langmuir*, 26(13), pp. 11446–11451. Available at: https://doi.org/10.1021/la100942h.

Scala, A. *et al.* (2022) 'Bimetallic Nanoparticles'.

Scaria, J., Nidheesh, P. V. and Kumar, M.S. (2020) 'Synthesis and applications of various bimetallic nanomaterials in water and wastewater treatment', *Journal of Environmental Management*, 259(January), p. 110011. Available at: https://doi.org/10.1016/j.jenvman.2019.110011.

Schöttle, C. *et al.* (2015) 'Sodium-Naphthalenide-Driven Synthesis of Base-Metal Nanoparticles and Follow-up Reactions', *Angewandte Chemie - International Edition*, 54(34), pp. 9866–9870. Available at: https://doi.org/10.1002/anie.201503269.

Schreyer, F. *et al.* (2020) 'Common but differentiated leadership: Strategies and challenges for carbon neutrality by 2050 across industrialized economies', *Environmental Research Letters*, 15(11). Available at: https://doi.org/10.1088/1748-9326/abb852.

Schulz-Dobrick, M., Sarathy, K.V. and Jansen, M. (2005) 'Surfactant-free synthesis and functionalization of gold nanoparticles', *Journal of the American Chemical Society*, 127(37), pp. 12816–12817. Available at: https://doi.org/10.1021/ja054734t.

Sedighi, A., Montazer, M. and Hemmatinejad, N. (2014) 'Copper nanoparticles on bleached cotton fabric: In situ synthesis and characterization', *Cellulose*, 21(3), pp. 2119–2132.

Available at: https://doi.org/10.1007/s10570-014-0215-5.

Semaltianos, N.G. (2010) ‘Nanoparticles by laser ablation’, *Critical Reviews in Solid State and Materials Sciences*, 35(2), pp. 105–124. Available at: https://doi.org/10.1080/10408431003788233.

Shankar, S.S. *et al.* (2004) ‘Rapid synthesis of Au , Ag , and bimetallic Au core – Ag shell nanoparticles using Neem (Azadirachta indica) leaf broth’, 275, pp. 496–502. Available at: https://doi.org/10.1016/j.jcis.2004.03.003.

Sharma, G. *et al.* (2019) ‘Novel development of nanoparticles to bimetallic nanoparticles and their composites: A review’, *Journal of King Saud University - Science*, 31(2), pp. 257–269. Available at: https://doi.org/10.1016/j.jksus.2017.06.012.

Singh Tomar, Rajesh; Singh Chauhan, Pallavi; Shrivastava, V. (2013) ‘A CRITICAL REVIEW ON NANOPARTICLE SYNTHESIS: PHYSICOCHEMICAL V/s BIOLOGICAL APPROACH’, *World Journal of pharmaceutical research*, 3(1), pp. 726–738.

Song, J.Y. and Kim, B.S. (2008) ‘Biological synthesis of bimetallic Au / Ag nanoparticles using Persimmon (Diopyros kaki) leaf extract’, 25(4), pp. 808–811.

Song, Q. and Zhang, Z.J. (2004) ‘Shape Control and Associated Magnetic Properties of Spinel Cobalt Ferrite Nanocrystals’, *Journal of the American Chemical Society*, 126(19), pp. 6164–6168. Available at: https://doi.org/10.1021/ja049931r.

Sui, Y. *et al.* (2003) ‘CoPt hard magnetic nanoparticle films synthesized by high temperature chemical reduction’, *Journal of Applied Physics*, 93(10 2), pp. 7571–7573. Available at: https://doi.org/10.1063/1.1544501.

Suzuki, M. (2020) ‘Boron neutron capture therapy (BNCT): a unique role in radiotherapy with a view to entering the accelerator-based BNCT era’, *International Journal of Clinical Oncology*, 25(1), pp. 43–50. Available at: https://doi.org/10.1007/s10147-019-01480-4.

Swierzy, A.P.- *et al.* (2022) ‘Metallic core-shell nanoparticles for conductive coatings and printing’, 299(November 2021). Available at: https://doi.org/10.1016/j.cis.2021.102578.

Szekeres, G.P. *et al.* (2018) ‘Copper-Coated cellulose-based water filters for virus retention’, *ACS Omega*, 3(1), pp. 446–454. Available at: https://doi.org/10.1021/acsomega.7b01496.

Tamuly, C. *et al.* (2013) ‘In situ biosynthesis of Ag, Au and bimetallic nanoparticles using Piper pedicellatum C.DC: Green chemistry approach’, *Colloids and Surfaces B: Biointerfaces*, 102, pp. 627–634. Available at: https://doi.org/10.1016/j.colsurfb.2012.09.007.

Umesh, N.M. *et al.* (2021) ‘Highly selective electrochemical detection of diphenylamine in apple samples using rod shaped CuCo 2 O 4 derived from bimetallic organic frameworks’, *Microchemical Journal*, 165(1), p. 106146. Available at: https://doi.org/10.1016/j.microc.2021.106146.

Vaudagna, M.V. *et al.* (2023) ‘Titanium Dioxide Nanoparticles in sunscreens and skin photo-damage. Development, synthesis and characterization of a novel biocompatible alternative based on their in vitro and in vivo study’, *Journal of Photochemistry and Photobiology*, 15(March), pp. 0–7. Available at: https://doi.org/10.1016/j.jpap.2023.100173.

Vollath, D. (2013) *Nanomaterials : An Introduction to Synthesis, Properties and Applications*.

2nd edn. John Wiley & Sons, Incorporated. Available at: https://ebookcentral.proquest.com/lib/aston/detail.action?docID=1273527#goto_toc.

Wang, Y. *et al.* (2020) 'Cobalt–copper–boron nanoparticles as catalysts for the efficient hydrolysis of alkaline sodium borohydride solution', *International Journal of Hydrogen Energy*, 45(16), pp. 9845–9853. Available at: https://doi.org/10.1016/j.ijhydene.2020.01.157.

Wu, Z. *et al.* (2018) 'Revealing the Role of Phase Structures of Bimetallic Nanocatalysts in the Oxygen Reduction Reaction'. Available at: https://doi.org/10.1021/acscatal.8b03106.

Wu, Z. and Ge, S. (2011) 'Facile synthesis of a Co-B nanoparticle catalyst for efficient hydrogen generation via borohydride hydrolysis', *Catalysis Communications*, 13(1), pp. 40–43. Available at: https://doi.org/10.1016/j.catcom.2011.06.017.

Wu, Z.G. (2011) 'A novel chemical reduction route towards the synthesis of nickel nanoparticles at room temperature', *Materials Science Forum*, 694, pp. 293–297. Available at: https://doi.org/10.4028/www.scientific.net/MSF.694.293.

Yan, C. and Wagner, M.J. (2013) 'Air- and water-stable gold-coated gadolinium metal nanocrystals', *Nano Letters*, 13(6), pp. 2611–2614. Available at: https://doi.org/10.1021/nl400720n.

Yu, Y. *et al.* (2021) 'Synergistic Effect of Cu Single Atoms and Au − Cu Alloy Nanoparticles on TiO 2 for Efficient CO 2 Photoreduction'. Available at: https://doi.org/10.1021/acsnano.1c03961.

Zhan, G. *et al.* (2011) 'Green synthesis of Au – Pd bimetallic nanoparticles : Single-step bioreduction method with plant extract', *Materials Letters*, 65(19–20), pp. 2989–2991. Available at: https://doi.org/10.1016/j.matlet.2011.06.079.

Zhang, J., Yu, Y. and Zhang, B. (2020) 'Synthesis and characterization of size controlled alloy nanoparticles', *Physical Sciences Reviews*, 5(3), pp. 1–19. Available at: https://doi.org/10.1515/psr-2018-0046.

Zheng, D. *et al.* (2010) 'Sensors and Actuators B : Chemical Preparation and application of a novel vanillin sensor based on biosynthesis of Au – Ag alloy nanoparticles', *Sensors & Actuators: B. Chemical*, 148(1), pp. 247–252. Available at: https://doi.org/10.1016/j.snb.2010.04.031.

Zhu, G., Jin, Y. and Ge, M. (2022) 'Simple and green method for preparing copper nanoparticles supported on carbonized cotton as a heterogeneous Fenton-like catalyst', *Colloids and Surfaces A: Physicochemical and Engineering Aspects*, 647(April), p. 128978. Available at: https://doi.org/10.1016/j.colsurfa.2022.128978.

Chapter 3 – Non-aqueous synthesis of nanoparticles with iron-boron core & gold shell.

3.1 Introduction

Magnetic nanoparticles (NPs) have gained a vast amount of interest over the years due to the range of properties that these particles gain at the nano scale compared to the material's bulk properties. For example, magnetic NPs can be used for targeted drug delivery because of the magnetic targeting mechanism and capability to produce a diverse cell response which is not possible with the bulk material *(Kianfar. 2021).* Magnetic NPs are effective in catalysis due to their ease in separation meaning good reusability *(Amiri et al. 2019).* They can also be used in agriculture by helping deliver specific nutrients to the plants and also as a nanosensor for the detection of pollutants *(Singh et al. 2021)*. In drug delivery, the magnetic NPs particles transport the necessary drug to desired tissue and cells for medical applications. This is done via drug conjugates. The medicine can be on the surface or encapsulated within the magnetic NPs and the surface functionalised with a linker or ligand that can attach to the desired cells where the drugs need to be delivered *(Cardoso et al. 2018)*. Another advantage of these magnetic NPs is that the particles are small enough to enter biological materials ranging from small cells to proteins and genes, varying in size from 100 micrometer down to 2 nm *(Kianfar. 2021).*

One challenge of using ferromagnetic metal NPs such as iron, cobalt, and nickel is that these particles are very susceptible to oxidation which can alter the properties and characteristics of the NP. To preserve these properties, a protective shell layer is placed around the core material to maintain its elemental state rather than its oxidised state to preserve the elemental properties. Core-shell NPs are an effective type of NP due to being able to obtain the properties of the core material that may otherwise be effected by the environment or in medical application may be highly toxic without an inert non-toxic shell. Core-shell NPs utilize the properties of both the core and shell material and these properties being highly tuneable by controlling the size and shape of the core / shell material *(Ghosh et al. 2012)*. Using these magnetic NPs, for example Fe NPs would oxidise it iron oxides, for medical applications detrimental effects on the cells due to the cytotoxicity that causes cells to enter apoptosis [programmed cell death of a cell] and die *(Feng et al. 2018)*. It has been reported that in certain cell types, iron NPs can increase reactive oxygen species (ROS) leading to oxidative stress and damaging the biological material *(Paunovic et al. 2020)*. Adding a gold shell around the iron core reduces the toxicity as gold has a lower cytotoxicity *(Jafari et al. 2010)*. Although gold is typically a very inert and low cytotoxicity material used frequently in medicine; gold is susceptible to generate ROS through the activation of auger electrons which are electrons that have been ejected from a shell due to the energy released from an electron that has dropped to a lower energy orbital. In *Mcquaid et al. 2016,* a model is suggested to show the photo interaction of gold NPs that produce the characteristic high energy photoelectron and a small amount of low energy auger electrons because of inner shell vacancy when irradiated with with x-rays. This can be an enhancement to the ionising dose of radiation delivered to tumours.

As discussed previously core-shell NPs can be synthesised in a range of methods, such as mechanical grinding *(Zhang et al. 2018)* laser-induced assembly *(Rashid et al. 2021),* chemical vapor deposition *(Withanage et al. 2021)* and self-assembly *(Wu et al. 2019)*. However, the correct technique is required to form the desired core-shell particles. Adding a shell upon an existing core can be challenging when the core and shell materials have different crystal structures and lattice constants. Elements that have similar crystal structures [such as silver and gold, which are face-centred cubic crystal structures with lattice constants of 4.079 Å and 4.065 Å, respectively *(Wheeler, 1925)]* have a small energy barrier for the particles of one of the metals to seed upon a core of the other to form a core-shell structure (or *vice versa*). Whereas, when there are significant differences in the crystal structures, such as between iron and gold (where the crystal structure of iron is body-centred cubic with a lattice constant of 2.856 Å), there is a significant energy barrier to seed gold particles onto an iron core or *vice versa (Benoit et al. 2016)*. The lattice differences between Fe and Au can be seen in Figure 3.1. Different types of crystal growth can occur depending on the lattice structures of the materials involved. Epitaxial growth is where a new crystalline layer is formed with one or more defined orientations in comparison to a surface crystalline layer which is the expected growth process for elements with similar crystalline structures [such as silver and gold] *(Eres et al. 2011)*. Meanwhile, between elements with different crystalline structures, non-epitaxial growth of the heterostructures where amorphous growth occurs of one crystal lattice upon another due to the lattice mismatch, (such as iron and gold) *(Long et al. 2011).*

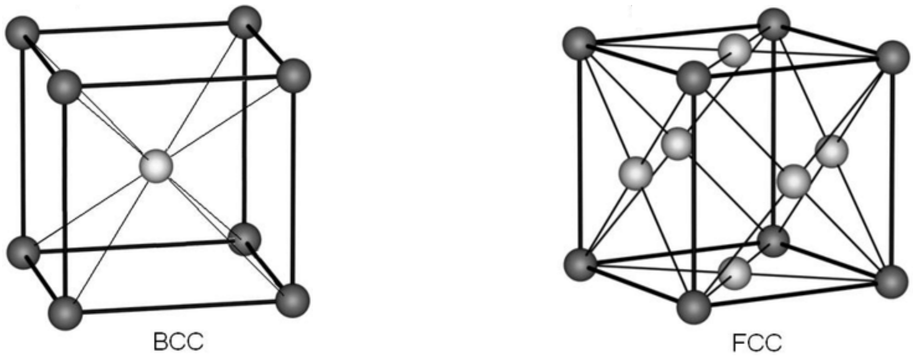

Figure 3.1: Body-centred cubic and face-centred cubic lattice structures for Fe (left) and Au (right), respectively. Adapted from *(Yeh, 2006)*.

It is critical to pick a method to synthesise core-shell NPs that promotes the seeding of different lattice structures upon a pre-existing lattice. For NCT, there is a requirement for boron for the toxic dose of radiation to kill the cancerous cells, but also a gold shell to attach a targeting peptide to deliver the treatment to the desired area of the body. *Corrias et al. 1993* has used sodium borohydride as both a source of boron and a reducing agent with iron chloride to produce a alloyed core of iron-boron. However, as discussed above and in Figure 3.1,iron-boron core and a gold shell have a lattice mismatch that means there is a high energy barrier to seed gold upon the core. Therefore, the chosen synthesis route requires to force and promote the seeding of gold at the surface to overcome the lattice mismatch. Redox-transmetalation is an effective route for forming a shell on top of a core with different lattice properties *Ban et al. 2005*. The redox-transmetalation process works when the core material has a more negative reduction potential than the shell material, leading to spontaneous reduction of the shell material and oxidation of the cores surface layer. This leads to the shell material forming nanoseeds at the surface of the core. These reactions occur spontaneously under favourable redox conditions where the electrochemical potential (ΔE) is thermodynamically favourable and occurs selectively on the metal surface. It is an efficient formation technique for bimetallic structures *(Lee et al. 2005)*. Table 3.1 lists the reduction potentials of transition metal elements and typical shell coatings that may be used to stabilise the core to minimise oxidation. The advantage of using this method for shell formation is that no additional reducing agent is required, and a thin shell is formed to keep the NPs small while protecting the core. When the shell has seeded onto the surface of the core, a reduction site has been removed , meaning large shells cannot form and reduces over erosion *(D. Chen et al. 2009)*.

Table 3.1: Electrode potentials and half equations of different elements. *(Milazzo et al. 1978)*.

Element	Half equation	E° / V
Fe	$Fe^{2+}(aq) + 2e^{-} \rightleftharpoons Fe(s)$	-0.440
Co	$Co^{2+}(aq) + 2e^{-} \rightleftharpoons Co(s)$	-0.277
Ni	$Ni^{2+}(aq) + 2e^{-} \rightleftharpoons Ni(s)$	-0.257
Fe	$Fe^{3+}(aq) + 3e^{-} \rightleftharpoons Fe(s)$	-0.037
H_2	$2H^{+}(aq) + 2e^{-} \rightleftharpoons H_2(g)$	0.000
Ag	$Ag^{+}(aq) + e^{-} \rightleftharpoons Ag(s)$	0.780
Au	$AuCl_4^{-} + 3e^{-} \rightleftharpoons Au(s) + 4Cl^{-}$	1.002

This chapter focuses on non-aqueous methods using redox transmetalation. The method has been evaluated for its effectiveness in forming a gold shell around an iron-boron core. Other parameters, such as boron content, has been assessed to quantify its efficacy in the treatment of glioblastomas. Redox-transmetalation is the chosen technique to overcome the lattice mismatch between the iron-boron core and the gold shell due to being able to use iron as a sacrificial layer to reduce the gold at the surface of the core and promoting seeding of gold on top of the core rather than forming monometallic gold NPs. As the iron is not required for NCT, this would promote and increase the concentration of boron in the core with a gold shell surrounding it. This method forms thin gold shells as once the gold seed has formed on the surface of the core it removes a reduction site which means no further gold can be reduced at the specific spot leading to thin shells. This also means that any remaining iron, the magnetic properties would not be affected drastically due to a thick gold shell. This research aims to produce a core-shell NP of Fe-B@Au that can be used for neutron capture therapy (NCT). The boron content needs to be optimised to increase the concentration in the core and quantification will be pivotal for its intended use, along with confirming a complete gold shell formation.

3.2 Methodology

This method was adapted from *Ban et al. 2005* and *Corrias et al. 1993*. Anhydrous iron(III) chloride, sodium borohydride, chloroauric acid ($HAuCl_4.xH_2O$), 1-methyl-2-pyrrolidinone (NMP) extra dry, 4-benzylpyridine and ethanol were all purchased from Fisher Scientific and used without further purification. All synthesis steps were carried out under inert conditions using nitrogen gas.

Synthesis procedure was completed under inert conditions using N_2 flow in a Schlenk line. Initially, 2 mmol (0.324 g) of $FeCl_3$ were dissolved in 50 ml of NMP to form an orange / yellow solution. Then a second solution containing 6 mmol (0.225 g) of $NaBH_4$ in 50 ml of NMP was formed to produce a colourless solution. $NaBH_4$ solution just made was then added rapidly to the $FeCl_3$ solution and allowed to mix for two hours to ensure complete reaction to form $Fe(BH_4)_3$ and sodium chloride (NaCl) as seen in Equations 3.1 to 3.3. The overall reaction scheme can be seen from Equation 3.4. The colour of the solution changes from orange to reddish-orange and finally a light green colour. A 1:3 ratio of $FeCl_3$:$NaBH_4$ were used so that there was no excess BH_4^- to affect the redox-transmetalation process. A small amount of hydrogen bubbles is visible from the minor amount of water that may be present leading to the hydrolysis of the $NaBH_4$. The complex formed is then heated to 95-100 °C to start the decomposition of the complex and form the core as seem in Equation 3.2 *(Glavee et al. 1995)*. The diborane can then further be decomposed by using the FeB core as a catalyst to form additional boron to be incorporated into the core as seen in Equation 3.3 *(Glavee et al. 1995)*. The overall equation for the synthesis route is shown in Eq 3.4 *(Glavee et al. 1995).*

$$(L)_nFe^{3+} + 3BH_4^- \rightarrow (L)_nFe^{3+}(BH_4^-)_3 \qquad \text{Eq 3.1}$$

$$(L)_nFe^{3+}(BH_4^-)_3 \rightarrow FeB + 3H_2 + B_2H_6 \qquad \text{Eq 3.2}$$

$$B_2H_6 \rightarrow 2B + 3H_2 \qquad \text{Eq 3.3}$$

$$(L)_nFe^{3+} + 3BH_4^- \rightarrow FeB + 2B + 6H_2 + nL \qquad \text{Eq 3.4}$$

After two hours of mixing, 2 ml of 4-benzylpyridine were added dropwise as a stabiliser, which adjusted the colour from an orange/red colour to a greenish colour and still contained NaCl. The solution was then heated up to 100 °C for 1 hour to start the hydrolysis of $Fe(BH_4)_3$ to form Fe-B core NPs, leading to a black solution. The Fe-B solution was then cooled down to 60 °C. 0.848mmol (0.288 g) of $HAuCl_4$ were added to 25 ml of NMP. The gold solution was added slowly at a rate of 25 ml/hr to the Fe-B solution. Upon complete addition of the gold solution, the mixture was heated up to 125 °C for 30 minutes to initiate the redox-transmetalation process where the surface of the core is used as the reducing agent to reduce Au^{3+} ions and form a uniform shell around the Fe-B core as seen from Figure 3.2 and Equations 3.5-3.7. Currently, it is unknown whether boron will also reduce the gold in the same redox-transmetalation method as iron. However, boron will most likely take part in the redox-transmetalation process but the reaction kinetics in the reduction of gold it be slower and less effective which may reduce the boron content slightly during the shell formation. The solution was allowed to return to room temperature and then washed several times with ethanol (EtOH) and methanol (MeOH) to remove by-products. This was followed by magnet separation and a 10 % nitric acid wash to purify the sample. Magnet separation removes monometallic gold particles, and acid washing removes any uncapped Fe-B core particles. The samples were then washed three times with methanol and stored in methanol for further analysis. In Figure 3.3, a simple process flow chart overviewing the synthesis methodology explained within the methodology for the synthesis of Fe-B@Au NPs.

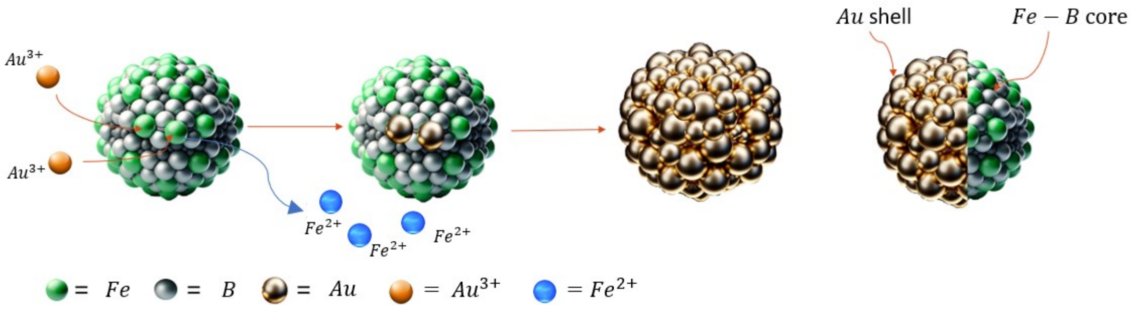

Figure 3.2: Diagram of redox-transmetalation process.

$$Fe^{2+} + 2e \rightarrow Fe \qquad E^{o} = -0.44V \qquad \text{Eq 3.5}$$

$$Au^{3+} + 3e^{-} \rightarrow Au \qquad E^{o} = 1.52V \qquad \text{Eq 3.6}$$

$$3Fe + 2AuCl_4^{-} \rightarrow 3Fe^{2+} + 2Au + 8Cl^{-} \qquad \text{Eq 3.7}$$

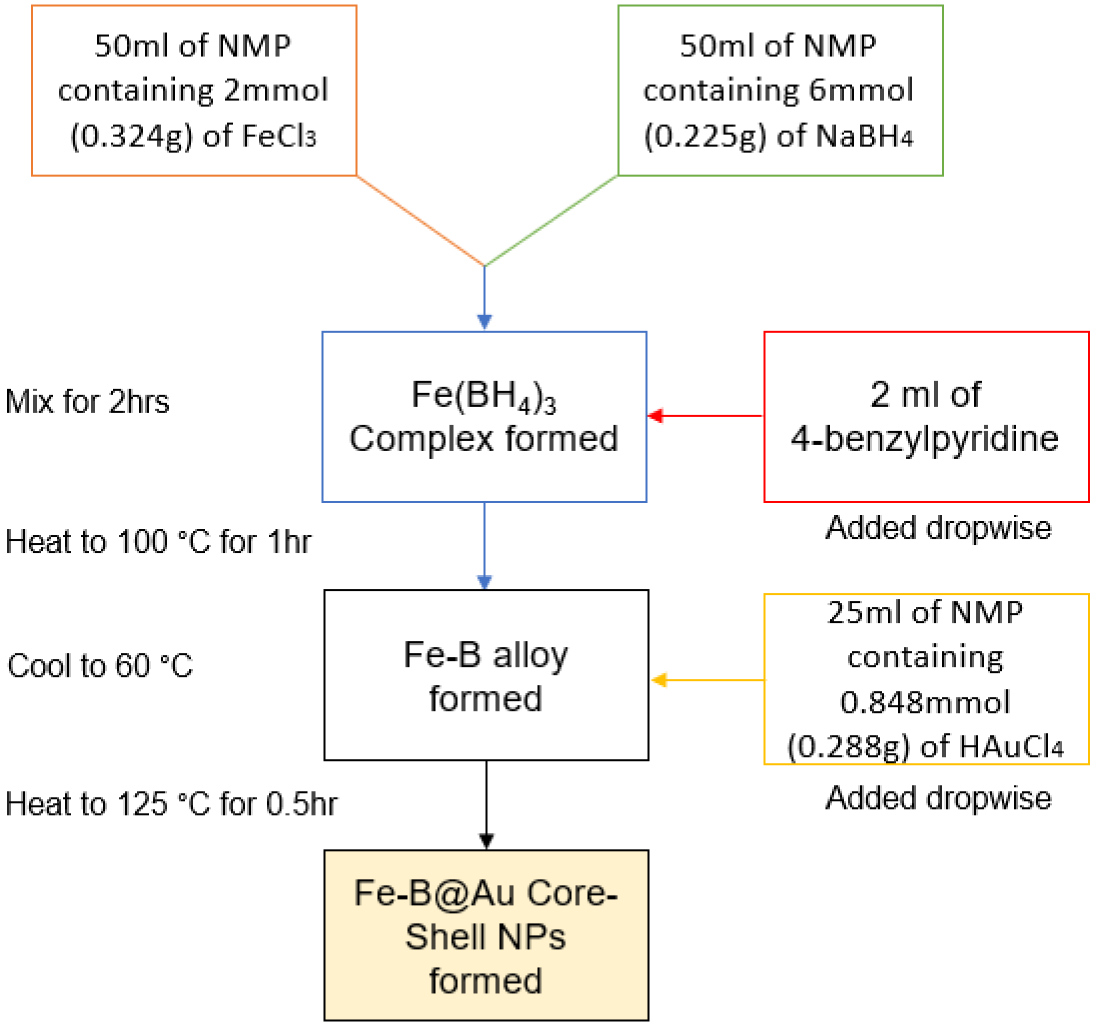

Figure 3.3: Simple process flow chart of non-aqueous redox-transmetalation process for synthesising Fe-B@Au NPs.

3.3 Characterisation

3.3.1 SEM / EDX

Scanning electron microscopy and energy-dispersive X-ray spectroscopy (SEM/EDX) analyses were conducted using a Quattro SEM (Thermo Fisher Scientific, USA) coupled with an EDS UltraDry 60M (129 eV) detector. STEM mode was used and copper / polycarbon grids with a mesh size of 300 squares per inch was used for this analysis. The operating parameters used for the analysis were high vacuum mode with an acceleration voltage of 15 kV with a spot size of 3 microns. To gain a high resolution image and obtain a signal during EDX for both gold and iron. A resolution of 1536x1094 pixels was chosen for the photos at 45 μs dwell time, to strike a balance between time acquisition and image clarity. Both Bright Field and High Annular Angular Dark Filed images were obtained from this analysis.

15 kV was used as the acceleration voltage to excite the electrons in the material enough to remove an electron from one of the inner shells. A voltage above its relative X-ray intensities is required. Iron (Ka shell) is 6.4 keV, and gold (La1 shell) is 9.71 keV. Ideally, to ensure excitation and a strong signal for the material, 1.5 x the values above are used, and 15 kV is a good value that reaches these requirements. Boron was checked for by EDX; however, boron is a very light element with only five electrons, one inner shell containing two electrons that can be ejected from the shell to give a signal and detection.

3.3.2 DLS

DLS was carried out with a Nanolive Zetasizer using methanol as the solvent. The operating parameters of refractive index (1.33) and viscosity (0.56 cP) were set to methanol values which were already stored in the Malvern software. For each sample, five runs were carried out to compare the stability within the sample from each run. The equilibrium time between each run was set at 2 minutes. The refractive index of the material was set at irons RI of 2.9304.

3.3.3 XPS

XPS analysis was conducted in a Thermofisher ESCALAB 250 electron spectrometer equipped with a hemispherical sector energy analyser at source excitation energy of 15 KeV and emission current of 6 mA; analyser pass energy of 20 eV with step size of 0.1 eV and dwell time of 50 ms were used throughout the experiments. The base pressure within the spectrometer during examinations was always better than 5 x 10^{-10} mbar and this ensured that all signals recorded were from the sample surface. In all samples the analysed area was 500 mm diameter.

3.3.4 UV-Vis

Ultraviolet–visible spectroscopy (UV/VIS) spectra of the nanoparticles were recorded using a UV–VIS spectrophotometer (Jenway 7615). 2 ml of the sample was loaded into a quartz cuvette with the path length set to 10 mm with increments in wavelength of 1 nm.

3.3.5 ICP-OES

ICP-OES was carried out on a Thermo Fisher iCAP 7000 series ICP-OES Spectrometer. A concentration curve was set up gold, iron and boron using standards purchased from Fisher Scientific. The concentration curve was set up from 0.1 ppm going up in increments of 10 x to 10,000 ppm. For the preparation of the samples, 500 mg of the sample were digested in 0.5 ml aqua regia to digest all three materials present. Upon the samples being completely digested, the solutions were diluted with 4.5 ml of deionised water and analysed to give exact bulk concentrations of all three materials present.

3.4 Results and discussion

3.4.1 Fe-B Core synthesis

The experimental procedure was done where one set of variables were tested while keeping all other variables constant to find optimal conditions for the synthesis. The variables found to increase the boron content and reduce the size of the core are used for the synthesis of the shell material.

3.4.2 Effect of surfactant

The particles require to be less than 50 nm to pass through the blood-brain barrier to reach the glioblastoma. It is critical that the size of the particles is controlled to have a narrow size distribution that is able to pass through the blood brain barrier (BBB). Initially, the experiment was run in the same way as explained above in the experimental procedure, with a slight change to whether a stabiliser was used or not and also what type of stabiliser was used as seen in Table 3.2.

Table 3.2: Experimental conditions altered to ascertain their effect on particle size.

Experiments	Conditions
1	Without
2	4-benzyl pyridine
3	PVP-30k

Ban et al. 2005, reported on the use of 4-benzyl pyridine as the stabiliser for the Fe core and Fe@Au particles. In this work, they suggested that a small amount of 4-benzyl pyridine was added after centrifugation. Due to a ‘small amount’ being very unclear on exactly how much was added to the iron borohydride solution, different amounts were trialled from 200 µl to 2 ml to verify its effect on the size of the particles. It was expected that the more stabiliser added, the more uniform the particles distribution is. The initial colour of the complex solution before adding the 4-benzyl pyridine was a light green. However, once the stabiliser was added to the solution, the colour adjusted to a greenish/yellow colour, indicating that a reaction of some kind was taking place upon addition of the stabiliser. After that, once the solution was heated to 100 °C to reduce the complex, reduction did not occur, and the solution did not turn black, regardless of the amount of 4-benzyl pyridine added to the solution. The stabiliser, 4-benzyl pyridine, was affecting the complex somehow, so the reduction was unsuccessful. A possible explanation for the unsuccessful reaction is in *Ban et al. 2005* , sodium metal was used as the reducing agent rather than sodium borohydride, and unwanted reaction occurred between the 4-benzyl pyridine and the sodium borohydride. In the experimental procedure of *Ban et al. 2005* , to form the iron core the solution was refluxed at 160 °C. Whereas, *Glavee et al. 1992* used sodium borohydride as the reducing agent, the reduction took place at 100 °C and this was used in this experimental design. As 4-benzyl pyridine was unsuccessful, further tests were carried out using no stabiliser and PVP-K30 to analyse the effects of different stabilisers. Further testing was carried out on adding the stabilisers at different timepoints; before and after the reduction of the $Fe(BH_4)_3$ reduction.

Adding the stabiliser after the formation of Fe-B core is less effective. However, agglomeration will be reduced when the stabiliser is present. Figure 3.4, shows three different experiments were analysed via DLS. One with no stabiliser, and then two different stabilisers were used. In Figure 3.4a, no stabiliser was used, leading to large particles and broad size distribution of 658.5 ± 275.3 nm. It was noted that after storage in MeOH, particle sedimentation would occur. In Figure 3.4b, when using 4-benzyl pyridine, after the solution had turned black, it led to a size distribution of 72.45 ± 11.76 nm leading to a much narrower size distribution. With further investigation, by adding the stabiliser before the reduction would be expected to produce a smaller core particle. Figure 3.4c shows that when PVP-K30 was used as a stabiliser, two size distributions are picked up: a lower concentration of very small NPs of 13.24 ± 3.209 nm and a more significant size distribution of 102.5 ± 41.35 nm. Even though there is a small concentration of smaller NPs, a high proportion has a mean size of 102.5 nm. Both stabilisers have shown that with further optimisation narrower size distributions are attainable.

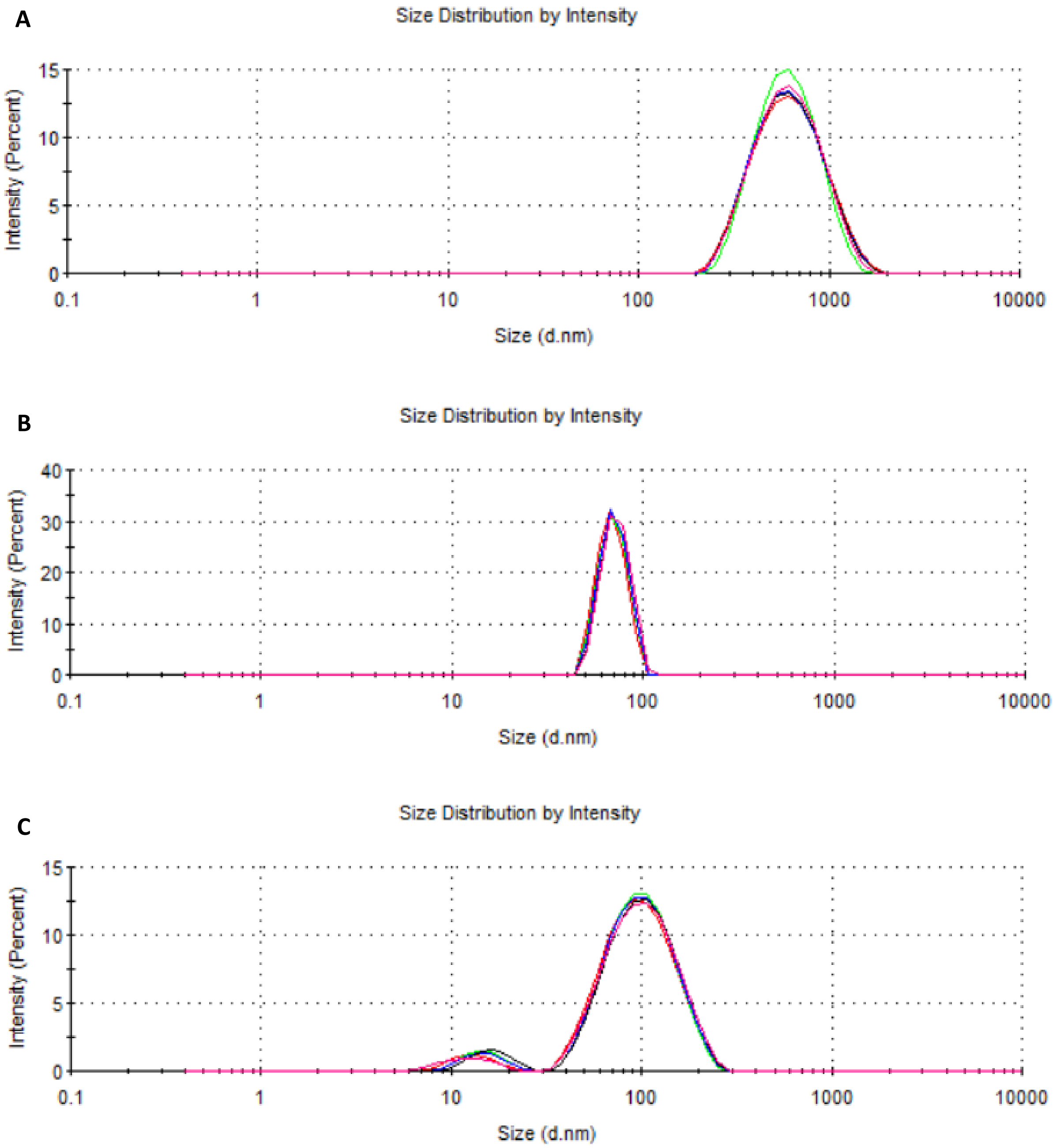

Figure 3.4: The DLS size distribution of synthesised NPs: (A) without stabiliser; (B) with 2 ml of 4-benzyl pyridine and (C) with 1g of PVP-K30.

3.4.3 Effects of ionic state of iron

An essential requirement for NCT is the boron content. ^{10}B can absorb neutrons causing it to be promoted to ^{11}B where it is destabilised and breaks down to release a localised amount of radiation to treat glioblastomas *(Suzuki, 2020)*. It is pivotal to analyse and optimise process variables to increase the boron content. Table 3.3 displays the two experiments that were carried out that impact the boron content. As 4-Benzyl Pyridine negatively impacted the synthesis of the core when added prior to the reduction taking place, the 4-Benzyl Pyridine was added directly after the reduction and the solution turned black.

Table 3.3: Experimental conditions trialled for boron content.

Experiments	Conditions	Stabiliser
4	Slow addition rate of $NaBH_4$ to Fe^{2+}	4-Benzyl Pyridine
5	Slow addition rate of $NaBH_4$ to Fe^{3+}	4-Benzyl Pyridine

Linderoth et al, 1990, Corrias et al. 1993, Glavee et al. 1995, Linderoth et al. 1998 all report on how different variables effect the boron content of the transition metal-boron alloy. The mixing pattern of the $NaBH_4$ and $FeCl_3$, the pH of the solution, and the concentration of the $NaBH_4$ solution all effect the boron incorporation. In *Glavee et al. 1995*, by mixing the iron solution into the borohydride dropwise led to a boron content in the range of 32 - 37 atomic %, determined by X-ray powder diffraction and Mossbauer Spectroscopy. However, when adding the borohydride solution in dropwise to the iron solution leads a boron content of 28-33 atomic % was achieved *(Linderoth et al. 1998)*. As the addition rate and/or the concentration of borohydride increases, the amount of incorporated boron is reduced. Rather than forming amorphous Fe-B alloyed NPs, crystalline Fe particles form with little to no boron incorporation *(Linderoth et al. 1998)*. *Cho et al. 2006* reported the synthesis of Fe@Au core-shell NPs with no aim to incorporate boron into the core. However, after elemental analysis was carried out, 7.5 atomic % of boron was in the Fe core. When the gold shell was added to the core, 2.22 atomic % of boron was present *(Cho et al. 2006)*. Even with standard protocols for Fe@Au NPs with no intent to incorporate boron, 7.5 atomic % or 2.22 atomic % was still incorporated into Fe and Fe@Au, respectively. A higher oxidation state of iron, *i.e.*, Fe^{3+} instead of Fe^{2+}, leads to higher boron incorporation due to a higher Fe:BH_4^- ratio. *Glavee et al. 1992*, compared the boron incorporation when using $FeBr_2$ and $FeBr_3$ in non-aqueous conditions. *Glavee et al. 1992* showed that using an Fe^{3+} salt, the molar ratio of Fe/B was 0.92. Using the same process but Fe^{2+} led to a molar ratio of Fe/B of 2. If aqueous conditions were used for the synthesis, the Fe/B ratio was further increased to above 4.

Surface elemental analysis was carried out by XPS which is summarised in Table 3.4. The results obtained support *Glavee et al. 1992* reports and a clear increase in boron content when using Fe^{3+} in comparison to Fe^{2+}. By using a higher ionic state iron produces a core particle that is more effective for NCT with a greater boron enrichment

Optimisation around boron incorporation is critical for NCT, more specifically the ^{10}B enrichment that is required for BNCT. When using Fe^{2+}, the boron/iron ratio is 0.32, and when specifically focussing on boron and iron, as these are the desired products, an atomic concentration of 24.5 %. The boron content is almost doubled when using Fe^{3+} with a boron/iron ratio of 0.91 and an atomic concentration of boron of 47.5 %. This follows literature findings as more BH_4^- ions are required to the reduce the Fe leading to a higher amount of boron being produced and a higher content within the alloy. Although, carbon is always present when carrying out analysis through contaminants, there is a high atomic concentration. The presence of C-C and C=O suggests that the NMP residue has not been removed through the washing procedure and that sticky residues remain.

Table 3.4: XPS data and surface characterisation with different reaction conditions.

Conditions	Atomic Concentration %							
	C-C	C=O	O	Fe	B	N	Na	B/Fe
$FeCl_2$ with $NaBH_4$	20.0	8.9	49.5	10.8	3.5	-	7.3	0.32
$FeCl_3$ with $NaBH_4$	29.8	12.5	40.4	7.4	6.7	-	3.2	0.91

For Fe^{2+} and Fe^{3+}, 1:2 and 1:3 molar ratios of Fe:BH_4^- were used, respectively. An excess was not used to minimise the impact on the redox-transmetalation process of the Au on the surface of the core particles. The Na atomic concentration was relatively high. This indicates that the washing procedure is not effectively removing all by-products such as NaCl from the reaction mixture. With the high carbon content, it is expected that some residuals of the solvent are still present. However, there is no signal for N to further indicate the presence of the solvent and the stabiliser. At these high concentrations of C-C and C=O, nitrogen would be expected to be present in the XPS data. It is unlikely that the nitrogen concentration is below the detectable limit. As the Cl was not analysed by XPS, it is expected to have a similar atomic concentration to the Na from the 1:1 molar ratio. There is a high oxygen content, and the XPS data showed that the Fe was predominately in its oxidative state, Fe_2O_3, due to no protective layer and the boron signal was of borate. The intermetallic bonding between iron and boron where oxidation has occurred forms $(Fe_xB_{x-1})_2O_3$. However, *Glavee et al. 1992* suggests that when the Fe-B alloy is oxidised, it breaks down into two separate compounds of iron and borates, as seen from Equation 3.8. Subsequently, the Fe oxidises to an iron oxide. It is pivotal to keep inert conditions throughout the entire process until a protective shell layer of gold is implemented.

$$2FeB + 1.5O_2 \rightarrow 2Fe + B_2O_3 \qquad \text{Eq 3.8}$$

3.4.4 pH analysis

pH can have an impact on the amount of boron that is incorporated *(Linderoth et al. 1990)*. The $FeCl_3$ solution is slightly acidic with a pH of 4.5. When the complex is formed between the iron ions and the borohydride ions, and heat is applied to start the reduction, the complex of $Fe(BH_4)_3$ becomes unstable and breaks down, causing the reduction and incorporation of boron into the core material *(Glavee et al. 1995)*. The colour of the complex is greenish and, upon heating the solution becomes colourless where there is vigorous hydrogen evolution from the breakdown of the $Fe(BH_4)_3$ complex, as seen in Equation 3.2. During the colour change the pH increases. When the pH is approximately 7, the colour of the solution starts to turn black as the reduction of iron ions begins at this elevated pH and stabilises. At the same time, hydrogen gas evolves, and iron reduction occurs. Measuring the pH while effectively ensuring inert conditions are maintained would show the interesting dynamics of the process where the pH equilibrates during iron reduction and hydrogen production *(Glavee et al. 1995)*. For this research, no further studies were carried out on altering the initial and final pH with acidic or basic components to see the effects on boron content.

In some cases, upon heating, the solution does not turn colourless, followed by the precipitation of the black Fe-B NPs. However, the solution stays green with no precipitation of Fe-B NPs. Unsuccessful reactions occur due to lack of inert conditions leading to the breakdown of the $Fe(BH_4)_3$ complex, dissolved oxygen (DO) or absorbed water in the solvent leading to the breakdown of the complex and unwanted reactions. For the non-aqueous synthesis of Fe-B, it is critical to ensure the correct reaction conditions are obtained otherwise the reaction will not occur in the required way. A requirement to degas and dry the solvents through N_2 bubbling and molecular sieves respectively and clean glassware are a requirement to ensure optimal conditions. The process requires stringent and specific conditions to achieve successful reactions, which may increase the difficulties for scaled-up procedures.

Figure 3.5 displays the relative stabilities of different Fe compounds at different pH. When the reduction does not occur around pH 7, the borohydride will continue to decompose under heating, leading to an increase in pH beyond 7 and other Fe compounds becoming more stable at elevated pH. In *Scholz. 2006*, when the pH exceeds 8.5, DO can oxidise iron to its hydroxide forms. During an unsuccessful reaction, whereby the solution turns green rather than black, other compounds such as $Fe(OH)_3$ are possible unwanted products.

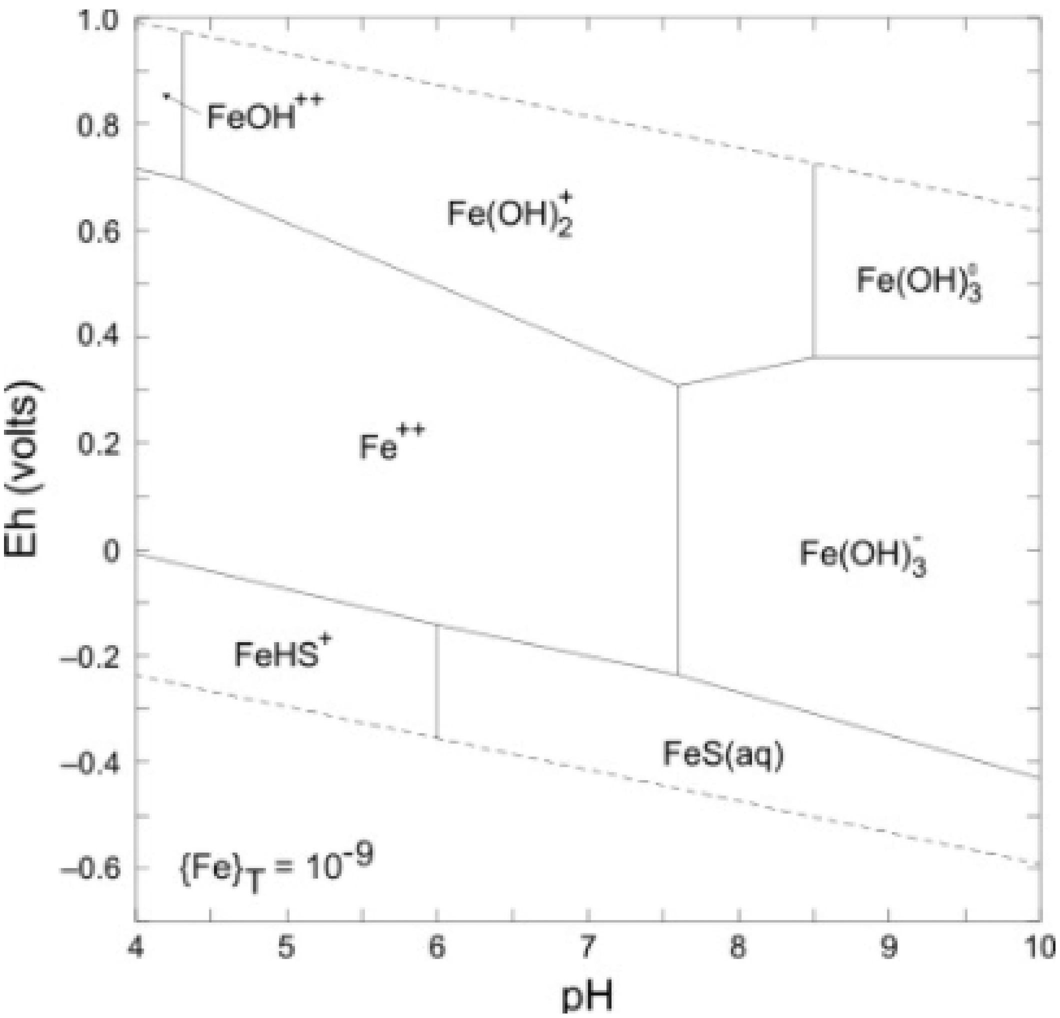

Figure 3.5: Relative stability of Fe compounds at different pH. *(Rickard. 2012)*.

3.4.5 Troubleshooting

Using non-aqueous conditions was pivotal for a successful reaction by minimising the amount of borohydride that would hydrolyse leading to effective complex formation, as seen in Equation 3.1. If water is present, the reaction scheme would not occur in the expected way, and the borohydride would start to hydrolyse via Equations 3.9 and 3.11 reducing the BH_4^- availability for $Fe(BH_4)_3$ formation. Using non-aqueous conditions means Equations 3.9-3.11 should not occur. However, if the water content increases this would have significant detrimental effects to the process.

$$BH_4^- + 2H_2O \rightarrow BO_2^- + 4H_2 \qquad \text{Eq 3.9}$$

$$BH_4^- + 2M^+ + 2H_2O \rightarrow 2M + BO_2^- + 2H_2 + 4H^+ \qquad \text{Eq 3.10}$$

$$BH_4^- + H_2O \rightarrow B + OH^- + 2.5H_2 \qquad \text{Eq 3.11}$$

Li et al. 2015 suggest ligand formation occurs between the NMP and $FeCl_3$ complex whereby using FTIR, the peak at 1674 cm^{-1} for the stretching of C=O within the NMP splits into two, with the second peak at 1623 cm^{-1} for the coordination bonds formed between C_5H_9NO and $FeCl_3$. The formation of the oxygen to metal coordination bond reduces the coupling between the C=O stretching and the NH_2 bending vibrations leading to the peaks becoming separable. However, *MaryMartinette et al. 1959*, suggested that when coordination bonds are formed between the double bond oxygen and the metal ion, the wavelength shifts to a lower frequency to indicate ligand formation rather than the splitting of the peak at 1674 cm^{-1}.

FTIR was carried on a sample of NMP and NMP containing $FeCl_3$. There were no changes between the two spectra, as seen in Figure 3.6a and b. It appears the indication of ligand formation is missing and no coordination bond between the C=O and Fe ions due to no splitting or shift in the peak at 1674 cm^{-1}. The reaction pathway suggested in *Glavee et al. 1995* is not occurring in this process with no ligand formation which causes instability and unsuccessful reaction that occur due to no ligand formation on the $Fe(BH_4)_3$ complex. Further investigation into the coordination bond complex is required to understand the formation. As the core was still being successfully synthesised without the formation of the coordination bonds between C_5H_9NO and $FeCl_3$, no further investigation was done during this research.

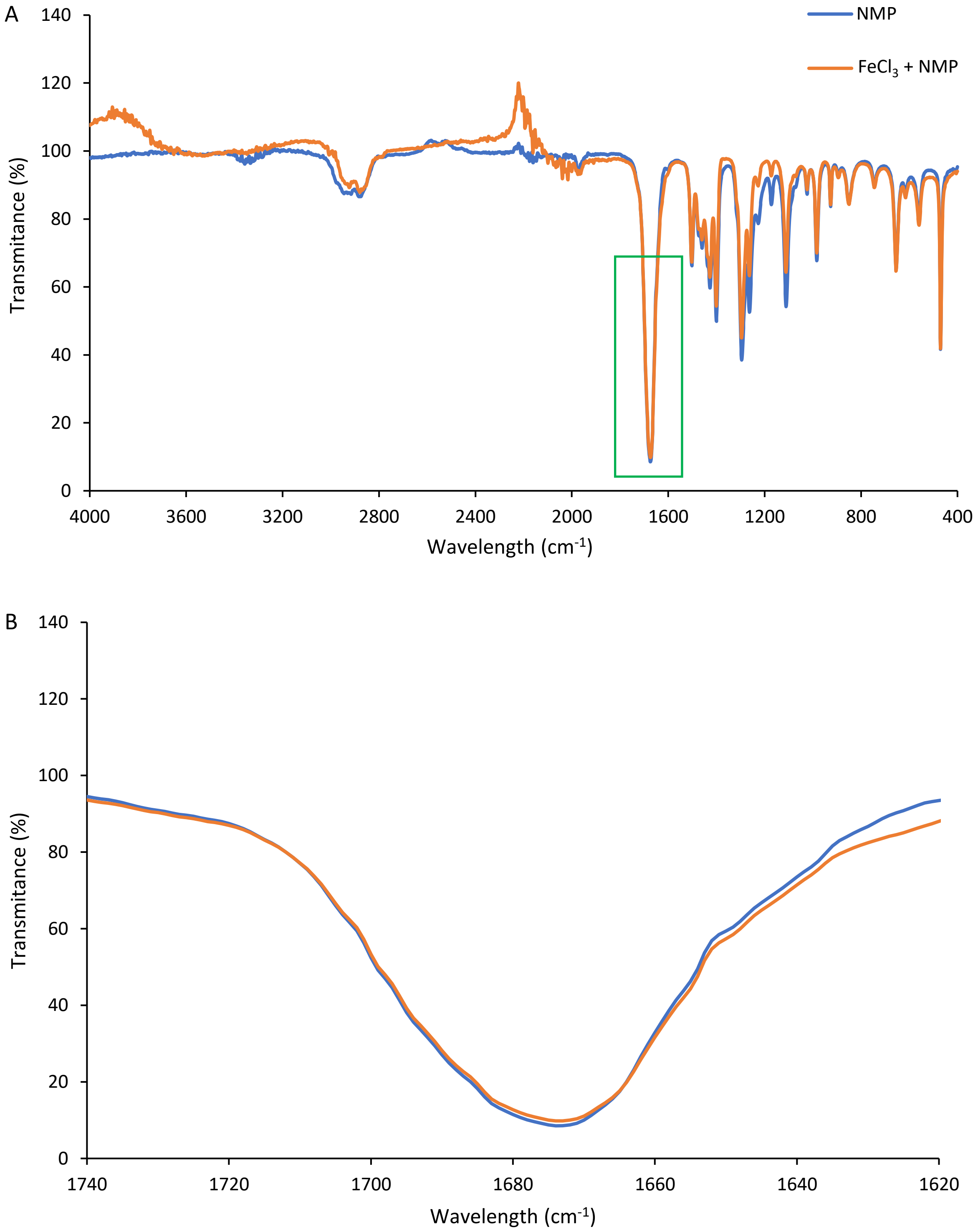

Figure 3.6: A – Full FTIR spectra of NMP and NMP + $FeCl_3$, B – FTIR spectra zoomed in at peak with wavelength of 1675cm^{-1}.

During $Fe(BH_4)_3$ complex formation as seen in Equation 3.12, a reaction between the $NaBH_4$ and the $FeCl_3$ forms NaCl waste product. The NaCl white precipitate is insoluble in NMP and the only solid within the reaction mixture before the reduction. At this stage of the process, the NaCl can be removed by centrifugation, or left in the reaction mixture.

$$FeCl_3\,(aq) + 3NaBH_4(aq) \rightarrow Fe(BH_4)_3\,(aq) + 3NaCl(s) \qquad \text{Eq 3.12}$$

In Glavee et al. 1992, during non-aqueous synthesis of the Fe-B core, the NaCl was left in the reaction mixture and removed during post processing with water and acetone washing. Whereas *Ban et al. 2005*, removed the NaCl via centrifugation before initiating the reduction of the Fe ions. It is unknown whether leaving the NaCl in the reaction mixture will disrupt the addition of the Au shell via redox-transmetalation. It is expected that it would have a detrimental effect on the synthesis of a gold shell due to another lattice being present. If the NaCl is incorporated into the core and appears at the surface, this will remove a reduction site for the Au leading to a negative impact on the shell formation. However, current operating conditions, it is not effective to centrifuge the sample to remove NaCl due to removing the solution from inert conditions. From the trial centrifugation, the pellet was predominately white, indicating NaCl. However, there was a slight green colour to the pellet where an amount of the complex had broken down and reacted with a small amount of water within the solution. Upon the addition of small amount of water to the pellet led to immediate hydrogen evolution and the solution turning black for the reduction of Fe^{3+} as displayed in Equation 3.10.

After the solution was centrifuged, the colour of the solution appeared light green / colourless rather than green due to removing and solid products, leaving behind the aqueous iron borohydride product. Upon heating the solution to 100 °C, the solution turned black for the synthesis of the Fe-B core with the removal of NaCl during centrifugation. This would lead to the removal of Na in the XPS data. However, there is an increased number of unsuccessful reactions when centrifuging the $Fe(BH_4)$ due to taking the sample out of inert conditions for a short period. For the experimental procedure, the NaCl was not removed to reduce the number of unsuccessful experiments. Until the solution can be sealed under inert conditions, this process should not be done.

Although, in *Glavee et al. 1992*, the reduction of the iron borohydride complex took place at 95 - 100 °C; it was found that upon heating to 40 °C, the reduction had started with the production of H_2 bubbles. At lower temperatures, the reduction process would take place slowly giving more control over the reduction of the complex. One reason the reduction may have started at lower temperatures is due to the ligand formation between the NMP and $FeCl_3$ not occurring that offers some stabilisation to the complex. As the temperature is increased, the rate of H_2 evolution increased and continued for approximately 10 minutes. At low temperatures enough energy is supplied to reduce the iron boron complex and as the temperature is increases, the reaction rate also increases. For future work, carrying out the reduction at lower temperatures would be interesting to analyse.

The time the complex is left forming is essential as, presumably, the process is sequential, where one BH_4^- becomes bonded to the Fe^{3+} to form $Fe^{2+}(BH_4)$, followed by $Fe^{+}(BH_4)_2$ and finally $Fe(BH_4)_3$. Leaving the reaction for a shorter period is expected to lead to partial formation of the complex leading to a reduced boron content.

NMP is hygroscopic and readily absorbs water from the air, which ultimately affects the process. The NMP should appear colourless. However, over time, the solvent degrades, and contaminants increase causing the solution to appear a yellowish colour *(Lertsuphotvanit et al. 2023)*. Once the yellowish colour of the solution appears, the chance of successful reduction of the iron borohydride complex decreases. As soon as the yellowish colour appears, the solvent requires cleaning and drying to regenerate the effective solvent.

Analysing the complex and core material is challenging due to both materials being affected by atmospheric conditions. The analysis that has been carried out on these materials will not be a direct comparison to the material formed under inert conditions due to the decomposition of the complex and oxidation of the core.

3.5 Fe-B@Au synthesis

The addition of a gold shell around a Fe-B core has yet to be researched, and the optimal reaction conditions not yet established. This novel research aims to bridge the gap in knowledge of NCT and a method to synthesise a particle capable of the NCT process. The conditions need to be optimised to overcome the lattice mismatch between the core and the shell material. Two variable that significantly changed the optical properties and colour of the solution that can give a crude method of analysis of success of core-shell formation was the temperature at which the gold solution was added to the Fe-B core solution and the rate of addition. Table 3.5 displays different reaction conditions that were tested. Some experiments showed two separate distributions of monometallic iron and gold particles, and other reaction conditions show the formation of partial core-shell structures. In most cases, when the solution went a typical burgundy colour to indicate gold NPs, there was no core-shell formation or very poor core-shell formation. However, then the solution turned a blue / black colour, the samples appeared to show a more interesting core-shell structure.

Table 3.5: Different process variables tested and results. (Rapidly indicates that the 50 ml of gold solution was injected into the core solution over five seconds to achieve a rapid temperature drop).

Exp	Gold solution addition rate (ml/hr)	Temperature of gold solution (° C)	Temperature of core solution (°C)	Colour of mixture	Core-Shell formed?
M1	25	19	60	Burgundy	No
M2	25	19	125	Burgundy	Partial
M3	Rapidly	4	125	Black/blue	Partial
M4	Rapidly	19	125	Black/blue	Partial
M5	25	19	25	black	No

After several purification steps washing with ethanol, there were still sticky residues of NMP acting as a glue that both the core (Fe-B) and the shell material (Au) stuck to rather than forming a core shell material. This led to false positives when visually observing the sample. The sample was magnetic and had the characteristic optical properties of gold with a burgundy / purple colour. The burgundy Au NPs being pulled towards to magnet would indicate that they are bound to Fe.

By taking a small amount of sample and washing with acid, was a quick method to test if a successful core-shell structure was formed. If the materials magnetic properties cease to exist, this would confirm no complete shells of gold have formed around an Fe-B core. The acid wash confirms two possibilities: one being two separate distributions of monometallic Fe-B and Au or secondly partial core-shell structures. Numerous occasions when analysing via STEM, the NMP acted as a sticky residue where monometallic distributions of both Fe-B and Au were attached to it. In Figure 3.7, the STEM photos of sample M1 show a mixture of monometallic particles of iron (yellow circles) and gold (green circles). The misty background, which the particles are stuck to, appears to be the NMP residue.

STEM mode: Bright Field

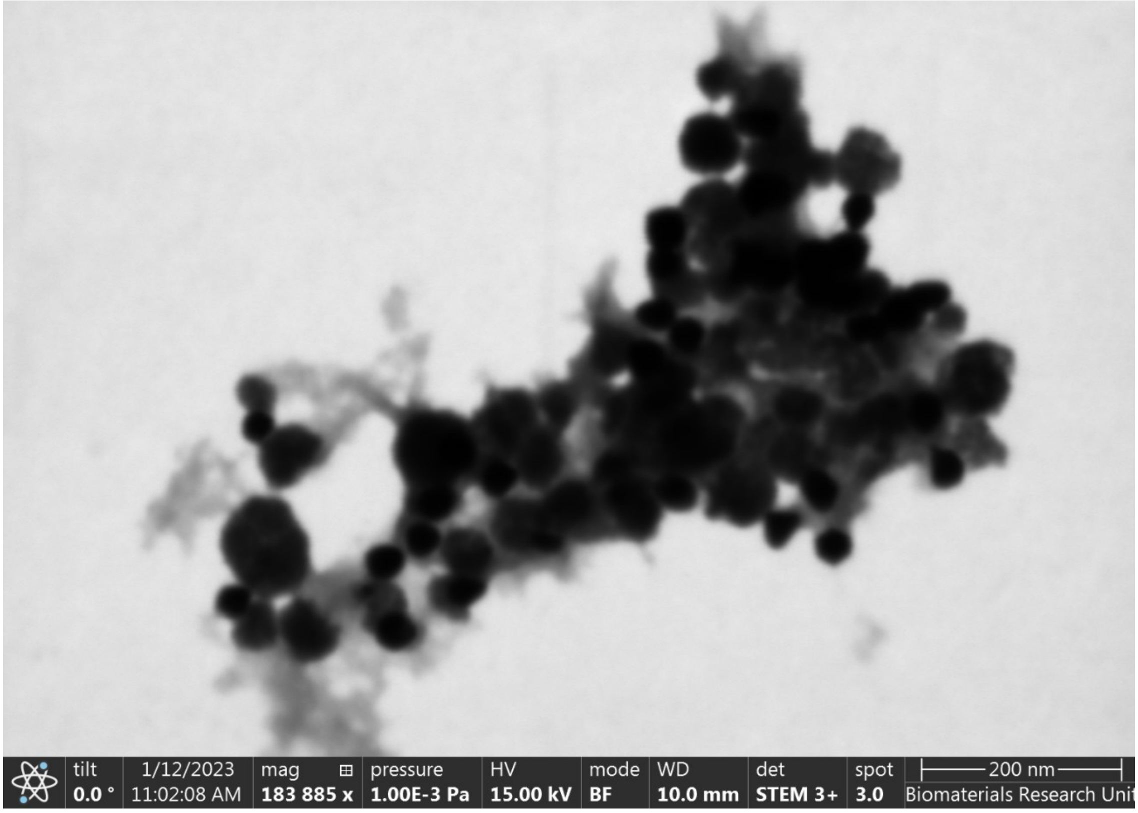

STEM mode: High Annular Dark Field

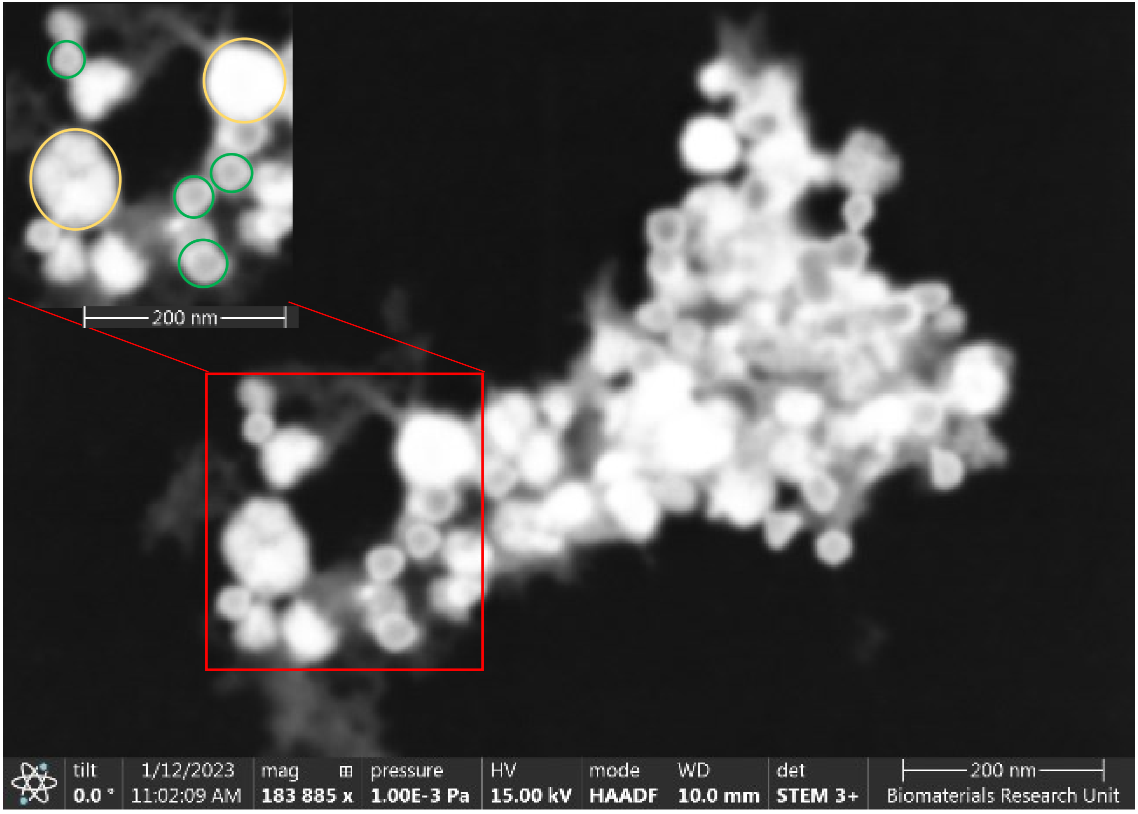

Figure 3.7: STEM images of non-aqueous sample M1. (yellow circles indicate Fe particles, green circles highlight Au particles).

In Figure 3.7, two distributions are visible in M1 [highlighted via the circles]. The STEM images confirmed that the visual appearance of the sample gives a false positive as the particles are sitting in residue NMP which has not been removed during the washing stage. The larger white amorphous particles, between 50-100 nm, are the magnetic cores [yellow circles]. The amorphous structure gives an indication that an amount of boron has been incorporated into the core. Au NPs are formed with a size between 20-25 nm [green circles]. The gold ions have been reduced indicating the redox-transmetalation process is occurring, but not in the desired way of forming core-shell structures. It is known there is a large lattice mismatch between the Fe and Au, that leads to a significant energy barrier. If the core-shell is not forming, although the reduction is occurring at the iron surface, it is still energetically favourable for the gold nanoseeds to move away from the surface and form monometallic Au NPs. Another reason for core-shell particles not forming is the boron at the surface may be incapable of reducing the Au. With 30 – 50 % B content, there is limited reduction sites for Au and the formation of a core-shell.

In Equation 3.13, *Bard, 1985* shows a route for how boron can reduce gold at its surface, with a reduction potential of 0.89 V in comparison to Au which has 1.002 V but this again only has a small difference and energetically unfavourable. However, for this reaction route, aqueous conditions are required. The chloroauric acid contains a small amount of water that could allow the boron to be used as a reduction site. However, this mechanism and in non-aqueous conditions, it is unknown if other reaction pathways can take place.

$$B(OH)_3 + 3H^+ + 3e^- \rightleftharpoons \mathrm{B}(s) + 3H_2O(l) \qquad \text{Eq 3.13}$$

If the reduction of gold is occurring at both iron and the boron, another cause for no shell formation is the molar ratio of Fe and B to the Au. Three Fe atoms are required to reduce two Au^{3+} ions. If there is an excess of Au ions this will lead to an increase in Au nanoseeds that increases the energetics towards forming gold NPs. It can also lead to over erosion of the core material and using a high amount of the Fe that will lead to the dismantle of the core material leading to the Au having no core to seed upon. To confirm this, in a trial reaction, the Au molar amount was doubled, which led to little magnetic particles being present at the end of the process. The best reaction conditions would be to use a low concentration solution of Au ions to minimise the amount of monometallic Au NPs formed.

If too little gold is used in the synthesis process, then there is not enough gold for a complete shell to form leading to partial or no shell formed around the core. *Chen et al. 2009* identified that the ratio between nickel and gold is critical to forming core-shell structures. In most cases, a mixture of both core-shell and gold NPs were formed. The addition time of the Au solution to the core can cause issues. If the core grows too large before Au addition, island growth will occur due to not enough gold to cap the larger particles. Additionally, when initially carrying out the STEM analysis, another false positive was observed. The smaller particles (20 - 25 nm), in Figure 3.7, have a contrast between the particle's core and shell in HAADF images, which is usually indicates different materials within the core and shell. However, in Figure 3.8, the EDX data shows that these particles are monometallic Au.

In *Chen et al. 2009*, there is a significant contrast between the Ni core and the gold shell. This is because in STEM mode, when using HAADF analysis, this measures the most scattered electrons. Heavier elements, such as gold, should appear brighter due to having a larger z-number and scattering the electrons more. Whereas Fe and B, which are lighter elements scatter the electrons less. Bright-field analyses particles that have not been scattered, and the electron beam goes through the sample. The analysis shows differences in thickness and would show the opposite of the HAADF images as the sample is thinner at the edges than in the centre of the material. Due to having the contrast present in the particles formed in Figure 3.7, this should show that core-shell particles have been formed as in *Chen et al. 2009*. With Figure 3.8 showing that this is not the case suggest that false positive results are being obtained from the HAADF. EDX is not a sensitive technique for lighter elements and would not detect boron as effectively due to having only two inner electrons to obtain a signal from. Even though an acceleration voltage of 15 kV should have a penetration depth of 550 nm, as taken from the Thermo Fisher Scientific training document for the equipment, the small Au particles are less than this and should not display a contrast between core and shell.

From Figure 3.8, the large amorphous balls are Fe and do not contain any form of the shell due to no overlap of the Fe and Au signal. The Au particles which displayed a contrast in HAADF does not show any Fe signal in the centre of the particles.

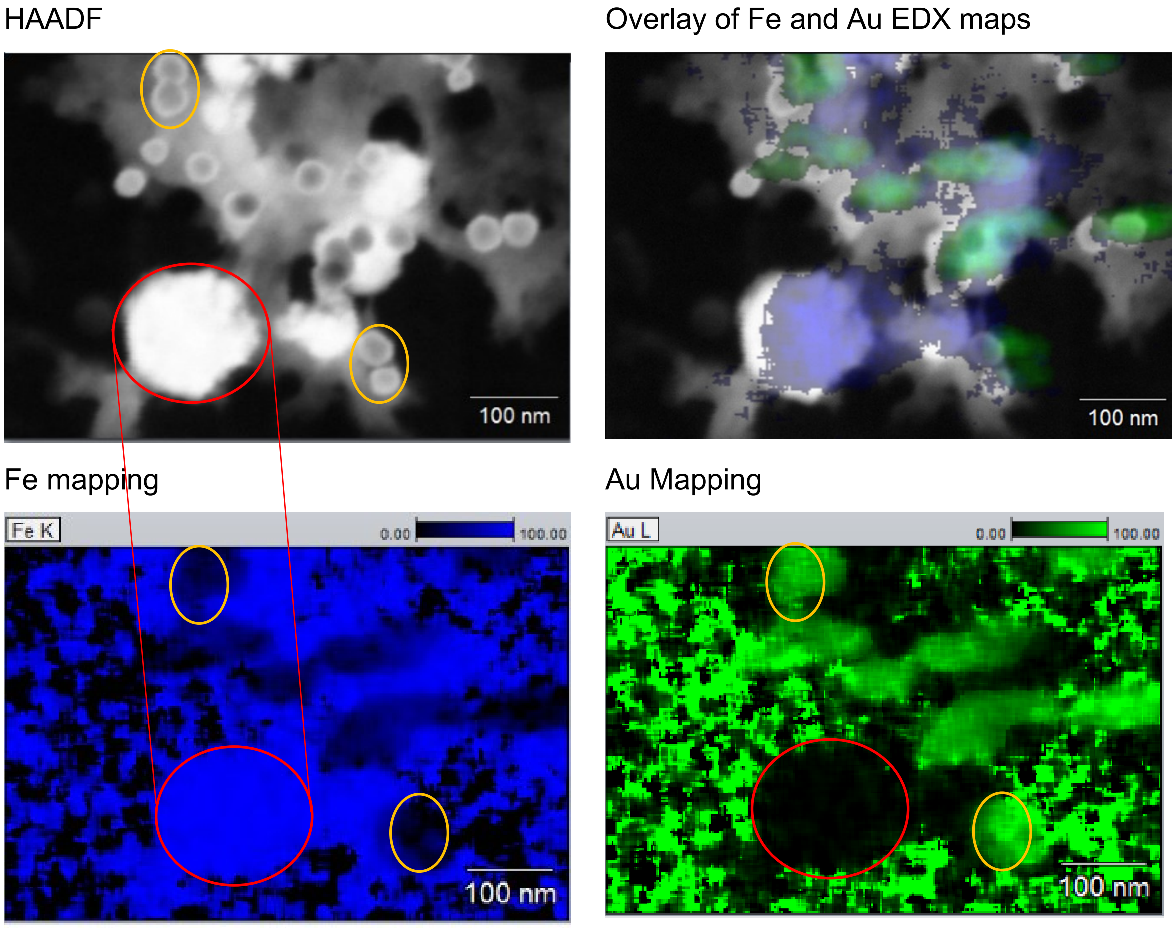
HAADF

Overlay of Fe and Au EDX maps

Fe mapping

Au Mapping

Figure 3.8: EDX mapping of sample M1 showing two distributions of larger Fe NPs and smaller Au NPs.

In *Ban et al. 2005*, the Fe core solution is cooled to 60 °C before adding the gold solution slowly and heating back up to achieve core-shell iron-gold NPs. In Table 3.5, a variation of these variables was tested to find optimal conditions for the synthesis.

In Table 3.5, experiment M1, the standard conditions from *Ban et al. 2005* were used to try and repeat the process. Upon the slow addition of the gold solution to the core material, the solution remained black at 60 °C. After raising the temperature to 125 °C and leaving the sample for 30 minutes for the reduction, the solution slowly turned burgundy, suggesting the reduction and formation of gold NPs. UV-Vis was carried out on 50 nm Au particles, M1 and M3 to compare monometallic Au to two separate distributions of Fe and Au and partial shell structures.

Gold NPs have distinct optical properties that give a characteristic curve when analysed by UV-Vis. In Figure 3.9, UV-Vis was carried out on both experiments M1 and M3 which was compared to a 50 nm gold colloid solution. The characteristic curve for the 50 nm gold NPs shows a peak at 540 nm. For experiment M1, where there is a segregation of Fe-B and Au NPs, a similar characteristic peak with a slight shift in wavelength to 550 nm occurs suggesting the formation of monometallic gold NPs. However, for M3, which in the STEM images in Figure 3.11, displayed partial core-shell structures showed completely contrasting UV-Vis spectra with a much broader peak with a shift to a higher wavelength. Experiment M1, followed the standard conditions listed in the methodology which was similar to *Ban et al. 2005*. The UV-Vis data in Figure 3.9shows a similar peak to that of 50 nm gold NPs with a blue shift. However, the UV-Vis results obtained in *Ban et al. 2005* do not match that obtained in M1. However, experiment M3, whereby different reaction conditions are used [rapid addition of Au solution into core solution] formed partial core-shell particles that closely matched the UV-Vis spectra of *Ban et al. 2005* with a broader peak. The properties of the material can be fine-tuned by adapting the shell thickness. The broader peak from UV-Vis, like in M3, suggests that there is a higher chance of a core-shell structure formed, in comparison to M1 where there is a sharper peak where typical gold NPs would appear in UV-Vis.

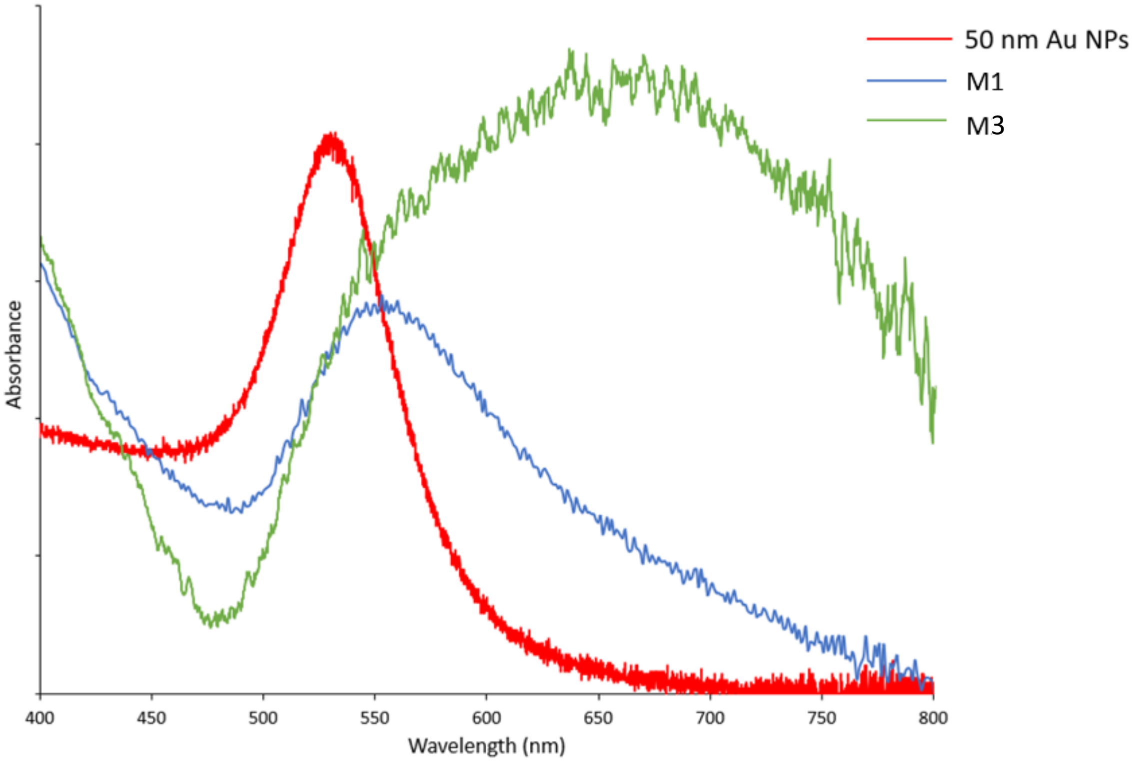

Figure 3.9: UV-Vis data of monometallic 50 nm Au particles, Exp M1 and M3.

Figure 3.10, the BF and HAADF images of M2 show no clear core-shell structure but appears more like monometallic Au particles that have then aggregated to the parts of the Fe-B core. This indicates island growth occurred or during the drying process for the STEM analysis, the particles aggregated to each other. There is still NMP present within the sample and not being completely washed out. Following the same reaction conditions and with small changes, it was not possible to achieve the same core-shell results as *Ban* *et al. 2005*. Some variables from the process may not be reported which causes a reproducibility issue.

STEM mode: Bright Field

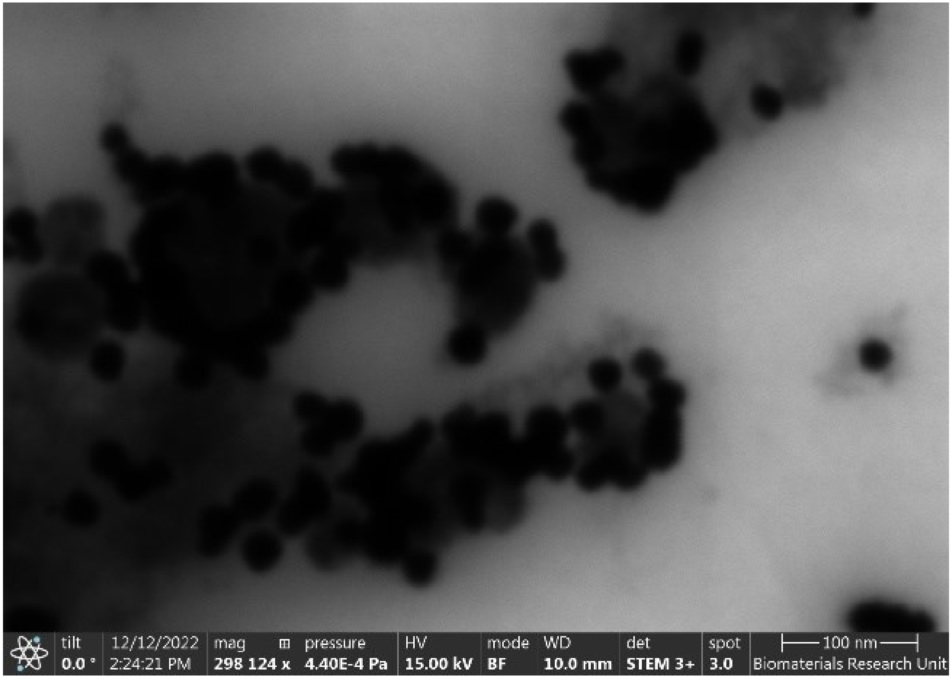

STEM mode: High Annular Dark Field

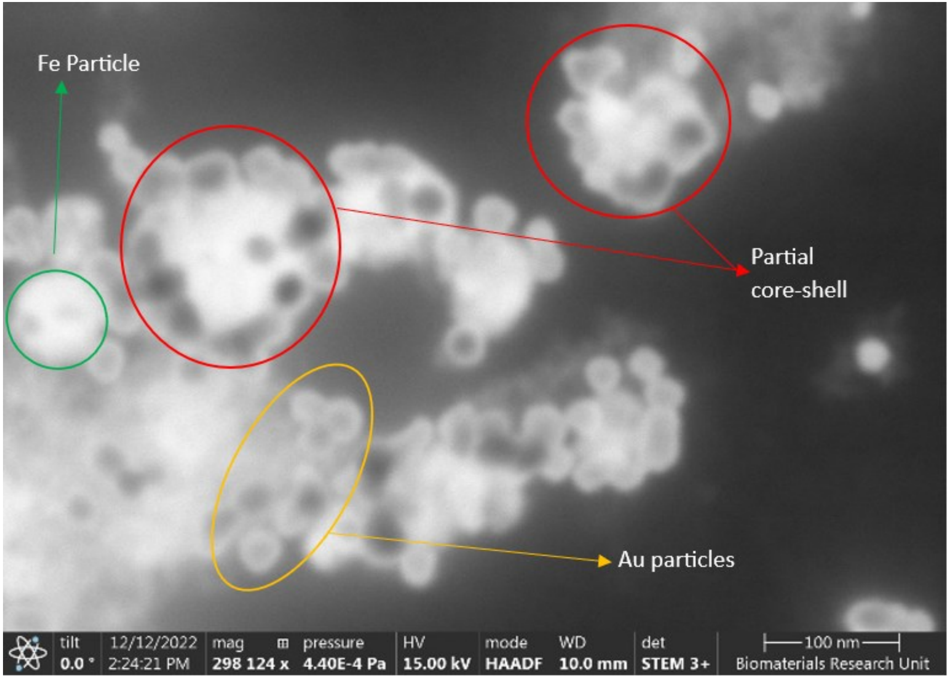

EDX

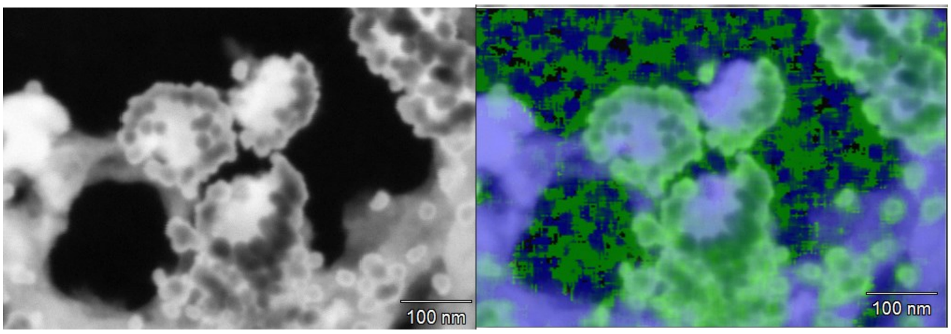

Figure 3.10: STEM images and of M2. (Red circles – possible partial shells, Yellow – Monometallic Gold, Green – Monometallic Iron). And EDX data of M2. (Blue – Fe, Green – Au)

The gold addition rate for both samples M1 and M2 were 25 ml/hr, but the difference was the temperature of the core solution upon gold addition. In M1, it was 60 °C, and in M2, it was already preheated to 125 °C. elevated temperatures are required to initiate the reduction process via redox-transmetalation. M2, with the addition taking place at 125 °C, leads to immediate gold nanoseed formation when encountering the core surface leading to more positive results than in M1. In M2, as the gold solution is added, the gold ions are reduced immediately, and only a tiny amount of gold seeds within the solution start to seed upon the core material. It was expected that these conditions would lead to negative results due to the rapid reduction of the gold ions.However, a better shell formation was found in comparison to M1. When adding the gold ions at 60 °C, the reduction of the gold ions would be slower. However, due to the initial slower reduction a lower temperature, as the solution heats up, there is simultaneous reduction of the gold ions that may push the gold ions to form monometallic gold NPs rather than a shell.

However, M5, where the core solution was cooled down to 25 °C, and the Au solution was added at 25 ml/hr gave negative results where the solution remained black and, after cooling down to room temperature, large agglomerates settled to the bottom of the flask. Cooling down the core solution too far seemed to change and affect the redox-transmetalation process.

The variable that appeared to have the most significant impact on core-shell formation was the addition rate of the of the gold solution. The rapid addition of the gold solution to the core solution at 125 °C led to partial core-shell structures. *Chem et al. 2012,* synthesised Ni@Au and Au@Ni NPs using non-aqueous conditions. After forming the nickel NPs, 5 mg of chloroauric acid ($HAuCl_4$) was added to form gold-seeded nickel NPs at 40 °C. The solution was then heated to 195 °C for 30 minutes before cooling to 150 °C. At this stage, the gold solution was injected rapidly to cause a temperature drop. The quenching process was vital in forming core-shell structures; if the temperature drop were not high enough, the shell formation would be incomplete. By injecting the gold solution allows for rapid formation of Au nanoseeds where the concentration of nanoseeds formed is inhibited by the temperature drop and stops homonucleation and starts hetronucleation. The energy shift promotes the formation of core-shell structures due to the temperature decrease leading to the gold ions not being able to be reduce at the lower temperatures. However, by forming those initial gold nanoseeds form on the surface of the core material meaning as the temperature increases and further gold ions are reduced the energy barrier for forming a shell is reduced due to the gold nanoseeds at the surface.

The temperature drop was investigated by adjusting the temperature of the gold solution when rapidly added to the core to promote minimal homonucleation followed by hetronucleation for core-shell synthesis. This was done by rapidly injecting gold ion solutions at different temperatures into a Fe-B solution. The nanoseeds are expected to form and attach to the surface of the core material so once the reduction continues, the energy barrier for seeding on a different lattice is reduced due to the presence of gold nanoseeds. Figure 3.11 and Figure 3.12 display the STEM BF / HAADF and the EDX data of M3 where the gold solution was at 4 °C, respectively. The red circles in HAADF STEM images of M3 indicate the positive results of core-shell / partial core-shell structures. The yellow circles indicate the monometallic gold particles. Figure 3.11 almost appears as a multilayer from the difference in contrast in the HAADF that shows a brighter centre, followed by a darker shell and then another brighter shell on the outside.

There are less monometallic Au particles in M3 when compared to M1 and M2 showing the rapid injection with a temperature drop followed by heating supported the formation of core-shell materials. Homonucleation was inhibited and promoted hetronucleation to minimise Au NP formation. From an acid wash, it appeared to show possibly incomplete shells with holes within the structure as the magnetic properties were removed after acid washing. Figure 3.12 and Figure 3.13 displays the EDX data for M3. The elemental analysis shows that there is a density of iron within the core of the material with gold appearing on the outside and overlaps where the iron signals are. The line analysis shows high signal for Au (green line) at the edge of the particles and low for Fe (blue line) and at the centre of the particle the Fe signal increases and the Au reduces as the core is larger in the centre than the edges. The injection of the 4 °C gold solution into the 125 °C core solution leads to a temperature drop to between 63-66 °C, which is close to the temperature initially being followed in *Ban et al. 2005.* When the Au solution was added at 19 °C to a core solution 125 °C as in experiment M4, there is a rapid drop in temperature again but less than in M3. In Figure 3.15, partial core-shell structures are formed again but less effectively when compared to M3. The gold NPs show island growth with gold NPs scattered across the surface of the Fe-B core. Whereas in M3, a more uniform core-shell structure appears to have formed. This shows that controlling the temperature drop is significant in forming core-shell NPs. When the Au solution is added at 60 °C, no Au nanoseeds are formed and only upon the temperature increase gold reduction starts but due to the high concentration in the solution leads to more monometallic Au NPs being formed. It is key to form a small amount of Au nanoseeds to promote shell formation.

STEM mode: Bright Field

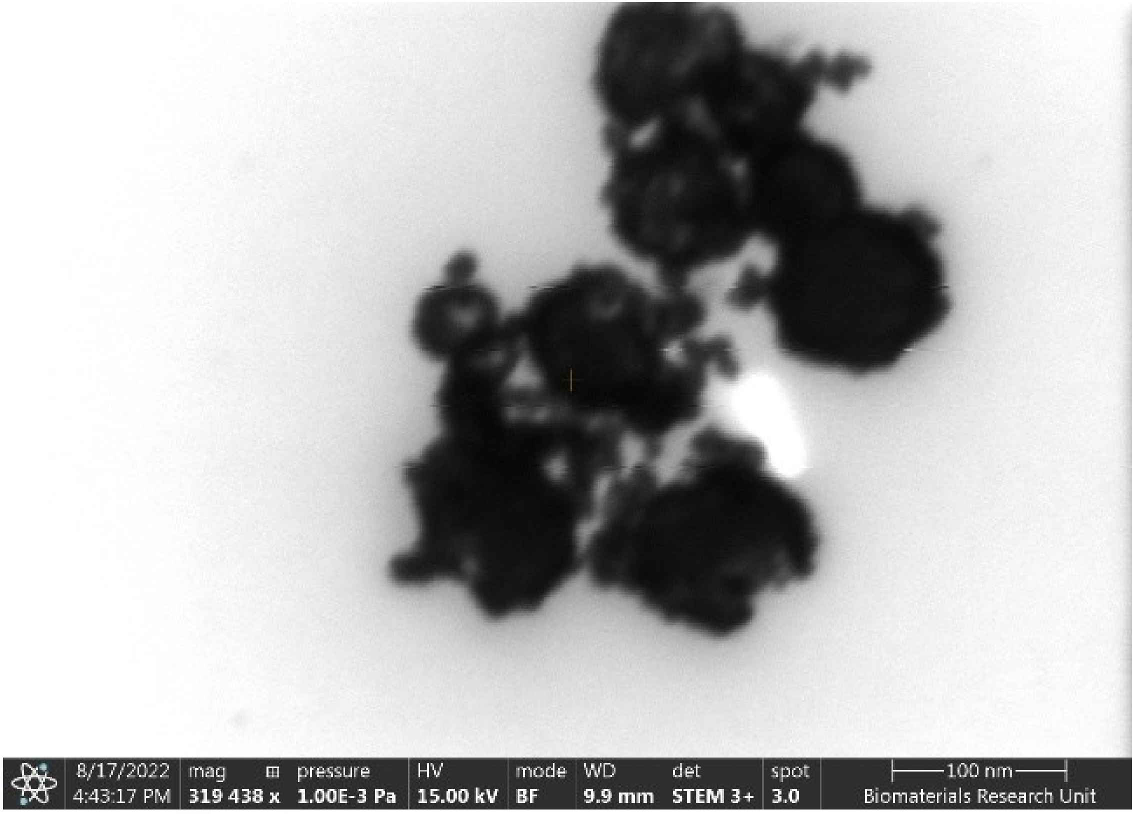

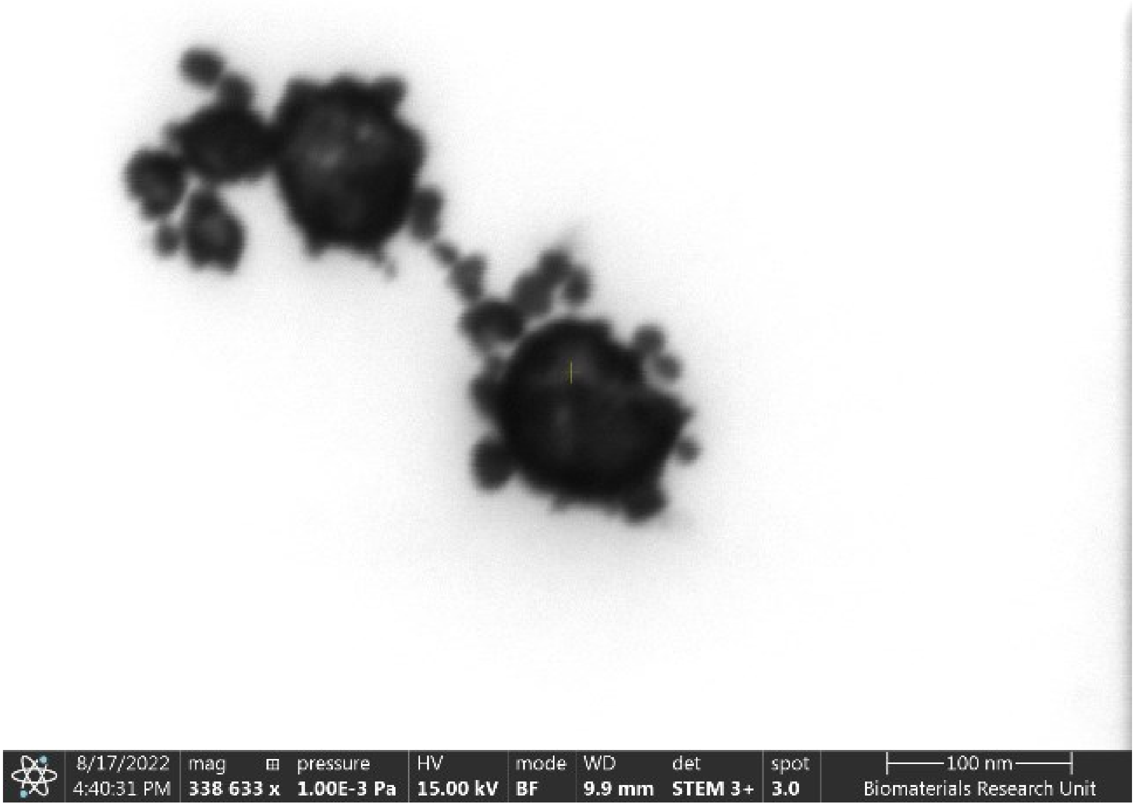

STEM mode: High Annular Dark Field

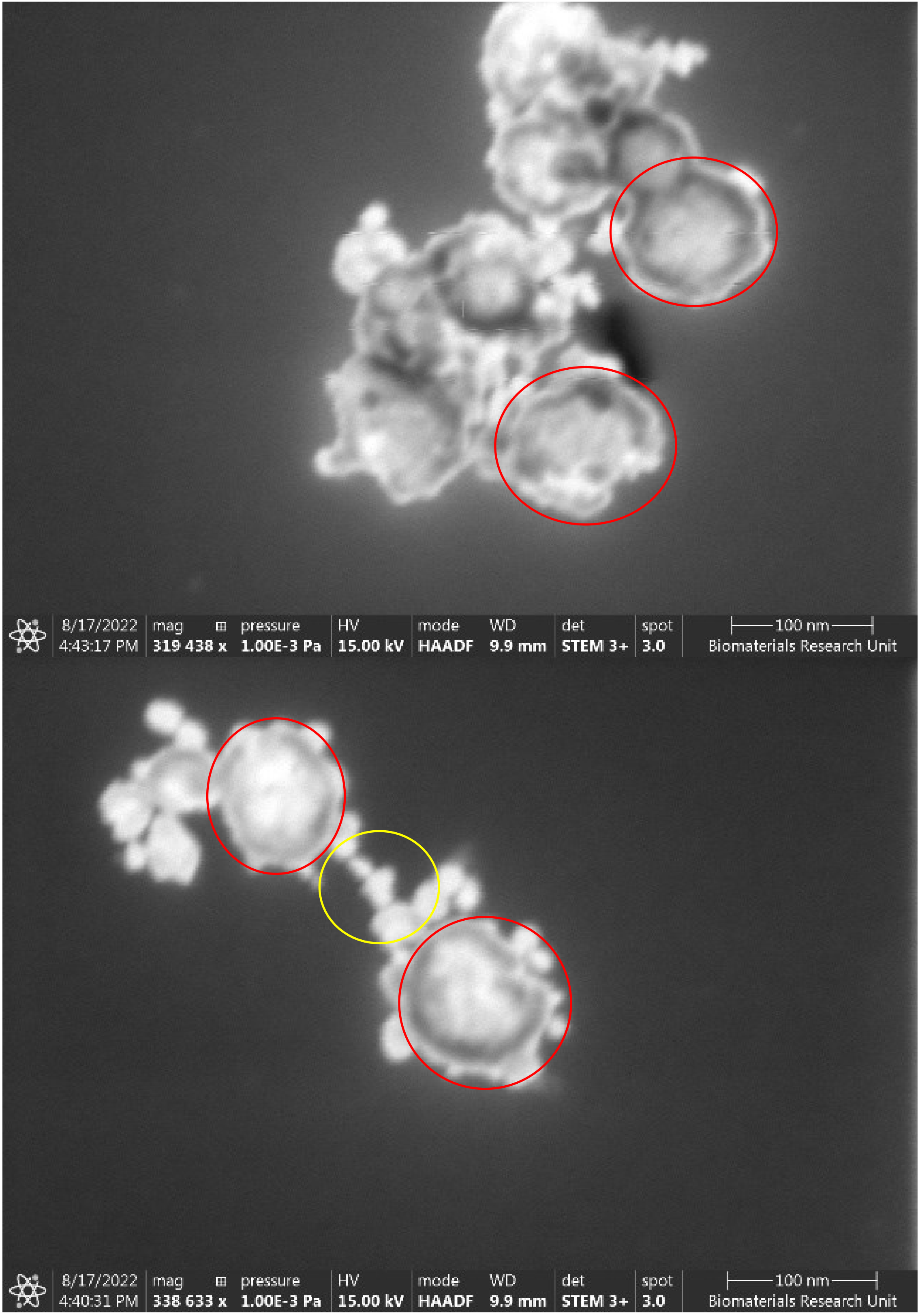

Figure 3.11: STEM images of M3. (Red circles – core-shell particles, Yellow circles – Au particles).

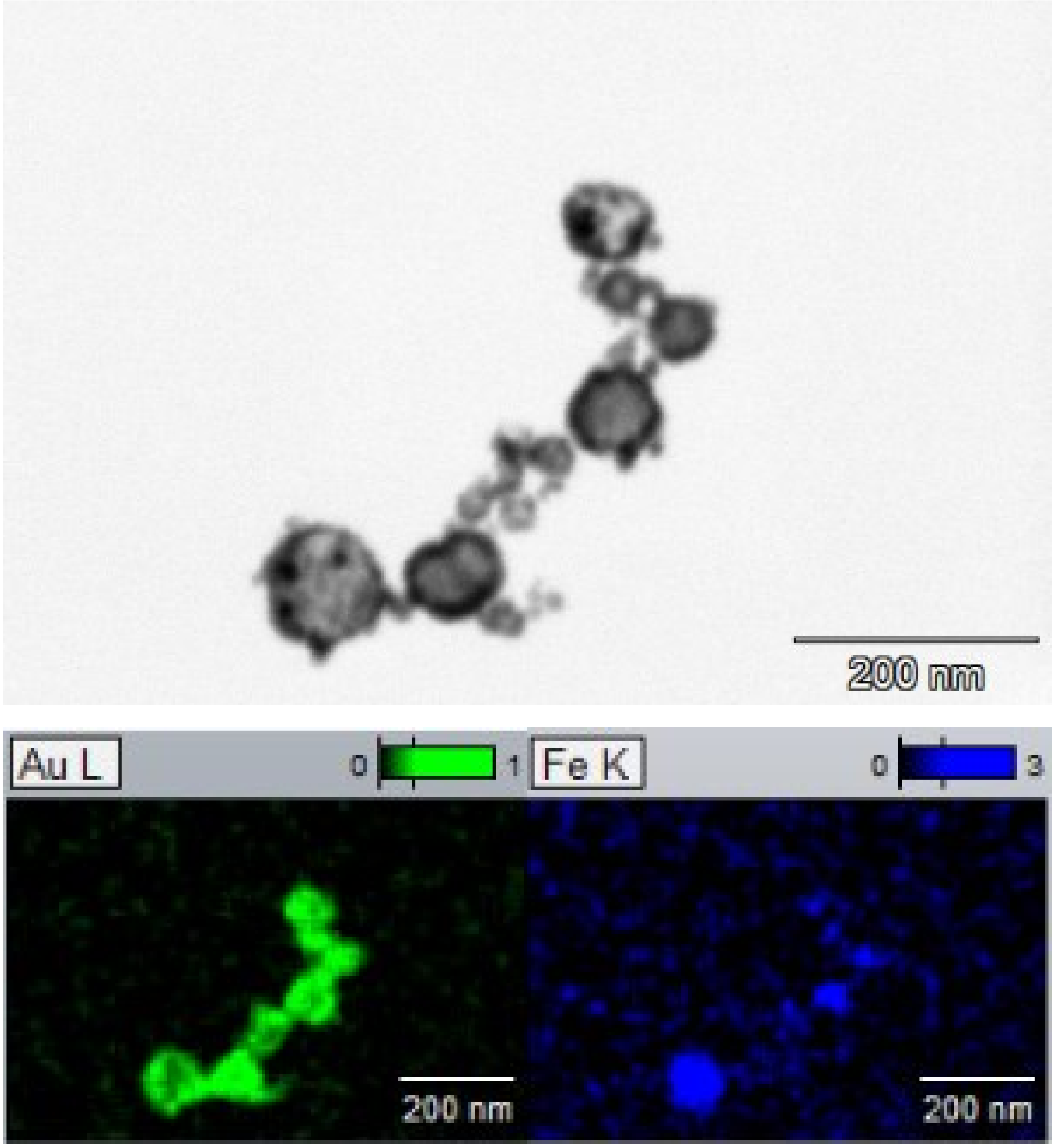

Figure 3.12: EDX data on experiment M3.

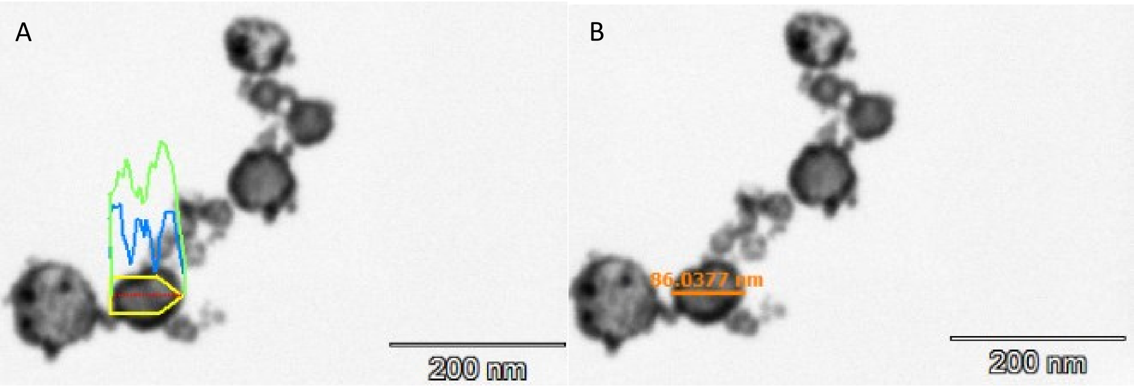

Figure 3.13: Line analysis and size measurement of M3. (Au – green, Fe – blue).

Figure 3.14 displays TEM of M3 where tilt angle has been applied to produce a 3D model of the particle. The rotated particle shows a spherical structure where a gold shell has formed round a core but via island growth where there are gaps within the shell. When comparing M3 to M1 and M2, there is an advancement in variable optimisation to synthesise core-shell particles.

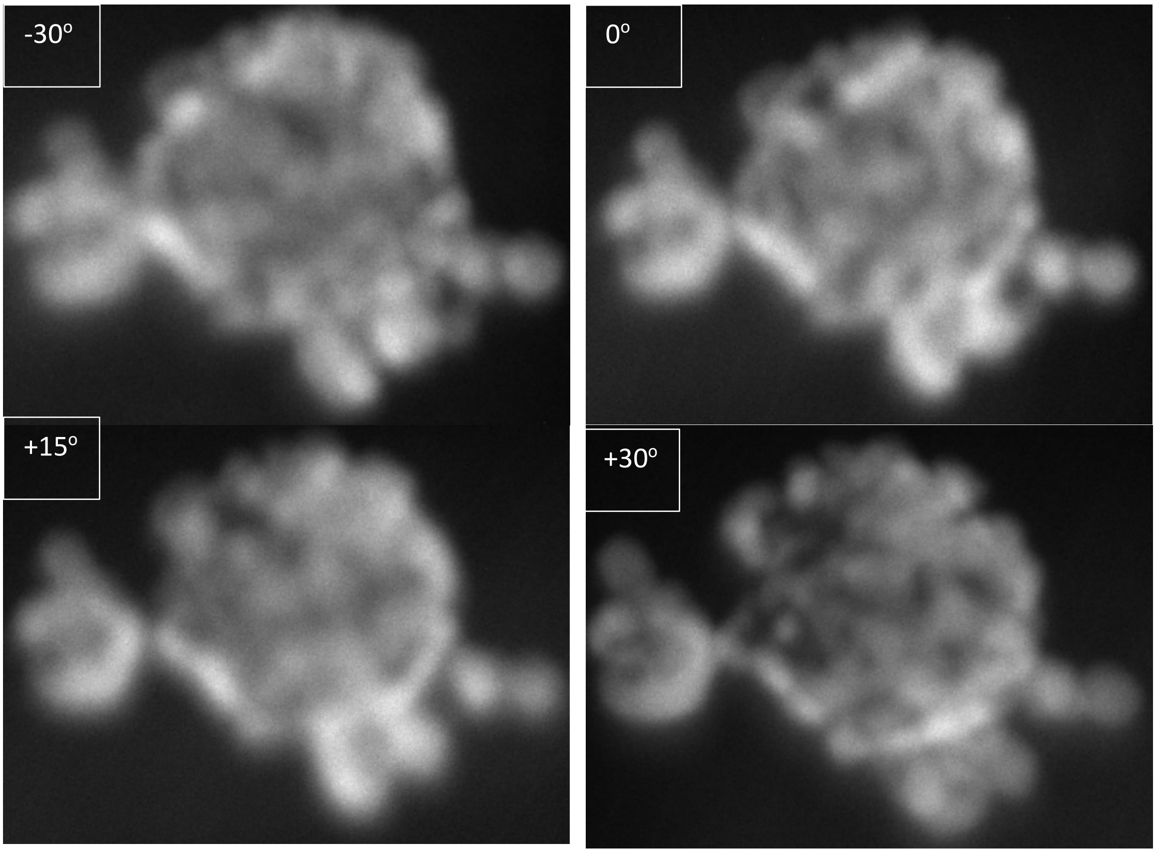

Figure 3.14: TEM images of M3 with tilt ranging from -30° to +30°.

To analyse the bulk concentration of iron, boron and gold, Inductively Coupled Plasma Optical Emission Spectroscopy (ICP-OES) was carried out on M3 to understand the ratios of the bulk material. Table 3.6 displays the ICP-OES results for M3. The results are promising and even though it cannot be directly linked to the core-shell elemental split, the bulk material analysis gives a good indication of the concentration of each element present. The positive results showing a high boron enrichment with almost 40 % in the bulk material which would be highly effective for BNCT.

Table 3.6: ICP-OES analysis of M3.

Element	Molar ppm	% split in whole particle	Fe/B
B	1.20	39.87	0.64
Fe	0.76	25.25	
Au	1.05	34.88	-

From M4, similar conditions and processes were used as to M3 but without the initial cooling of the gold solution and added at room temperature of 19 °C. Similar results were obtained in comparison to M3 but less effective. From Figure 3.15, the STEM photos show an interesting structure with where the Au particles have seeded upon a core but with less coverage compared to M3. In comparison to M1 and M2, there is some form of core-shell structure being formed, whereas M1 and M2 do not show similar results. There are different energetics occurring when the gold solutions are added slowly or rapidly. The difference in partial shell structures formed in M3 and M4 indicates there is a key variable based around the temperature drop to initiate shell formation to promote hetronucleation after a burst of homonucleation. From the experiments and analyses that have been carried out, injecting the solution proves to be more effective than when the gold solution is dripped into the core solution at high and low temperatures.

STEM mode: Bright Field

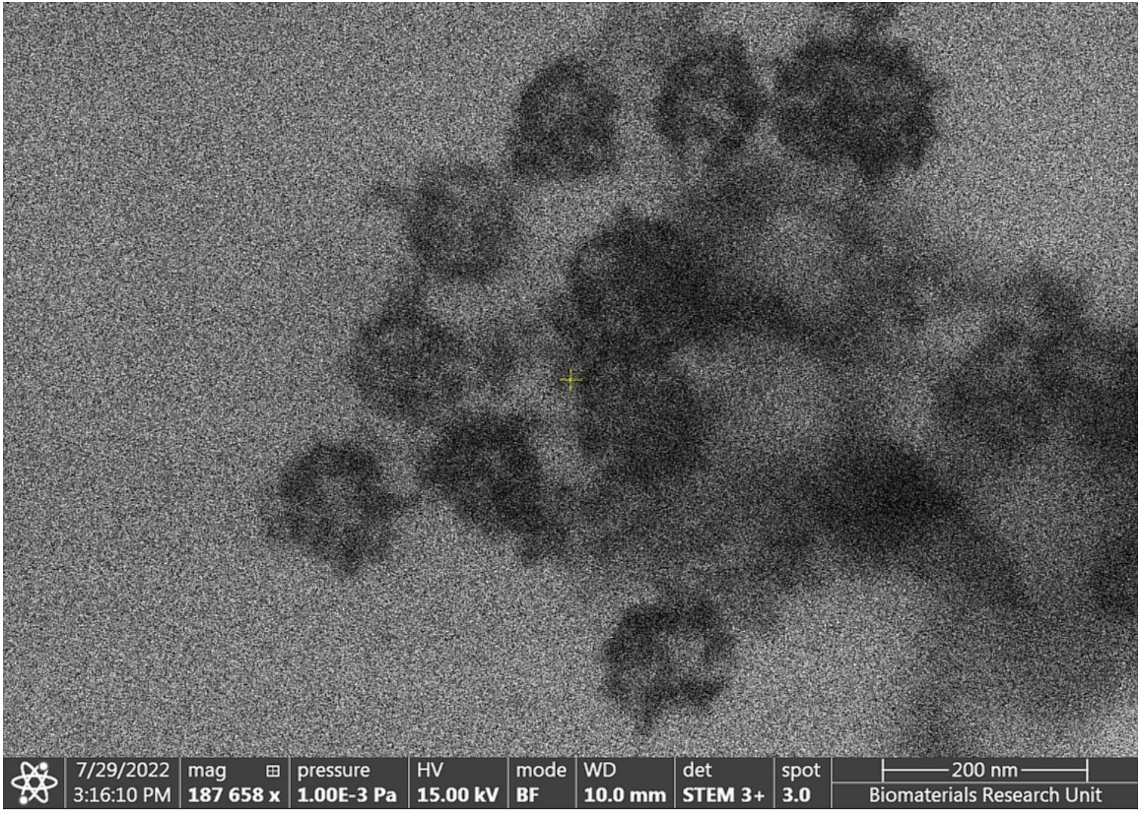

STEM mode: High Annular Dark Field

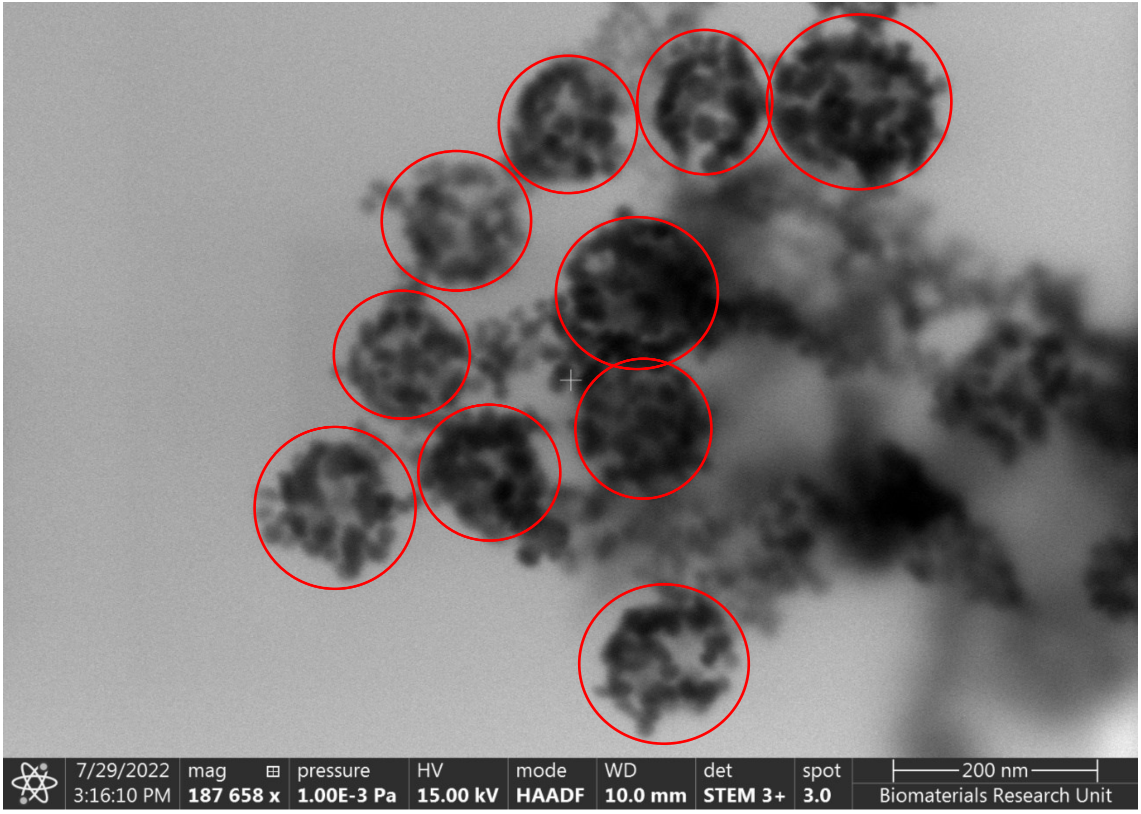

Figure 3.15: STEM photos of M4.(Red circles indicate partial core-shell structures).

3.6 Conclusions

Overall, using non-aqueous methods and redox-transmetalation to form core-shell NPs of Fe-B@Au was partially successful but showed promising results on the variables that can promote shell formation and boron enrichment. Optimisation is required around the variables to promote complete shell formation which include, temperature of solutions, concentrations heating rates are required.

For the synthesis of the core material, it is critical to increase the boron content as much as possible, as this is the crucial element in the trimetallic NPs for the end use of the particles of neutron capture therapy. The additional elements of iron and gold offer additional properties. Iron is magnetic and helps in the purification process and moving the particles within the body using magnets. Gold is an inert element with low cytotoxicity that can protect the core from oxidation and has strong optical properties that can be seen clearly in the body. Targeting peptides can be added to the gold shell to help guide the particles to the desired area (glioblastomas). Fe@Au particles are already regularly used in the body for MRI that have been formed by laser ablation *(Griaznova et al. 2022)* and chemically via reverse micelle synthesis *(Kayal et al. 2010)*. Adding one additional boron element can give the particles a new and effective cancer treatment particle.

During the core synthesis, boron content can be optimised to obtain almost a 1:1 ratio of iron to boron in the core material, which would make for a very effective particle for NCT. The concentration of borohydride and the ionic state of the metal used in the process can significantly change the amount of boron incorporated into the core. Using Fe^{3+} compared to Fe^{2+} can increase the boron content by 10-15 %. In *Glavee et al. 1992*, there was a higher amount of boron incorporated than expected due to the Fe-B NPs acting as a catalyst to break down the B_2H_6 to form more boron, which is incorporated into the structure. However, further analysis into the stabiliser is required as the 4-benzyl pyridine was not successfully used in the same capacity as in *Ban et al. 2005*. The solution colour was adjusted from light green to yellowish whenever the stabiliser was added. The breakdown of the $Fe(BH_4)_3$ complex was always unsuccessful and required to be added after the reduction, likely leading to particle growth. Other factors such as pH, dissolved oxygen, water presence can all impact the synthesis of the core and clean strict conditions are required for a successful formation of the core.

When the gold solution was added slowly into a preheated solution at 60 °C or 125 °C, the solution slowly turned a burgundy colour, suggesting that gold NPs were being formed and the redox-transmetalation process was working as expected. However, the process was not overcoming the lattice mismatch between the iron core and the gold shell, and shell formation was not occurring, or limited shells were being formed. Even though the samples were magnetic and appeared burgundy in colour, the residue solvent gave false positives, acting as a glue with monometallic gold and iron both sticking to the residue during STEM analysis. Although, in *Chem et al. 2012*, it was suggested that the rapid addition of the gold solution was required to obtain a temperature drop in the solution. This would lead to gold nanoseeds initially being formed but then homonucleation being suppressed and hetronucleation starting. As can be seen from the results above, this process obtained exciting results where a gold shell starts to form around a magnetic core but with holes in the shell leading to the core oxidising. The temperature drop may be significant in forming the gold nano seeds on the cores for the growth to continue on the surface.

For this research to progress further, additional analysis should be carried out around the rapid addition of the gold solution and the optimal temperature drop to help complete a gold shell around the core. Doing this, along with the optimisation around the stabiliser used, could lead to a complete core-shell structure forming and the particles being in the correct size range of less than 50 nm for the designed use for NCT. This research has proven that the processes reported in the literature are challenging to reproduce, and some key variables about the synthesis process may need to be detailed further so more advancements can be made in the area. Another area for improvement with the non-aqueous process was the maintenance of the solvents. It was challenging to keep pure, dry and oxygen-free for the process, which would have significant effects on the process if not maintained with most likely unsuccessful reactions. It would be more effective to employ a process that takes advantage of molecular sieves to ensure the solution is dry and that non-aqueous conditions are kept the complex between the iron ions and borohydride ions is successful.

References

Amiri, Mahnaz, Khalil Eskandari, and Masoud Salavati-Niasari. 2019. “Magnetically Retrievable Ferrite Nanoparticles in the Catalysis Application.” *Advances in Colloid and Interface Science* 271: 101982. https://doi.org/10.1016/j.cis.2019.07.003.

Bard, Allen. 1985. *Standard Potentials in Aqueous Solution*. 1st ed. New York: Routledge.

Ban, Z. et al. (2005) ‘The synthesis of core-shell iron@gold nanoparticles and their characterization’, Journal of Materials Chemistry, 15(43), pp. 4660–4662. Available at: https://doi.org/10.1039/b504304b.

Benoit, Magali, Nathalie Tarrat, and Joseph Morillo. 2016. “Adsorption Energy of Small Molecules on Core-Shell Fe@Au Nanoparticles: Tuning by Shell Thickness.” *Physical Chemistry Chemical Physics* 18(13): 9112–23. http://dx.doi.org/10.1039/C5cp06258f.

Chem, J.M. *et al.* (2012) ‘Structure , optical and magnetic properties of Ni @ Au and Au @ Ni’, pp. 2757–2765. Available at: https://doi.org/10.1039/c1jm14479k.

Chen, D. *et al.* (2009) ‘Nanometre Ni and core/shell Ni/Au nanoparticles with controllable dimensions synthesized in reverse microemulsion’, *Journal of Alloys and Compounds*, 475(1–2), pp. 494–500. Available at: https://doi.org/10.1016/j.jallcom.2008.07.115.

Cho, S. *et al.* (2006) ‘Magnetic and Mo 1 ssbauer Spectral Study of Core / Shell Structured Fe / Au Nanoparticles’, (4), pp. 960–967.

Corrias, A. *et al.* (1993) ‘Amorphous Transition Metal-Boron Ultrafine Particles Prepared by Chemical Methods’, *Chemistry of Materials*, 5(12), pp. 1722–1726. Available at: https://doi.org/10.1021/cm00036a009.

Eres, G. *et al.* (2011) ‘Real-time studies of epitaxial film growth using surface X-ray diffraction (SXRD)’, *In Situ Characterization of Thin Film Growth*, pp. 239–273. Available at: https://doi.org/10.1533/9780857094957.3.239.

Feng, Qiyi et al. 2018. “Uptake, Distribution, Clearance, and Toxicity of Iron Oxide Nanoparticles with Different Sizes and Coatings.” *Scientific Reports* 8(1): 1–13. http://dx.doi.org/10.1038/s41598-018-19628-z.

Ghosh Chaudhuri, Rajib, and Santanu Paria. 2012. “Core/Shell Nanoparticles: Classes, Properties, Synthesis Mechanisms, Characterization, and Applications.” *Chemical Reviews* 112(4): 2373–2433.

Glavee, G.N. *et al.* (1992) ‘Borohydride Reductions of Metal Ions. A New Understanding of the Chemistry Leading to Nanoscale Particles of Metals, Borides, and Metal Borates’, *Langmuir*, 8(3), pp. 771–773. Available at: https://doi.org/10.1021/la00039a008.

Glavee, G.N. *et al.* (1995) ‘Chemistry of borohydride reduction of iron(II) and iron(III) ions in aqueous and nonaque-ous media’, *Inorganic Chemistry*, 34(1), pp. 28–35.

Griaznova, O.Y. *et al.* (2022) ‘Laser Synthesized Core-Satellite Fe-Au Nanoparticles for Multimodal In Vivo Imaging and In Vitro Photothermal Therapy’.

Jafari, T., Simchi, A. and Khakpash, N. (2010) ‘Synthesis and cytotoxicity assessment of superparamagnetic iron-gold core-shell nanoparticles coated with polyglycerol’, *Journal of Colloid and Interface Science*, 345(1), pp. 64–71. Available at: https://doi.org/10.1016/j.jcis.2010.01.038.

Kayal, S. and Ramanujan, R.V. (2010) ‘Anti-Cancer Drug Loaded Iron – Gold Core – Shell Nanoparticles (Fe @ Au) for Magnetic Drug Targeting’, 10(9), pp. 5527–5539. Available at: https://doi.org/10.1166/jnn.2010.2461.

Kianfar, Ehsan. 2021. “Magnetic Nanoparticles in Targeted Drug Delivery: A Review.” *Journal of Superconductivity and Novel Magnetism* 34(7): 1709–35. https://doi.org/10.1007/s10948-021-05932-9.

Lee, Woo Ram et al. 2005. “Redox-Transmetalation Process as a Generalized Synthetic Strategy for Core-Shell Magnetic Nanoparticles.” *Journal of the American Chemical Society* 127(46): 16090–97.

Li, Fa Tang et al. 2015. “An Inexpensive N-Methyl-2-Pyrrolidone-Based Ionic Liquid as Efficient Extractant and Catalyst for Desulfurization of Dibenzothiophene.” *Chemical Engineering Journal* 274: 192–99. http://dx.doi.org/10.1016/j.cej.2015.04.027.

Lertsuphotvanit, N. *et al.* (2023) ‘Sublimation/evaporation behaviors of borneol in-situ forming matrix’, *Materials Today: Proceedings* [Preprint], (xxxx). Available at: https://doi.org/10.1016/j.matpr.2023.03.768.

Linderoth, S. and Mørup, S. (1990) ‘Chemically prepared amorphous Fe-B particles: Influence of pH on the composition’, *Journal of Applied Physics*, 67(9), pp. 4472–4474. Available at: https://doi.org/10.1063/1.344885.

Linderoth, S. and Morup, S. (1998) ‘Amorphous TM 1 − x B x alloy particles prepared by chemical reduction.’, *Journal of Applied Physics*, 5256(August).

Long, N.V. *et al.* (2011) ‘Synthesis and characterization of Pt-Pd alloy and core-shell bimetallic nanoparticles for direct methanol fuel cells (DMFCs): Enhanced electrocatalytic properties of well-shaped core-shell morphologies and nanostructures’, *International Journal of Hydrogen Energy*, 36(14), pp. 8478–8491. Available at: https://doi.org/10.1016/j.ijhydene.2011.03.140.

MaryMartinette, Sr., Mizushima, S. and Quagliano, J.V. (1959) ‘Infrared absorption spectra of inorganic co-ordination complexes—XIX’, *Spectrochimica Acta*, 15(2), pp. 77–81. Available at: https://doi.org/10.1016/s0371-1951(59)80291-5.

Mazhar, T., Shrivastava, V. and Tomar, R.S. (2017) ‘Green synthesis of bimetallic nanoparticles and its applications: A review’, *Journal of Pharmaceutical Sciences and Research*, 9(2), pp. 102–110.

Milazzo, G., Caroli, S. and Braun, R.D. (1978) ‘Tables of Standard Electrode Potentials’, *Journal of The Electrochemical Society*, 125(6), pp. 261C-261C. Available at: https://doi.org/10.1149/1.2131790.

Paunovic, J. *et al.* (2020) 'Iron-based nanoparticles and their potential toxicity: Focus on oxidative stress and apoptosis', *Chemico-Biological Interactions*, 316(December 2019). Available at: https://doi.org/10.1016/j.cbi.2019.108935.

Rashid, T.M. *et al.* (2021) 'Synthesis and characterization of Au:ZnO (core:shell) nanoparticles via laser ablation', *Optik*, 244(July), p. 167569. Available at: https://doi.org/10.1016/j.ijleo.2021.167569.

Rickard, D. (2012) 'Sedimentary Iron Biogeochemistry', in *Developments in Sedimentology*. elseveir. elseveir, pp. 85–114. Available at: https://doi.org/10.1016/B978-0-444-52989-3.00003-9.

Scholz, M. (2006) 'Coagulation and flocculation', in *Wetland Systems to Control Urban Runoff*. Elseveir, pp. 43–50.

Singh, Raghvendra Pratap, Rahul Handa, and Geetanjali Manchanda. 2021. "Nanoparticles in Sustainable Agriculture: An Emerging Opportunity." *Journal of Controlled Release* 329(July 2020): 1234–48. https://doi.org/10.1016/j.jconrel.2020.10.051.

Suzuki, Minoru. 2020. "Boron Neutron Capture Therapy (BNCT): A Unique Role in Radiotherapy with a View to Entering the Accelerator-Based BNCT Era." *International Journal of Clinical Oncology* 25(1): 43–50. https://doi.org/10.1007/s10147-019-01480-4.

Wheeler, D. (1925) 'PRECISION MEASUREMENTS OF THE LATTICE CONSTANTS OF TWELVE COMMON METALS', 538(1922).

Withanage, S.S., Charles, V. and Chamlagain, B. (2021) 'Synthesis of highly dense MoO 2 / MoS 2 core – shell nanoparticles via chemical vapor deposition'.

Wu, Q. *et al.* (2019) 'Interaction-Induced Self-Assembly of Au@La2O3 Core-Shell Nanoparticles on La2O2CO3 Nanorods with Enhanced Catalytic Activity and Stability for Soot Oxidation', *ACS Catalysis*, 9(4), pp. 3700–3715. Available at: https://doi.org/10.1021/acscatal.9b00107.

Yeh, Jien Wei. 2006. "Recent Progress in High-Entropy Alloys." *Annales de Chimie: Science des Materiaux* 31(6): 633–48.

Zhang, J. *et al.* (2018) 'In Situ synthesis of SiC-graphene core-shell nanoparticles using wet ball milling', *Ceramics International*, 44(7), pp. 8283–8289. Available at: https://doi.org/10.1016/j.ceramint.2018.02.012.

Chapter 4 – Reverse micelle synthesis of Fe-B@Au

4.1 Introduction

Core-shell NPs have attracted much attention in recent years due to their ability to obtain the properties of both materials. These properties are highly tuneable by controlling the size of the core and shell materials *(Peng et al. 2021)*. There are several ways that core-shell NPs can be formed, as discussed in the literature review [chapter 2] of this thesis. Reverse micelle synthesis *(Jafari et al. 2010)*, chemical vapour deposition (Kuang et al., 2019), sol-gel *(Mahajan et al. 2020)* and many other methods have been studied to optimise the formation of these core-shell NPs for various uses of medical, environmental, catalysis or electrical properties. Size, shape, morphology and structure of the core-shell NP significantly affect and alter the properties of the NP. By controlling the structure of Ag@Pt NPs it was possible to combine the plasmonic properties of Ag while keeping the high catalytic performance of Pt which leads to great potential for a plasmonic catalyst *(Fan et al. 2023)*. Cabazitaxel Loaded Core-Shell Mesoporous Silica Nanoparticles were synthesised with different morphologies to test the efficacy of the particle for prostate cancer therapy. It was found that dependant on the cell type used different morphologies had a better toxicity. For example, in PC3 cell lines a better uptake of the drug loaded core-shell NP was observed with a hexagonal prism structure in comparison to its spherical counterpart *(Mohanan et al. 2023)*.

Micelles have been extensively researched and used as a synthesis technique for monometallic NPs and, more recently, core-shell bimetallic NPs. Reverse micelles are formed via a water-in-oil microemulsion technique. It relies on the self-assembly of the surfactants around the aqueous water phase to form nanodroplets stabilised by the surfactant to form a micelle. The solutes are soluble in the aqueous phase which leads to the ions being present within the micelle of the microemulsion *(D. Chen et al. 2009)*. Mixing of the organic and aqueous phase creates an isotropic liquid media with stabilised nanowater droplets. The surfactant reduces the micelles' aggregation and stops the water nanobubbles' growth. The stabiliser works effectively to form these micelles due to having a polar hydrophilic headgroup which attaches to the water particles and then a long chain non-polar or hydrophobic tail that forces the micelles apart via steric effects *(Jafari et al. 2010)*. Cetyltrimethylammonium bromide (CTAB), as displayed in Figure 4.1, is a common stabiliser for micelles. CTAB is a cationic surfactant with a positively charged hydrophilic headgroup with a neutral and hydrophobic tail that repels other micelles via steric effects.

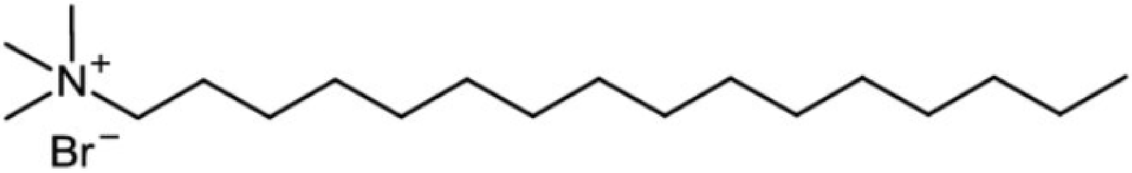

Figure 4.1: Chemical structure of CTAB. *(Janosevic-Lezaic et al. 2014)*.

A key variable is the critical micelle concentration (CMC) in the formation of micelles. When the concentration of the stabiliser is below the CMC, no micelles are formed. As the concentration surpasses the CMC, micelle formation begins as seen in Figure 4.2. The CMC is the lowest concentration of stabiliser required for micelle aggregation to begin and measures the thermodynamic stability of the micelles *(Goronja et al. 2016)*. By using CTAB as the stabiliser for the micelle and having a hydrophobic tail and a polar hydrophilic headgroup, by being above the CMC hydrophilic heads cluster together to form the core of the micelle while the hydrophobic tails remain on the outside surface of the micelle.

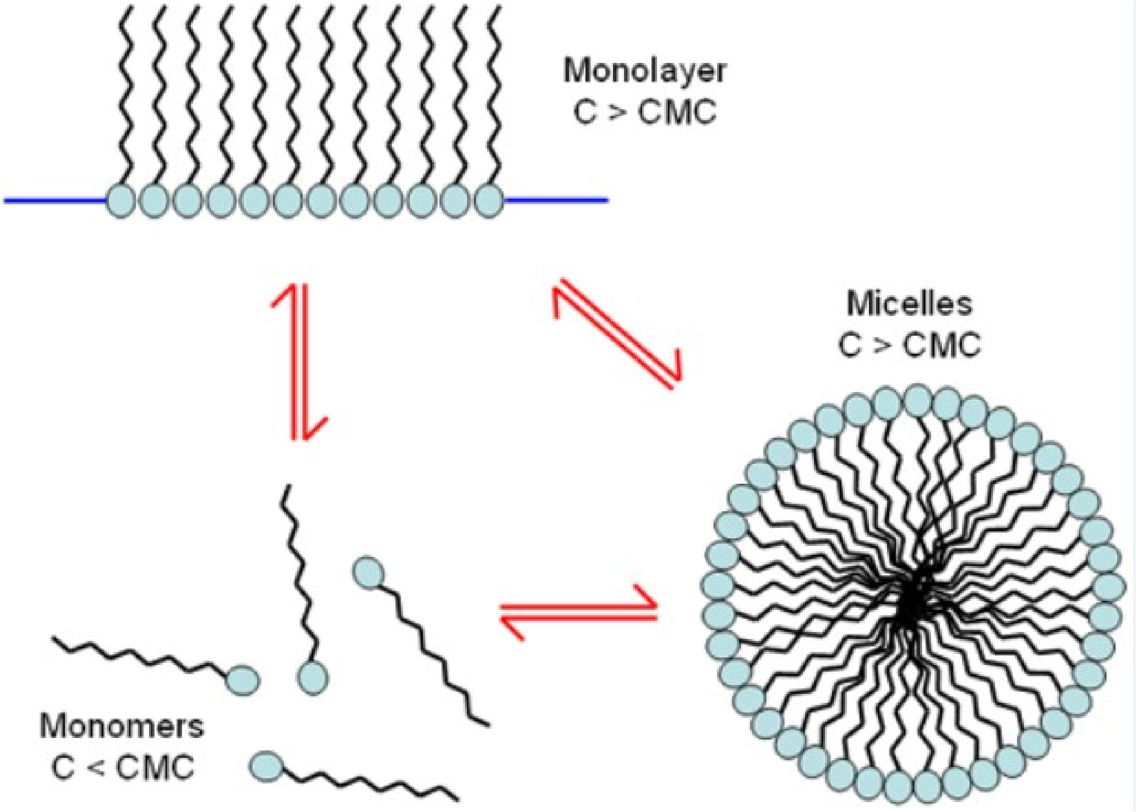

Figure 4.2: Formation and deformation of micelles. *(Malvern Panalytical, 2010)*

When using CTAB as the surfactant, in most cases, a co-surfactant, n-butanol, is used to increase the polarity of the CTAB and helps stabilise the micelle *(Carpenter, 2001), (Kvitek et al. 2019).* This stabilisation occurs by forming covalent bonds with specific domains of the micelle which reinforces weak intermolecular interactions *(Lu et al. 2018)*. The n-butanol concentration is critical to the stability of the micelle. Without the additional n-butanol, the amount of free water available for the reaction is reduced as the water molecules are locked up in the headgroups of the CTAB *(Carpenter, 2001)*. The n-butanol mole fraction needs to be controlled, as when increased above 0.03, the micelles have a looser structure and the n-butanol penetrates the hydrocarbon core of the micelle and become adsorbed by the head group of the CTAB leading to no micelle formation *(Oakenfull, 1982)*.

Before mixing, the reactants are in separate micelles but as the micelle solution are mixed together the two separate micelles containing the reactants mix and the reaction begins within a single micelle. The advantage of the micelle method is the size of the NPs formed are tightly controlled by the water to stabiliser molar ratio (W). Decreasing the W will reduce the size of the micelle as there is an increase in stabiliser to form a smaller micelle. An increase in W means there is a higher amount of water and less stability in the micelle that leads to growth in micelle size. In *Chen et al. 2009*, a comprehensive set of research was summarised that shows how the size of the NPs changes with the increase in the W value. When W = 3, the diameter of the core-shell NPs is 7.5-8.5 nm; when the W = 11, the core-shell NPs are in the range of 29-31 nm. By controlling W, the NP core and shell size can be tightly controlled and optimised. For an iron core and gold shell, the core size can be initially controlled by controlling the water-to-stabiliser ratio to obtain a core size of 20 nm. For a thin shell, the gold micelle solutions W ratio can be controlled so that there is only a small expansion in the micelle size so the gold ions are packed around the synthesised core. It is hypothesised that as further reducing agent is added, [same W as gold solution], the gold ions, which have combined with the core micelle are reduced very closely to the core when the reducing solution also combines with the core micelle promoting the shell formation of gold upon iron.

The micelle method is advantageous due to the controllability of the micelle size. Figure 4.3 displays the schematic of the micelle combination of reactants to form a core that grows to the size of the micelle. This research requires the core-shell NPs to be less than 50 nm and increase the boron content. The iron-boron core offers properties of magnetism and radioactive dose for NCT while a thin layer of gold adds stability to the core, reduced cytotoxicity, and optical properties to the particle.

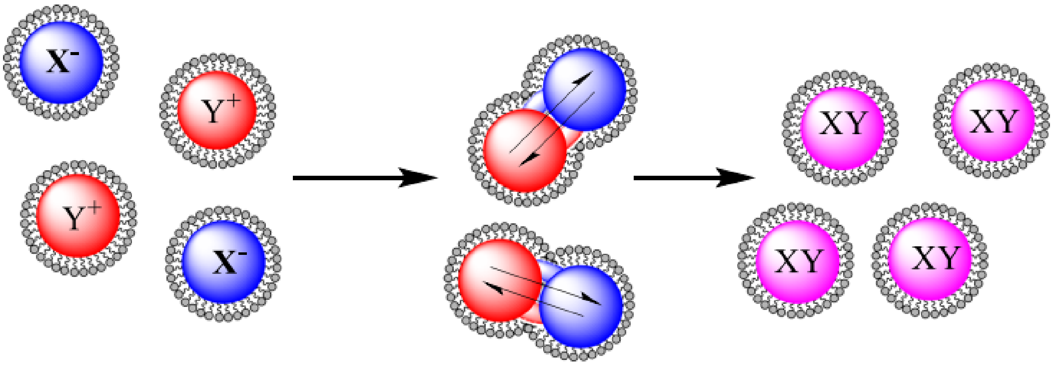

Figure 4.3: Reactant micelles combining and forming the core material where X^- and Y^+ are reactants and XY is the product. *(Anderson et al. 2019).*

Combining the research carried out in Chapter 3, redox-transmetalation coupled with the reverse micelle method takes advantage of both methods of tightly controlling the size of the core and shell without any further reducing agent. This process would take advantage of the reduction potential difference between the iron and the gold allowing the use of iron as a sacrificial layer to reduce the gold ions at the surface of the core while the micelles with a tight control of the size of them can minimise the particles that can move away from the core surface.

Chen et al. 2009 carried out a similar method where a nickel core and a gold shell were formed by reverse micelle method coupled with redox-transmetalation to obtain core-shell NPs. Coupling the methods removed variables from both processes if carried out individually to promote core-shell formation.

This chapter will investigate the reverse micelle process and the effects of changing some variables of the process to form core-shell NPs of iron-boron core and a gold shell. Due to the significant lattice mismatch between iron and gold with a crystal structure of body centred cubic and a lattice constant of 2.856 Å and face-centred cubic crystal structure with a lattice constant of 4.065 Å respectively, the method aims to overcome the energy barrier between the two metals and promote non-epitaxial growth. It is still critical to incorporate as much boron into the core as possible to optimise the particles for neutron capture therapy.

Further research will be conducted by testing the coupling of the reverse micelle method with the redox-transmetalation process to evaluate whether this further promotes the formation of core-shell NPs than each method individually. The method that has been developed and adapted from several papers *(Carpenter, 2001), (D. Chen et al. 2009) (Kvitek et al. 2019), (Jafari et al. 2010)* that carry out the same procedure with differences in post-processing and stabiliser used for the particles. At the end of this chapter, the findings will be concluded, and recommendations will be made on further research to be carried out to progress the field and research area further.

4.2 Experimental

4.2.1 Reverse Micelle method

The method was adapted from *D. Chen et al. 2009* and *Kvitek et al. 2019*. The reverse micelle process and a combination of reverse micelle and redox-transmetalation to form the core-shell NPs were trialled. N-octane, iron chloride ($FeCl_3$), sodium borohydride ($NaBH_4$), n-butanol, cetyltrimethylammonium bromide (CTAB), chloroauric acid ($HAuCl_4.xH_2O$) were all purchased from Fisher scientific and of analytical grade and used without further purification.

All three solvents were degassed via bubbling with nitrogen for two hours. The reaction is carried out under nitrogen protection to avoid oxidation of the core material. All the reverse micelle solutions were prepared using CTAB as the surfactant and n-butanol as a co-surfactant to increase the polarity of the CTAB and stabilise the micelle solution. N-octane was used as the oil phase, and deionised water as the aqueous phase. The size of the NPs can be tightly controlled by the surfactant-to-water molar ratio (H_2O/CTAB) = W. The first micelle solution contained 2.4 ml 0.5 M aqueous $FeCl_3$ solution mixed with 6 g CTAB, 6.25 ml n-butanol and 21.42 ml of n-octane. The second micelle solution contained 2.4 ml of 1.5 M aqueous $NaBH_4$, which contained the same proportions of CTAB, octane and butanol as the iron solution to maintain the W value. The W value was set at 8. These solutions were formed and mixed for two hours individually to ensure complete formation and stabilisation of the micelles.

After two hours, the $NaBH_4$ micelle solution was added at 150 ml/hr into the $FeCl_3$ micelle solution. The iron solution changed from yellow/orange to black, indicating the formation of Fe NPs. The solution was left for two hours to ensure the complete reaction between the Fe and borohydride ions. A third micelle solution containing 1.8 ml of 0.44 M aqueous $HAuCl_4$ was mixed with 3 g of CTAB, 3 ml n-butanol, and 14.28 ml of n-octane. This solution was left to form for two hours, and the colour was reddish/orange. The W ratio was set to 12 to slightly expand the micelle. The gold solution was added to the Fe-B core solution at a 50 ml/hr. Upon the addition of the gold, the solution stayed a black colour. After the gold solution addition, 1.8 ml of 1.6 M aqueous $NaBH_4$micelle solution with the same amount of CTAB (3 g), butanol (3 ml) and octane (14.28 ml) as the gold solution was added at 150 ml/hr 7 minutes after the gold addition to reduce the gold to form a shell on the core. The colour of the solution would initially have a burgundy colour to it suggesting gold NP synthesis, but once left for two hours for the shell formation, the solution appeared to be black with a slight blue/purple tinge. After the synthesis, the sample was centrifuged to pellet the NPs formed during the synthesis process at 10’000 RCF for five minutes. The solvent was removed and the sample was washed several times using 25 ml of a 1:1 mixture of chloroform/methanol to remove all surfactants. Between each centrifugation, the solvent was removed and fresh solvent added followed by sonication for five minutes to resuspend the particles. A magnet separation and a 10 % nitric acid wash were completed to purify the sample. The sample was placed next to a magnet to pull across all magnetic material overnight. The solvent was removed it remove any non-magnetic material. Magnet separation would remove monometallic gold particles. 5 ml of 10 % nitric acid was added to the sample to remove any uncapped Fe-B core particles. The samples were washed three times with methanol and stored in methanol for further analysis. The process can be seen in Figure 4.4.

4.2.2 Reverse Micelle and redox-transmetalation method

For the reverse micelle and redox-transmetalation process, the same procedure from above was followed except, rather than adding in the second solution of sodium borohydride that would usually reduce the gold ions, the gold solution (1.8 ml of 0.44 M aqueous $HAuCl_4$ was mixed with 3 g of CTAB, 3 ml n-butanol, and 14.28 ml of n-octane) was added in slowly again and left for one hour before being heated up to 75 °C for 30 minutes to initiate the redox-transmetalation process where the iron is used as the reducing agent for the gold ions to promote the formation of a shell around the core. Due to the redox-transmetalation occurring within the micelle, the size of the shell can be tightly controlled via the size of the gold micelle solution ratio. No additional reducing agent was added to reduce the gold ions.

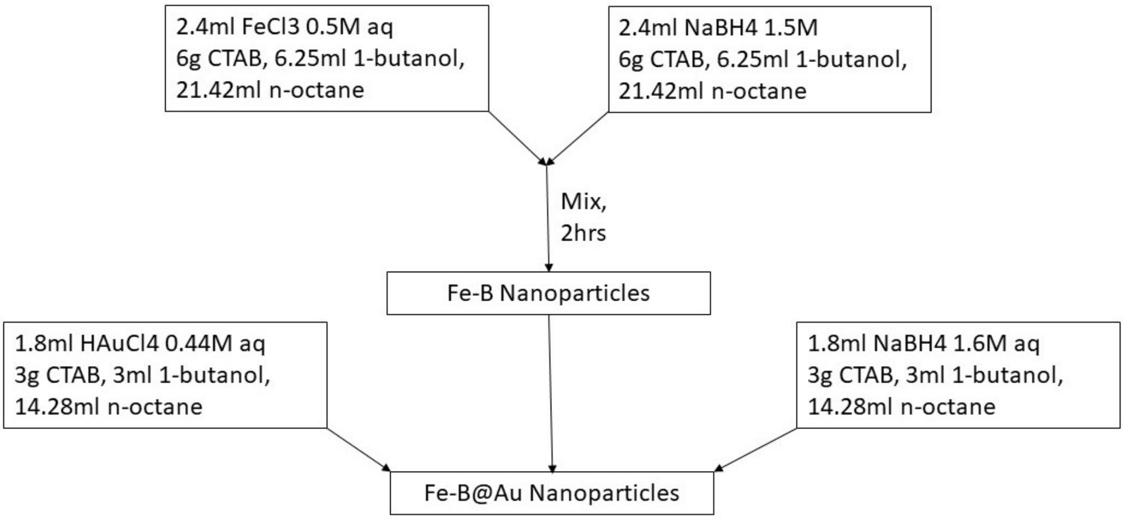

Figure 4.4: Flowchart of synthesis procedure to form core-shell Fe-B@Au NPs. Adapted from *(Jafari et al. 2010)*.

4.3 Characterisation

4.3.1 SEM / EDX

Scanning electron microscopy and energy-dispersive X-ray spectroscopy (SEM/EDX) analyses were conducted using a Quattro SEM (Thermo Fisher Scientific, USA) coupled with an EDS UltraDry 60M (129 eV) detector. STEM mode was used and copper / polycarbon grids with a mesh size of 300 squares per inch was used for this analysis. The operating parameters used for the analysis were high vacuum mode with an acceleration voltage of 15 kV with a spot size of 3 microns. To gain a high resolution image and obtain a signal during EDX for both gold and iron. A resolution of 1536x1094 pixels was chosen for the photos at 45 μs dwell time, to strike a balance between time acquisition and image clarity. Both Bright Field and High Annular Angular Dark Filed images were obtained from this analysis.

15 kV was used as the acceleration voltage to excite the electrons in the material enough to remove an electron from one of the inner shells. A voltage above its relative X-ray intensities is required. Iron (Ka shell) is 6.4 keV, and gold (La1 shell) is 9.71 keV. Ideally, to ensure excitation and a strong signal for the material, 1.5 x the values above are used, and 15 kV is a good value that reaches these requirements. Boron was checked for by EDX; however, boron is a very light element with only five electrons, one inner shell containing two electrons that can be ejected from the shell to give a signal and detection.

4.3.2 DLS

DLS was carried out with a Nanolive Zetasizer using methanol as the solvent. The operating parameters of refractive index (1.33) and viscosity (0.56 cP) were set to methanol values which were already stored in the Malvern software. For each sample, five runs were carried out to compare the stability within the sample from each run. The equilibrium time between each run was set at 2 minutes. The refractive index of the material was set at irons RI of 2.9304.

4.3.3 XPS

XPS analysis was conducted in a Thermofisher ESCALAB 250 electron spectrometer equipped with a hemispherical sector energy analyser at source excitation energy of 15 KeV and emission current of 6 mA; analyser pass energy of 20 eV with step size of 0.1 eV and dwell time of 50 ms were used throughout the experiments. The base pressure within the spectrometer during examinations was always better than 5×10^{-10} mbar and this ensured that all signals recorded were from the sample surface. In all samples the analysed area was 500 mm diameter.

4.3.4 UV-Vis

Ultraviolet–visible spectroscopy (UV/VIS) spectra of the nanoparticles were recorded using a UV–VIS spectrophotometer (Jenway 7615). 2 ml of the sample was loaded into a quartz cuvette with the path length set to 10 mm with increments in wavelength of 1 nm.

4.3.5 ICP-OES

ICP-OES was carried out on a Thermo Fisher iCAP 7000 series ICP-OES Spectrometer. A concentration curve was set up gold, iron and boron using standards purchased from Fisher Scientific. The concentration curve was set up from 0.1ppm going up in increments of 10 x to 10,000 ppm. For the preparation of the samples, 500 milligrams of the sample were digested in 0.5 ml aqua regia to digest all three metals present. Upon the samples being completely digested and solution turning colourless, the solutions were diluted with 4.5 ml of deionised water and analysed to give exact bulk concentrations of all three materials present.

4.4 Results

The reverse micelle technique for forming NPs is very well researched (*D. Chen et al. 2009*), (*Kvitek et al. 2019*), *(Khan et al. 2013) (Ma et al. 2022)*. A critical step is degassing the solvents to avoid oxidation. When the iron-boron core becomes oxidised, the magnetic properties and the stability become effected *(Devi et al. 2019)*, *(Glavee et al. 1995)*, leading to further challenges of adding a gold shell. When redox-transmetalation is coupled with the micelle methods and the core becomes oxidised, the redox reactions are affected due to the reduction potentials not being favourable to form a gold shell. It is hypothesised that this means the redox-transmetalation method of using Fe as the reducing agent and sacrificial layer for gold reduction would not occur.

When the solvents were being degassed for the process, the gas bubblers are set up sequentially, the nitrogen flows from octane to butanol to water. Throughout deoxygenation process, the solvents would slowly evaporate from the gas flow and contaminate the solvents being degassed further down the chain. Hence, the butanol would be contaminated with octane, and the water would become contaminated with butanol and a smaller amount of octane. The measured values of each solvent used for the experiment would not match the desired values and lead to the detrimental effect in micelle formation. In some cases, as the butanol was used to increase the polarity of the CTAB, too little butanol was being added to the micelle solution leading to an increased amount of water being locked up in the head group and an increased viscosity of the solution. To avoid this problem and more effectively degas the solvents without contamination, each solvent was degassed individually on separate nitrogen lines to prevent any contamination.

D. Chen et al. 2009 and *Kvitek et al. 2019*do not detail all necessary steps for the synthesis of the core-shell NPs. Such variables as the period of time left for the complete reduction of the core, after what period of time the gold solution was added, the length of time before adding the second borohydride solution and the period of time for the shell formation to be completed. This leads to challenges in reproducing and building upon published data to advance the science further. Extensive testing is required to find the optimal conditions.

4.4.1 Micelle size measurements

DLS was used as an indication of the stability and size of the micelle as shown in *Malvern Panalytical, 2010*. This was done by setting the parameters within the DLS software the solvent as octane with a viscosity and refractive index of 0.543 mPa.s and 1.41 respectively and the particle parameters as water with a viscosity and refractive index of 1.0 mPa.s and 1.33 respectively which is built into the malvern DLS software. Different concentrations of CTAB and butanol were trialled against the procedure above to confirm that changing the W value leads to an increase of decrease in the micelle size. Using DLS can give an indication where the CMC is.

The micelle formation may not occur due to the butanol affecting the amount of free water for the formation. In Table 4.1, the CTAB and butanol concentrations have been adjusted, and the water and octane concentrations were kept constant in each experiment. The butanol and CTAB values have been adjusted and compared to the experimental procedure in exp 1. In each case, the CTAB was increased, butanol was kept constant or vice versa to see the effect on the micelles.

Table 4.1: Experimental values tested for micelle formation.

Exp	CTAB mass (g)	n-butanol volume (ml)	Water volume (ml)	n-octane volume (ml)
1	6.00	6.25	2.40	21.42
2	3.00	6.25	2.40	21.42
3	1.50	6.25	2.40	21.42
4	9.00	6.25	2.40	21.42
5	6.00	3.15	2.40	21.42
6	6.00	9.39	2.40	21.42

The DLS measurements corresponding to the values in Table 4.1 can be seen in Figure 4.5. Exp 1 DLS results show a range of sizes, which suggest that the stability of the micelles is low due to the range of sizes being produced with two significant distributions at 1.89 nm and 6.10 nm of smaller-sized micelles being formed and then a small intensity of larger sized micelles of 272 nm. Although there is a range of sizes, most of the micelles appear to be 6.10 nm or lower and only a small majority that are unstable. The micelles formed would be small enough to produce NPs that can passthrough the blood brain barrier.

The DLS results for exp 2, again reducing the amount of CTAB but keeping the n-butanol and water amount the same leads to more instability in the solution and an indication that the critical micelle concentration has not been reached. The distribution suggests that micelles are forming around 10nm, but due to the reduced amount of CTAB in the solution agglomerating or collapsing due to instability, leading to water molecules that are uncapped.

Exp 3 DLS data, where the CTAB concentration was decreased again, there is another shift in the spectrum. It is a slightly larger micelle formation, with the main distribution having a size of 19.56 nm and a smaller distribution at 227.2 nm. There are appearances of instability within the micelle solution but exp 1-3 do show an expected trend that as the W value is increased, there is a general trend of the micelle size increasing.

In exp 4, when the CTAB concentration was increased compared to exp 1 above the standard amount, the viscosity of the solution was very high and gel-like rather than a solution. The increased CTAB concentration led to the water being locked up in the headgroups of the CTAB, meaning there is very little available for micelle formation for the reaction to take place. It was not possible to carry out DLS on this solution.

In exp 5, where the CTAB was kept constant and the N-butanol was halved in comparison to exp 1, the best stability of micelle solutions was obtained with a size of 10.63 nm that accounts for 96.6% of the counts. Exp 5 has the most uniform distribution and stable micelle compared to other experiments carried out in Table 4.1. With the n-butanol value halves suggests that the CTAB head group is optimally polarised to form micelles without causing a looser structure allowing the n-butanol to penetrate the headgroup of CTAB.

Exp 6, with an increased amount of butanol, appeared to have a negative effect on the micelle formation when compared to exp 1. It had a more prominent peak with a size of 5.53 nm but then a much larger distribution at 1112 nm, which shows the instability of the micelles as the headgroup becomes saturated with n-butanol. *Gornji et al. 2016*, reported if the mole ratio of butanol increases above 0.03, then micelles do not form due to the looser structure and saturation of headgroups with the butanol.

Half butanol appeared more stable and optimal and was used going forward for all other experimental procedures. These findings suggest that the butanol-to-CTAB ratios are vital in obtaining a stabilised micelle solution. When the CTAB concentration is increased and the N-butanol is constant, the CTAB headgroup is not polarised enough and leads to the water being held by the headgroup. When the CTAB concentration is low the higher molar ratio of n-butanol leads to the penetration and occupying the head group of the CTAB.

Exp 1

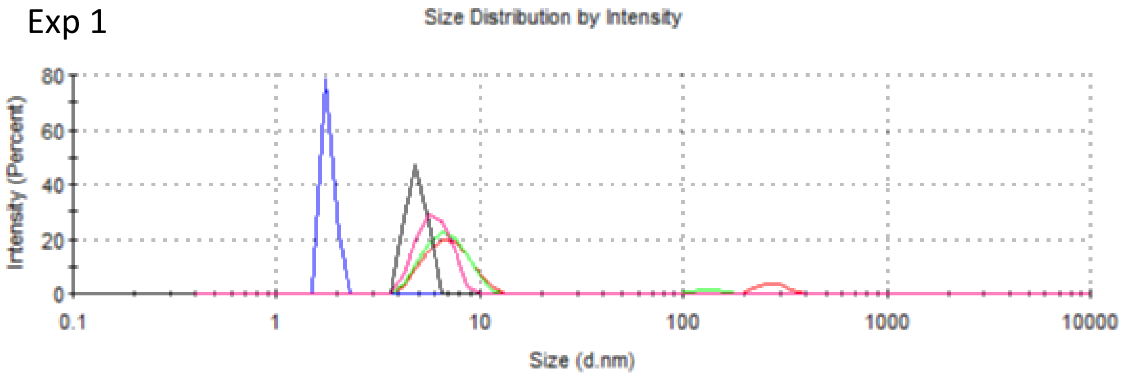

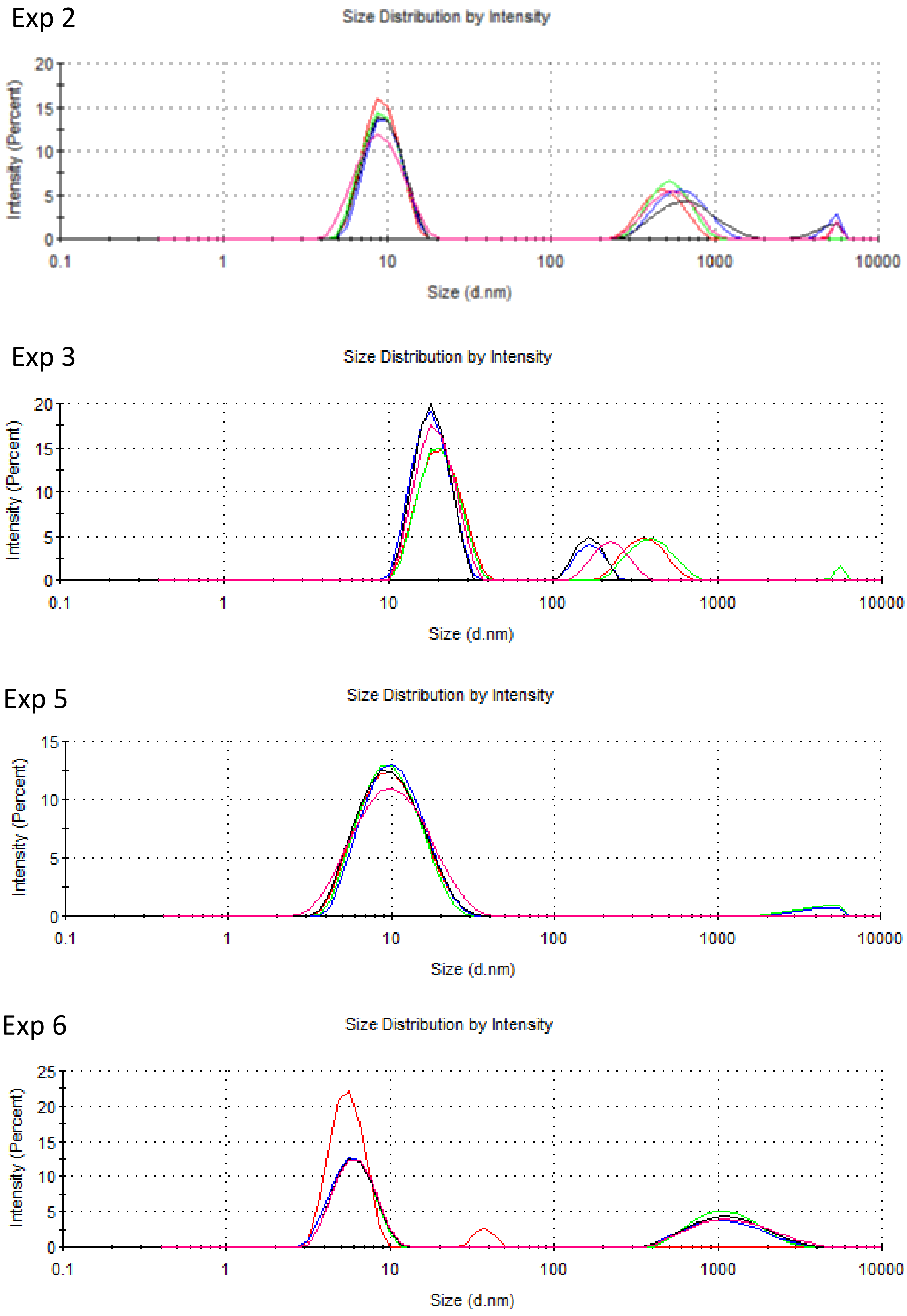

Figure 4.5: DLS measurements of different micelle solutions to analyse stability.

Chen et al. 2009 reported using Brij 30 as the stabiliser and surfactant for the micelle solution rather than CTAB and butanol as cosurfactants. When producing the micelle solution, the water/Brij 30 ratio of 7, should lead to NPs with a size range of 15-30 nm. (*Chen et al. 2009)*. As a comparison, a trial experiment was done to set the micelle stability using Brij 30 in comparison to CTAB and butanol. The Brij 30 micelle was made by using 9 ml of Brij 30, 3 ml of water and 27 ml of octane as carried out in *Chen et al. 2009.* The results for the comparison test are shown in Table 4.2 and the DLS measurements in Figure 4.6.

The DLS results of the micelle solution appears to be significantly unstable in the solution with a range of sizes. There is a smaller distribution at 9.31 nm that would follow a similar trend to what would be expected from the DLS measurements to match that from the literature. However, there is a much larger distribution at 244 nm.

Table 4.2: Values used for Brij 30 surfactant micelle formation.

Exp	Brij 30 volume (ml)	Water volume (ml)	n-octane volume (ml)
7	9	3	27

Exp 7

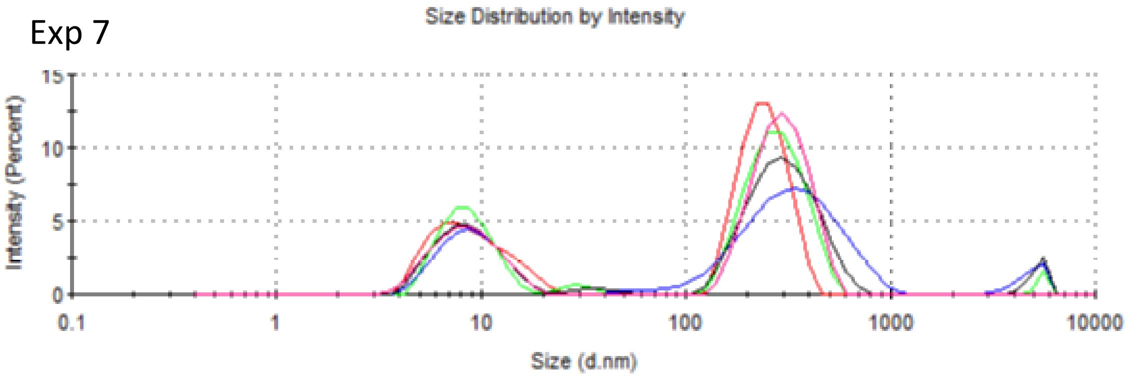

Figure 4.6: DLS results of Brij 30 surfactant for micelle formation.

4.4.2 Reverse micelle reaction

The solutions were made to the amounts used in exp 5 from the results obtained about the micelle stability. The first two micelle solutions were made; the iron chloride solution was orange, and the sodium borohydride solution was colourless. Initially, when the sodium borohydride was added to the iron chloride, hydrogen gas evolved briefly before the mixture went from orange to colourless and finally, black. Both mixing patterns were trialled; $NaBH_4$ into $FeCl_3$ and vice versa. When mixing the iron solution into the borohydride solution, the colour quickly changed from colourless to black due to an excess of BH_4^- for each Fe^{3+} initially. *Glavee et al. 1992* discussed when the borohydride is slowly dropped into the iron solution, the colour of the solution slowly changes from orange to yellow to colourless before turning black to reduce the iron ions. When the BH_4^- is added to the Fe^{3+} there is an excess of Fe_3^+ initially leading to a longer period of time before the solution turned black.

A reasoning for the slower kinetics is the pH and the redox potentials. The iron chloride micelle solution has a pH of 4.2. At this pH, hydrogen ions can be reduced due to the redox potentials in Equations 4.1 to 4.3. As the hydrogen gas evolved, the pH starts to increase, which leads to the colour of the solution slowly changed from orange to yellow and to colourless as the pH increased to around 6.8 to 7. The colour started to change to the typical black colour as elemental iron formed within the micelles. At this pH, both the iron reduction and the hydrogen evolution are in equilibrium, keeping the pH relatively constant until the iron ions' reduction has occurred. This is not the case when the iron solution is added to the borohydride as the pH is already higher at 6.5, so when the iron solution is added, the reduction can occur immediately, forming the Fe NPs immediately.

$$Fe^{2+} + 2e \rightarrow Fe \qquad E^o = -0.44V \qquad \text{Eq 4.1}$$

$$BH_4^- \rightarrow B + 2H_2 + 2e \qquad E^o = -1.31V \qquad \text{Eq 4.2}$$

$$2H^+ + 2e \rightarrow H_2 \qquad E^o = 0.00 \qquad \text{Eq 4.3}$$

The reduction of the iron to form the black solution typical of iron NPs does not always occur, and the solution turns a greenish colour with a dark green precipitate. In this case, the reduction and formation of the core have been unsuccessful. When the reduction does not occur, and the pH rises above seven, more hydrogen gas is evolved as the borohydride hydrolyses in the aqueous solution.

Figure 4.7 displays where the differences between a successful and unsuccessful reaction can be seen where one appears pure black, suggesting the formation of iron NPs and magnetic material being present. Meanwhile, when the solution turns green, with no magnetic particles present within the solution. Over time, the green colour changes to orange / yellow if the solution encounters the atmospheric conditions. An unsuccessful reduction occurs because there is still dissolved oxygen (DO) within the solutions, and the sodium borohydride continues to hydrolyse, meaning that when the two solutions are mixed, the pH increases and a slower rate of reduction Fe ions.

At a pH of 8.5, the dissolved oxygen within the micelles will cause oxidation of the iron ions, leading to the greenish colour forming rather than a black Fe particle. This indicates iron hydroxides are forming initially in the solution corresponding to the greenish colour. Over time, with air contamination, the greenish colour turns into an orange/yellow precipitate, indicating iron oxides/iron oxyhydroxides. This indicates that degassing the solvents is critical to minimise unsuccessful reactions occurring.

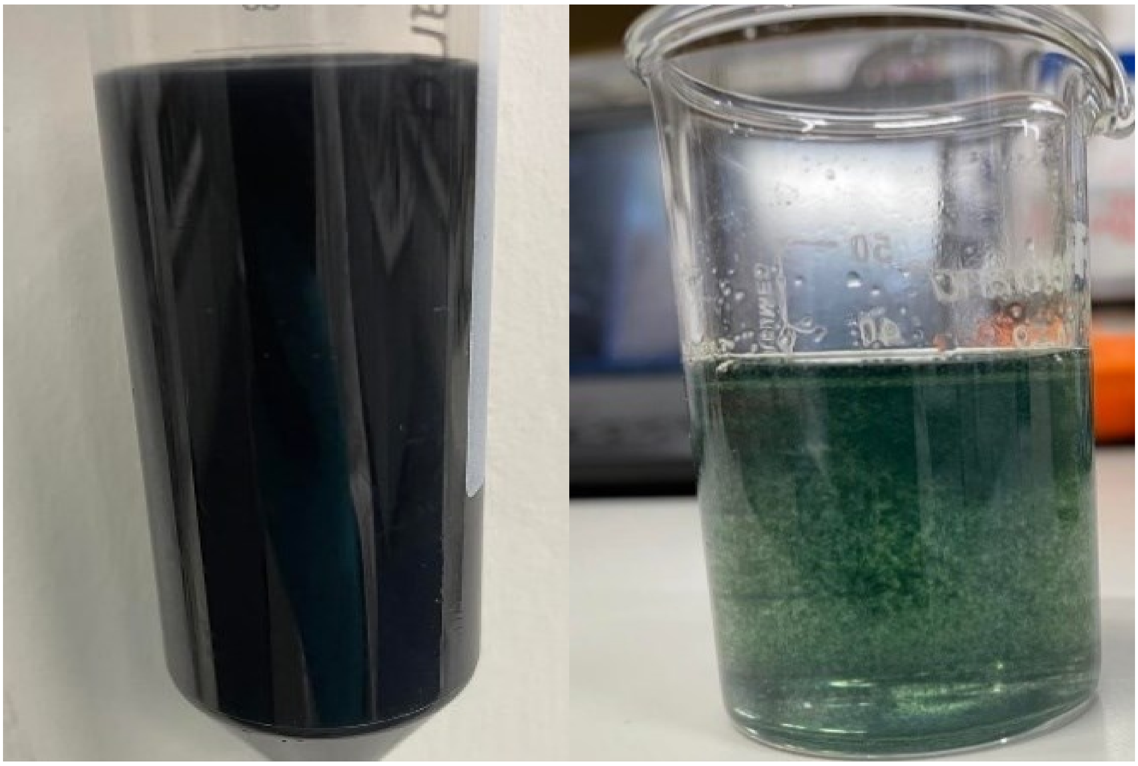

Figure 4.7: Successful reduction of iron ions (left) vs unsuccessful reduction of iron ions (right).

In Figure 4.8, pH measurements were carried out on two different experiments; one successful, and the pH reached equilibrium around pH 7, before increasing once the solution had turned black. In an unsuccessful reaction, the pH continues to rise throughout the experiment, with the solution's colour turning green and increasing to a pH of 9.4. This is an indicator that shows when a reaction is successful and unsuccessful.

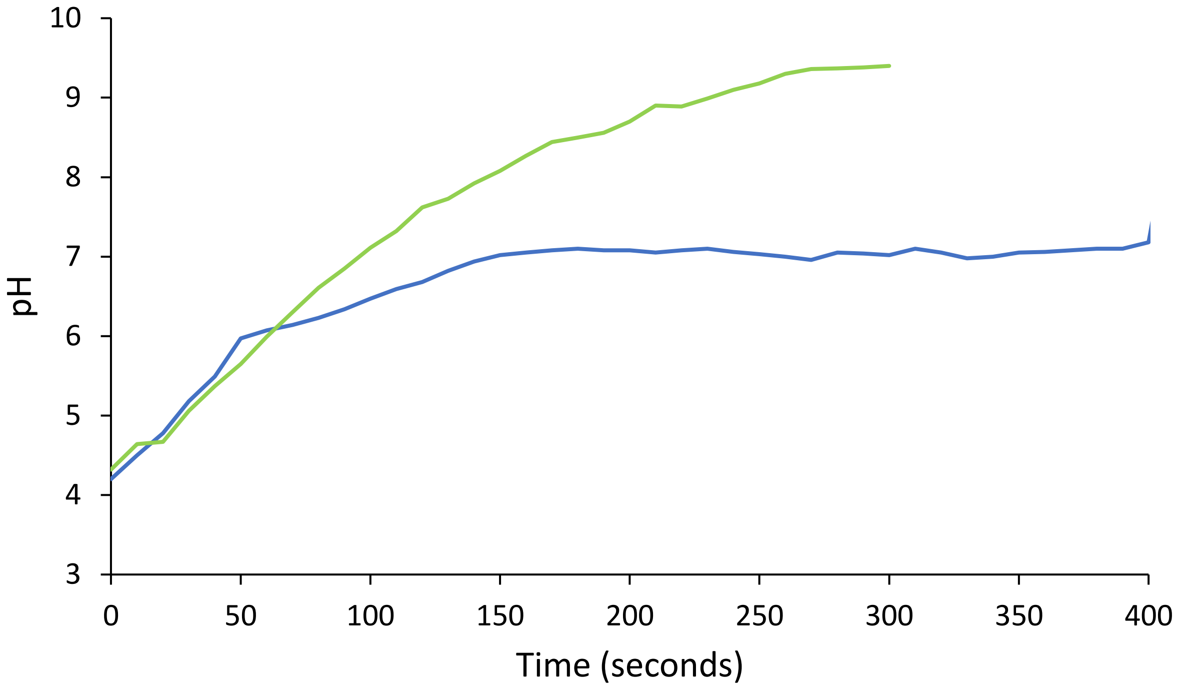

Figure 4.8: pH measurements of a successful (blue) reaction and unsuccessful (green) reaction.

4.4.3 Boron content

Upon successful reduction of Fe^{3+}, the boron content is a critical factor to determine the success of the core synthesis. The main factors impacting the amount of boron incorporated are the addition rate, the mixing pattern, and the borohydride concentration *(Linderoth et al. 1998)*. *Glavee et al. 1995* discusses the differences between non-aqueous and aqueous formation of the Fe-B core. Aqueous synthesis led to a lower amount of boron incorporation *(Glavee et al. 1995)*. Although aqueous conditions leads to a lower boron content, there are multiple papers published where a successful gold shell has been placed upon an iron core and overcome the lattice mismatch (*D. Chen et al. 2009), (Kvitek et al. 2019), (Khan et al. 2013) (Ma et al. 2022)*. In aqueous methods by trying to sacrifice the boron content for a proven method for core-shell synthesis.

In the non-aqueous method, a 1:1 ratio of boron and iron can be achieved when using a Fe^{3+} ion solution, as more borohydride is required to reduce the iron, and a complex is formed containing $Fe(BH_4)_3$. Whereas, when using aqueous conditions, the reaction starts instantaneously via reaction Equations 4.4 and 4.5, where the hydrolysis of borohydride occurs in the water, which then starts the reduction of the metal ions to form the bimetallic core of iron and boron. As no complex is formed like in non-aqueous conditions and immediate reduction starts, the boron incorporation reduces significantly.

Glavee et al. 1995 experimental work in aqueous conditions led to an iron to boron ratio of 4.46.

$$BH_4^- + 2M^+ + 2H_2O \rightarrow 2M + BO_2^- + 2H_2 + 4H^+ \qquad \text{Eq 4.4}$$

$$BH_4^- + H_2O \rightarrow B + OH^- + 2.5H_2 \qquad \text{Eq 4.5}$$

Table 4.3 displays the ICP-OES analysis from the synthesis of the Fe-B core to measure the amount of boron incorporated under different reaction conditions. All micelle solutions were made in the same way with reduced n-butanol as found to give highest micelle stability.

In exp 1, the reaction was carried out as reported in the methodology. The boron content of the core under these conditions led to a 10.02 % boron content. The boron content is much lower when compared to synthesis under non-aqueous conditions but with the advantage of a tighter control over the core size through the micelle. In exp 8, when the mixing pattern was reversed, led to a non-significant change in the boron content of 9.28 % and very similar to exp 1.

Linderoth et al.1998, suggested that the key variables that affected the boron content are the concentration and addition rate of the borohydride solution. Exp 9 confirmed this when reducing the addition rate from 150 ml/hr to 50 ml/hr and reducing the concentration of the borohydride solution by half led to a boron increase to 16.70 % with an increase when compared to exp 1. With further concentration decreases and slower addition rates, it is expected that the boron content would increase further. Exp 10 further supported this; adding the borohydride solution rapidly into the iron chloride solution led to a negligible amount of boron incorporated. *Linderoth et al. 1998* suggested the rapid reduction of the iron ions leaves little time for the boron to be incorporated into the iron particles, leading to α-iron particles being formed with a crystalline structure rather than amorphous particles.

Table 4.3: ICP-OES results of Fe-B core synthesis under different reaction conditions.

Exp	Conditions	Boron (molar ppm)	Iron (molar ppm)	Boron %
1	Standard reaction conditions	8.77	78.68	10.02
8	$FeCl_3$ added to $NaBH_4$	8.60	84.00	9.28
9	Half concentration of $NaBH_4$ and addition rate of 50ml/hr	10.05	50.13	16.70
10	Rapid addition of the $NaBH_4$	1.05	225.80	0.46

4.4.4 Addition of gold

It is pivotal to have a protective gold layer around the core to eliminate oxidation and to attach the targeting peptide to help deliver the particles to the glioblastoma for NCT.

Via the reverse micelle process, to add a gold layer, the W value needs to be increased to incorporate the gold ions around the core, which is subsequently reduced near the surface of the core and form a thin shell layer as seen in Figure 4.9. No excess borohydride was used to avoid the gold ions being reduced immediately by excess borohydride. Once the gold addition is completed a short period of time is left to ensure the gold ions are surrounding the Fe-B core before the slow addition of the second borohydride solution. If the addition of the second borohydride solution was left longer, redox-transmetalation would start which may be beneficial for shell addition.

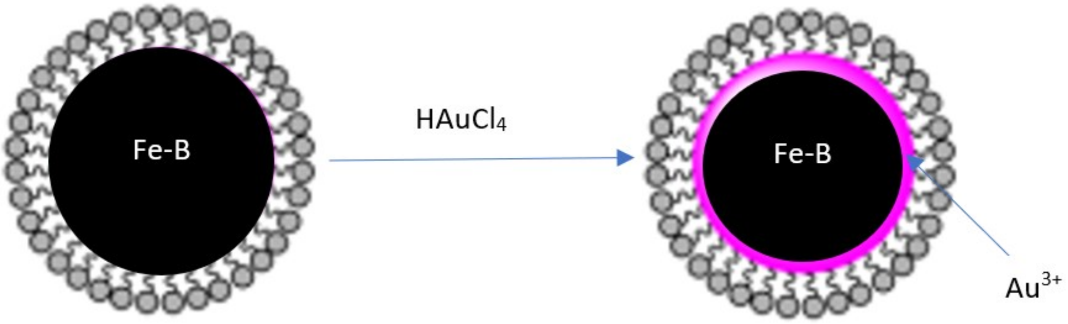

Figure 4.9: The expansion of the iron-boron micelle to incorporate the gold ions around the core.

When the chloroauric acid was added to the micelle solution, the yellow colour that would be expected, turned to an orange / red colour with a similar colour precipitate. *Podporska-Carroll et al. 2015* found a similar finding whereby dependant on the CTAB and gold concentration, a complex is formed which leads to an adjustment in colour. With an increase in gold concentration, the colour would turn brownish and with further increases a turbid yellow colour. The change in colour is attributed to the interaction between the gold ions and the headgroup of the CTAB that forms a complex of $AuCl_4^-$-CTA that can partially protect the gold ions from reduction due to the encapsulation. It has not been reported and unaware in this research whether this interaction causes instability and effects micelle formation. It is expected to affect the micelle formation and the reduction of the gold ions at the surface of the core due to the reaction causing a precipitation of $AuCl_4$—CTA meaning the gold ions are not within the micelle around the core to promote the shell formation. The concentration of free CTAB to form micelles are reduced leading to the reduction process via reverse micelle not occurring as expected.

Although each experiment was carried out in the same manner, in some cases when the gold solution was added, there was a slight colour change to the solution where the black colour for Fe would go greenish. The chloroauric acid solution is acidic and could lead to additional interactions at lower pH or even oxidation occurring from the addition of the Au solution. Upon successful addition of the Au solution, the second borohydride is added slowly at 50 ml/hr to control the reduction rate of the gold ions and minimise the number of monometallic particles formed. This may lead to a mixture of gold reduction via redox-transmetalation and via $NaBH_4$ to promote the gold shell formation.

After the addition of the second borohydride solution, the colour would change to a black/blue colour indicating the formation of larger Au particles and left for two hours to mix. This is not desired and possibly due to the $AuCl_4^{-}$CTA being reduced by the $NaBH_4$ without effective stabilisation. The final colour of the sample was black/purple and contained magnetic particles indicating that both Fe and Au particles were present.

UV-Vis was carried out on the samples to analyse the optical properties. Exp 1 UV-Vis spectroscopy has been compared to 50nm gold colloid solution as seen in Figure 4.10. The gold colloid solution has a red shift with a peak at 527 nm that indicates monometallic gold. As the particles become larger a blue shift occurs and expected with the visual colour of the synthesised solution of black / purple. The results for exp 1 have a very low intensity gold peak that has a blue shift to 557 nm with a relatively broad peak in comparison to the gold colloid solution. The results suggest that a smaller concentration of Au NPs were produced that is due to the complex formed between the chloroauric acid and CTAB. *Ban et al. 2005* and *Jafari et al. 2010* indicated that UV-Vis gave a good indication of core-shell NPs by seeing a blue shift in the wavelength and broadening of the peak. It was also reported that a sharper peak indicates monometallic Au particles. In experiment one, noisy signals were found between 200-250 nm as the limits of the equipment are reached. However, iron signal via UV-Vis is between 200-400 nm and the iron peak may be lost in the signal *(Bouafia et al. 2021).*

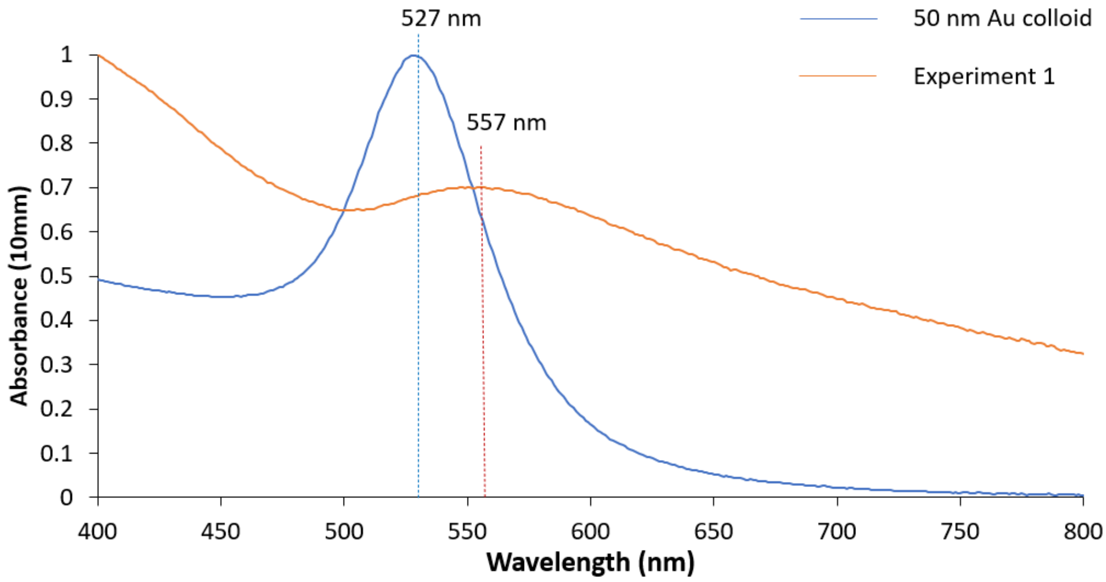

Figure 4.10: UV-Vis of 50 nm gold colloid (blue) and Experiment 1 (orange).

Different analysis techniques were carried out to analyse the oxidative state of the iron and confirm whether a core-shell structure was formed. Initially, a small sample was taken and washed in a 10 % nitric acid solution to confirm whether an entire shell had been formed around the core to protect it from acid digestion. From this quick test, after the acid addition no magnetic particles were present suggesting no full shell formation.

STEM analysis was carried out focussing on High Annular Angular Dark Field (HAADF) and bright field (BF) images. HAADF analyses the in Z number. Gold is a heavier element than iron, and appears brighter than iron; hence, the particles have a brighter outside compared to the centre of the particles. Boron is a light element, and this technique is not sensitive towards light elements as boron only has two inner electrons that can be removed to give a signal. In BF, the analysis gives information on material's thickness. BF should appear opposite to the HAADF as spherical particles are thicker in the centre compared to the edges of the material.

Figure 4.11 displays experiment 1 STEM data. HAADF shows contrast between some particles core and shell which is a positive indication of different materials. However, as discussed in the previous chapter [chapter 3], false positives have been noticed where contrasts between monometallic particles are present. If the beam was not penetrating through the entire particle, a contrast will appear due to limited signal reaching the detector, although, using an acceleration voltage of 15 kV has a penetration depth of 800 nm which the particles are not greater than this thickness. The BF does not show any contrast between the core and the shell of the material, which would be expected as the particles' thickness should be different from the centre to the outside. However, as no additional stabiliser was used after washing, agglomeration would occur when the particles dry on the copper/polycarbonate grid.

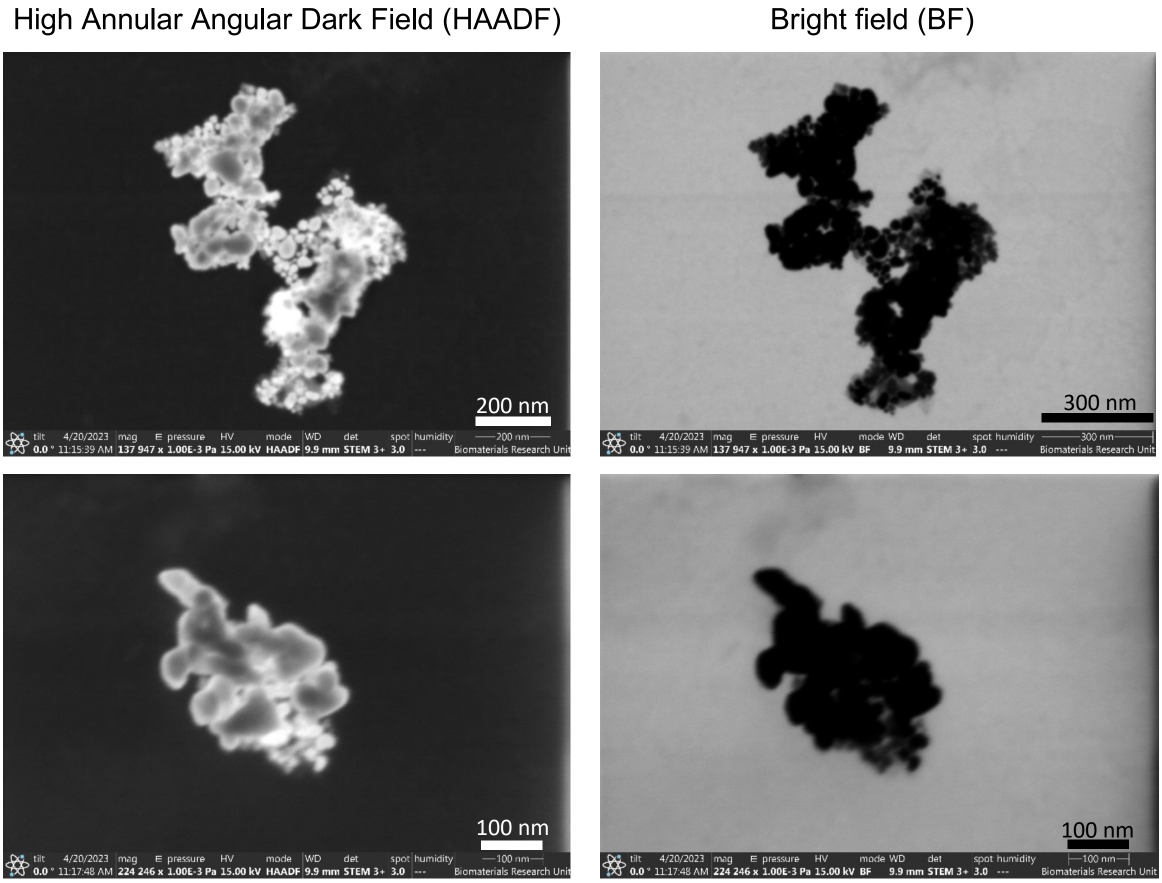

Figure 4.11: STEM photos of experiment 1.

To obtain a good signal via Energy Dispersive X-Ray (EDX), 1.5 x the energy of the shell is required to excite the electron to knock them from that shell. Iron (Ka shell) is 6.4 keV, and gold (La1 shell) is 9.71 keV. 15 kV was chosen as the acceleration voltage to obtain signals from the materials.

To obtain the composition of the material, EDX was carried out as seen in Figure 4.12. The EDX data for exp 1 shows an overlap of gold and iron in Figure 4.12b and Figure 4.12c. The particles being observed are clustered together leading to difficulty in distinguishing whether there is core-shell structures or monometallic distributions of both materials. The EDX data is inconclusive as to whether the reaction is successful. From the acid wash test of a small portion of the sample suggests that there are two single distributions of iron and gold NPs. Using the STEM and EDX data, can indicate the size distribution of the NPs formed in the sample. From the results, a range of sizes is formed, ranging from 10 nm up to approximately 100 nm NPs. The large size distribution is due to no stabiliser being used after completing the synthesis process leading to agglomeration while drying the sample out. However, another reasoning that would cause the size distribution is the micelle formation is not occurring in the expected way, and the stability of the micelles is low. Micelle stability is critical to form a narrow size distribution. The repeatability of the experiments is challenging leading to the requirement of reestablishing an optimal procedure.

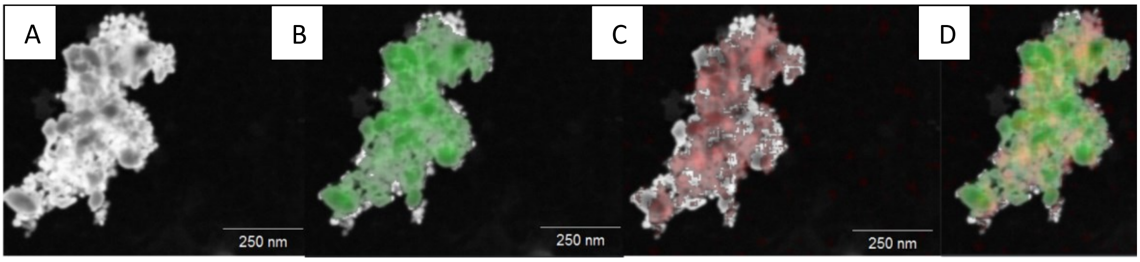

Figure 4.12: EDX data of experiment 1. A – HAADF image, b – gold mapping, c – iron mapping, d – overlay of iron ang gold mapping.

TEM analysis is required as a more sensitive technique to obtain lattice information and more detailed analysis via electron microscopy. Iron and Gold have different lattice structures and through TEM would be able to distinguish the change in lattice from the centre to the edges of the material with an amorphous structure in the centre and crystalline gold lattice on the edges. Figure 4.13 displays STEM mapping coupled with EDX to analyse the composition of the particles at a higher resolution. STEM carried out in TEM rather than SEM gives a clearer picture of what has been produced during the synthesis process. The electron mapping shows two distributions of brighter-appearing particles and a grey set of amorphous particles. The EDX mapping clearly shows that the brighter particles are of gold NPs, and the grey amorphous particles are of iron, and that there are two different distributions of particles rather than any form of core-shell or partial shell formed. The amorphous structure of the iron indicates that boron has been incorporated into the iron core. The oxygen mapping is similar to the iron. The mapping of oxygen indicates that iron is in its oxidative state rather than elemental iron, which is expected with no protective layer. Figure 4.14 of the TEM images shows the difference in particle morphology between the gold and iron NPs and the lattice structure. The particle size from the TEM images is less than 50 nm, meaning each distribution is of the correct size for NCT but not in the correct formation.

The narrow size distribution via TEM suggests that the micelle formation is occurring and controlling the size of the NPs but not promoting the formation of a gold shell around the Fe-B core. With the results obtained, the Fe-B micelle and the Au^{3+} solution is not combining correctly to form a shell.

The results differ from the published research following the same methodology for synthesising iron@gold NPs. The presence of a higher percentage of boron within this research may lead to the further difficulties in forming a shell around the synthesised core. As the boron incorporation leads to an amorphous Fe-B particle, this may lead to higher energetics in forming a gold shell when compared to a crystalline Fe core. All other experiments carried out using the reverse micelle method continued to give two separate distributions of iron and gold NPs.

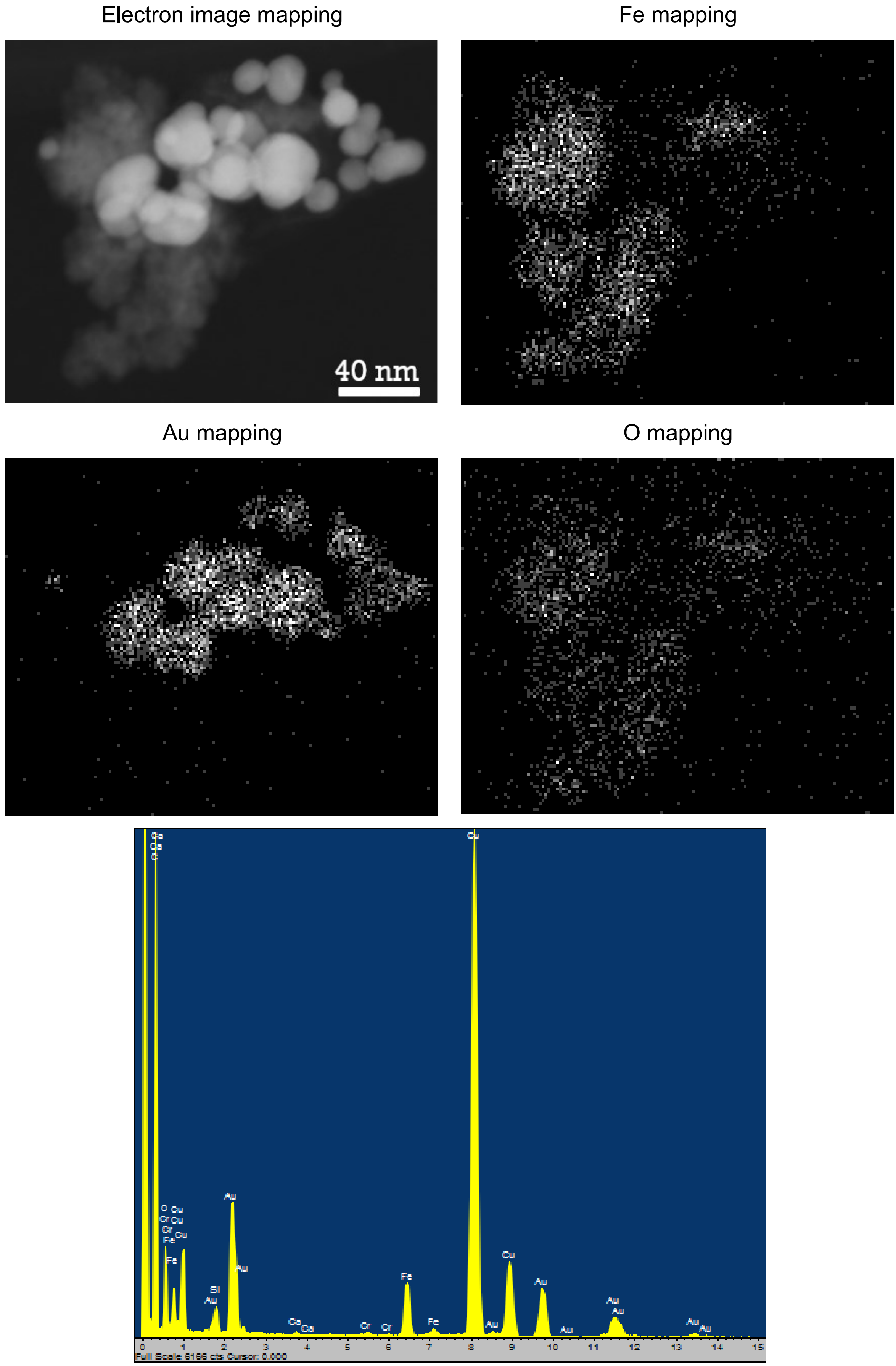

Figure 4.13: STEM and EDX mapping of experiment 1.

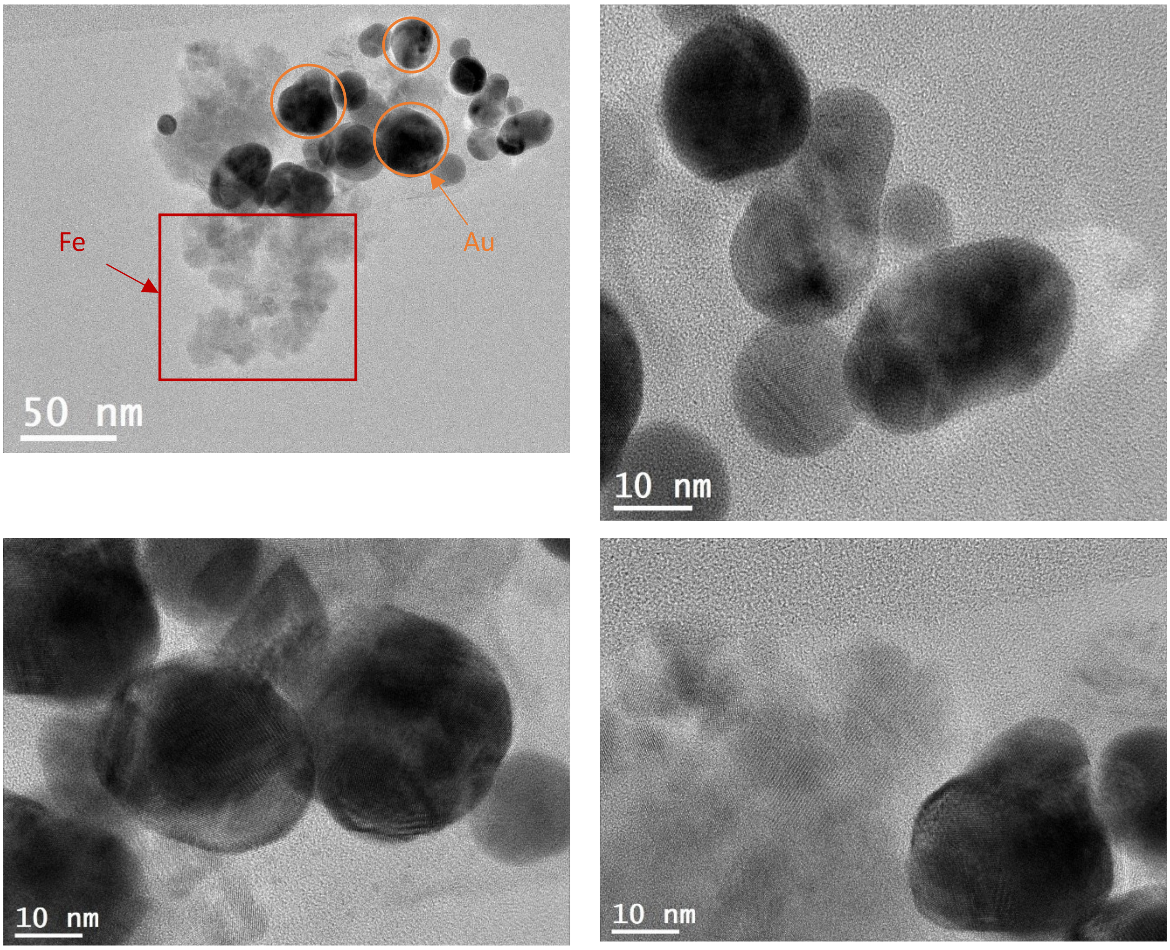

Figure 4.14: TEM images of experiment 1 at different magnifications (particles surrounded with a orange circle are monometallic Au, particles highlighted in red box a monometallic Fe).

4.4.5 Reverse micelle + redox transmetalation synthesis

The synthesis process was adapted to a dual method process where reverse micelle synthesis was used for the core synthesis and redox-transmetalation was used for the shell synthesis to obtain the positives of both methods to improve shell formation. *Chen et al. 2009* uses a similar process where reverse micelle was coupled with redox transmetalation for forming Ni@Au NPs taking advantage of both methods to form the desired NPs. The advantages are controlling the size of the NP by micelle size and the overcoming the lattice mismatch by redox-transmetalation is fewer chemical reagents are required, and less waste produced due to one micelle solution not being required.

After the gold addition, the solution was left for a period with different timings tested: 0, 30,120 minutes and overnight where then the solution was heated up to 75 °C for 30 minutes to promote and speed up the reduction process via redox-transmetalation. When left overnight, it was also trialled where heating and no heating were carried out. Over an extended period, the reduction process will occur at room temperature, and the heating process is unnecessary. For the reduction process to occur effectively, the core must contain elemental iron and not iron oxides to ensure that the reduction process can occur as expected due to the significant difference in the reduction potentials between iron and gold.

Similar issues can occur for the experiments carried out this way, where the pH drops more than expected upon the gold addition leading to the solution changing from black, corresponding to the magnetic core, to a greenish colour with no magnetic particles. This suggests that the drop in pH value lower than magnetic iron particles can survive before being digested, there will be no core and reducing agent available to reduce the gold ions. Another reasoning for this observation is that the iron has already oxidised upon the addition of the Au ion solution which means no reduction can take place and no redox-transmetalation.

Table 4.4 displays the XPS data where exp 1 was carried out via the normal reverse micelle synthesis process and led to a 10 % boron content and 1.3 % gold content. Magnetic separation was repeated three times to ensure only magnetic material was being analysed. Only gold material that is pulled along with the magnetic material is present.

Exp 11 was carried out with the same reaction conditions as exp 1 but immediately heated up to 75 °C for 30 minutes to encourage redox-transmetalation. The small change led to a similar boron content of 14 %, which would be expected with similar conditions. In exp 11, there was over double the amount of gold present in the sample after magnetic separation of 3 %, suggesting that more core particles are pulling gold across during magnetic separation indicating more successful shell formation via redox-transmetalation.

Exp 12 was completed with the slower addition of the initial sodium borohydride and lower concentration, leading to increased boron incorporation in the core. The solution was left for 30 minutes before the gold addition and heated to 75 °C for 30 minutes. The gold atomic concentration again is higher than that of Exp 1, suggesting that there is a promotion of seeding at the core, allowing the partial gold shells to be pulled across by the magnet compared to monometallic gold, which would be left behind.

An experiment was carried out where, after the gold addition, the sample was stirred overnight. However, overnight stirring led to the solution appearing a deep red colour, indicating small gold NPs and no magnetic particles present at the end of the experiment. With prolonged exposure to the gold ions leads to over erosion of the core via redox-transmetalation and an optimal time is required to promote shell formation and reduce over erosion.

It appears that coupling the two methods together promotes the formation of the core-shell NPs and takes advantage of the two reaction processes. Although optimisation is required to avoid the negatives the core being completely used in the reduction process.

The XPS binding energy for exp 1, the likely chemical state of iron is FeOOH or (Fe_xB_{1-x})OOH. Hence, the surface state of Fe is likely to be the hydroxide. The binding energy for exp 11 and 12 indicates that it is likely to be either Fe_2O_3 or $(Fe_xB_{1-x})_2O_3$. This indicates that no complete shell has been formed in the experiment due to all the cores being oxidised at some stage of the process.

Table 4.4: XPS data of both reverse micelle and coupled with redox transmetalation methods (RM – Reverse micelle, RT – Redox-transmetalation) (B(1) - Fe_xB_{x-1}, B(2) - (Fe_xB_{1-x})OOH or $(Fe_xB_{1-x})_2O_3$).

Experiment	Atomic concentration (%)						
	Fe	B(1)	B(2)	Au	Na	Cl	B/Fe
Exp 1 (RM)	16.1	-	1.6	1.3	0.3	0.6	0.1
Exp 11 (RM + RT)	20.7	-	2.9	3.0	0.7	-	0.14
Exp 12 (RM + RT)	15.8	-	5.3	2.8	0.7	1.2	0.34
Exp 13 (RM + RT)	45	1.2	1.1	1.1	1.4	0.7	0.11

However, in Table 4.4, exp 13 showed promising results which was left for 2 hours before heating to 75 °C for 30 minutes. After washing the sample and magnetic separation, the sample was also washed in a 10 % nitric acid solution. After the acid washing, there was still magnetic material in the acidic solution being pulled across to a magnet, suggesting the core is protected from acid digestion. Over 14 days, the magnetic material slowly reduced, suggesting that the protection, if a shell of gold, had defects or cracks that allowed the acid solution to diffuse from the surface of the shell to the core over time suggesting the stability of the particle needs improving. The XPS data for Exp 13 has a lower amount of gold in the sample that was pulled across to the magnet of 1.1 atomic % in comparison to exp 11 and 12 which was 3.0 % and 2.8 % respectively. However, there was some form of protective layer in exp 13 in comparison to exp 11 and 12. XPS binding energy peaks for boron are split in two. The B 1s consisted of 2 peaks, B (2) a boron hydroxide and B(1) a Fe-B compound of Fe_xB_{x-1}. The energy of B(1) indicated that no oxygen was associated with this peak. B(2) was likely to be $(Fe_xB_{x-1})_2OOH$ corresponding to the FeOOH. The B1 peak indicating no oxygen presence after several washes, an acid wash, and the sample being dried out in an oven ready for the analysis, suggests that a small amount of these particles have a protective shell around the core material.

STEM and EDX analysis were carried out on exp 13 as seen in Figure 4.15 to identify any clear core-shell structures in the sample, to support the XPS data. There is no clear indication of the core-shell structures. A contrast in the HAADF between the core and the shell of the material, which would indicate a core-shell structure, but as previously understood the analysis equipment gives false positive results of this nature. Most of the particles are less than 100 nm and a proportion around 50 nm which is ideal for the end use. The EDX data shows an overlap of both Fe and Au but no clear core-shell structure can be identified from the data. The oxygen mapping closely follows that of the particles, which suggests that the cluster of particles where iron is present is most likely in the form of iron oxides and oxyhydroxides.

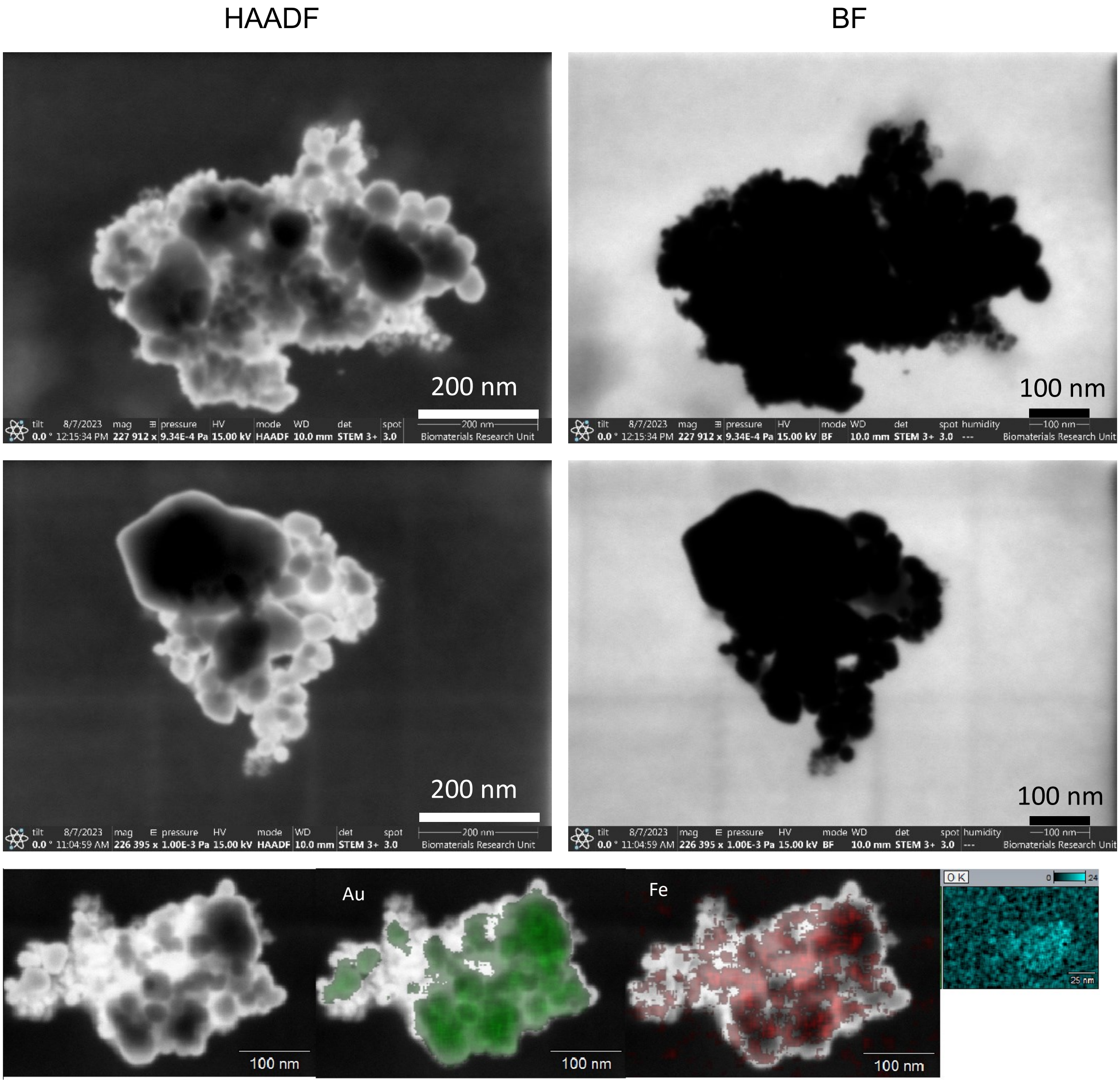

Figure 4.15: STEM and EDX data for experiment 13.

TEM couple with EDX was carried out on exp 13 to understand if any core-shell structures were present. In Figure 4.16, the TEM data seems to show a monometallic distribution with no clear difference in lattice structure between the core and shell of the particles. It is unclear what protection was been offered to the magnetic core from the acid wash with no indication of core-shell structure. The EDX data further suggests that there are no core-shell structures formed.

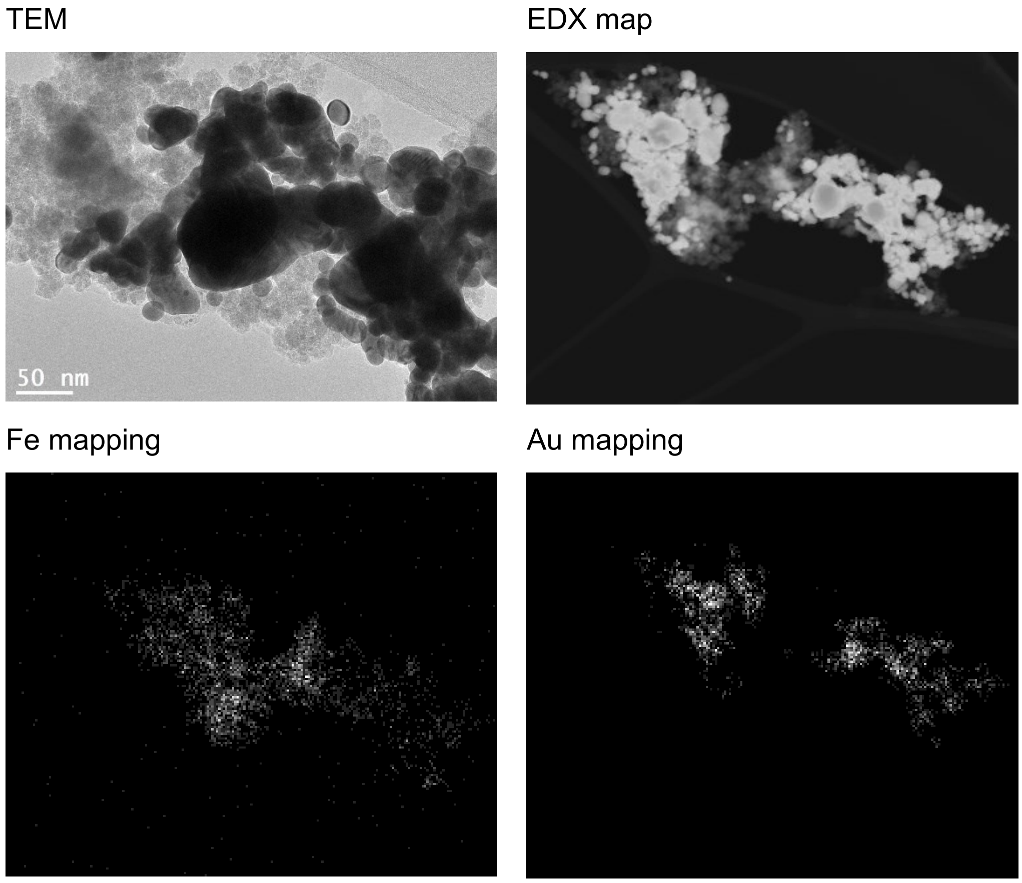

TEM

EDX map

Fe mapping

Au mapping

Figure 4.16: TEM and EDX data of experiment 13.

In exp 11, there appeared to be interesting STEM results, as seen in Figure 4.17. In low concentration, some form of shell appears to be covering the core but incomplete.

The particle appears to be over 200 nm in diameter, suggesting the micelle formation was unstable and particle growth continued with no inhibition from the micelle. Darker particles started to surround the brighter particle in the centre, which was seen similarly in the non-aqueous method. In the BF image, there is a contract in the outside partial shell particles compared to the core, which has not been seen in any other BF images, which is a positive indication of two different materials being present at the core and shell. The low concentration of particles in this format suggests only a small amount led to this partial core-shell structure.

There combination of the reverse micelle and redox-transmetalation method appear to give more positive results than just using reverse micelle alone indicating that the dual method can overcome some of the limitations of reverse-micelle.

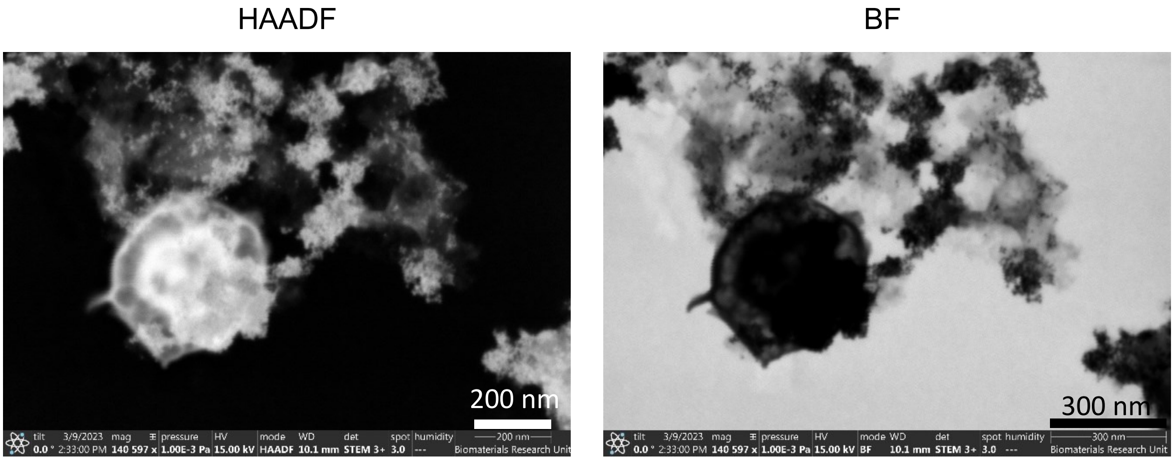

Figure 4.17: STEM images of experiment 11.

4.5 Addition of water gold sol

Due to the possible instability of the micelles of iron-boron core and the gold solution and the micelles not combining to form a shell layer, a trial experiment was carried out where the gold solution was added in aqueous form where the gold is dissolved in 1.8 ml of water only. By removing the micelle solution of gold and adding the gold solution directly to the Fe-B would expand the core micelle solution by itself and better force the gold ions to be incorporated into the Fe-B micelle. This process was trialled with the reverse micelle method coupled with the redox-transmetalation process since it appeared to promote more shelling on the core NPs. However, a lack of gold signal and gold NPs was produced as seen from Figure 4.18. In the STEM and EDX data, there appear to be fewer gold NPs in the sample. One reasoning is that the Au ions react directly with the CTAB in the solution and destabilise the micelle which contain the Fe-B. This leads to the redox-transmetalation reaction not occurring due to no incorporation of the gold ions into the micelle. Another reason is the gold ions react with the CTAB to produce a precipitate which means the ions cannot be incorporated into the Fe-B micelle as the precipitate is larger than the micelle.

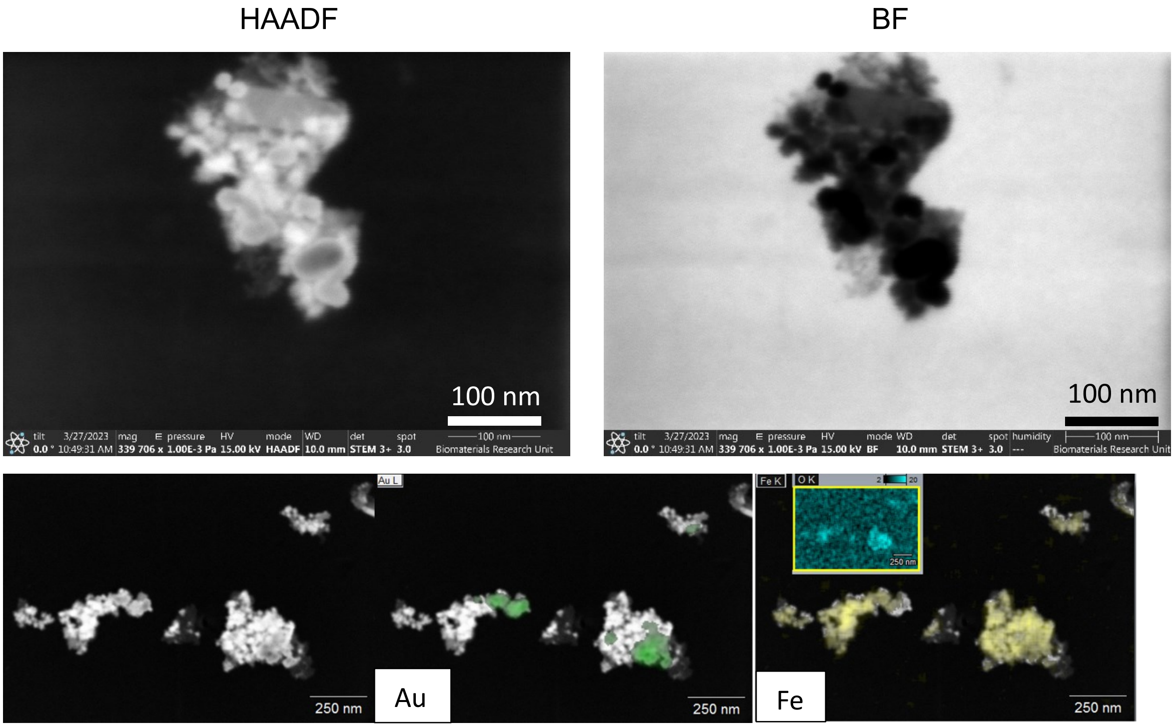

Figure 4.18: STEM and EDX data of results of the gold solution added directly to core micelle solution.

4.6 Conclusion

Overall, several interesting findings on how certain variables can affect the synthesis process of the NPs has been understood. The process can be split into two major synthesis procedures: the synthesis of the core and the synthesis of the shell. From the results obtained, an effective and optimised core with high boron incorporation for effective cancer treatment for glioblastomas via neutron capture therapy can be produced. By optimising the reaction pattern, the addition rate, and the concentration of the chemicals in this process, an increased amount of boron can be incorporated into the core to make the particle more effective for NCT. However, further advancements would be required to make it optimal for NCT.

This was similar to the Chapter 3, non-aqueous techniques, where enough boron could be incorporated for its final use. However, trying to form a shell was less successful and appeared to form partial shells or two distributions of magnetic core and gold NPs. It was exp 13, which appeared to be the most successful, with it being able to resist acid washing for some time before the diffusion of the acidic solution to the core led to dissolution. Some form of core protection was present to avoid damage to the core as the XPS data for exp 13 suggested that a Fe-B was exhibiting no oxygen, after all the washing procedures and drying in an oven in atmospheric conditions that some protection is present. The concentration of the particles may be low that it is challenging to visualise them in all the other partial shells. In STEM and EDX, no such protective layer was observed which led to unknown reasons as to why the acid wash did not digest the core.

The synthesis method was adapted from several papers *(D. Chen et al. 2009), (Zelenakova et al. 2023), (Jafari et al. 2010)* and *(Kvitek et al. 2019)* to understand and use already published methods to adapt and improve for the desired use of NCT and enhance gold shell formation. In the published work, successful results were achieved using similar reaction conditions where an iron core and a gold shell or nickel core and gold shell were synthesised very effectively. However, within this research, the micelle stability was low, and changing the water to CTAB ratio did not alter the size of the micelle in the same highly controllable way as suggested in the literature.

Following these reaction conditions, no core-shell particles were formed. Reproducing the publications was challenging, and the process variables that could significantly affect the reaction have not been reported. For example, the pH of the solutions; in a few cases, the pH changed significantly in the process and significantly affected the core material, leading to acidic digestions. The gold ions reacting with CTAB to change colour from yellow to an orange/red colour with a similar colour precipitate was noticed. However, this reaction was not reported in the experimental procedures. It is unclear whether this is an expected reaction a side reaction is occurring, which affects the shell formation and stability of the micelle. A much more detailed synthesis procedure needs to be established to understand the small variables that cause effects on the process.

Future work to advance this research needs to focus on the gold shell formation. The synthesis of the magnetic core with boron enrichment has been proven but maintaining inert conditions leads to challenges for shell formation. However, if successful shell formation occurred then the particles would be optimised for NCT. Rather than carrying out the process using a Schlenk line, a glovebox would make keeping inert conditions easier. Focusing the research at the coupled reverse micelle and redox transmetalation process would be effective as it showed promising results and waste produced lower if scaled to an industrial scale.

Some results have shown that the particles resisted acidic digestion for some time but were not stable over long periods. This research has tried to narrow down the process to a more detailed one and understand which variables have more of a significant effect on process parameters.

References

Anderson, S. D., Gwenin, V. V, & Gwenin, C. D. (2019). *Magnetic Functionalized Nanoparticles for Biomedical , Drug Delivery and Imaging Applications*. *6*.

Ban, Z., Barnakov, Y. A., Li, F., Golub, V. O., & O'Connor, C. J. (2005). The synthesis of core-shell iron@gold nanoparticles and their characterization. *Journal of Materials Chemistry*, *15*(43), 4660–4662. https://doi.org/10.1039/b504304b

Bouafia, A., & Guemari, F. (2021). Effect of Ferric Chloride Concentration on the Type of Magnetite (Fe 3 O 4) Nanoparticles Biosynthesized by Aqueous Leaves Extract of Artemisia and Assessment of Their Antioxidant Activities. *Journal of Cluster Science*, *32*(4), 1033–1041. https://doi.org/10.1007/s10876-020-01868-7

Carpenter, E. E. (2001). Iron nanoparticles as potential magnetic carriers. *Journal of Magnetism and Magnetic Materials*, *225*(1–2), 17–20. https://doi.org/10.1016/S0304-8853(00)01222-1

Chen, D., Liu, S., Li, J., Zhao, N., Shi, C., Du, X., & Sheng, J. (2009). Nanometre Ni and core/shell Ni/Au nanoparticles with controllable dimensions synthesized in reverse microemulsion. *Journal of Alloys and Compounds*, *475*(1–2), 494–500. https://doi.org/10.1016/j.jallcom.2008.07.115

Devi, S. M., Nivetha, A., & Prabha, I. (2019). Superparamagnetic Properties and Significant Applications of Iron Oxide Nanoparticles for Astonishing Efficacy—a Review. *Journal of Superconductivity and Novel Magnetism*, *32*(2), 127–144. https://doi.org/10.1007/s10948-018-4929-8

Glavee, G. N., Klabunde, K. J., Sorensen, C. M., & Hadjapanayis, G. C. (1992). Borohydride Reductions of Metal Ions. A New Understanding of the Chemistry Leading to Nanoscale Particles of Metals, Borides, and Metal Borates. *Langmuir*, *8*(3), 771–773. https://doi.org/10.1021/la00039a008

Glavee, G. N., Klabunde, K. J., Sorensen, C. M., & Hadjipanayis, G. C. (1995). Chemistry of borohydride reduction of iron(II) and iron(III) ions in aqueous and nonaque-ous media. *Inorganic Chemistry*, *34*(1), 28–35.

Goronja, J. M., Ležaić, A. M. J., Dimitrijević, B. M., Malenović, A. M., Stanisavljev, D. R., & Pejić, N. D. (2016). Određivanje kritične micelarne koncentracije cetiltrimetilamonijum bromida: Različite procedure analize eksperimentalnih podataka. *Hemijska Industrija*, *70*(4), 485–492. https://doi.org/10.2298/HEMIND150622055G

Jafari, T., Simchi, A., & Khakpash, N. (2010). Synthesis and cytotoxicity assessment of superparamagnetic iron-gold core-shell nanoparticles coated with polyglycerol. *Journal of Colloid and Interface Science*, *345*(1), 64–71. https://doi.org/10.1016/j.jcis.2010.01.038

Janosevic-Lezaic, A., Paunovic, N., & Pejic, N. (2014). Thermodynamics of micellization of hexadecyltrimethylammonium bromide in propylene glycol-water mixture: A conductivity study. *Facta Universitatis - Series: Physics, Chemistry and Technology*, *12*(1), 17–26. https://doi.org/10.2298/fupct1401017j

Khan, Z., Singh, T., Hussain, J. I., & Hashmi, A. A. (2013). Au(III)-CTAB reduction by ascorbic acid: Preparation and characterization of gold nanoparticles. *Colloids and Surfaces B: Biointerfaces*, *104*, 11–17. https://doi.org/10.1016/j.colsurfb.2012.11.017

Kuang, D., Hou, L., Wang, S., Luo, H., Deng, L., He, J., & Song, M. (2019). *Applied Surface Science Facile synthesis of Fe / Fe 3 C-C core-shell nanoparticles as a high-e ffi ciency microwave absorber*. *493*(July), 1083–1089. https://doi.org/10.1016/j.apsusc.2019.07.073

Kvitek, O., Reznickova, A., Zelenakova, A., Zelenak, V., Orendac, M., & Svorcik, V. (2019a). Immobilization of Fe@Au superparamagnetic nanoparticles on polyethylene. *European Polymer Journal*, *110*(November 2018), 56–62. https://doi.org/10.1016/j.eurpolymj.2018.10.043

Kvitek, O., Reznickova, A., Zelenakova, A., Zelenak, V., Orendac, M., & Svorcik, V. (2019b). Immobilization of Fe@Au superparamagnetic nanoparticles on polyethylene. *European Polymer Journal*, *110*(July 2018), 56–62. https://doi.org/10.1016/j.eurpolymj.2018.10.043

Linderoth, S., & Morup, S. (1998). Amorphous TM 1 − x B x alloy particles prepared by chemical reduction. *Journal of Applied Physics*, *5256*(August).

Ma, W., Zhang, G., Zhang, P., & Fu, Z. (2022). Ag-Pd bimetallic hollow nanostructures with tunable compositions and structures for the reduction of 4-nitrophenol. *Journal of Alloys and Compounds*, *925*, 166689. https://doi.org/10.1016/j.jallcom.2022.166689

Mahajan, P., Singh, A., & Arya, S. (2020). Improved performance of solution processed organic solar cells with an additive layer of sol-gel synthesized ZnO / CuO core / shell nanoparticles. *Journal of Alloys and Compounds*, *814*, 152292. https://doi.org/10.1016/j.jallcom.2019.152292

Malvern Panalytical. (2010). *SURFACTANT MICELLE CHARACTERIZATION USING*. https://www.malvernpanalytical.com/en/learn/knowledge-center/application-notes/an101104surfactantmicellecharacterization

Oakenfull, D. (1982). Effects of t-butanol on micelle formation by a series of long chain alkyltrimethylamonnium bromides. *Journal of Colloid and Interface Science*, *88*(2), 562–573. https://www.sciencedirect.com/science/article/abs/pii/0021979782902843#:~:text=When mole fraction of t -butanol reaches 0.03,and is adsorbed at the head group region.

Peng, L., Peng, H., Hung, C. Te, Guo, D., Duan, L., Ma, B., Liu, L., Li, W., & Zhao, D. (2021). Programmable synthesis of radially gradient-structured mesoporous carbon nanospheres with tunable core-shell architectures. *Chem*, *7*(4), 1020–1032. https://doi.org/10.1016/j.chempr.2021.01.001

Podporska-Carroll, J., Panaitescu, E., Quilty, B., Wang, L., Menon, L., & Pillai, S. C. (2015). Antimicrobial properties of highly efficient photocatalytic TiO2 nanotubes. *Applied Catalysis B: Environmental*, *176–177*, 70–75. https://doi.org/10.1016/j.apcatb.2015.03.029

Zelenakova, A., Szuscova, J., Huntosova, V., Hrubovack, P., & Zelenak, V. (2023). Magnetic Properties and Cytotoxicity Study of Iron Oxide. *AIP Advances*, *040029*.

Chapter 5 – Synthesis and biological analysis of model plastic nanoparticles.

5.1 Introduction

There are hundreds of different plastics that are synthesised for the desired use, which can generally be split into two different categories: general plastics and engineering plastics. General plastics are typically single use plastics such as coffee cup lids. Engineering plastics are usually reusable and have improved properties for a desired use, such as acrylonitrile butadiene styrene (ABS) which is used in 3D printing *(Ai et al. 2022)* These commonly used plastics have led to growing concerns about the impact on the environment *(Nielsen et al. 2020)*. For example, Polyethylene (PE), polypropylene (PP), polystyrene (PS) and polyurethane (PU) are some of the common general plastics used for plastic packaging and single-use products such as drinks bottles and lids. The demand for single-use plastics has been ever-growing, with the demand for these plastic products reaching 390 metric tonnes in 2021 *(Plastics Europe, 2022)*. This accounted for 50 % of the total production of plastics. A primary concern with these figures is that only 9 % of single-use plastics are recycled and the rest sent to landfills or incinerated, leading to a waste of valuable resources in a circular economy *(MacLeod et al. 2021)*.

These polymer plastics are made from non-renewable resources such as crude oil and natural gas, which is a finite resource *(Koczoń et al. 2022)*. This is concerning due to the pollution caused during the synthesis of the plastics when using petroleum sources, but also the pollution caused to the environment due to improper disposal of the plastics to the environment. Plastic waste has been found in the ocean over 50 years ago *(Carpenter et al. 1972)*. Due to the rise in population and the demand for plastics, waste plastics are found ever more regularly due to the slow degradation. Media reports and literature suggest that plastics bags can take anywhere between 10-20 years to degrade *(The Ocean Concervency, 2006), (Ali et al. 2021)* and according to the World Wildlife Fund (WWF), takeaway coffee cups take 30 years, plastic bottles 450 years and plastic straws 200 years *(WWF, 2021)* degrade *(Gosalvitr et al. 2023)*. Therefore, there is a significant need exists to move to biodegradable environmental alternatives to combat these petroleum single-use plastics and analyse the impact of plastic waste products on the environment and human health.

When considering the degradation of petroleum-based plastics into NPs and their impact on the above, it's important to take a comprehensive approach. This includes examining any additives that are incorporated into the plastic that will also degrade into NPs for its intended use. Simply using the raw material may not be sufficient. For instance, in the case of coffee cup lids, plasticisers like phthalates or phthalic acid esters are often added to increase flexibility, making the plastic more suitable for its purpose

(Chen et al. 2021). These phthalic acid esters have been found in popular drinks plastic bottles such as, lemonade, cola and mineral water in Turkey *(Ustun et al. 2015)*. The concern with these additives and the expansion in the production of antimicrobial plastics is that the toxicity of plastic particles is elevated due to the toxicity of the additives. After the outbreak of COVID-19, there have been more concerns about the spread of bacteria and viruses, leading to increased use of antibiotics. The concern around increase in microbial resistance could have a detrimental effect on human health due to general resistance / robustness to deal with toxic compounds *(Kumar et al. 2023)*. A series of inorganic and organic materials can be accountable for increased microbial resistance. For example, Cd, Cr, Pb, Ag, Cu, Sb, Hg, Fe and Mn have all been used as additives in different petroleum-based plastics PE, PP, PS, PA, and PVC in a case study in China from three different soil sites *(Tang et al. 2010)*. Another additive which has been found in white and black plastic film is dibutyl phthalate which has been found to kill 50 % of human blood lymphocytes after 12 hours of exposure.*(Kumar et al. 2023)* (Zarei, 2024).

The need for bioplastics is increasing that are environmentally friendly and degrade readily when disposed of and a much better understanding of the impact of the plastic degradation products on the environment and human health. To address the "enviro friendliness, a detailed study on the synthesis and biodegradation of bioplastics was carried out, which can then be compared to petroleum-based plastics to see the impact of switching to an environmentally friendly plastic. *Wahyuningtyas et al. 2017* produced bioplastics from waste cassava with alternative amounts of glycerol to aid decomposition. The plastics were buried in soil to replicate the effect of landfill. With glycerol contents 2% and above, the bioplastic was decomposed entirely in nine days, and for 1% glycerol was completely decomposed in 12 days, showing the ease for the bioplastics to be broken down by microbes in the soil. This has been analysed by the visual eye and does not examine whether the plastic has decomposed into micro or nanoplastics before complete degredation. When compared to the *WWF, 2021* which suggests that a plastic bag can take between 10-20 years to decompose, there is a significant difference between the two. The biodegradability of plastics is heavily influenced by the water/moisture content, oxygen levels, and other additives to the plastic, such as plasticizers, that can affect the degradation of the plastic. *Nachod et al. 2021* compared bioplastics and petroleum plastics degradation in anaerobic conditions. polyhydroxybutyrate-valerate (PHBV), polylactide (PLA), and cellulose-based bioplastic (CBB) are common bioplastics which were tested against polyethylene terephthalate (PET) as the petroleum-based plastic. The amount of methane (CH_4) was measured to evaluate the decomposition via anaerobic digestion. In all cases, bioplastics produced more CH_4 than PET, showing a better circular economy in recycling bioplastics as an energy source compared with petroleum-based plastics. However, if these bioplastics are not recycled and controlled, there is a possibility of a dangerous amount of methane being released into the environment that will increase global warming.

From the human (and animal) health perspective, a primary concern of plastic pollution in the environment is the inevitable breakdown into micro and nanoplastics, followed by oligomers and finally soluble or volatile chemicals. Studies are underway as these plastics of varying sizes have been found in soil *(Yu et al. 2021)*, in marine environment *(Peng et al. 2020)* and the food chain *(Wang et al. 2022)*. Only recently have the possible hazards and risks of plastic waste been considered. Damage to marine life has been going on for many years *(Peng et al. 2020)*, but now the possibility of human life being affected via consuming these micro and nano plastics through the food chain and contaminated water sources has sparked a vast amount of research into what damage could be caused to human cells*. Rubio et al. 2020* carried out a study using 50 nm PS nanoparticles on human hematopoietic cell lines. It was found that the biological effects of the PS NPs depend on the cell line used and the endpoints analysed. The phagocytic cellular function with the THP-1 cell line offers some resistance to the PS NPs. However, in Raji-B and TK6 toxicity, reactive oxygen species (ROS) production and genotoxicity were detected. Testing plastic nanoparticles and understanding the effects that are caused to an array of cell lines is required. *Guzmán et al. 2022* tested PET NPs less than 250 nm on RAW 264.7 macrophage cells. The results display that the NPs are easily internalised by the cells, exhibiting effects in cell proliferation and slightly increasing ROS production. These preliminary tests show plastic pollution's toxicity, and the extent of potential damage is still not completely understood. It may be that concentrations must be very high to see any effect on the cells, which would not be expected in the environment but an accumulation over a longer period could lead to significant effects. Alternatively, specific cell lines may show immediate damage at low concentrations or due to additives within the plastic. *Pérez-albaladejo et al. 2020*, studied what damage plastic particles and additives caused to human and aquatic life. Both plastic and additives induce oxidative stress. Bisphenol A (BPA), a plasticiser, has been reported to induce ROS in human erythrocytes, such as JEG-3 human placental cells *(Pérez-albaladejo et al. 2017).* In *Soo et al. 2018*, PE microspheres between 150-180 µm were found that in sheepshead minnow [Cyprinodon variegatus], and altered ROS key-related genes Cat and Sod3 were found, suggesting that the genes were being damaged due to the presence of these plastic particles. *Soo et al. 2018* also studied the difference in effects between spherical particles and irregular plastic particles. Both microplastics caused ROS. However, the irregular microplastics decreased the total distance travelled and maximum velocity of sheepshead minnows. Both plastics accumulated in the in digestive system causing intestinal distension but the irregular plastics caused a more significant effect. This suggests that the plastic NPs produced in the environment are more damaging that model spherical plastic NPs.*Roursgaard et al. 2022* displayed that PP and PET with sizes between 100-600nm and 100-300nm respectively did not cause a significant cytotoxic effect towards Caco-2 and HepG2 cell lines but a moderate amount of DNA damage was measured through DNA strand breaks within the cells after exposure. *Brandts et al. 2022* Showed DNA damage after longer exposure of PS NPs with an average size of 44nm over 30 days. PS NPs were detected in goldfish liver and muscle with higher concentrations in liver than in muscle. There were no changes to the haematology parameters, cortisol and glucose levels in plasma. However, DNA damage was caused showing after long exposure the NPs can reach the nucleus and cause genotoxic effects.

This chapter will focus on the synthesis and testing of the potential biological hazards of these nanoplastics that are found in the environment due to plastic degradation by preparing model chemically and geometrically well-defined nanoparticle models for biological studies from commercially available plastic materials. Most studies look at polystyrene micron and nanoplastics and the damage caused to different cells. However, in this research, polystyrene nanoparticles will be synthesised from different sources to test for any additives within the plastics, such as organic and inorganic material, to improve the properties for the intended use. Some of the most common waste plastics found in the environment will be tested to gain a deeper understanding of the possible concerns raised by the public. The plastics which will be tested are polystyrene (PS) from beanbag filling and coffee cup lids, Polymethyl methacrylate (PMMA), which is commonly known as plexiglass, polyethylene (PE) and polypropylene (PP), which again account for a large amount of plastic waste found in the environment. Creating these model NPs will hopefully enable more precise biological analysis to understand the environmental and health impacts in well-controlled experiments. So far, extremely limited testing has been done on PMMA *(Mahadevan et al. 2021)* , PE *(Wang et al. 2022)* and PP (*Roursgaard et al. 2022)* for cell toxicity and wider biological responses and moreover only on one type of cell line, adding to the current research being carried out for a deeper understanding. The model plastic nanoparticles will be chemically synthesised through a dissolution and reprecipitation process, whereby a stabiliser will control the size of the plastic particles.

5.2 Plastic synthesis methodology

All plastics used in the synthesis were from common materials used in everyday life or commonly found as waste pollutants in the environment. Raw polystyrene (PS) was sourced from foam bean bag filling, and processed PS was sourced from commercial coffee cup lids to synthesise PS NPs. Polymethyl methacrylate (PMMA), also known as plexiglass, was sourced from cuvettes within the university. Polyethylene (PE) and Polypropylene (PP) were purchased from CD Bioparticles with the size range of 50-100 nm and dispersed in 0.1 % Tween 20 and the concentration of 1x10^{14} particles per ml.

5.2.1 Chemical synthesis of raw PS, PS coffee lid and PMMA nanoparticles

Dichloromethane (DCM) causes immediate damage to the plastics and DCM acts as a plasticiser to dissolve the polystyrene and PMMA. To dissolve the plastics in DCM, 25 mg of the plastics were added to 5 ml flask. 0.5 ml of DCM was then added to the plastic and it was magnetically stirred at 1200 rpm for 30 minutes until completely dissolved in the solution. After 30 minutes, 1 ml of a 5 % sodium dodecyl sulphate (SDS) solution was added dropwise and allowed to stir for one minute to form an emulsion. After one minute, the emulsion mixture is sonicated with a sonicating probe for two minutes to disrupt the emulsion and break any clusters of plastic particles to ensure a uniform distribution. During the reprecipitation and sonication, the DCM with a low boiling point of 39.6 °C will evaporate quickly at room temperature compared to water leaving residual amount of DCM in the solution.

The solution is then centrifuged at 12500 G for 10 minutes to collect a pellet of plastic NPs and redispersed in a 0.1 % Tween 20 solution. This process is repeated three times to ensure that all DCM and SDS is removed from the solution to a negligible amount. The washed plastics were then filtered through a 200 nm filter to obtain the smallest and narrow distribution of the nanoplastic.

5.3 Biological testing methodology

The model cell line used for the biological experimentation were MRC-5 cells. This is a diploid cell line made up of fibroblasts isolated from lung tissue that derived from a 14-week-old embryo in 1966 *(Voicu et al. 2015)*. These cells were obtained from American Type Culture Collection (ATCC). The cells were maintained routinely in Dulbecco's Modified Eagle's Medium (DMEM) media for cellular maintenance as seen Table 5.1. In each biological experiment, biological triplicates were carried out whereby the experiment was carried out three times to ensure that data is reliable and that there is no anomalies. This cell line is a widely used human model system for cytotoxicity and genotoxicity studies tested previously with multiple experimental and environmental agents *(Uemura et al. 2021)*.

Table 5.1: Cell Culture Media used for MRC-5 cell line.

Medium	**Culture Purpose**	**Medium Type**	**Medium Content**	**Medium Supplement**
DMEM	Cellular Growth	Dulbecco's Modified Eagle's Medium	high glucose, L-glutamine, sodium bicarbonate and without sodium pyruvate	FBS up to a final concentration of 10% (v/v) and penicillin (100 µg/ml)/ streptomycin (100 µg/ml) solution to a 1% (v/v) final concentration

5.3.1 Cell Culture maintenance

MRC-5 cells were routinely cultured in 25 cm^2 (T25) flasks in a humidified environment at 37 °C with 5 % carbon dioxide (CO_2) as standard conditions. The cells were incubated until they reached 90 % confluence (Where 90 % of the surface area of the 25 cm^2 flask is occupied by cells) , at which point they were passaged (whereby the cells are processed to occupy only 20 % of the flask surface area) inside a laminar flow hood [Envair Lab-VCS2-4, Lancashire, UK] under sterile conditions. For experimental settings, cells were used up to passage 40.

Seeding or passaging actions were performed after cells were detached by adding 2 ml of 1 % trypsin [Sigma-Aldrich, Gillingham, UK] and incubated for 5 minutes at 37 °C with 5 % CO_2. Neutralisation of trypsin was carried out with the cDMEM media. Briefly, 5 ml of fresh pre-warm cDMEM were added to the MRC-5 cells. The content was transferred into a 15 ml Falcon cell culture tube [Eppendorf #5702, Hamburg, Germany] and centrifuged at 200 g for 5 minutes. The supernatant was discarded, and the cell pellet was resuspended into fresh warm cDMEM medium to obtain the desired cell concentration per ml. 150’000 cells were seeded in each T25 for general maintenance. 5 ml of warmed cDMEM was then added to a T25 flask for maintenance.

5.3.2 Testing cell viability after plastic NPs exposure

To test the effects of the plastics on the MRC-5 cells, 75’000 cells were seeded in a 24 well plate with 0.5 ml of cDMEM and incubated overnight at 37 °C and a CO_2 concentration of 5 %. The next day, the media was removed, and fresh media was added with a plastic treatment making up 10 % of the media solution and again incubated overnight. Initially each plastic was tested at 100 % (2.79 x 10^{12} particles per cell) of its concentration as seen in Table 5.2 to identify if there are any effects at all in terms of cell death or decrease in cell growth from the treatment. In this experiment using 100 % of the concentration of the plastic solutions, a concentration of 2.79 x 10^{12} particles per cell were loaded onto the cells. The cells were then incubated overnight again using the same conditions. The next day, each well was counted. This was done by removing the media and washing the cells with 0.5 ml of PBS. The cells were then trypsinised with 0.2 ml of 1 % Trypsin (uplifting the cells from the surface of the flask) and incubating for 5 minutes. The Trypsin was then neutralised with 0.8 ml of cDMEM media. 20 µl of this solution was taken and a 1:1 dilution was carried out with a 1 % Trypan blue solution which would identify whether the cells were dead or alive. Healthy cells would not uptake the dye due to an intact cell membrane, but a dead cell would absorb the dye. A healthy cell has an intact cell membrane and stops the typan blue from entering the cell. However, a dead cell has damaged membrane which the trypan blue is absorbed by. The cells were counted using a haemocytometer and then calculated to identify quantity of living and dead cells. Within the haemocytometer, there are nine grids as seen from Figure 5.1. Sections A, B, C, D and E were counted for the cells that were dead and alive. To calculate the concentration in cells per ml, the equation 5.1 was used. The dilution factor was two as a 1:1 ratio of cells and trypan blue were mixed.Each test was compared to the control to identify cell viability under plastic treatment.

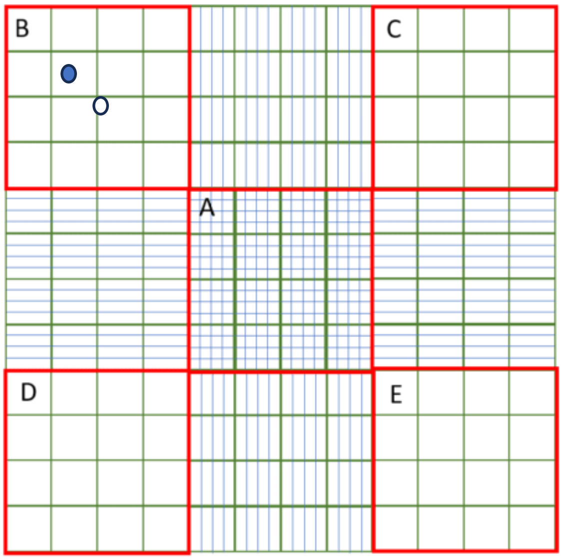

Figure 5.1: Diagram of a haemocytometer. (In quadrant B, an example of an alive cell (white) and a dead cell (blue) have been shown)

$$\frac{Cell}{ml} = \frac{Total\ cells\ counted \times dilution\ factor\ x\ 10'000 \frac{cells}{ml}}{Number\ of\ squares\ counted} \qquad \text{Eq 5.1}$$

Table 5.2: Treatments carried out for cell toxicity (concentration of 2.79 x 1012 particles per cell for plastic treatment and 10% dilution for 0.1 % Tween 20 solution).

Treatment - 2.79 x 10^{12} particles per cell	
1. Control – no treatment	5. Polystyrene coffee cup lid
2. 0.1 % Tween 20	6. Polypropylene
3. Raw Polystyrene	7. Polyethylene
4. Poly(methyl methacrylate)	

5.3.3 Concentration curve for plastic treatment

From the preliminary cell viability test with the different plastic treatments, it was found that the polystyrene coffee cup lid leads to significant cell damage / cell death with a single, relatively high, NP concentration so a dose-response experiments were set up to establish the concentration curve of the effect. The different ratios of NP per cell used in these tests are described in Table 5.3. The same experimental procedure was used as in 5.2.2 for the preliminary cell viability testing.

Table 5.3: Concentration curve plastic treatment on MRC-5 cells.

Treatment	Concentration (particles per cell)
Control	No treatment
Raw polystyrene	2.79 x 10^{12}
Poly(methyl methacrylate)	2.79 x 10^{12}
Polypropylene	2.79 x 10^{12}
Polyethylene	2.79 x 10^{12}
Polystyrene coffee cup lid 100%	2.79 x 10^{12}
Polystyrene coffee cup lid 50.00%	1.40 x 10^{12}
Polystyrene coffee cup lid 25.00%	6.98 x 10^{11}
Polystyrene coffee cup lid 12.50%	3.49 x 10^{11}
Polystyrene coffee cup lid 6.25%	1.75 x 10^{11}
Polystyrene coffee cup lid 3.13%	8.72 x 10^{10}
Polystyrene coffee cup lid 1.56%	4.36 x 10^{10}
Polystyrene coffee cup lid 0.78%	2.18 x 10^{10}

5.3.4 γH2AX foci Immunofluorescence analysis

The foci experiment is a immunostaining of a specific protein (y-H2AX) that finds the break on DNA and because there are many thousands of the copies of the protein sitting on the break it is possible visualise the breaks through foci. The γH2AX foci Immunofluorescence specifically looks for double-strand breaks in the DNA. These are key to analyse as double-strand breaks are the most difficult for the cells to repair *(Jeon et al. 2024)*. The following methodology was used to analyse the γH2AX foci Immunofluorescence:

For each experiment being carried out a 16 mm round glass coverslip was added to each well of a 24 well plate for the cells to grow on. To set up the experiment, 75’000 cells were seeded into 10 different wells of a 24-well plate with 1 ml of DMEM to test the plastics. The treatments carried out can be seen from Table 5.4.

Table 5.4: Treatments carried out for foci experiments.

Experiment	Treatment
1. Control	No
2. Positive Control	1Gy irradiation
3. Raw PS	2.79 x 10^{12} particles/cell
4. PMMA	2.79 x 10^{12} particles/cell
5. PE	2.79 x 10^{12} particles/cell
6. PP	2.79 x 10^{12} particles/cell
7. Coffee Lid 25 %	6.98 x 10^{11} particles/cell
8. Coffee Lid 12.5 %	3.49 x 10^{11} particles/cell
9. Coffee Lid 6.25 %	1.75 x 10^{11} particles/cell
10. Coffee Lid 3.125 %	8.72 x 10^{10} particles/cell
11. Coffee Lid 1.5 %	4.36 x 10^{10} particles/cell
12. Coffee Lid 0.75 %	2.18 x 10^{10} particles/cell

Once the cells had been seeded in the respective wells, the cells were left overnight to proliferate. This procedure requires the cells to be confluent to achieve the best results. The next day, treatments, other than the positive control were added to the cells. This was done by doing a 10 % dilution in the media. For example, for 1 ml of media, 0.1 ml of the plastic solution and 0.9 ml of the DMEM media to total 1 ml of solution. The cells were left overnight. The following day, photos were taken on the microscope to compare the differences between the treated and untreated cells.

The positive control was then irradiated with 1 Gy of radiation and all cells were kept on ice to minimise the amount of repair the cells do. In order to fix the cells to the coverslip, 1 ml of ice cold 1:1 acetone:methanol mixture was added to the cells and left on ice for 15 minutes. After 15 minutes, the cells were gently washed with 1 ml of PBS three times. To extract the DNA for analysis, 1 ml of chilled pre-extraction buffer was added to each well for 7 minutes and incubated on ice. After this step the ice was discarded and all steps here on are done at room temperature. The cells are then washed with 1 ml of PBS three times to ensure all pre-extraction buffer is removed. 1 ml of 10 % protein blocking solution (0.1 ml of fetal bovine serum (FBS) and 0.9 ml PBS) was added to each well and placed on the rocking platform at speed 25 rpm for one hour at room temperature. The cells are then washed again three times with 1 ml of PBS.

0.15 ml of the primary antibody solution containing 2 µL of mouse antibody, 980 µL of PBS and 18 µL of FBS, was added to each well and incubated again on the rocker platform at speed 25 RPM overnight in a cold room at 4 °C. The cells were washed three times with 1 ml of PBS. Between each wash the plate was put on the rocker at a speed of 25 rpm at room temperature for 5 minutes. 0.15 ml of the secondary antibody solution containing 2 µL of goat anti mouse antibody, 980 µL of PBS and 18 µL of FBS,was added to the cells for one hour and kept in the dark on the rocker plate at speed 25 rpm. The cells were kept in the dark after adding the secondary antibody as the fluorescence diminishes in the light. The cells were then washed three times with 1 ml of PBS with 5 minutes between each wash on the rocker plate at speed 25 rpm. The PBS was also removed in the dark.

The cells were then mounted onto a microscope cover slide by 10 µL of Vectashield which mounts the cover slip to the slide and introduced a blue 4′,6-diamidino-2-phenylindole (DAPI) staining. The cover slips are then left in the dark for 1 hour for the Vectashield to dry. The slips are sealed around the edges with clear nail varnish and left for 15 minutes to dry. Afterwards, images were taken on a fluorescent microscope and the number of Foci were counted and analysed.

5.3.5 Cell cycle experiment

The cell cycle is a complex process that cells go through to grow, proliferate, regulate DNA damage (regulate the repair of DNA damage), and deal with diseases like cancer. For the cells to go through the cell cycle phases, numerous proteins are required to direct the cells through the specified sequence, as seen in Figure 5.2 *(Schafer, 1998)*. The critical proteins that guide the cells through the cycle are the cyclin proteins that regulate the cells through the different phases of G1/G0, S, G2 and M phase *(Williams et al. 2012)*. G1 and G2 are predominantly growth phases for the main two stages of the S phase, where a second copy of the DNA is synthesised and then mitosis, where the two daughter cells are produced.

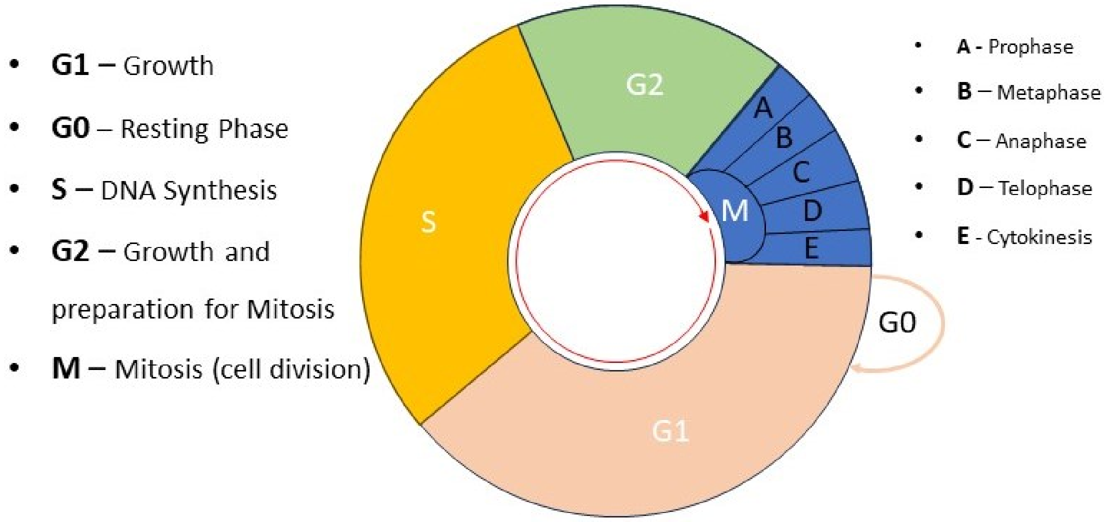

Figure 5.2: Phases of the Cell cycle. Adapted from (Leal-Esteban et al. 2020)

If the cells are damaged by a treatment carried out, the cells repair the damage before moving to the next stage of the cell cycle. The two main phases, S and M would be delayed and lead to a delay in moving into G1 and G2 respectively. Whereas the healthy control cells would progress through the cell cycle normally with no delays. Multiple timepoints are required to see when the delay begins and when the repair is fixed and the cells start to cycle again. However, in this experiment, one time point was used to see the differences after 6 hours from treatment. In order to analyse the phase of the cell cycle the cells are in after plastic treatment, the following method was used:

In this experiment, cells are required to be exponentially growing to ensure that most of the cells are actively cycling whereby the cells are moving through the different phases of the cell cycle (G1, S, G2, M) to proliferate. Initially 400’000 cells were seeded in a T25 flask with 4 ml of DMEM and left overnight to incubate. The next day, the cells approximately double to 800’000 cells and the necessary treatments were added to each flask and left for 6 hours as seen from Table 5.5. The treatment was added in a 10 % dilution to 3 ml of media. The cells are incubated at 37 °C and 5 % CO_2.

Table 5.5: Treatments carried out for cell cycle experimentation.

Experiment	Treatment (particles / cell)
Control	N/A
Coffee lid 12.5%	4.36×10^5
Coffee lid 6.25%	2.18×10^5
Coffee lid 3.125%	1.09×10^5
Coffee lid 1.5%	0.55×10^5
Coffee lid 0.75%	0.27×10^5
PS	3.49×10^6
PMMA	3.49×10^6
PE	3.49×10^6
PP	3.49×10^6

After 6 hours, the DMEM is removed and 3 ml of fresh DMEM containing 20 mM of bromodeoxyuridine (BrdU) is added to each flask and left for 20 minutes in a humidified chamber. The cells are then uplifted from the T25 flask by adding 2 ml of trypsin for five minutes in a humidified chamber. The trypsin is then neutralised by adding 5 ml of DMEM and the cells are spun down at 200 RCF for five minutes and the media discarded to leave the pellet of cells at the bottom of the Eppendorf tube. 1 ml of PBS was added to the pellet and resuspended and moved into a 1.5 ml tube and spun down again at 200 RCF. The PBS is then discarded and 40 µl of fresh PBS is added and resuspended. To this, 1 ml of ice-cold ethanol is added dropwise while gently vortexing the cells to avoid clumping. The cells are then stored at -20 °C.

After the 48 hours, the cells are centrifuged at 200 relative centrifugal force (RCF) for 5 minutes and the ethanol is removed, and the cells resuspended with 1 ml of PBS to wash and remove all the ethanol. The cells are centrifuged again and resuspended in 1 ml 2 M HCl containing 0.1 % pepsin and left at room temperature for 20 minutes. After 20 minutes, 0.5 ml of PBS is added to the mixture and centrifuged again at 200 RCF for 5 minutes. The solution is discarded and cells resuspended in 0.5 ml of PBS and centrifuged again. The PBS is discarded and cells resuspended in 0.1 ml of PNT [PBS containing 0.5 % normal goat serum and 0.5 % tween 20] and anti-BrdU antibody [1:50 ratio of PNT to antibody]. Leave at room temperature for 60 minutes, after which 1 ml of PBS was added and mixture gently vortexed. The cells are then centrifuged at 200 RCF for 5 minutes. The solution is discarded and cells resuspended in 1 ml of PBS after which the cells are centrifuged again. The cells are resuspended in 0.1 ml of PNT containing the secondary antibody [1:50], AlexaFluor 488 conjugated goat-anti-mouse secondary antibody and leave in the dark for 60 minutes. The cells are centrifuged and then washed twice with 1 ml of PBS before being resuspended in in 0.5 ml of PBS containing 20 µl /ml propidium iodide and then analysed using a Coulter Elite flow cytometer using UV and 488 nm lasers for excitation in order to measure the fluorescence of the cells which are in different phases. Gating is used to analyse the cells of interest and remove the debris signals. In Figure 5.3A, the area below the red line are the debris of cells or other contaminants that do not need to be analysed and been removed from the analysis. Above the red line is the nuclei generated signals. In Figure 5.3B, within the red area are the singlet cells that have passed the flow cytometer laser as single cells and not clumps which could effect the analysis. This ensures the cells being analysed represent a single cell population. From excluding the unwanted cells in Figure 5.3A and B, the Figure 5.3C can be produced which analyses the cells in each of the cell cycle phases. R1 is all the cells that have been positively stained, R2 is all the cells in the G1 phase, R3 are the cells in the S phase and R4 are the cells in the G2/M phase.

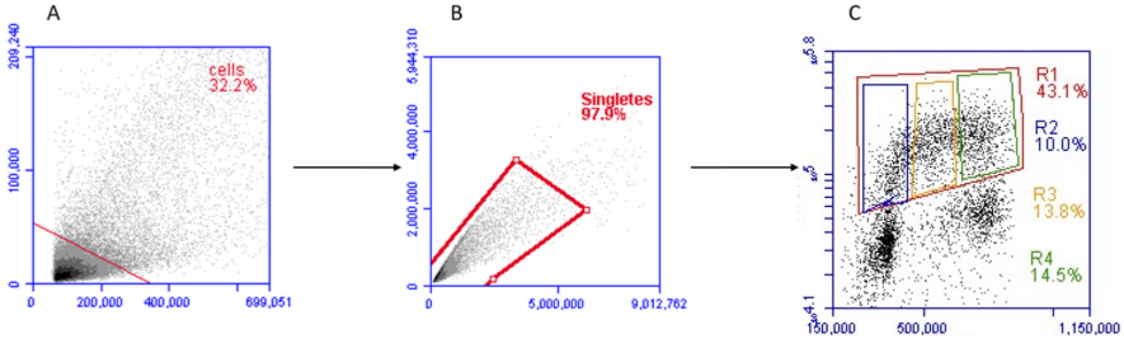

Figure 5.3: Example gating of A – Cells from Debris (debris below red line), B – Singlets from doublets (singlets within red area) and C – Cell Cycle data obtained from gating (R1 – all positively stained cells, R2 – G1 cells, R3 – S phase cells, R4 – G2/M cells) .

5.3.6 Apoptosis analysis

The kit used for this experiment was an Annexin V (AV)/Propidium Iodide (PI) kit. (Biolegend). This kit contains the Annexin V and Propidium Iodide required for the experiment to get positive results on apoptosis. AV binds to negatively charged phospholipids which are produced by cells that are in apoptosis and PI binds to the DNA but can traverse into cells with intact cell membranes.

The MRC-5 cells were seeded in a 6 well plate at a seeding density of 300’000 cells per well with 2 ml of DMEM and incubated overnight. The next day, the treatments were added to the cells where the DMEM was diluted by 10 % and then incubated overnight. Initially to test that the kit and dyes used are working correctly several controls were carried out. The tests carried out can be seen from Table 5.6.

Table 5.6: Treatments carried out for Apoptosis experiment.

Experiment	Treatment
Control 1	No staining
Control 2	AV only stained
Control 3	PI only stained
Control 4	AV and PI stained
Positive control	Ethanol
Control	No Treatment
PS	1.5×10^7 particles per cell
PMMA	1.5×10^7 particles per cell
PE	1.5×10^7 particles per cell
PP	1.5×10^7 particles per cell
Coffee lid 25 %	1.89×10^6 particles per cell
Coffee lid 12.5 %	9.43×10^5 particles per cell
Coffee lid 6.25 %	$4\ .71 \times 10^5$ particles per cell
Coffee lid 3.125 %	2.36×10^5 particles per cell
Coffee lid 1.5 %	1.18×10^5 particles per cell
Coffee lid 0.75 %	5.89×10^4 particles per cell

After the treatment the DMEM was discarded and cells washed with 1 ml of PBS followed by incubation with 1 ml of trypsin for 5 minutes until the cells have been uplifted. The trypsin is then neutralised with 3 ml of DMEM and centrifuged at 200 RCF for 5 minutes. The media is discarded and the pellet is resuspended in 1 ml of PBS to wash the cells before centrifuging again at 200 RCF. The PBS is discarded and the cells are resuspended in 1 ml of binding buffer and centrifuged once again. The cells are then resuspended in cold binding buffer and counted to ensure the concentration is at least 1×10^6 cells/ml. Enough of the suspension was taken so that 250’000 cells were collected and transferred to the to a different tube for staining.

5 µl of AV and PI were added to the cells and then vortexed gently for 2 seconds. The cells were then incubated for 15 minutes in the dark. To the solution, add fresh binding buffer to top up the tube to a total of 500 µl and mix up and down to get a uniform distribution. The samples can then be run on the flow cytometer to obtain a minimum of 10’000 events.

The initial gating strategy involves plotting all events according tothe singlets vs the debris.. Events are then sorted as Annexin V-FITC vs PerCPcy5-5 for PI stain which are the signals used for the specific kits dyes provided for the florescence. To generate a cell population without debris, Figure 5.3A shows that gating required. The red area is the selection of singlet cells that have passed through the laser beam as singlets. The area outside the red zone are of debris which would give negative results for apoptosis. In Figure 5.3B, four different gating boundaries were applied: necrotic cells, late apoptosis, live cells and early apoptosis. On the X-axis, which displays the annexin-V shows when there is an increase in apoptosis, there is more binding of the annexin-V to negatively charged Phospholipids like phosphatidylserine which is induced when the cells start to enter apoptosis. Propidium iodide binds to DNA. However, it cannot traverse into the cells. Healthy alive cells will not uptake the fluorescent molecule due to having an intake membrane. But, as the cells enter late apoptosis and necrosis, there is damage to the membrane wall leading to the propidium iodide binding to the DNA giving a signal. A representative gating and analysis of the four different boundaries is displayed in Figure 5.4.

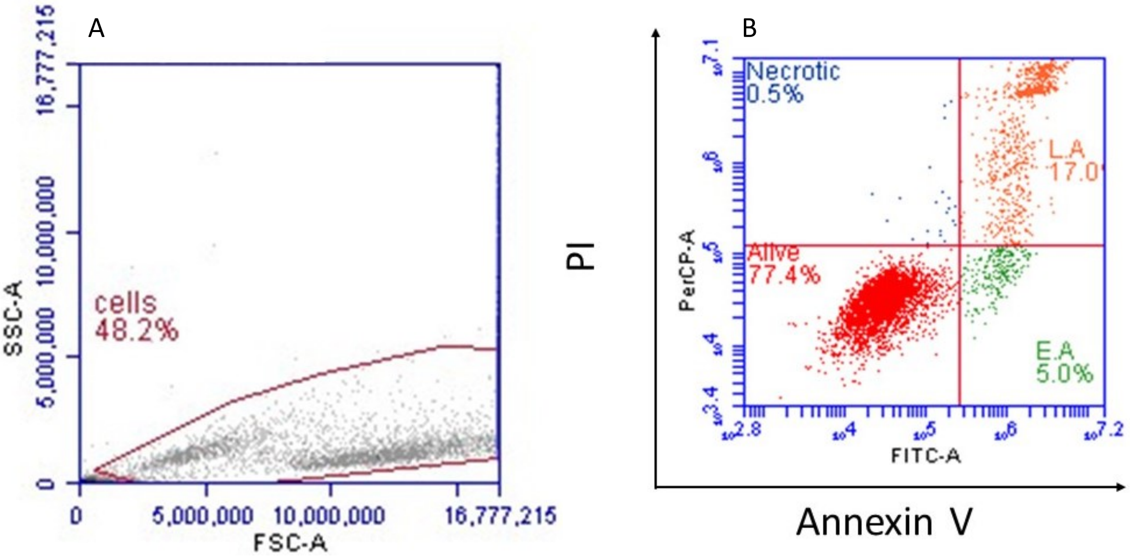

Figure 5.4: Example gating of A – to select singlet cells (within the red area is the singlets, outside is debris), B - Representative diagram of annexin V staining vs PI quadrants. (Events were plotted according to AV vs PI to exclude debris. Cells that are in apoptosis will give a positive result for AV. Cells that are healthy will give negative results for both AV and PI.).

5.4 Characterisation

5.4.1 SEM / EDX

Scanning electron microscopy and energy-dispersive X-ray spectroscopy (SEM/EDX) analyses were conducted using a Quattro SEM (Thermo Fisher Scientific, USA). As the plastic materials being analysed are non-conductive, the samples were loaded onto an aluminium stub with copper tape to help dissipate the charge buildup. To avoid damage to the sample and higher focus upon capturing an image high vacuum was used with a 5 kV acceleration voltage to balance resolution with charge buildup. The spot size used was 3 µm while using an Everhart–Thornley detector (ETD) and looking at SE which have been ejected from the material.

5.4.2 DLS

DLS was carried out with a Nanolive Zetasizer using water as the solvent. The operating parameters of refractive index (1.33) and viscosity (1.0) were set to water values which were already stored in the Malvern software. For each sample, five runs were carried out to compare the stability within the sample from each run. The equilibrium time between each run was set at 2 minutes. The refractive index of the material was set at polystyrenes RI of 1.59.

5.4.3 XRF

Wavelength-Dispersive X-ray Fluorescence (WD-XRF) spectroscopy was conducted at the University of Warwick X-Ray Diffraction Research Technology Platform (RTP) using a Rigaku Primus IV system, equipped with a 4 kW Rh tube. Samples were analysed as solids under a 10mm mask, using an ‘EZ Scan’ protocol which performs an element sweep from B-Cm. Elemental compositions were calculated in a semi-quantitative manner via the Fundamental Parameters (FP) method using intensity libraries derived from standards analysed by the instrument manufacturer. The elemental compositions are reported as mass % for major components and ppm for minor ones, with a relative error of approximately 5 % between samples.

Access was granted through the Warwick Analytical Science Centre (WASC) Seedcorn Access Program, funded under grant EP/V007688/1.

5.4.4 XRD

The crystallographic information of the plastics was obtained via X-ray diffraction (XRD) using a Rigaku Miniflex X-ray diffractometer. The XRD patterns were acquired using Cu radiation at 40 kV and 15 mA in the range 3–90 2ϴº. The XRD patterns were used to relate to elemental composition but not used to identify the materials present. Many materials have very similar XRD patters due to having similar lattice structures. Each sample was cryogenically milled to form a powder and loaded into a holder and levelled. During the analysis, the software identified compounds that most likely match the spectra produced. The data was related back to the SEM and XRF to identify which peaks are most likely caused by the compounds present.

5.4.5 NMR

Proton Neutron Magnetic Resonance (^{1}H NMR) was carried out on a Magritek Spinsolve 60 MHz device using the proton protocol which is built into the spinsolve software. Before running the samples a check shim was carried out, followed by a shim using a deuterated water sample to eliminate inhomogeneities in the magnetic field. All the samples were analysed in non-deuterated H_2O due to the analysis being carried was for the purpose of identifying if waste products were present in the final product whose peaks did not overlap with the water peak. A fast scan was used for the analysis as it provided high enough resolution for the intended use.

Solid-state NMR experiments were carried out at room temperature using a Bruker Avance Neo spectrometer. ^{13}C cross polarisation (CP) MAS was achieved by using a 90-100% amplitude ramp34 on 1H. SPINAL-6435 1H decoupling at a nutation frequency of 100 kHz was applied during an acquisition time of 30 ms. ^{13}C chemical shifts are referenced with respect to tetramethylsilane (TMS) via L-alanine at natural abundance as a secondary reference (177.8 ppm for the CO ^{13}C resonance) corresponding to adamantane at 38.5 ppm (13C).

Access was granted through the Warwick Analytical Science Centre (WASC) Seedcorn Access Program, funded under grant EP/V007688/1.

5.4.6 FTIR

Fourier-transform infrared spectroscopy (FTIR) was carried out on a Perkin Elmer Frontier FTIR using an ATR accessory which was a GoldenGate ATR with a ZnSe crystal. A background was taken with no sample present to ensure as much noise is removed from the spectra. For this analysis the number of scans used was 8. All data collected was normalised for comparison.

5.4.7 NFCM

The Nanoanalyzer flow cytometer (NanoFCM) is equipped with 488 nm and 640 nm lasers, along with single-photon counting avalanche photodiode detectors. Manufacturer-recommended laser settings and bandpass filters (SSC-488/10) were implemented. Side scatter-based triggering enabled the detection of nanoparticles larger than 40 nm in diameter. Each sample was analysed for 1 minute, collecting approximately 10’000 events at a sampling pressure of 1.0 kPa to maintain an optimal event rate. To determine particle concentration, a 250 nm silica bead standard (NanoFCM Inc., 250 nm Std FL SiNP) was used to calibrate the flow rate.

5.4.8 XPS

The examination was conducted by means of X-ray Photoelectron Spectroscopy (XPS). This involves irradiating a sample with X-rays of a characteristic energy causing photo electrons to be ejected with a range of energies depending on the element from which they are emitted and the chemical state of that element. The emitted electrons are then collected and transferred through apertures and focused onto an energy analyser entrance to be sorted by their energies. From this electron energy identification, XPS provides information on the elements present at a sample surface and their chemical and bonding states. Under the conditions of this analysis, XPS gives quantitative information on all elements excluding H and He at a detection limit of 0.1%.

XPS analysis was conducted in a Thermofisher ESCALAB 250 electron spectrometer equipped with a hemispherical sector energy analyser at source excitation energy of 15 KeV and emission current of 6 mA; analyser pass energy of 20 eV with step size of 0.1 eV and dwell time of 50 ms were used throughout the experiments. The base pressure within the spectrometer during examinations was always better than 5 x 10^{-10} mbar and this ensured that all signals recorded were from the sample surface. In all samples the analysed area was 500 mm diameter.

5.4.9 Thermogravimetric Analysis

TGA analyses were carried out in a Mettler Toledo TGA/DSC 2 STA system using nitrogen as an inert atmosphere with a flow rate of 40 mL min^{-1}. 0.5 g of each sample were used for the analysis. Under nitrogen conditions, the temperature of the furnace was held at 30 °C for 5 minutes before increasing the temperature to 600 °C at a rate of 10 °C / minute. The temperature was then held at 600 °C for 2 minutes to ensure stabilisation of the scales. The sample was then further heated from 600 °C to 950 °C at a rate of of 40 °C / minute and then held there for 5 minutes before allowing to slowly cool down. Measurements were recorded and compared for any drops in weight at specific temperatures to identify compounds within the plastics.

5.5 Results & Discussion

5.5.1 Synthesis and particle size

A more detailed study was carried out to understand the effects of SDS concentration on plastic particle size. Several different concentrations of SDS were used. Table 5.7 displays that in general as the surfactant's concentration increased, the PS NPs' size decreased, and the standard deviation of the particles also decreased in general. It is hypothesised that if the surfactant was continually increased, this would start to have a detrimental effect on the particle size due to the viscosity inhibiting the movement or the particles and a higher chance of coalescence meaning there is an optimal amount of stabiliser for particle size. With the higher amount of surfactant, there is more stabiliser to cap and protect the plastic particles from aggregation. Reprecipitation of the particles took place by increasing the water content of the solution, which the plastics are not soluble in, to reduce the concentration of the DCM leading to the reprecipitation with SDS stabiliser present.

Table 5.7: Polystyrene experimental data at different SDS concentrations.

Experiment	Plastic	SDS Concentration (%)	Particle size (nm)
PS-1	Polystyrene	5.00	52.62 ± 18.71
PS-2	Polystyrene	2.50	115.0 ± 42.43
PS-3	Polystyrene	1.25	168.4 ± 74.45
PS-4	Polystyrene	0.75	139.4 ± 54.85
PS-5	Polystyrene	0.25	187.2 ± 66.49

Figure 5.5 displays the DLS graphs where the shift in size distribution and the standard deviation of the peak is increased as the SDS concentration decreased. In all cases, the polydispersity index (PDI) for the DLS data was less than 0.1, suggesting a narrow distribution and more reliable data.

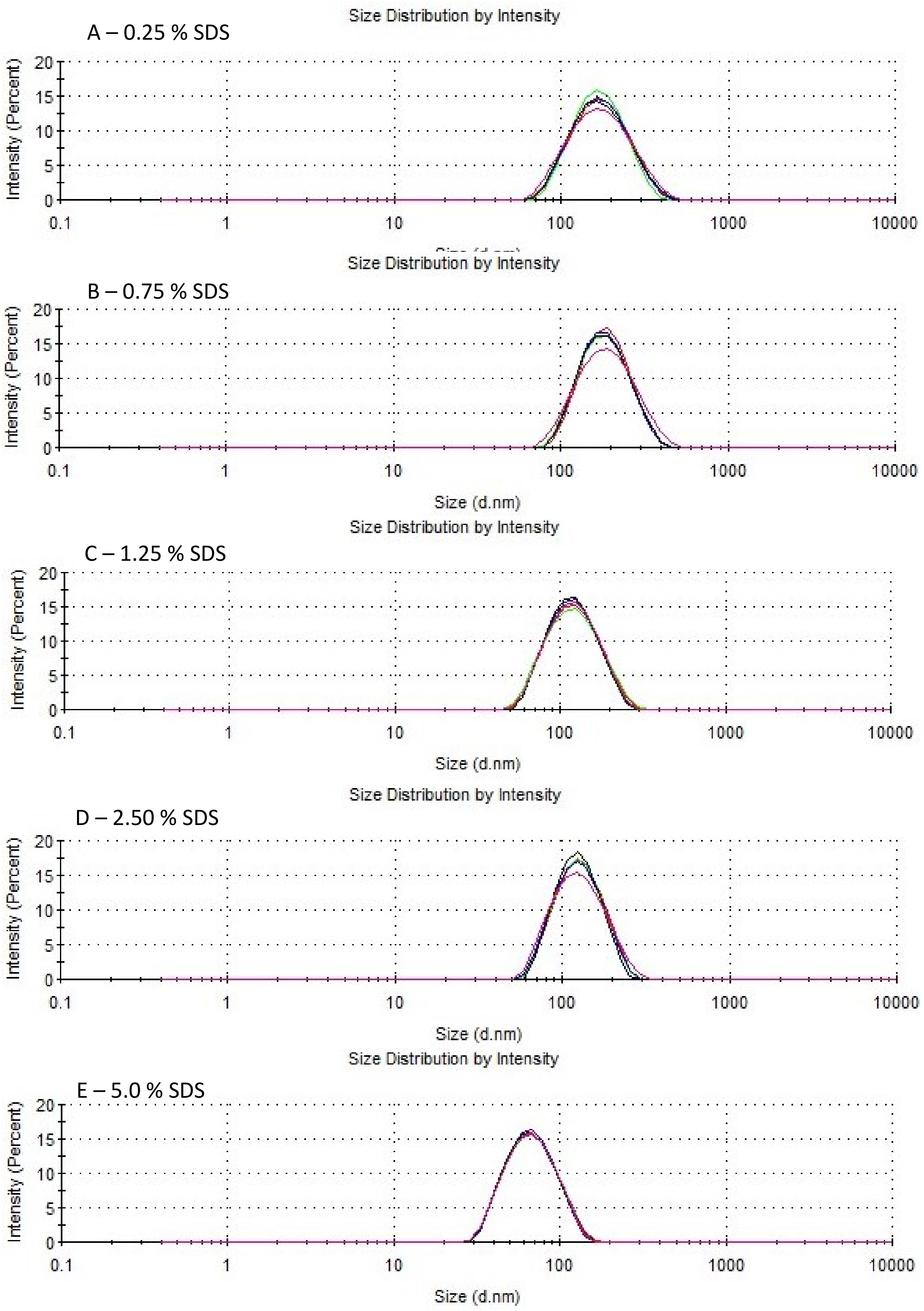

Figure 5.5: DLS size distribution of PS NPs synthesised with different amount of SDS. A – 0.25 %, B – 0.75 %, C – 1.25 %, D – 2.5 %, E – 5 %.

The data obtained from the DLS data was plotted in Figure 5.6 to visualise the trend of the SDS concentration on plastic particle size. A trend is clear in the size of the particle synthesised with different amounts of SDS stabiliser. The size of the particles reduces with the amount of stabiliser used. A key observation is that the more stabiliser used, the narrower size distribution acheived. From the data obtained from the concentration curve, all synthesis experiments were carried out with an SDS concentration of 5 %.

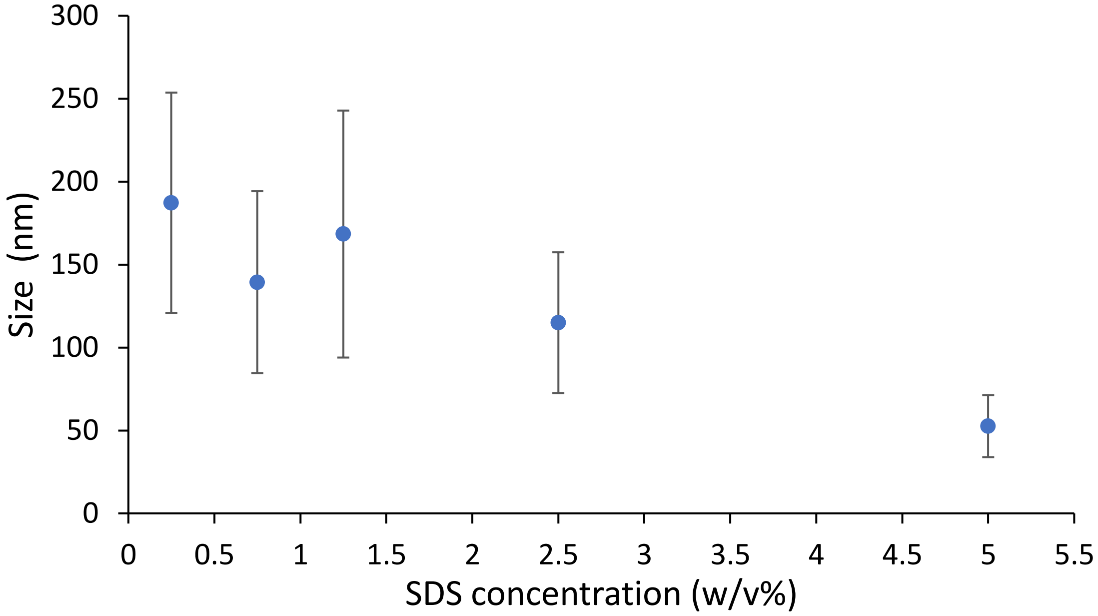

Figure 5.6: Particle size trend with changing SDS concentration.

The PS NPs from the coffee lid and the PMMA NPs from the cuvettes were synthesised using 5 % SDS. Table 5.8 displays the conditions used and particle size distribution of these two samples. The PS NPs from Coffee lids have a small size distribution and size less than 100 nm. Using the same reaction conditions for PMMA, a larger plastic NP is produced with a wider size distribution as seen in Figure 5.7. A reasoning for this is that the PMMA chemical structure does not bind as effectively with the SDS offering poor stabilisation when compared to PS leading to a greater amount of agglomeration.

Table 5.8: Reaction conditions and particle size distribution of PS coffee lids and PMMA.

Experiment	Plastic	SDS Concentration (%)	Particle size (nm)
Coffee-1	Polystyrene	5.00	85.81 ± 27.77
PMMA-1	PMMA	5.00	233.4 ± 94.28

A – PS Coffee lid

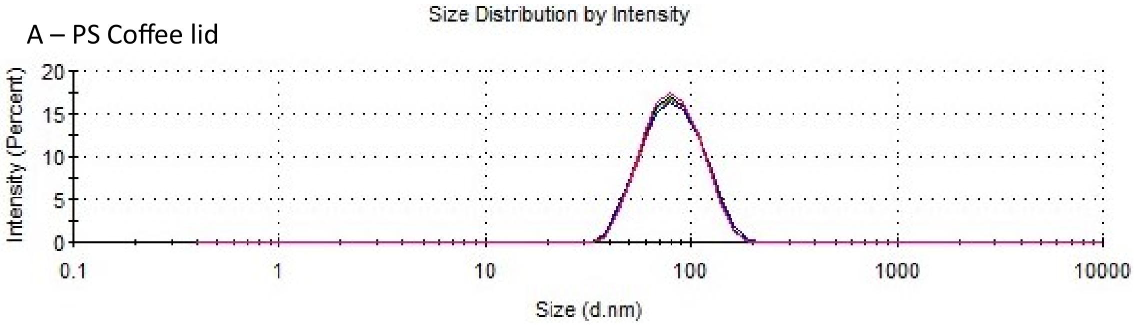

B – PMMA

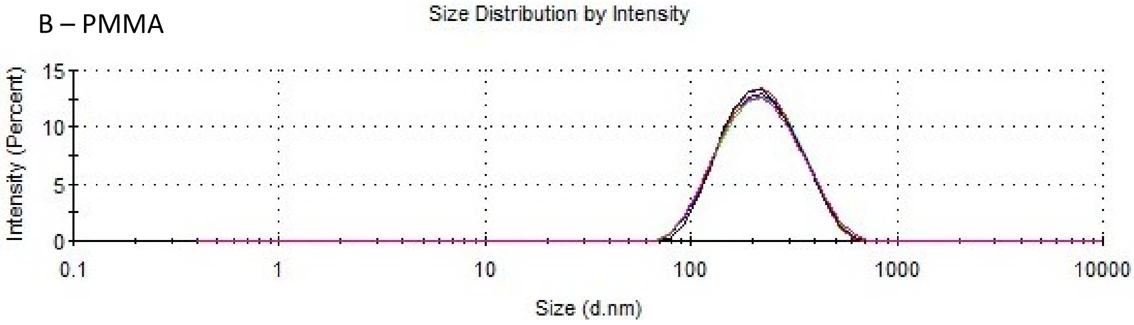

Figure 5.7: DLS Graphs of A –Coffee cup lids, B – PMMA.

For biologial testing, it is necessary to know the concentration of particles per cell to understand whether the particle concentration per cell causes different responses. Nanoflow cytometry (NFCM), was carried out on the samples to find the concentration per ml and compare size distribution data to the DLS. Spherical silica nanoparticles with a size up to 200 nm was used as the standard. As the standard sample is up to 200 nm, the equipment cannot read any sizes larger than 200 nm.

In Figure 5.8, the size distributions and particle concentration can be seen. From the synthesised plastics, the raw PS and the coffee lid have a similar size distribution of 93.2 nm and 85.8 nm respectively, with only a small percentage greater than the limit of 200 nm. This data closely resembles the data obtained via DLS. The sizing data obtained across multiple analytical techniques is reliable. The PMMA appears to have two size distributions from the data. One at 70 nm, and then one which starts at the limit of the equipment at 200 nm, which is expected to continue to approximately 400 nm. In this case, the DLS and NFCM data align with the results. The two plastics purchased, PP and PE, have a narrow distribution, with an average particle size of 42.9 and 53.2 nm, respectively.

A - Raw PS

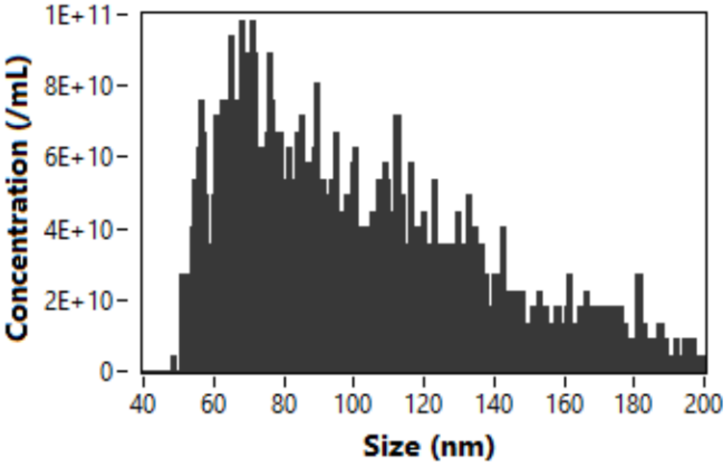

Size Information:

Median: 93.2 nm

Mean: 100.6 ± 34.2 nm

Concentration Information:

9.05 x 10^{12} particles / ml

B – Polystyrene Coffee Lid

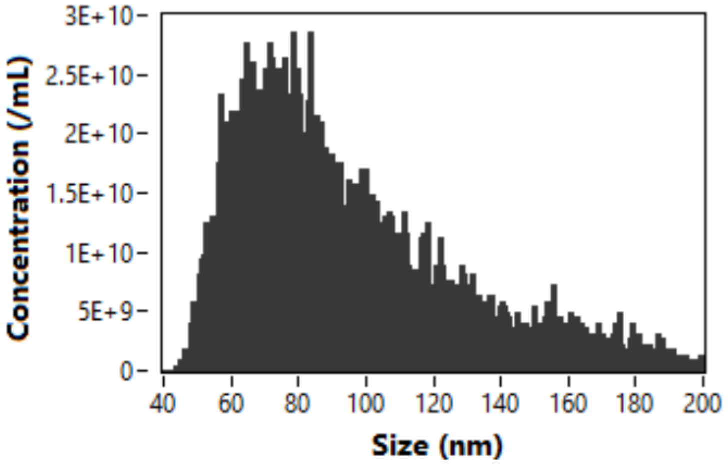

Size Information:

Median: 85.8 nm

Mean: 94.1 ± 32.4 nm

Concentration Information:

2.79 x 10^{12} particles / ml

C - PMMA

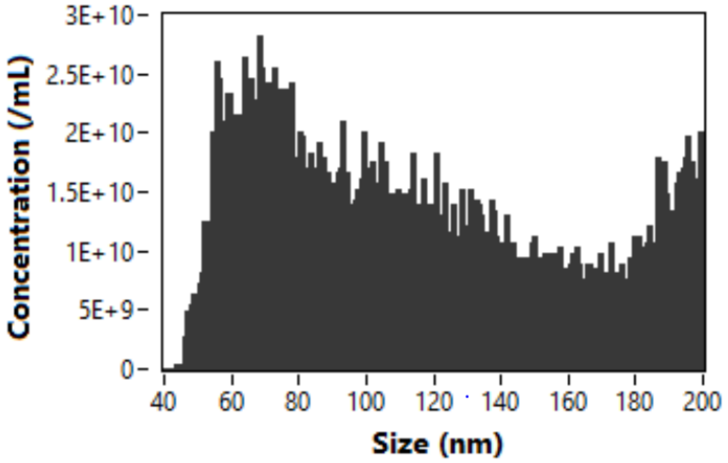

Size Information:

Median: 109.2 nm

Mean: 117.6 ± 46.6 nm

Concentration Information:

4.08 x 10^{12} particles / ml

D - PE

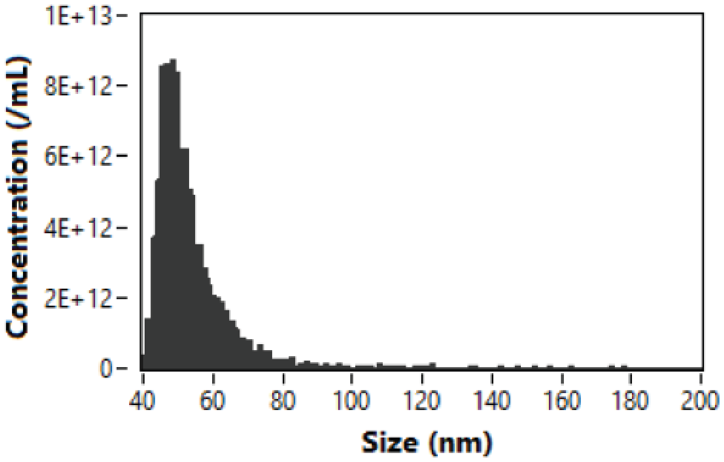

Size Information:

Median: 50.8 nm

Mean: 53.2 ± 10.1 nm

Concentration Information:

2.07 x 10^{14} particles / ml

E – PP

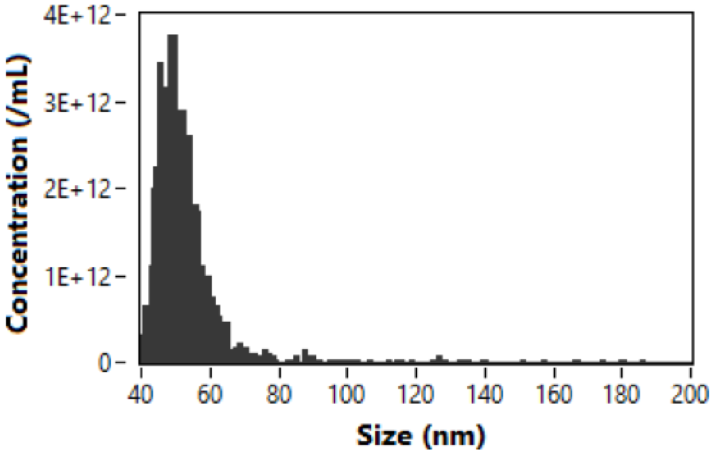

Size Information:

Median: 50.8 nm

Mean: 42.9 ± 12.3 nm

Concentration Information:

8.29 x 10^{13} particles / ml

Figure 5.8: NFCM data for A – Raw PS, B – Coffee lid, C – PMMA, D – PE, E- PP.

The concentration of particles per ml is an essential data set for understanding how many particles are loaded per cell. The raw PS, PMMA, and coffee lid samples, the particle concentration above 1 x 10^{12} particles per ml. which can be used for cell biology to test for toxicity damage. The particle concentration of PP and PE extremely high of 8.29 x 10^{13} and 2.07 x 10^{14} particles per ml respectively. Both sets of data align closely with the supplier's datasheet. The coffee lid has the lowest concentration of 2.79 x 10^{12} particles per ml, all other samples for preliminary cytotoxicity testing will be diluted to the same concentration to maintain uniformity.

SEM was carried out on the plastics to compare the results from DLS and NFCM. The SEM images can be found in Figure 5.9. From Figure 5.9A, the size distribution of the raw polystyrene shows a size distribution from 500 nm to 50 nm, closely resembling the DLS data obtained in Figure 5.5E. During the SEM imaging, a small amount of sample was distributed on copper tape to minimise the charge buildup from the electron beam.

Drying the sample out will lead to agglomeration and the size of the particles in the solution would be more uniform compared to the dried-out sample.

Figure 5.9B and C of the coffee lid and PMMA show a more uniform distribution of particle sizes, which appear between 100 and 200 nm. This follows the DLS data in Figure 5.5 for the two plastics. However, the PMMA in both the DLS and NFCM there is a broader range of sizes. This is not apparent in the SEM imaging and a narrow size distribution. This difference in sizes can be accounted to the DLS using light to scatter the particles. In cases where the several small NPs have agglomerated together would give a signal in DLS for the agglomerate rather than the individual particles.

Since the particles were synthesised chemically via dissolution and reprecipitation, the particles are uniformly spherical. This is a difference that is noted from plastics which have degraded in the enivronment that would have an amorphous structure from shearing effects. This needs to be taken into consideration as shape effects may play a significant role cell damage.

A - Raw PS

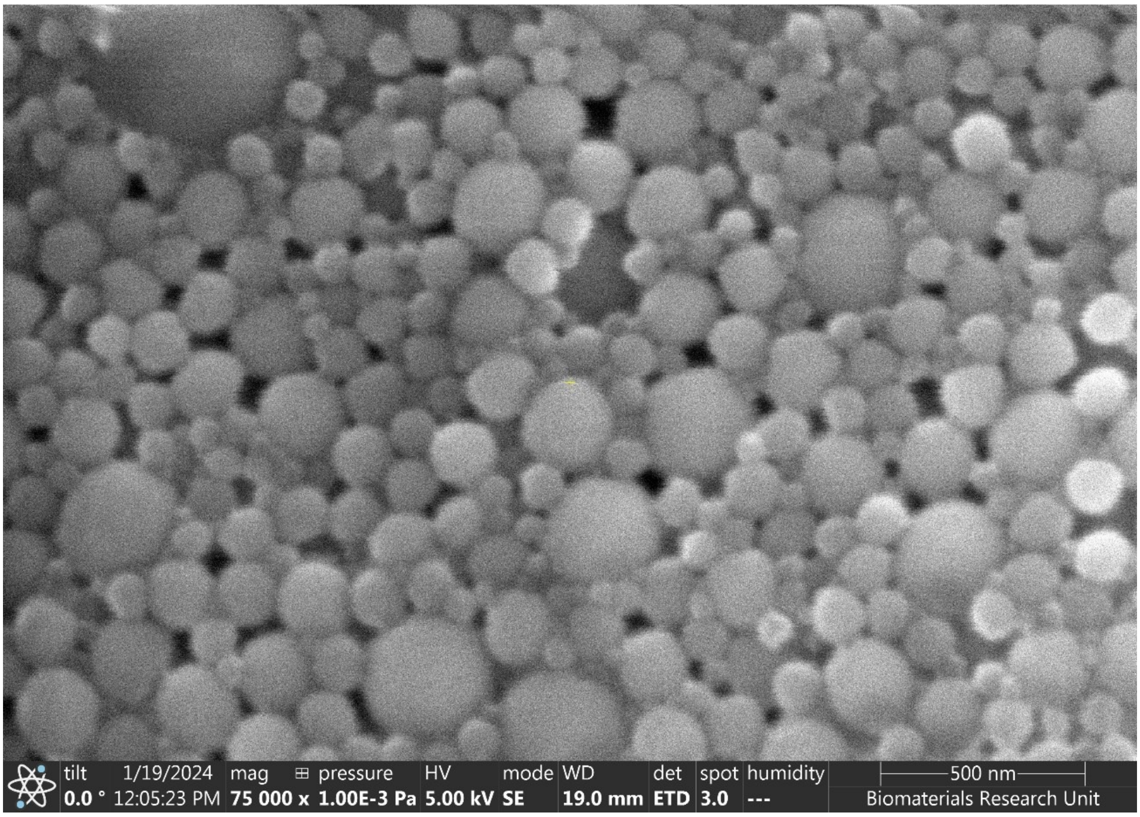

B - Coffee Lid

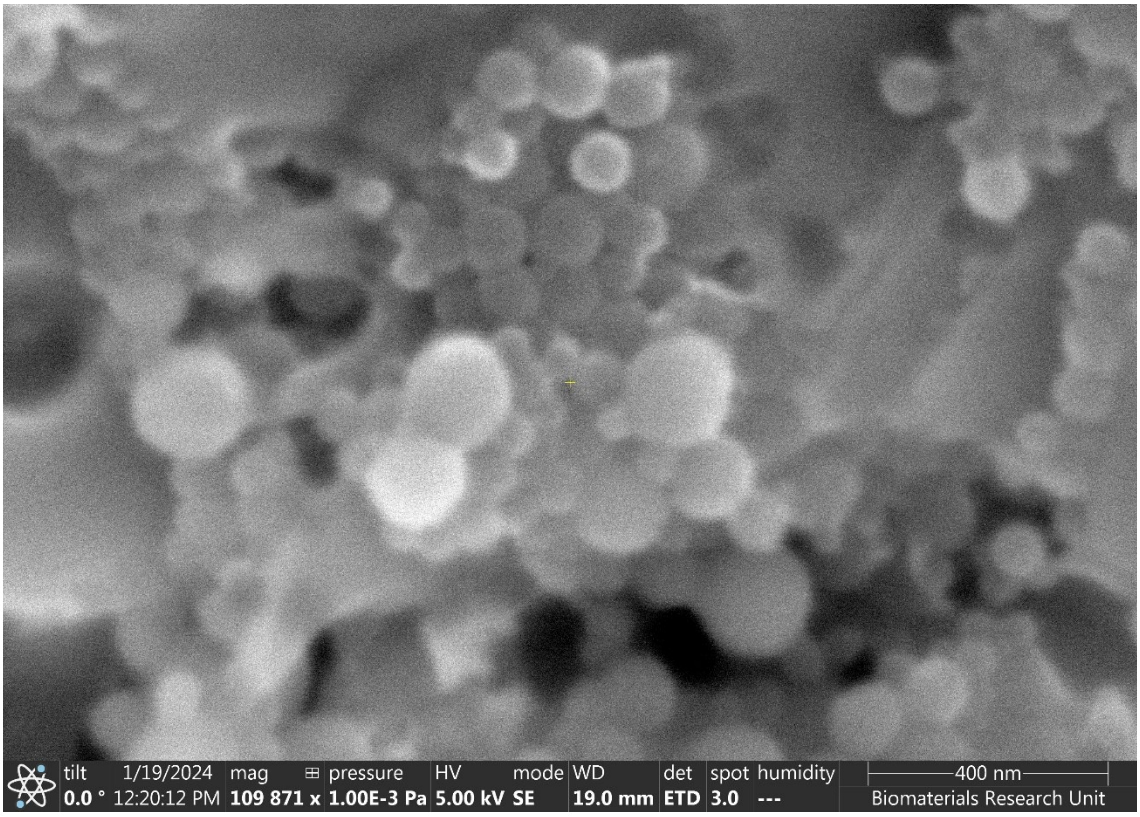

C - PMMA

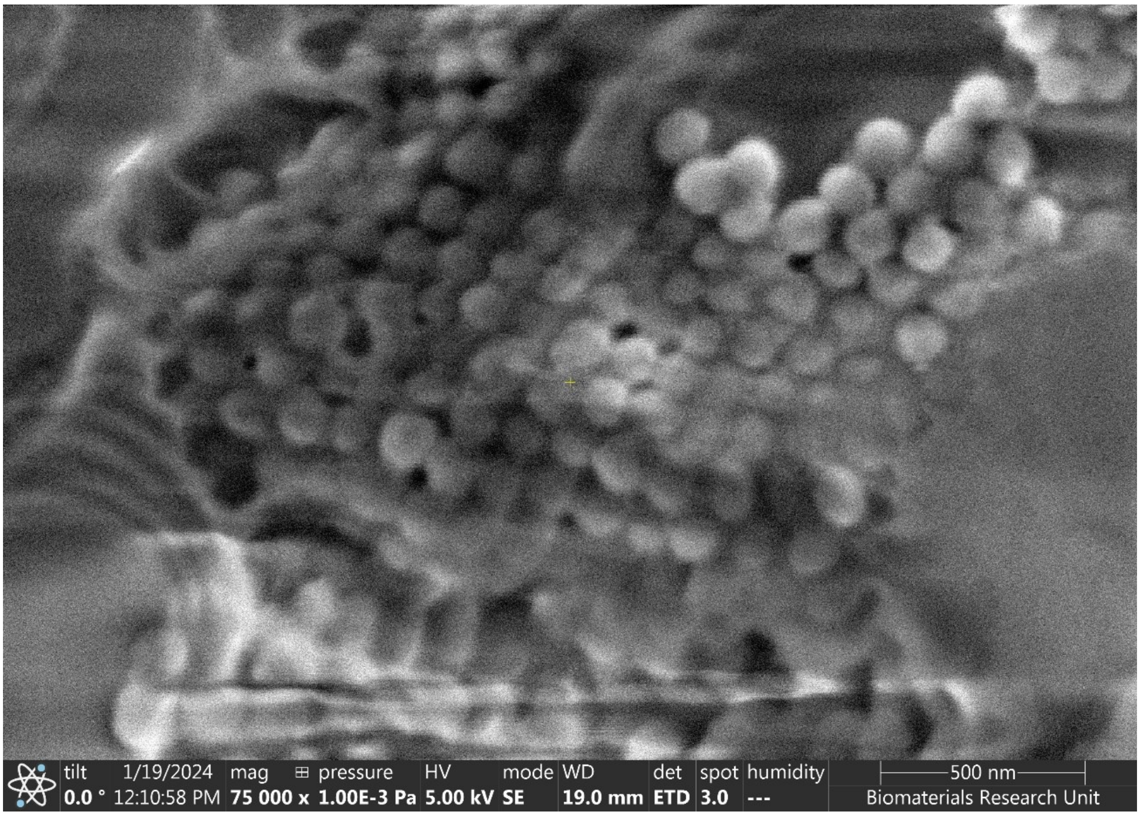

Figure 5.9: SEM photos of Plastic NPs. A – Raw PS, B – Coffee lid, C – PMMA.

Some coffee cup lids were cryogenically milled to obtain a powder without any chemical alteration. A comparison in biological testing between chemical and mechanical synthesised particles will be tested for cytotoxicity. The plastic has been produced mechanically, which leads to a larger size distribution than the chemically synthesised method. Figure 5.10 shows a broader and more irregular size distribution. The average size distribution was 236.6 nm ± 53.7 nm. Small NPs can still be formed via mechanical synthesis but with a larger size distribution. Due to the irregular size and particles being above 200nm, it is not possible to use nanoflow cytometry to obtain a particle concentration per ml.

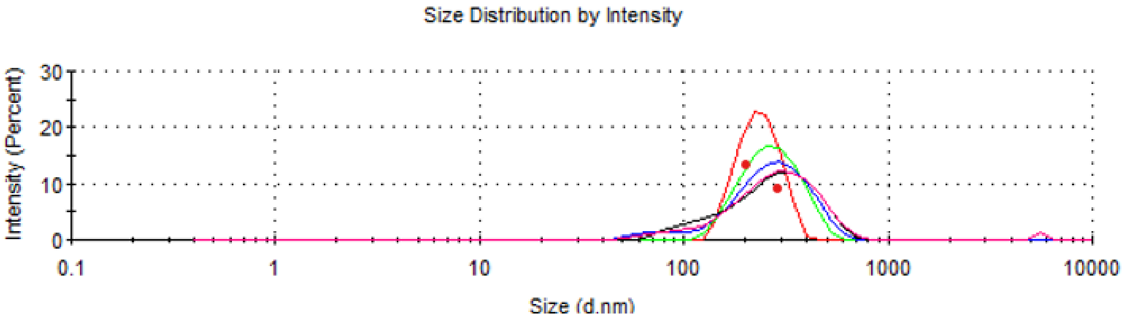

Figure 5.10: Size distribution of cryomilled polystyrene coffee lid.

Figure 5.11 displays the SEM images of the cryo-milled sample and confirm a broad size distribution with large micron-size particles but also small amorphous particles less than 500 nm. In the biological testing, a range of sizes are added to the cells which will better replicate environmental conditions and give an indication on how morphology effects cell toxicity.

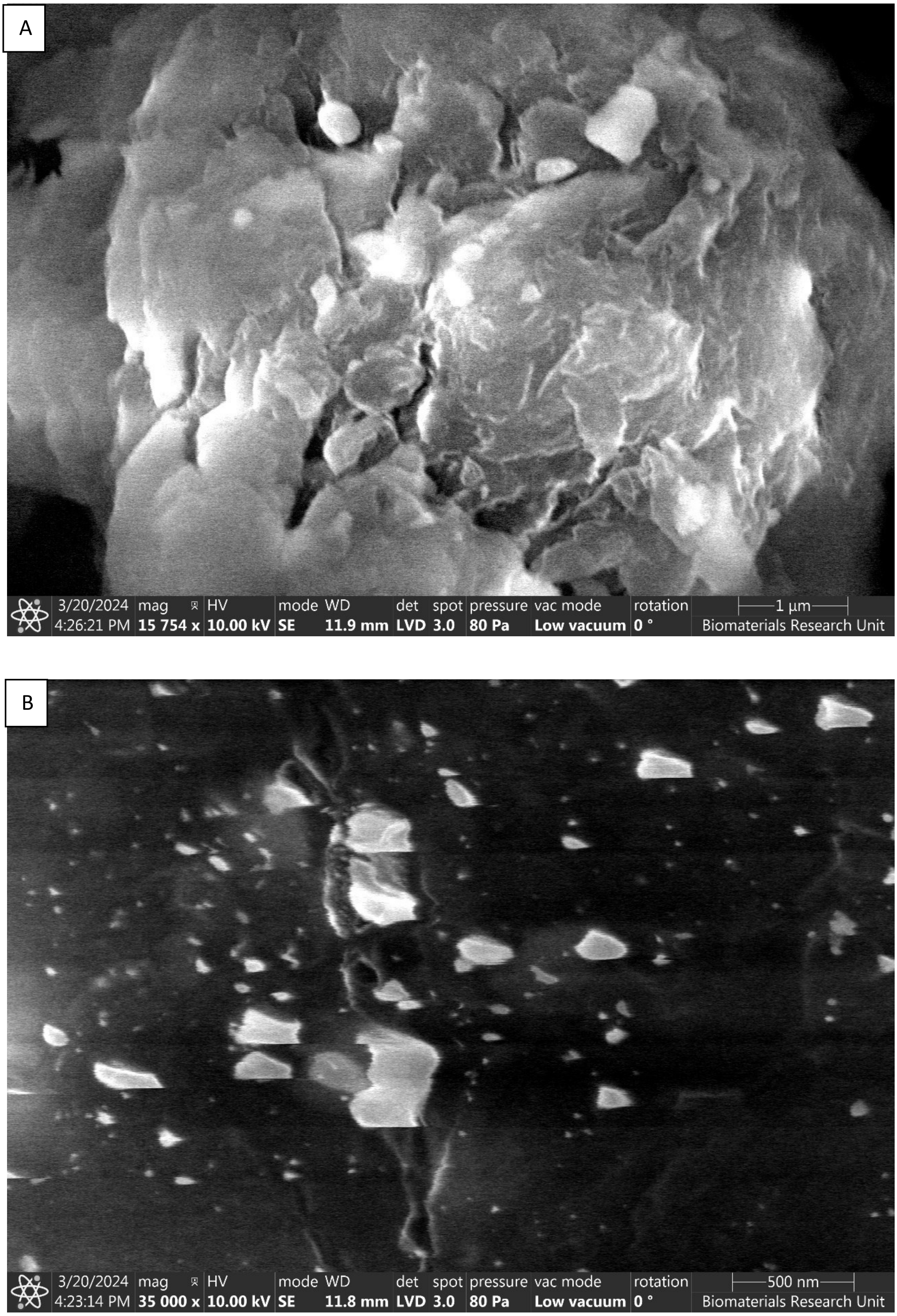

Figure 5.11: SEM images of cryomilled polystyrene coffee cup lid. (A – Larger plastic particle, B – Smaller nanoplastics).

5.5.2 Elemental analysis

EDX was carried out on both the raw PS and the coffee lid to compare the elemental composition of the materials. Table 5.9 and Figure 5.12 display the net count and peaks for each material. From Table 5.9B and Figure 5.12B, the raw PS composition shows that the main component is carbon, as expected due to being raw polystyrene. The C atomic percentage is 99.6 %, and Al is 0.3 %. However, the Al signal is from the stub used to mount the sample. The remaining elements that were detected accumulate less than 0.1 % and are most probably contaminants. In Table 5.9 and Figure 5.12A, the main composition of the coffee lid is C, with a anatomic percentage of 96.9 %. Most other elements are contaminants/errors. However, a Ca atomic percentage of 2.5 % is present in the material as a colourant and additive to ensure the product appears white. $CaCO_3$ is a common additive to plastic products to make them appear white. Ti atomic percentage of 0.3 % is likely present in the coffee lid rather than a contaminant due to the count and the peaks in Figure 5.12A. Titanium dioxide is vastly used in plastic production as a colourant and as an antimicrobial *(Trento et al. 2023)*. TiO_2 would be present in the coffee lid to improve the colour of the lid, increase heat resistance and as an antimicrobial *(Younis et al. 2023)*.

Table 5.9: EDX data for A - coffee lid and B – raw polystyrene at 15 kV acceleration voltage.

A – C.L	Element	Net Count	Weight %	Atom %
	C K	838619	90.3	96.9
	Mg K	1244	0.2	0.1
	Al K	2208	0.2	0.1
	Si	1047	0.1	0.1
	Cl K	1043	0.2	0.1
	Ca K	37724	7.9	2.5
	Ti K	3037	1.0	0.3
	Ni K	144	0.2	0.0
B - PS	**Element**	**Net Count**	**Weight %**	**Atom %**
	C K	728935	90.3	99.6
	Na K	0	0.0	0.0
	Al K	4704	0.7	0.3
	P K	429	0.1	0.0
	S K	582	0.1	0.0
	Ca K	521	0.1	0.0

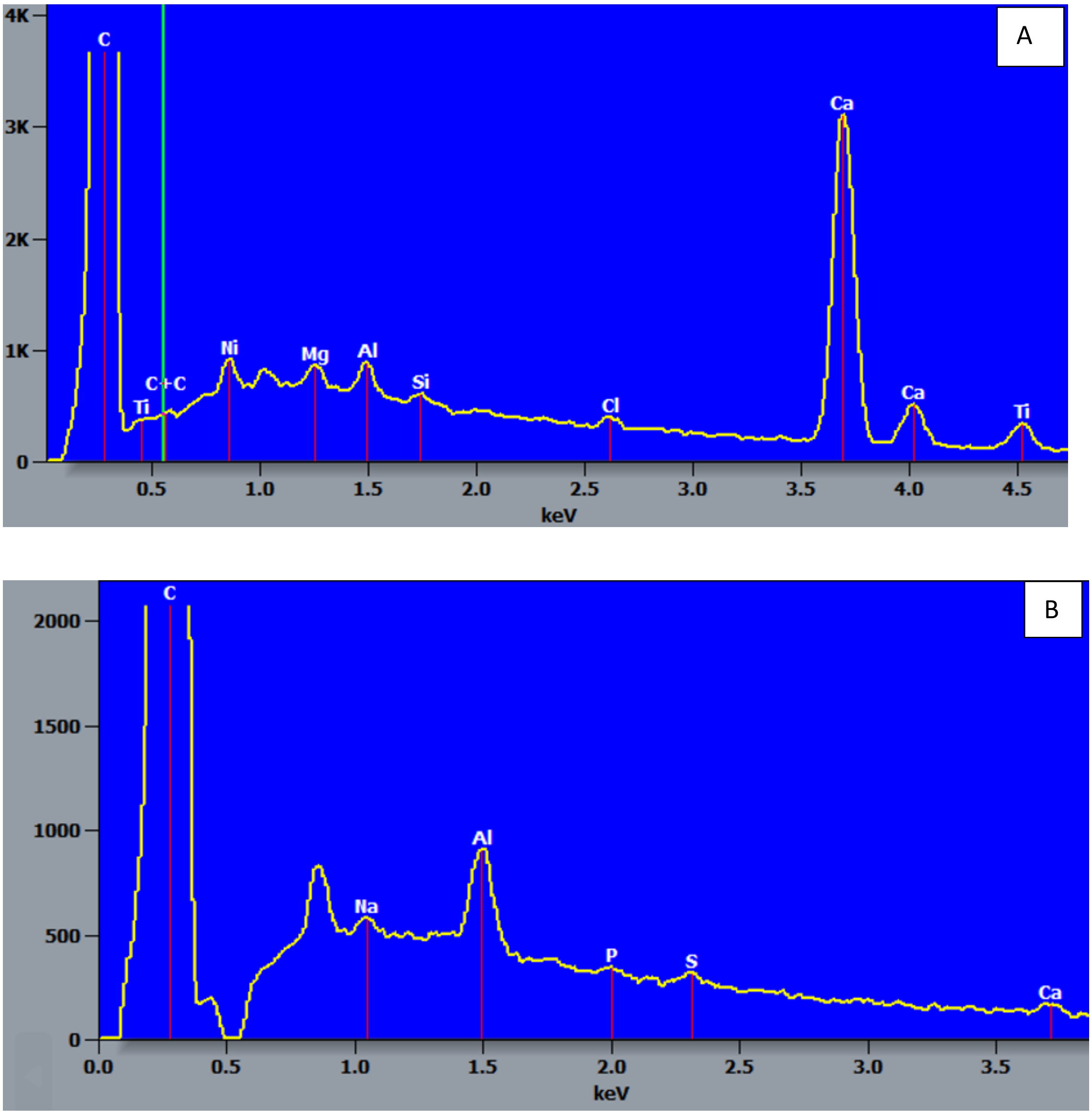

Figure 5.12: EDX data for A – Coffee lid, B – raw PS at 15kV acceleration voltage.

XRF was used as another elemental characterisation technique to measure the fluorescence of the elements in both materials and compare what additives are in the coffee lid. From Table 5.10, the main element in both materials was C. Several elements were picked up in the coffee cup lid that can be disregarded due to the low percentage of material detected. Mg, Al, Si, P, S, Fe and Zn could all be disregarded due to contamination that is present in glassware. The coffee lid was cryogenically milled, so the Fe could also be from that process. The most significant results are the Ti and Ca, which have a mass percentage of 0.444 and 4.33, respectively. This compliments the EDX data, with both elements present in both analytical techniques.

$CaCO_3$ and TiO_2 are most likely the compounds within the coffee cup lid that have been used as colourants to improve the properties of the plastic for its desired use. This indicates why the coffee lid results have a high O percentage. For the raw polystyrene, The elements present ae most likely contamination through handling and processing, such as Si, P, S, Fe, and Zn have a negligible count. The presence of Ca, although a low mass percentage of 0.0239 %, indicates a small amount of $CaCO_3$ to enhance the colour of the raw material. There is no presence of Ti in the XRF and EDX with a much higher C percentage of 99.4 mass % compared to the coffee lid of 89.5 mass %. The high percentage of Br present was a surprise and an unknown form of contamination within the raw polystyrene.

Table 5.10: XRF data for A – coffee lid, B – Raw Polystyrene.

A – C.L	Element	Result	
	C	89.5	Mass %
	O	5.56	Mass %
	Mg	0.0259	Mass %
	Al	0.0301	Mass %
	Si	0.0248	Mass %
	P	45.7	ppm
	S	56.3	ppm
	Ca	4.33	Mass %
	Ti	0.444	Mass %
	Fe	0.0126	Mass %
	Zn	0.0194	Mass %
B - PS	**Element**	**Result**	
	C	99.4	Mass %
	Si	72.6	ppm
	P	58.9	ppm
	S	15.9	ppm
	Ca	0.0239	Mass %
	Fe	92.0	ppm
	Zn	0.0120	ppm
	Br	0.581	Mass %

XRD was carried out to characterise the materials crystallographic structure to relate to the elemental analysis. XRD is not effective compared to EDX for elemental analysis as numerous compounds have similar crystal structures, such as Cubic Close Packed (CCP) or Hexagonal Close Packed (HCP) structures. This means that different compounds have similar peak patterns. XRD is used to supplement other analysis techniques and provides information on the sturcture of the material which the other analysis techniques do not. In Figure 5.13 the XRD data for both materials was normalised to the highest peak for comparison. There are numerous additional peaks in the coffee lid compared to the raw polystyrene. The majority of the additional peaks in he coffee lid are from $CaCO_3$ where only a small amount was present in the raw PS which is further supported by *Achour et al. 2017* XRD pattern of $CaCO_3$.

The XRD pattern for the coffee lid also suggests that rutile (TiO_2) is present in the material (which is further backed up by XRD pattern in *Fischer et al. 2017)*, which is missing from the raw polystyrene XRD pattern. Many materials have a similar XRD pattern to rutile, such as $AgTi_3$ *(Shen et al. 2021)*. However, from the XRF and EDX data, there is no indication of Ag, therefore, the $AgTi_3$ is unlikely to be present. Only five peaks within the raw polystyrene overlap with the peaks in the coffee lid. The material appears to be iron oxide from the XRD data. This is a likely contaminant from cryogenic milling, and a small debris from the impactor broken off within the material. XRF data supports this with a small percentage of Fe present.

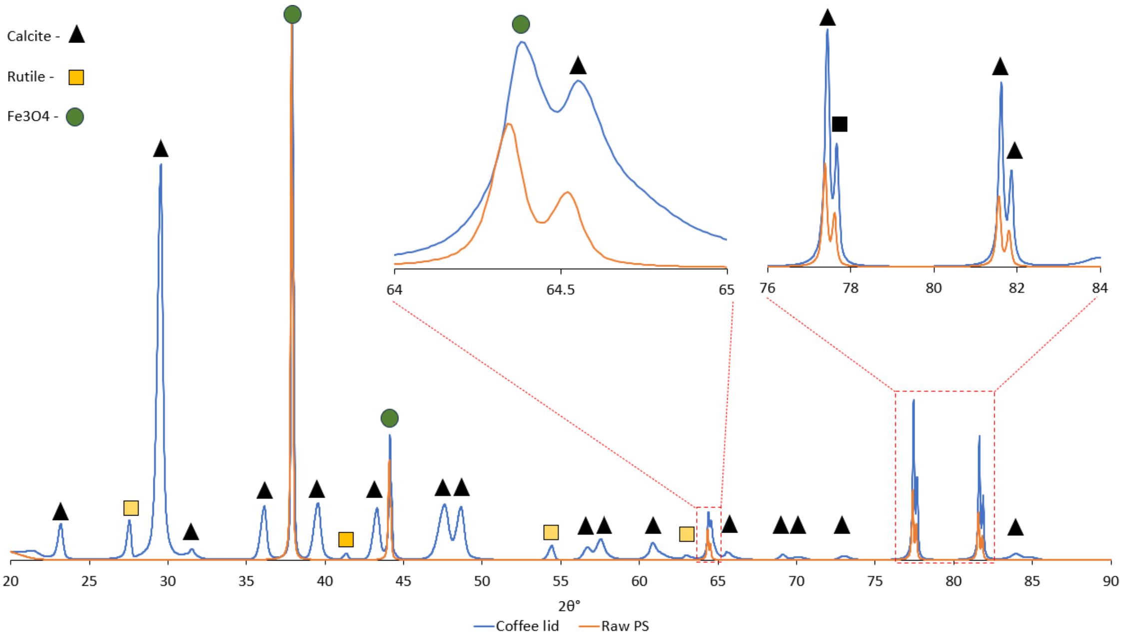

Figure 5.13: XRD pattern for raw polystyrene and the coffee lid.

XPS was carried out on raw polystyrene, the coffee lid, and the two solvent-extracted unsoluble pellets from the coffee lid to understand what additives are present. Table 5.11 shows raw polystyrene has a high atomic concentration of C-C / C-H bonds of 97 %, which is expected as the polystyrene structure comprises only C and H. A small amount of $CaCO_3$ is present in the raw polystyrene, which supports the XRF along with the small signal for C-O, C=O and the Ca, CO_3 and O atomic concentrations.

From the coffee lid, there is a significant reduction in the C-C / C-H bonds to an atomic concentration of 70.4 %. An increased amount of Ca and CO_3 is present in the coffee lid. There is a much larger atomic concentration of C-O, C=O and O if $CaCO_3$ is the only compound attributing to the signal. This does not eliminate that other organics may be in the coffee lid also adding to the C-O, C=O and O signal. Na, Si, Cl, and S, are expected contaminants through contact with glassware. A relatively high atomic concentration of N within the coffee lid of 1.1 % indicates that another organic additive is present in the coffee lid to improve its properties. There was no Ti signal as the concentration is below the detectable limit of the equipment.

As there are clear indications of additives within the coffee lid, solvent extraction was carried out to analyse the additves within the lid. This was done by dissolving the plastic in the DCM solvent and then centrifuging the sample to separate the materials that were soluble in DCM, such as the polystyrene from the $CaCO_3$ and any other additives whicg were present. After centrifugation, there were two pellets present; one on top of the DCM solvent and one at the botton. This suggests that one insoluble additve is less dense and one more dense than DCM.The samples were then dried and analysed by XPS compared to the coffee lid and raw polystyrene. Within the bottom pellet of the coffee lid, the Ca and CO_3 have been purified, and an increase in atomic concentration, suggesting that the bottom pellet is composed of predominately $CaCO_3$ during the solvent extraction. Within the top pellet, there is a reduction in the amount of $CaCO_3$ but a purification of the Na and S. As the expected contaminents have been purified during the extraction suggests that the Na and S are other compounds that are added to the material or contamination in the coffee lid during the synthesis.

Table 5.11: XPS data for different polystyrene materials.

Sample	Atomic concentration (%)										
	C-C/C-H	C-O	C=O	CO_3	O	Ca	Cl	Na	N	Si	S
Raw polystyrene	97.0	0.3	0.2	0.4	1.7	0.4	-	-	-	-	-
Coffee Lid	70.4	5.0	4.2	0.8	14.9	0.8	0.2	0.5	1.1	1.7	0.4
Top Pellet	76.0	3.2	1.3	0.3	14.0	0.3	-	1.9	0.4	1.6	1.0
Bottom Pellet	81.1	1.6	-	2.5	12.3	2.5	-	-	-	0.1	0.1

Carbon-13 (^{13}C) Solid-State NMR (S.S NMR) was carried out to identify differences between the raw PS and the coffee lid organic bonding through analysing the carbon atoms within the structure. Although carbon-13 makes up 1 % of the abundance of carbon atoms, a signal can be obtained through NMR due to the nucleus having a spin in comparison to carbon-12. From Figure 5.14, a spin speed of 12.5 KHz was used , which in S.S NMR causes spinning sidebands that are not peaks caused by the material itself. Spinning sidebands are separated from the isotropic frequency by a multiple of the spinning rate, which in this case is 12.5 KHz. The peaks marked with an astriks are the spinning sidebands.

The peak at 129 ppm is representitive of the aromatic ring of the polystyrene polymer and would represent carbons 3 to 8 labelled in Figure 5.14. In the raw PS, there is an additional peak at 196 ppm indicating aldehyde bondingwhen compared to the coffee lid. The peak at 60 ppm is in correspondence with the two carbon atoms along the straight chain of the polymer labelled 1 and 2 in Figure 5.14.

There are two additional peaks in the coffee lid at 28 and 32 ppm that corrospond to additional alkyl chains or an alkyl halide. The slight shift in some peaks may be accounted due to different polymer chain lengths. Overall, the spectra for both raw PS and the coffee lid are very similar with some small differences in the organic material present.

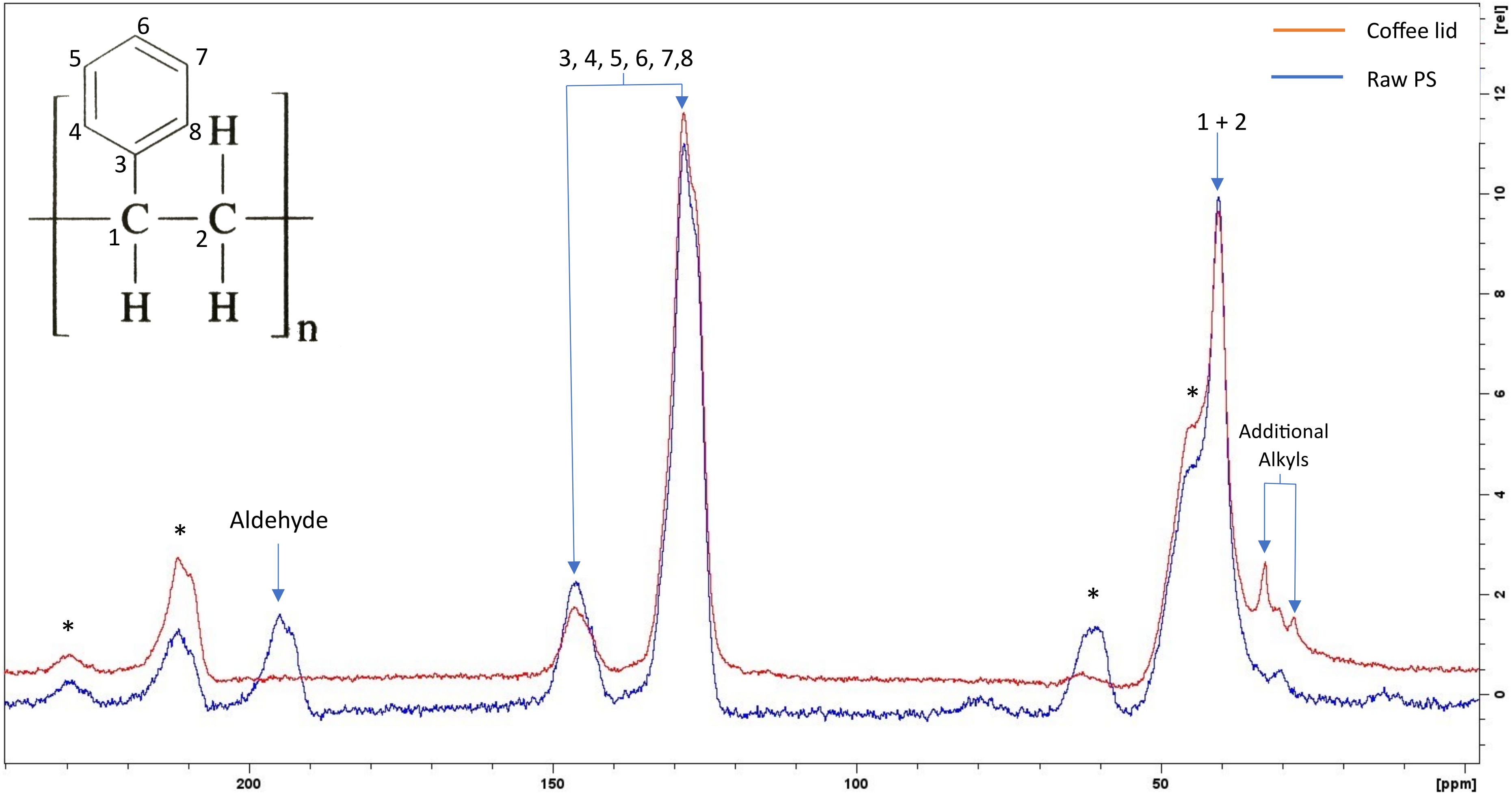

Figure 5.14: Solid-State NMR data for Raw polystyrene and Coffee Lid (* - Spinning sideband caused by S.S NMR).

FTIR was carried out on both materials and the solvent-separated pellets from the coffee lid to identify differences in bonding between the materials. From Figure 5.15, the spectra for the four materials are predominately matching with the main component still polystyrene. Differences at 1300 cm^{-1} and 850 cm^{-1} are highlighted in Figure 5.15 and focused upon in Figure 5.16. The peak at 1300 cm^{-1} and 850 cm^{-1} are from the high content of $CaCO_3$ within the coffee lid as a white colourant to the material. The peak at 1300 cm^{-1} for C=O, and at 850 cm^{-1} for C-O within the CO_3. The data aligns with standard spectra for the $CaCO_3$ peaks *(NIST, 2023)*. The presence of this material in the raw polystyrene is negligible or at a low concentration below the detection limit of the equipment.

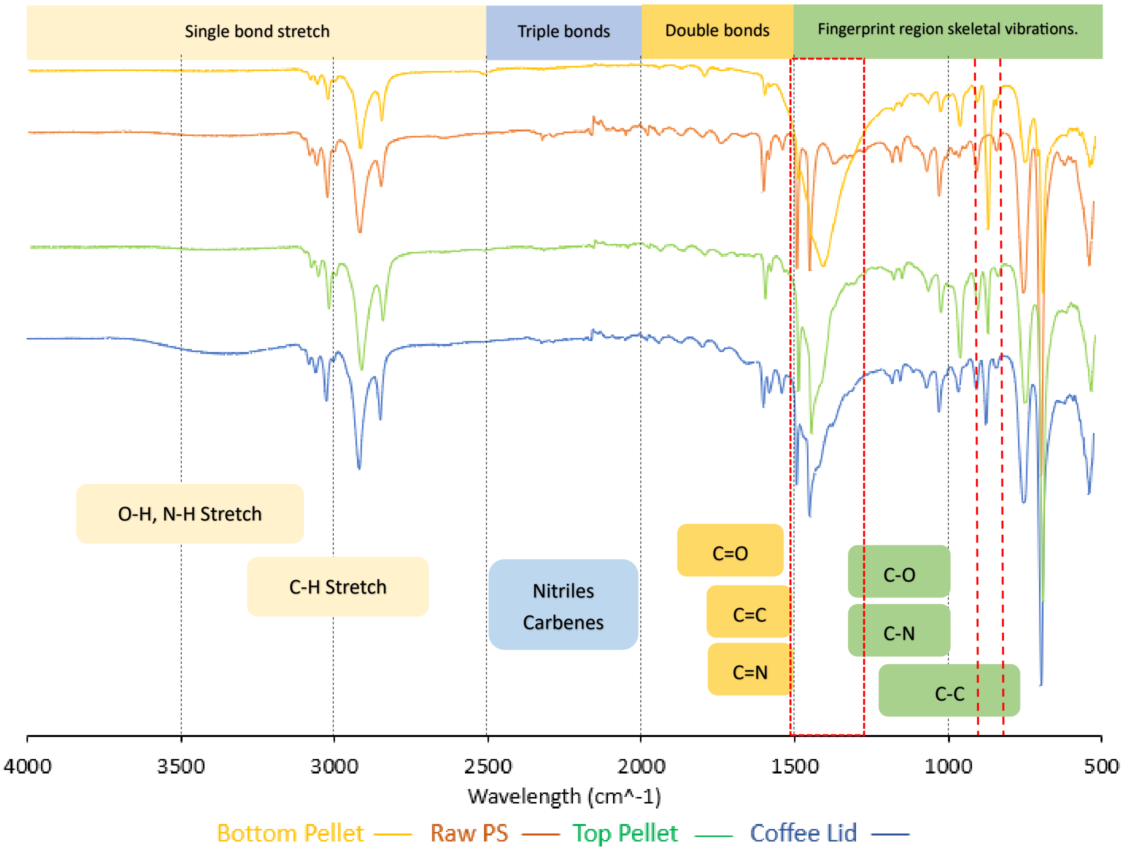

Figure 5.15: FTIR Spectra for samples raw polystyrene compared to the coffee lid and solvent separated samples.

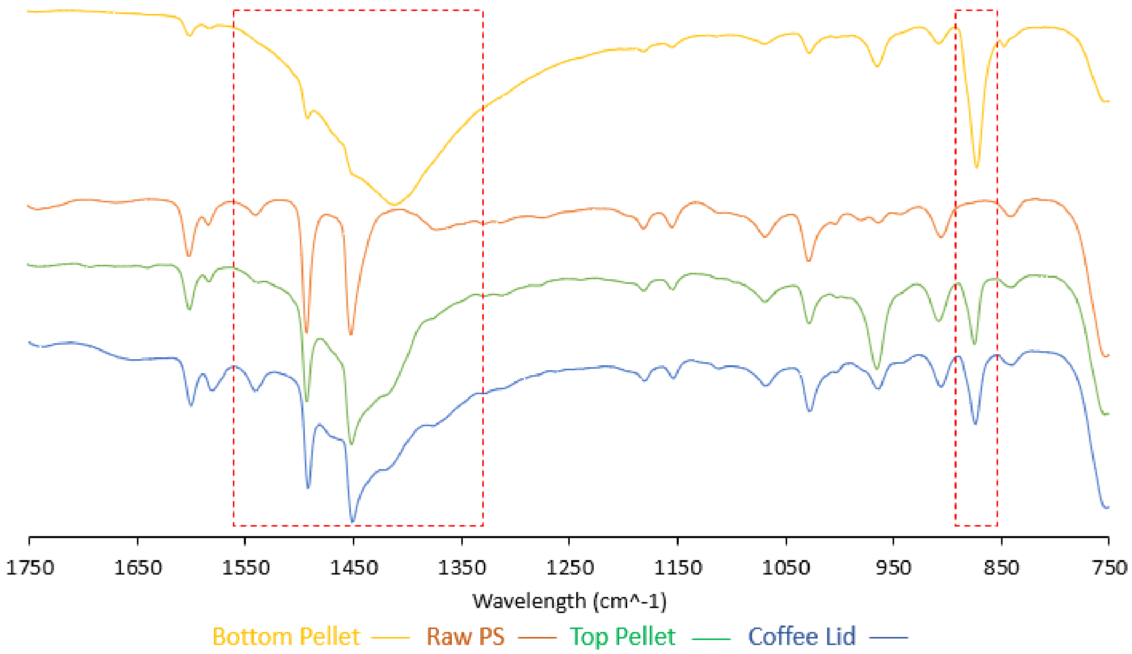

Figure 5.16: FTIR Spectra highlighting differences between the raw polystyrene and the coffee lid.

When these plastics break down in the environment, the plastic pollution and the additives cause the toxicity to marine life and elevate the impact plastic pollution has. Thermogravimetric analysis (TGA) was carried out to compare the raw polystyrene to the polystyrene coffee cup lid to confirm the presence of the additives within the coffee lid. In Figure 5.17, the graph shows a difference between the two materials. The raw polystyrene shows a smooth curve where the sample is completely decomposed at 400 °C, which aligns with research that has also been carried out TGA on polystyrene *(Rawi, 2017)*. There are no changes in the derived weight after this temperature and reached 0 weight %. The coffee cup lid shows multiple decompositions, with 87.58 % occurring at around 420 °C. However, between 620 °C and 740 °C, another 7.32 % of the material is decomposed and at the end of the heating to 950 °C, there is still a 5.10 % weight left, suggesting inorganic material within the sample. The decomposition between 620 °C and 740 °C would be the start of the decomposition of $CaCO_3$ as thermal decomposition is initiated slowly and then rapidly above 750 °C to CaO and CO_2 *(Karunadasa et al. 2019)*.

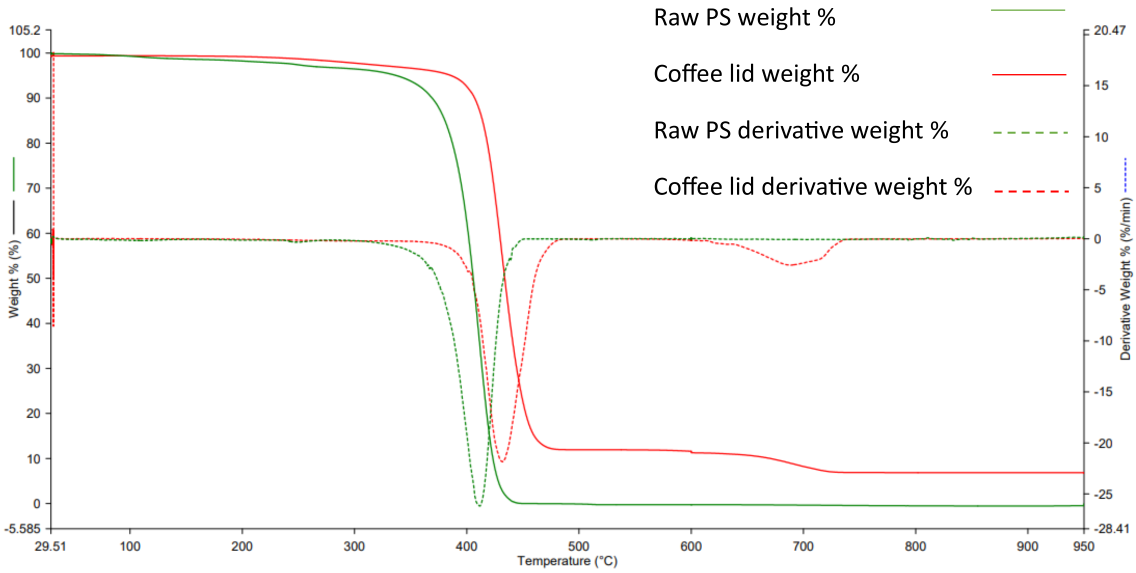

1) Hold for 5.0 min at 30.00°C
2) Heat from 30.00°C to 600.00°C at 10.00°C/min
3) Hold for 2.0 min at 600.00°C
4) Heat from 600.00°C to 950.00°C at 40.00°C/min
5) Hold for 5.0 min at 950.00°C

Figure 5.17: TGA of raw polystyrene compared to polystyrene coffee lid.

From all the characterisation, there are additives within the coffee lid. While synthesising the raw polystyrene and coffee cup lid, the raw polystyrene solution went colourless from the complete dissolution of the material in the DCM solvent. However, the coffee cup lid was a milky white solution, suggesting that not everything had dissolved in the DCM. At this stage, solvent extraction was carried out via centrifugation. The biological study will confirm whether the polystyrene plastic is inherently toxic to the cells or if the additives are.

5.6 Biological results and discussion

5.6.1 Preparation of samples for biological testing

It is critical to remove any residual DCM and SDS that cause damage to the cells and increase the difficulty in analysing the plastics damage caused. NMR was used to ensure all unwanted peaks [DCM and SDS] are removed from the material before cell testing. A concentration curve for SDS was analysed to find the lowest detection point. In doing so, the washing procedure can be evaluated for its effectiveness and ensure the lowest detectable limit causes negligible effects to the cells.

Figure 5.18 shows the tested SDS concentration NMR data. The prominent peak representing the SDS presence is the large peak at 1.3 ppm from the R-C-H bonds (R = C), with two other minor peaks at 0.8 ppm and 3.6 ppm, accountable for the C-H and C-O bonds, respectively. Figure 5.18A and Figure 5.18B, the amplitude of the main peak reduces from 825 to 190. As the concentration decreases the signal decreases at the same rate. In Figure 5.18D, it is challenging to identify the SDS peaks from the noise. The detectable limit for the SDS is less than 0.01 %. This concentration requires testing on the MRC-5 cell line to ensure no diverse effects are noticed.

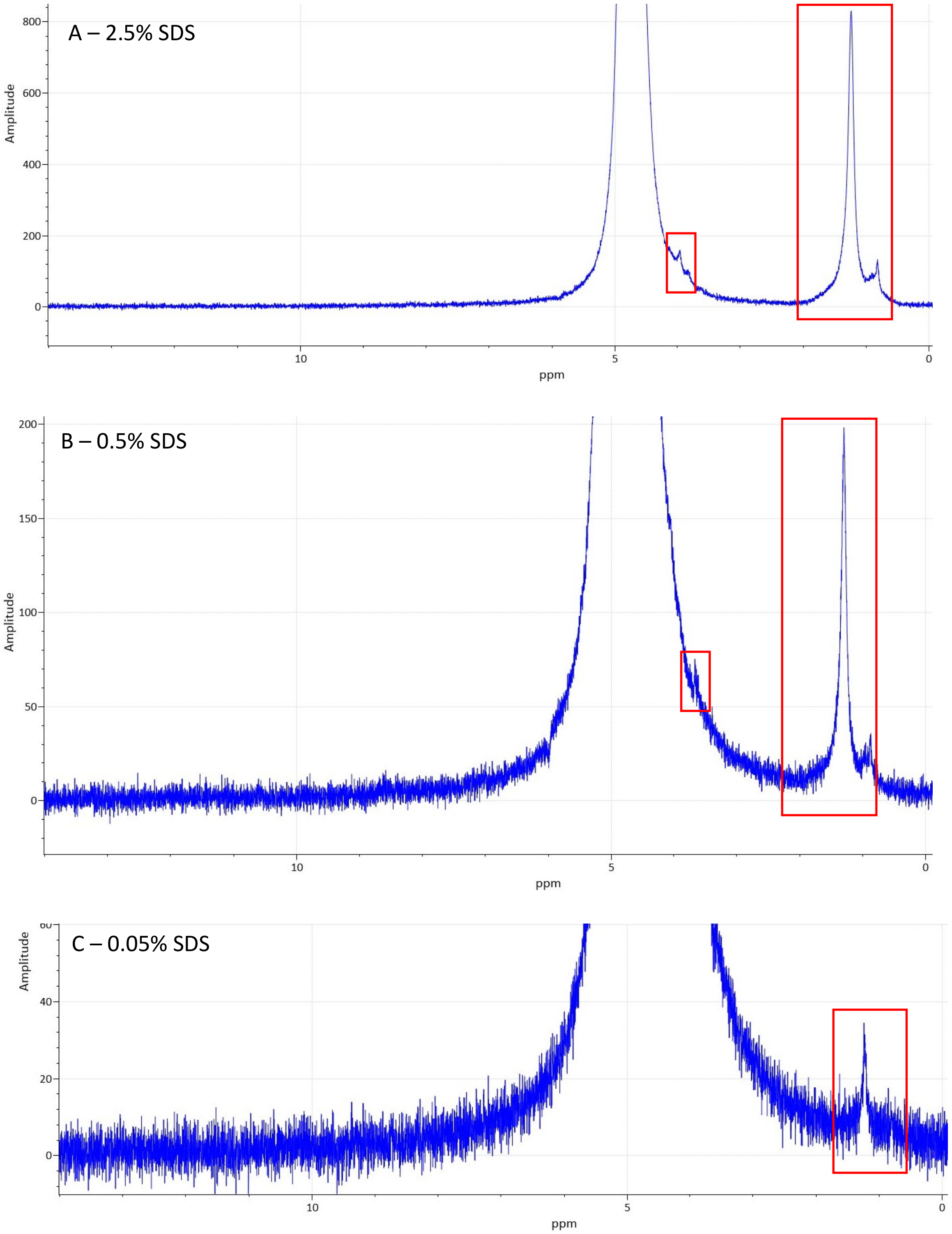

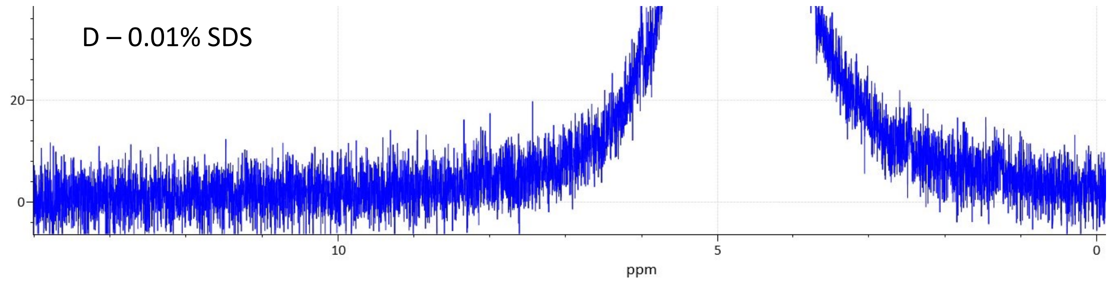

Figure 5.18: NMR data of different SDS concentrations. A – 2.5 %, B – 0.5 %, C – 0.05 %, D – 0.01 %.

Figure 5.19, the amplitude data have been plotted on a graph to see how the changing concentration of SDS affects the amplitude of the peak at 1.25 ppm for the repeating C-C bond within the SDS structure. The results are relatively linear, as expected when the concentration of the SDS is reduced, there are fewer bonds that resonate during the analysis.

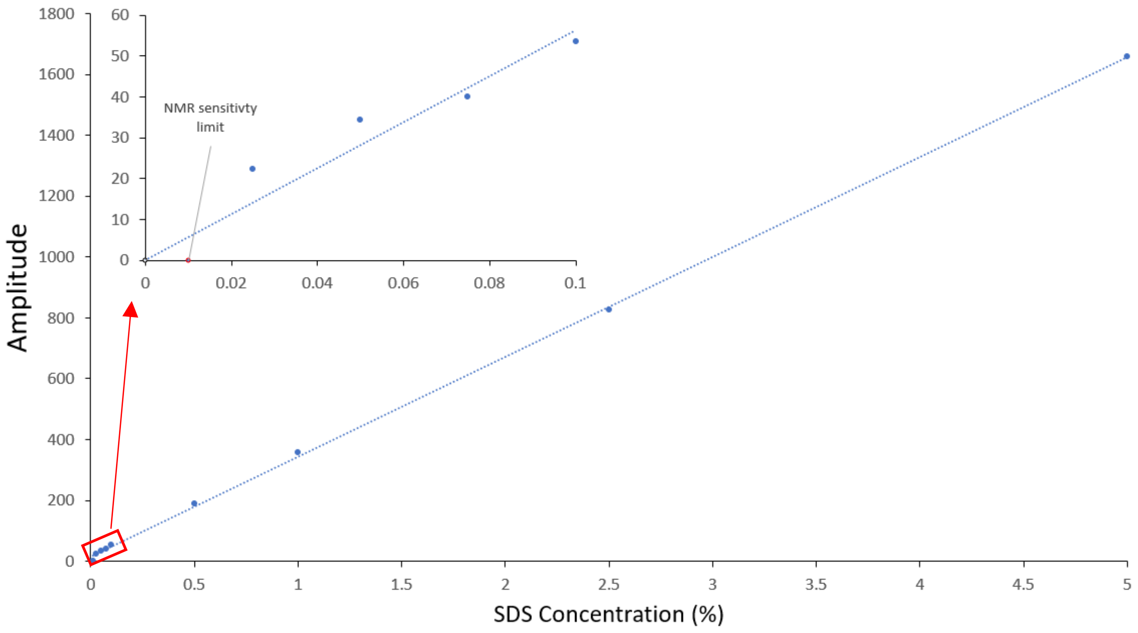

Figure 5.19: Amplitudes of SDS concentrations in NMR analysis.

The plastic samples are stored in a 0.1 % Tween 20 solution to stabilise the particles and minimise the amount of agglomeration and aggregation that occurs during storage. NMR was carried out on a 0.1 % Tween 20 solution to identify the necessary peaks expected in the plastic sample solutions. Figure 5.20 shows the NMR data for 0.1 % Tween 20 at 3.7 ppm.

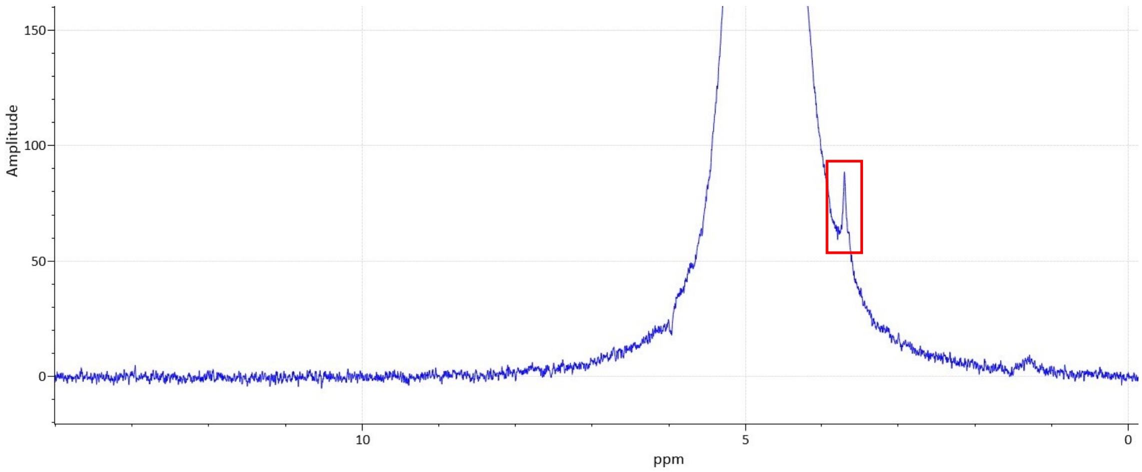

Figure 5.20: NMR data for 0.1 % Tween 20.

The final peak, which is pivotal to remove after washing, is the DCM peak. The halogenated solvent would be toxic to the cells and misrepresent the results obtained from cell testing. In Figure 5.21, the NMR data for DCM shows a sharp peak at 5.3 ppm. It is key to ensure that both the DCM peaks and SDS peaks have been removed in all washed products, ready for cell testing.

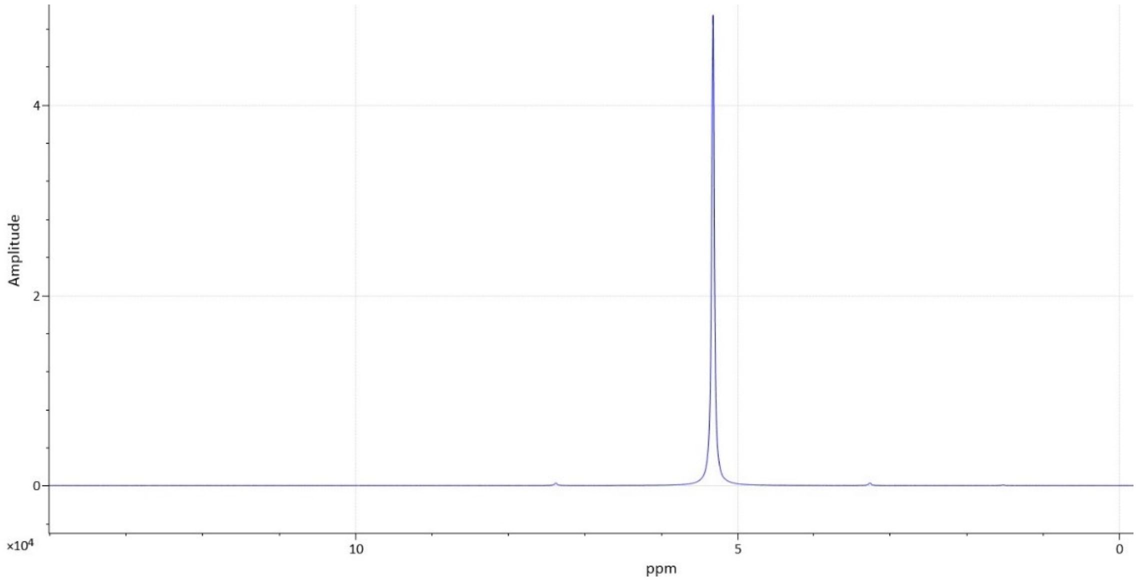

Figure 5.21: NMR data for DCM.

For the raw PS, coffee lid and PMMA, NMR was carried out to ensure that these key chemicals were removed from the plastic solutions. In Figure 5.22, all three plastics show the removal of DCM and the SDS to an undetectable and negligible amount.

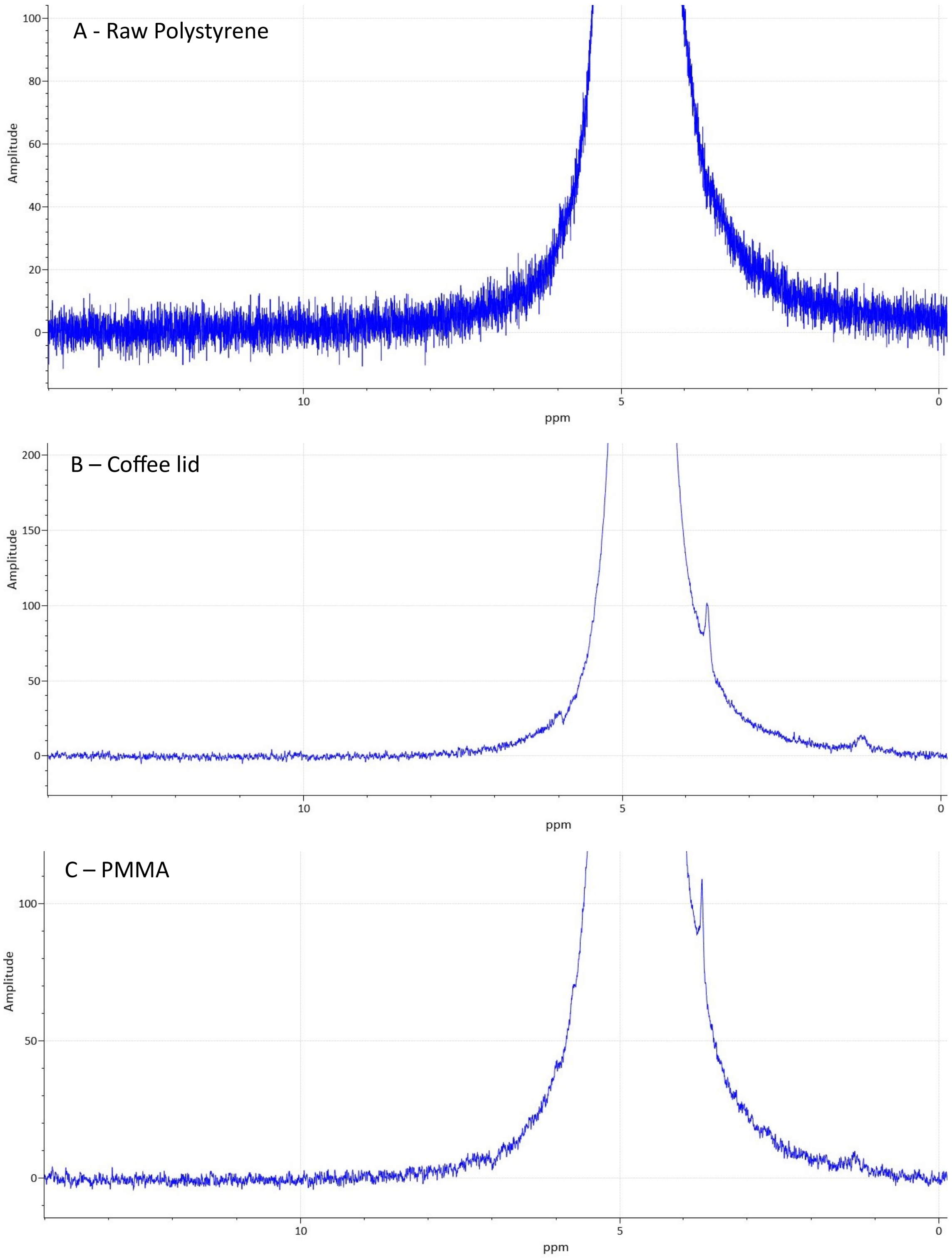

Figure 5.22: NMR data for A – Raw PS, B – Coffee lid, C – PMMA to show removal on contaminants. (Broad peak at 5 ppm is for H_2O as deuterated water was not used for this experiment and at 4.6 ppm is the presence of Tween 20).

5.6.2 Cell viability after exposure to nanoplastic NPs

As no previous data were available in the published literature for our experimental system a methodology was developed for a cell toxicity experiment. We have performed our initial cell toxicity screening with the highest concentration of NP - the NP suspension as achieved by the synthesis diluted 1 in 10 into the cell culture medium). For the preliminary experiment, 2.79 x 10^{12} particles per cell was the concentration used for the test. The total number of cells the particles were loaded onto was approximately 150’000 cells.

Figure 5.23 displays the cell viability graph. The 0.1 % solution of Tween 20 did not significantly affect the cells. Tween 20 was tested for its toxicity towards MRC-5 cells as the plastic NPs were stabilised in a 0.1 % Tween 20 solution. This confirms that the Tween 20 does not cause any adverse effects that would give misleading results. The raw PS and PMMA have a nonsignificant effect on cell viability and did not differ drastically from the control. With the PE, there is a drop in cell viability to 82 % alive cells after 24 hours of treatment but statistically nonsignificant. Significance was determined by ANOVA test followed by Sidak’s post-hoc test comparing treatments to control (untreated cells) whereby (***) represents significant statistical significance $p<0.0001$), (*) $p<0.05$ and ns non-significant). The ANOVA test is used to compare the results to the control and indicate whether any results are significanly different. The post-hoc analysis then compares between all groups to each other and not just the control. A further drop when using PP NPs to below 75 % viability, leading to an increase in cytotoxicity and inhibition in proliferation, this was a significant drop in the cell viability.

However, in both the cryo-milled and chemically synthesised coffee lid NPs, there is a significant drop in cell viability to 34.8 % and 10.3 %, respectively. The cryo-milled sample was mainly used to confirm whether the chemical synthesis process brought toxic chemicals into the sample, leading to an increased positive cell toxicity. An unknown concentration and size distribution was loaded onto the cells for the cryo-milled samples but used as an indicator if the plastic was inherently toxic. The importance of these results appears to show that the coffee lid samples are toxic to the cells due to the plastic and additives. One possibility is that the toxicity might be coming from the presence of TiO_2 within the coffee lid *(Gojznikar et al. 2022)*. In *Gojznikar et al. 2022*, TiO_2 Is toxic to Eukaryotic Cells and increases the reactive oxygen species (ROS) within the cells, leading to cell death. It is unlikely that $CaCO_3$ within the coffee lid causes significant cell damage, as cells have developed over time to use carbonate-based systems as a buffer. For example, in *Liendo et al. 2020*, $CaCO_3$ is highly biocompatible with zebrafish, which are vertebrate models causing no cell death, no increase in the levels of ROS, or DNA damage in the cell lines.

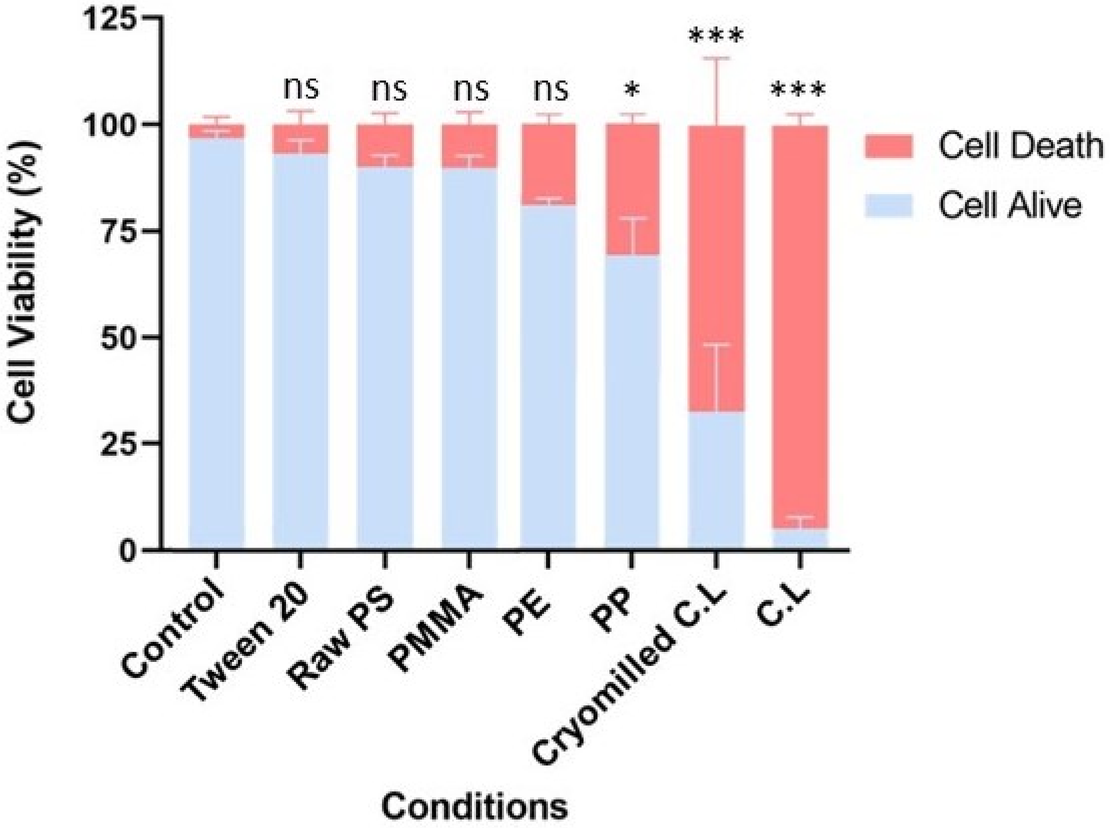

Figure 5.23: Cell Viability graph of MRC-5 cells against different plastic treatments. (Significance was determined by ANOVA test followed by Sidak’s post-hoc test comparing treatments to control (untreated cells), whereby (***) represents significant statistical significance p<0.0001), (*) p<0.05 and ns non-significant.)

From Figure 5.24, images captured on a microscope at 10 x magnification show how the cells appear after treatment. Figure 5.24A and B for the control and Raw PS, the MRC-5 cells look similar, with a small number of cells entering apoptosis. Figure 5.24 C and D, for the cryo-milled and chemically synthesised coffee lid, there is a significant difference where most of the cells are necrotic or in apoptosis due to the treatment. The control sample shows what healthy MRC-5 cells should look like. From this experiment, the coffee lid treatment leads to significant damage and a concentration curve is required to understand the toxicity levels.

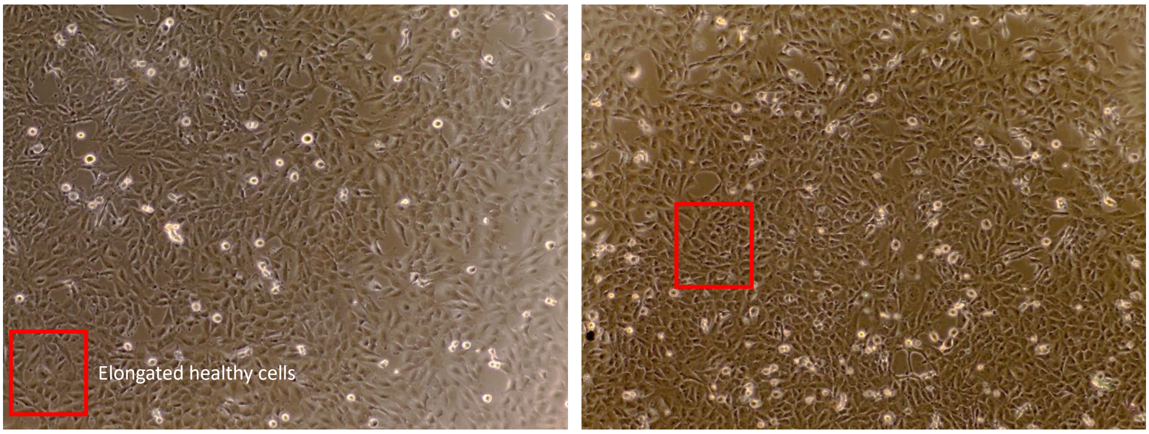

A - Control

B – Raw PS

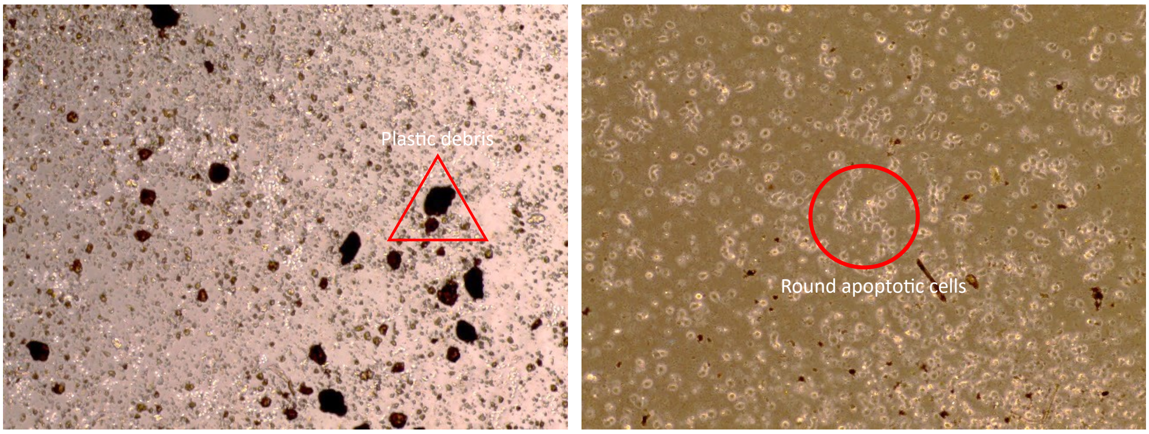

C – Milled Coffee lid

D – Coffee lid

Figure 5.24: Representative Microscopic images of treated MRC5 cells at 10 x magnification of A – Control, B – Raw PS, C – Cryomilled Coffee lid, D – Coffee lid.(The square represents healthy elongated cells, the circle represents apoptotic cells that are rounded and the triangle represents the plastic debris).

5.6.3 Dose-response cell toxicity assessment of the NPs prepared form the coffee lids.

Due to the initial toxicity found from the coffee cup lid NPs, dose response analysis was carried out to understand how the increasing range of plastic particle concentration would affect the viability of the cells. The process was carried out the same way as the initial toxicity test, in which the plastics were loaded onto 150,000 cells using 1:10 dilution with the cell medium. Figure 5.25 shows a trend in the graph as the concentration changes. The cell death decreases relatively linearly when the concentration is reduced by 50 % in each experiment. From the 100 % concentration at 2.79×10^{12} particles per cell compared to the 25 % at 6.98×10^{11} particles per cell, the cell viability increased from almost zero to 50 %. When the concentration is reduced to 1.75×10^{11} particles per cell, the cell viability is further increased to just above 75 %. At a concentration of 4.36 x 10^{10} and 2.18 x 10^{10}, there is almost no effect on the cells, and very similar to the control cell viability.

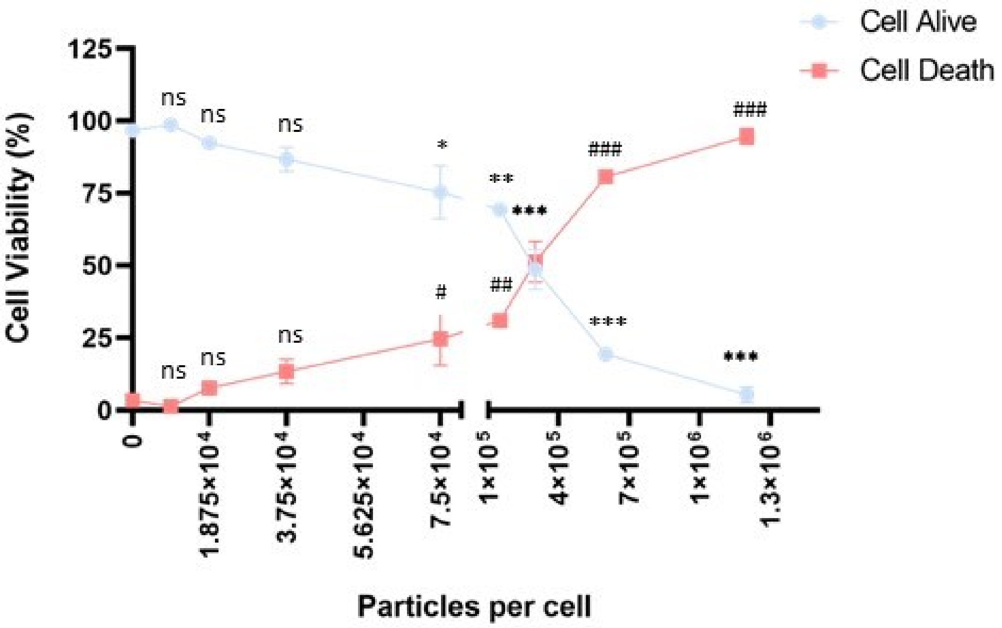

Figure 5.25: Cell Viability Curve for concentration gradient for coffee lid NPs. (Significance was determined by ANOVA test followed by Sidak's post-hoc test comparing treatments to control (untreated cells), whereby (***) represents significant statistical significance $p<0.0001$) and ns is nonsignificant).

Comparing the control from Figure 5.24A to the microscope images in Figure 5.26, the cell's morphology shows the clear signs of distress. The cells are entering into apoptosis as the morphology changes from elongated to shrunken and spherical.

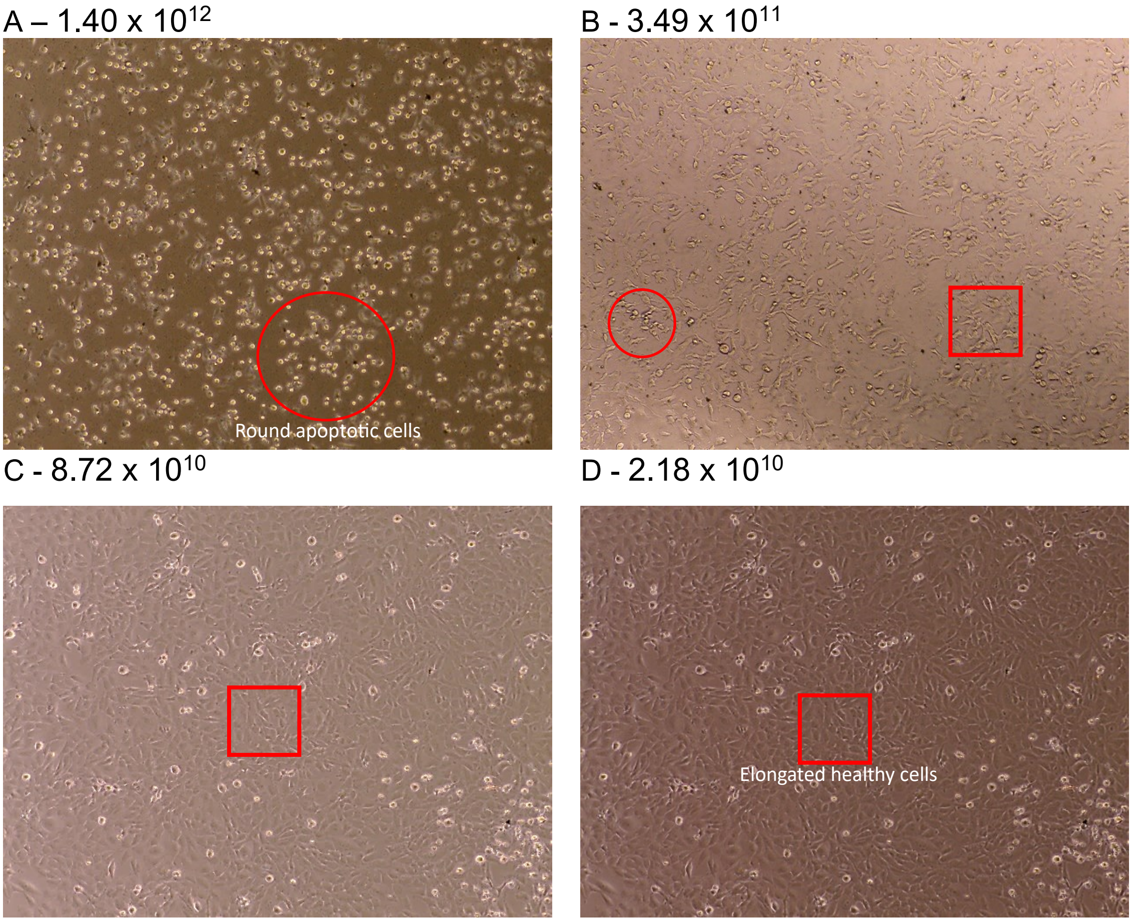

Figure 5.26: Microscope images at 10 x magnification from coffee lid treatment at A - 1.40 x 10^{12}, B - 3.49 x 10^{11}, C - 8.72 x 10^{10}, D - 2.18 x 10^{10} particles per cell. (The square represents healthy elongated cells, the circle represents apoptotic cells)

5.6.4 Apoptosis quantification of MRC-5 cells following plastic NP exposure.

From the biological experiments thus far, and noticeably the indication of toxicity from coffee lid NPs cause, apoptosis experiments were carried out to measure the number of cells entering apoptosis due to the treatment. Apoptosis is the process by which a cell goes from healthy to necrotic. A form of programmed cell death. There are many reasons that different types of cells enter apoptosis, but one of the critical reasons related to this research is that cells enter apoptosis when it has been damaged beyond repair *(Reed, 2000).* Caspase, a cysteine-aspartic protease, play a significant role in programmed cell death. Caspases 1 and 3 show the active enzyme is a heterotetramer that contain two large and two small subunits. During apoptosis and activation of caspase results in cleavage of the critical cellular substates which leads to the morphological changes *(Cohen, 1997).* It is a crucial function that cells have developed to know when to enter apoptosis. For example, cancerous cells rapidly proliferate, and the cells know that there is a defect within the cell and decide to enter apoptosis to start the cell death cycle. When apoptosis does not occur and uncontrolled proliferation occurs like in cancerous cells leads to the formation of a tumour*(Zhang et al. 2013)*. When cells enter apoptosis the shape of the cell changes From Figure 5.24A and Figure 5.24D, a healthy MRC-5 cell is elongated and stretched out, but unhealthy cells in apoptosis become shrunken and rounded. The triggering of an apoptosis process leads to a caspase activation. Caspase plays a vital role in regulating cell survival or death *(Ghorbani et al. 2023)*. As discussed earlier, apoptosis is a form of programmed cell death due to damage that has been caused to the cell. However, necrosis is the death of the cell due to adverse conditions which leads to the cell dying. Although both processes lead to the death of a cell, apoptosis goes through a series of biochemical reactions to reach death, whereas necrosis is due to adverse conditions killing the cell. There are four main stages that the cells can be in: alive, early apoptosis (E.A), late apoptosis (L.A) and necrotic. The main aim of this experiment is to measure the number of cells that are in apoptosis and preparing to die. E.A and the L.A have been combined.

From Figure 5.27 and Figure 5.28, the levels of apoptosis between the control and plastic samples have been compared. Figure 5.27 has been produced from the data obtained from Figure 5.28 by combining the early and late apoptosis percentages together to obtain the total amount of cells in apoptosis from the treatment. There is a significant number of cells in apoptosis for the C.L at 25 % concentration (1.89 x 10^6 particles per cell), which is 59 % compared to the control, which only had 22 % on average. A trend with the C.L samples that as the concentration is reduced, there is a decrease in the number of cells entering apoptosis to the lowest concentration (0.75 %) that has similar results to the control. The mechanism causing the cells to enter apoptosis is unknown. Whether the TiO_2 is causing damage to the mitochondria or if the particles are agglomerating around the nucleus, causing DNA damage and leading to the cells entering apoptosis. For future work, by carrying out a concentration curve with pure TiO_2 NPs would allow the understanding of the extent of damage caused via TiO_2.

The raw PS concentration used is 1.5 x 10^7 particles per cell which led to an apoptosis of 31 % in comparison to the control at 22 %. When the raw PS and the C.L are compared, there is a significant difference in the number of cells entering apoptosis. This indicates that the additives within the coffee lid do cause a severe amount of cell damage in comparison to the PS itself.

For PMMA and PE, there is an elevated apoptosis rate for the plastic in comparison to the control, which means the plastic is causing some damage. However, for PP, there is a higher and more significant increase in the apoptosis rate to 42 %. The PP is not as inherently toxic as the coffee lid but may cause damage to the DNA that led to the elevated apoptosis. Other than the C.L 0.75 % treated cells, all other plastics had an increased apoptosis rate showing that small and large amount of damage are caused by the plastic treatment.

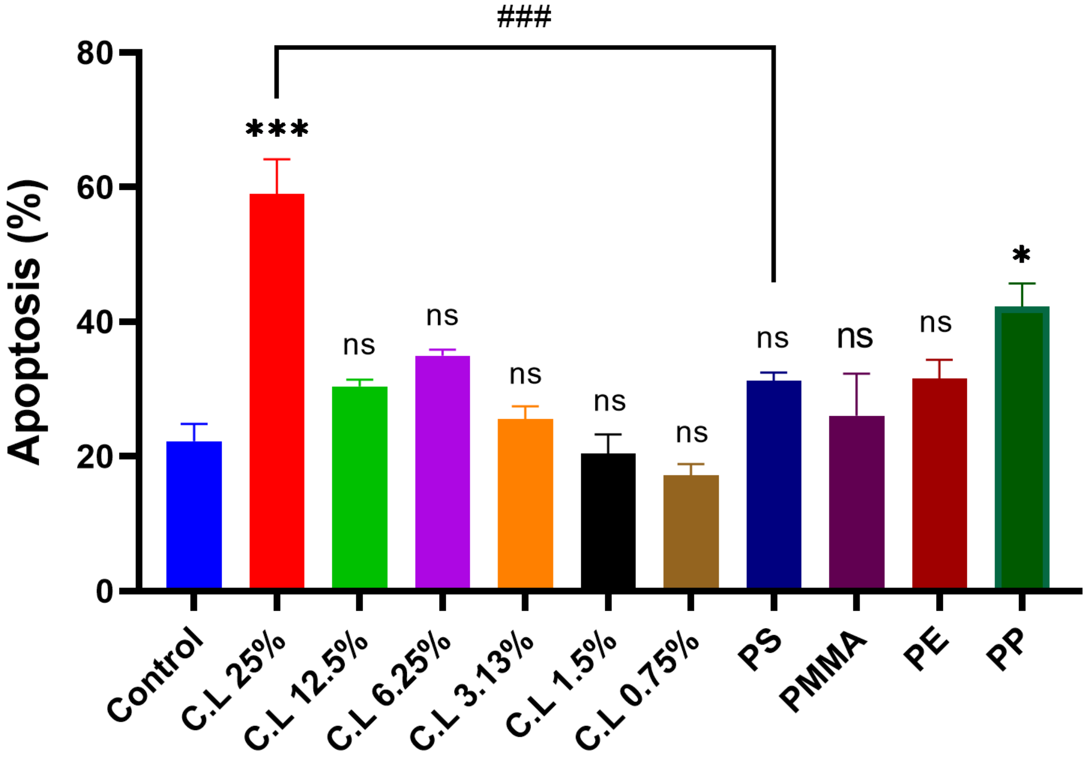

Figure 5.27: Apoptosis rates for control and plastic NP treated samples. (Significance was determined by ANOVA test followed by Sidak's post-hoc test comparing treatments to control (untreated cells), whereby (***) represents significant statistical significance p<0.0001), (*) p<0.05 and ns non-significant. (###) represents a comparison made between the C.L 25 % and PS with a statistical significance p<0.0001).

In Figure 5.28, the graphs from flow cytometry analysis of apoptosis show how the cells move from different quadrants (from alive, E.A, L.A and necrotic) depending on the phase and the treatment being carried out. Each dot on the graphs is an indication of a cell that has been analysed through the flow cytometer. The control is the baseline for the standard amount of cells that are in each phase. The treated cells are then compared to these to understand the effect in apoptosis rate caused from the treatment. When analysing Figure 5.28B-G, for the C.L, as the concentration is increased, there are a larger number of cells entering late apoptosis with a higher density of signal. The harsher the treatment, the more the cells move along the quadrant from alive to E.A and

L.A. It would be expected to have a high proportion of the cells in necrotic for the harsh treatments of C.L but as the necrotic cells are removed during the washing stage, only the apoptotic cells are visible.

In Figure 5.28K, the apoptosis results for PP show a late apoptosis rate of 38.7 % which is greater than the C.L 12.5 %. This suggests that the PP, with no additives like the coffee lid causes a high amount of apoptosis in comparison to the other plastic treated apoptosis levels and is a plastic of concern when considering human health with plastic degradation. In Figure 5.28 H and J, the raw PS and PE apoptosis rates are slightly elevated to 23.2 % and 25.8 % in comparison to the control but no significant increase in comparison to PP and the C.L 25 % samples. This displays a high difference between the raw PS and C.L which much higher rates of apoptosis in the C.L showing not only the plastic NPs can increase the damage caused but also the different additives within the processed plastic C.L.

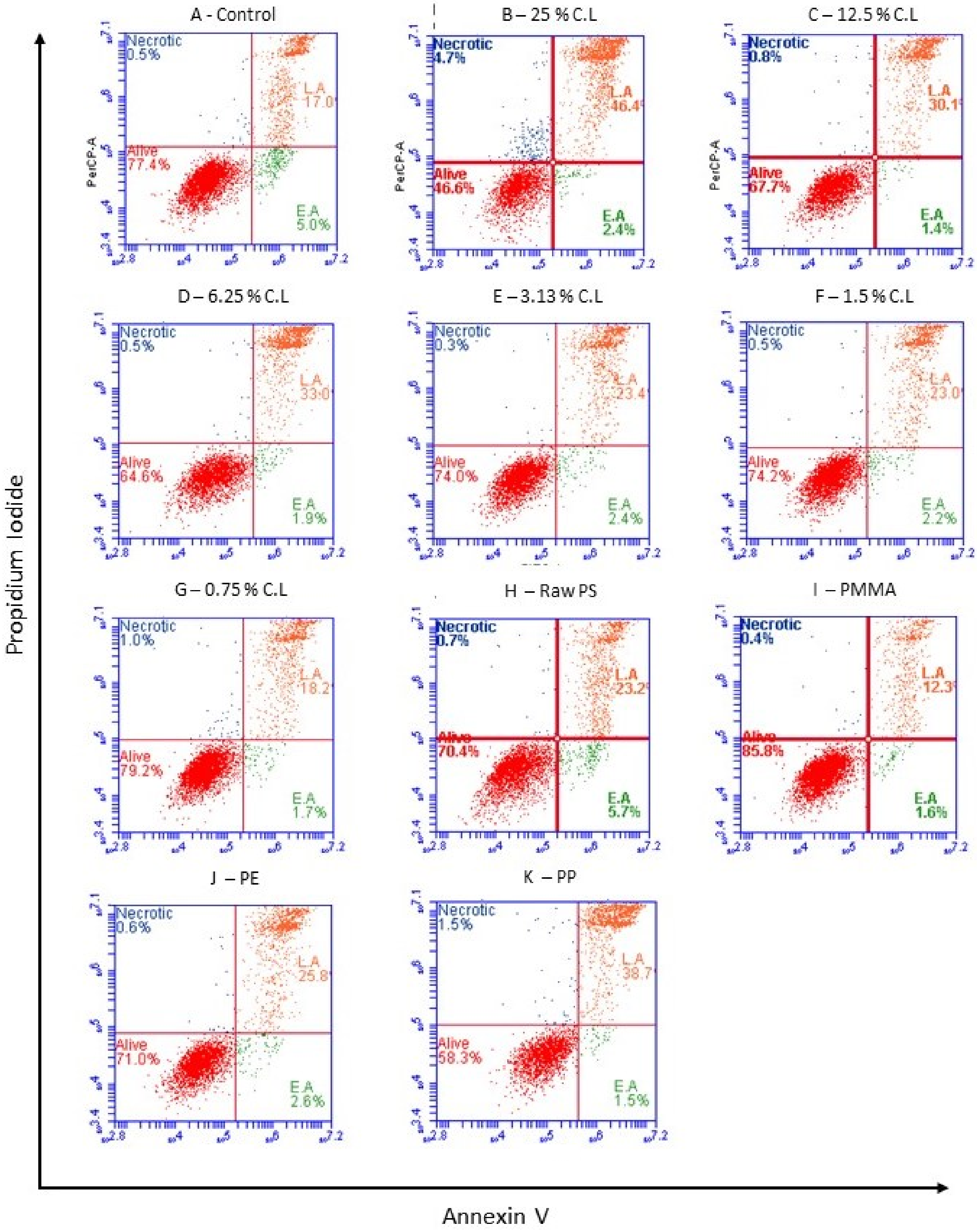

Figure 5.28: Flow cytometric primary plots analysis and quantification of apoptosis rate. (Increased AV shows cells being pushed into apoptosis due to damage caused, increased PI, shows cell membranes are damaged leading to dye penetration indicating late apoptosis or necrotic cells).

5.6.5 Cell Cycle analysis of MRC-5 cells from plastic NP treatment

In Table 5.13 and Figure 5.29and Figure 5.30, the data for the cell cycle analysis shows what phase of the cell cycle the cells are in. Figure 5.30 shows the dot plot of cells stained with propidium iodide (DNA content, horizontal axis) and FITC labelled secondary antibody (BrdU, vertical axis). Four regions are highlighted on the dot plot. The red box, R1, contains the BrdU positive cell population. Any cells counted which are outside the R1 area have not been positively stained with BrdU and are not used for the analysis of cell phases. The blue box, R2, contains those cells which are BrdU positive and have a singular DNA content representative of cells in the G1 phase of the cell cycle. The orange box, R3, contains those cells which are BrdU positive and are currently synthesising DNA and is representative of those cells in the S phase of the cell cycle. As there is a second copy of the DNA being synthesised, there is an increased amount of binding to the PI leading to the shift. The green box, R4, contains those cells which are BrdU positive and have twice the DNA content of cells in R2 which represents those cells in both G2 and M phases of the cell cycle. In the G2/M phase, the cells have two sets of DNA so a much higher DNA content in comparison which allows to distinguish between the different cells in different phases.

The primary findings that can be seen from Figure 5.30 is the number of cells which are being counted within each cell cycle. For example, in C.L. 25 %, fewer cells are in the cell cycle compared to the control. This is because the treatment being carried out pushes many of the cells into apoptosis and causes a significant amount of cell death causing the cells to not cycle. With a harsh treatment, most of the cells will be going through the programmed cell death cycle and enter apoptosis. This is further supported from the previous apoptosis experiments in 5.6.4. In the cell cycle data where the plastics were not inherently toxic to the plastics, there is an increased amount of positively stained cells that can be analysed.

There is a visible trend from Table 5.12 and Figure 5.29, where the treatments that do not push the cells to a high amount of apoptosis, leads to a major increase in the cells in the G2/M phase. The two main phases of the cell cycle are the S phase, DNA synthesis, and M phase, mitosis cell division. As the treatments may be causing damage to the DNA, before the cells go into mitosis and split into two daughter cells and move to G1, the cells are trying to repair the damaged DNA to ensure the damage is not carried into the daughter cells to avoid a mutation in the DNA and to the cells. There is a trend with the C.L plastic from 12.5 % to 0.75 % that shows an increase in cells in the G2/M phase. This is most likely due to less cells being push to necrosis. The plastics could interact with specific proteins within the cells, leading to epigenetic changes within the DNA. At this stage, the exact interactions of the different plastics within the cell are unknown and the mechanism for DNA damage needs further investigation. With all plastics indicating DNA damage is caused, the raw PS, which was not toxic to the cells and only increased apoptosis slightly in comparison to the control has the highest percentage of cell that were in the G2/M phase. This suggests that polystyrene NPs causes DNA damage and the processed C.L is toxic and DNA damaging leading to high concerns about plastic pollution and the damage it will cause to human health. Likewise, PP that also increased apoptosis rates and has an increased amount of cells in the G2/M suggests that DNA damage is being caused and that the toxicity and apoptosis rates found during cell viability and apoptosis quantification are due to the DNA damage being caused. Even PMMA, which seemed to have little to no effect on cell viability and apoptosis rates had an increased amount of cells in the G2/M phase. To further analyse how the damage is being caused to the cells, using fluorescent plastic NPs to analyse where the plastic NPs localise within the cells to further understand how the damage is caused to propose a mechanism for the damage.

This preliminary data with the one time point of 6 hours treatment indicates that there is some form of damage to the DNA caused with an elevated G2/M phase. To identify how the cells are cycling and repairing from the treatment a 24-48 hour time period is required, taking measurements every 2 hours. This would provide a significant amount of detail on the time it takes for the cells to repair the damage before entering mitosis and if there are any prolong effects from the treatment.

Table 5.12: Average percentage of cells in different phases of cell cycle.

	Percentage of gated cells									
	Control	C.L 12.5%	C.L 6.25%	C.L 3.13%	C.L 1.5%	C.L 0.75%	Raw PS	PMMA	PE	PP
G1	29.77	30.98	30.99	28.29	28.82	25.50	29.82	34.87	26.49	31.10
S	38.10	32.40	31.41	29.68	30.54	33.76	27.09	28.48	36.03	29.74
G2/M	32.13	36.62	37.61	42.02	40.64	40.74	43.09	36.66	37.48	39.17

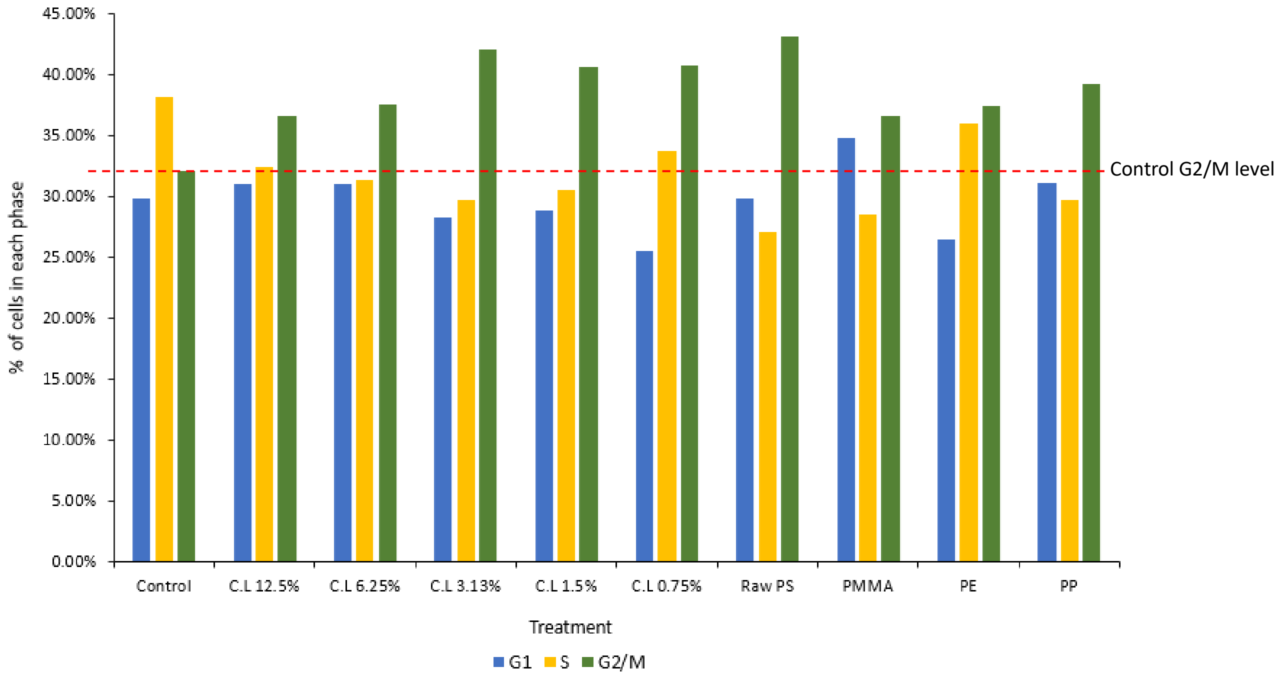

Figure 5.29: Percentage distribution of cells in each phase of the cell cycle. (Percentages taken from Table 5.12 to display the percentages visually for comparison)

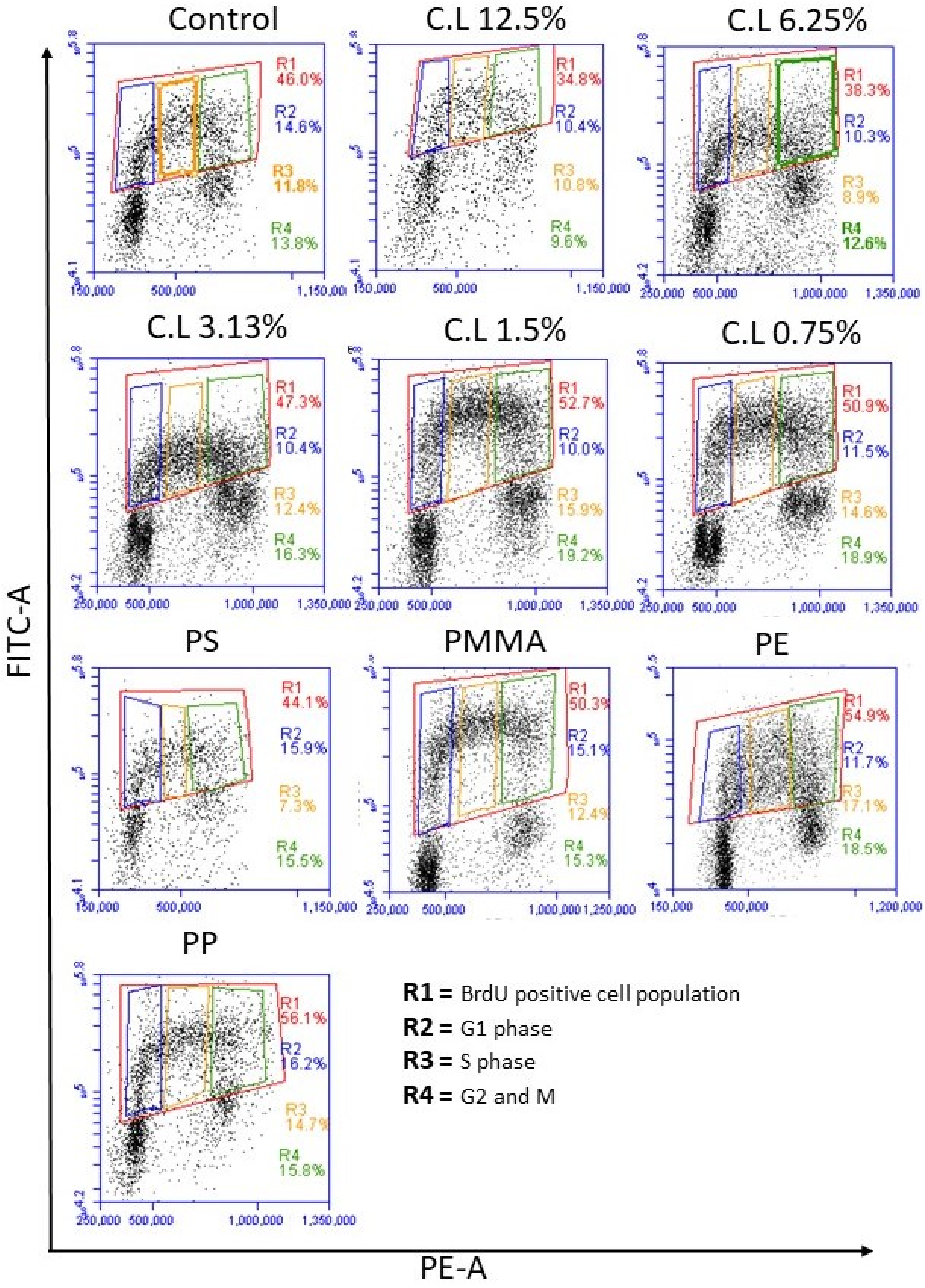

Figure 5.30: Cell cycle analysis of MRC-5 cells with different treatments.

5.6.6 DNA damage measurement of MRC-5 cells from plastic NP treatment.

DNA comprises four bases: adenine, cytosine, guanine and thymine. One or more of these bases may undergo mutation due to radiation or chemical exposure *(Ackerman et al. 2018)*. There are multiple different types of DNA damage from DNA strand breaks, oxidative damage, alkylation of the bases, base loss and bulky adduct formation *(Carusillo et al. 2020)*. In this experiment, the focus was based around DNA strand breaks, and more specifically double strand breaks as these are the most challenging for the cells to repair. It is essential to know what damage plastic pollution could cause to living organisms. If plastic NPs lead to DNA damage, most of the time, the cells will be able to recover due to the proteins within the cell inducing repair. However, if DNA damage occurs to a gene that is responsible for the DNA repair protein, the cells capability to recover will be significantly reduced, and the damaged cells will continue to replicate, which can lead to cancerous cells / tumours forming *(Prabhu et al. 2024)*. The primary concern when dealing with plastics is the toxic additives that are added to them. Two of the main potential culprits are bisphenyl A and phthalates which have indicated causing DNA damage *(Ackerman et al. 2018)*.

Very little research has currently tried to identify the damage that nanoplastics could cause to the different cell types and if this could increase the chance of cancerous cell buildup. To study this, plastic treatment is carried out on the MRC-5 cell line and the number of foci produced due to the treatment are counted. Foci is a signal when double-strand breaks have occurred within the DNA and the number of the foci reflects the numbers of the DNA double strand breaks. It can indicate the extent of damage being caused. When DNA is damaged, leading to double-strand breaks, it releases the protein y-H2AX.

A foci experiment was carried out to indicate the possible DNA damage caused by plastics and compared to a control to understand the effects of different plastics. The foci experiment is only a surrogate measure for DNA damage as DNA damage signalling and foci dynamics to signify double-strand breaks are entirely different depending on the chromatin modifiers *(Langlois et al. 2015)*. Therefore, to conclusively confirm the presence of double-strand breaks and DNA damage, pulse-field gel experiments are imperative. These experiments will provide the necessary data to confirm the extent of DNA damage. Nevertheless, even without a pulse field gel analysis the data provides the evidence that DNA double strand breaks are very likely produced by plastic NPs and the signalling cascades to detect DNA damage are activated.

In Figure 5.31, the mean number of foci from three independent experiments was counted and compared to each other to understand the difference in foci signal. In Figure 5.32, the foci images were taken to show how the cells appear after the treatment. The number of foci within higher concentrations of the coffee lid is evident at 25 % down to 1.5 %. At 0.75 %, there is still a small difference, but it is closer to the control sample. In all plastic-treated samples, double-strand breaks are increased.

Figure 5.31 – Control, there are very few Foci within the cells, with most cells having between 0-5 foci. A positive control was carried out to ensure the methodology and process worked as expected. In this case, 1 Gy of radiation was used that should produce 25-30 double-strand breaks per cell. Within Figure 5.31 – PC, there is a range of foci in the expected region with most of the cells having between 20-30 foci. There is a slightly broader range here with cells having 16-20 foci because as soon as the cells have been radiated, the cells will work immediately to start repairing the damage caused.

All the plastic treatments lead to an increased number of foci compared to the control, which suggests that due to the plastics being small enough, they migrate towards the nucleus, which potentially causes DNA damage. Even the plastics that did not affect the cell viability and lower apoptosis, such as PMMA and the raw PS, lead to a higher number of foci in the ranges of 6-15 foci. The more harmful treatments, as seen in Figure 5.31 – C.L 25 %, there is an increased number of foci again, with a shift in the histogram to the higher number of foci per cell.

The coffee lid is compared to the raw PS where both the plastic and the additives are causing the foci signal with the additives further adding to the DNA damage. The NPs are of a similar size and both the PS NPs and the additives appear to be reaching the nucleus. This is further supported by the cell cycle data that some form of damage or inhibition is caused by the plastics, leading to cells stuck in the G2/M phase for longer. Further investigation and analysis are required to understand and propose a mechanism for the DNA damage and what is occurring within the cell post-DNA damage.

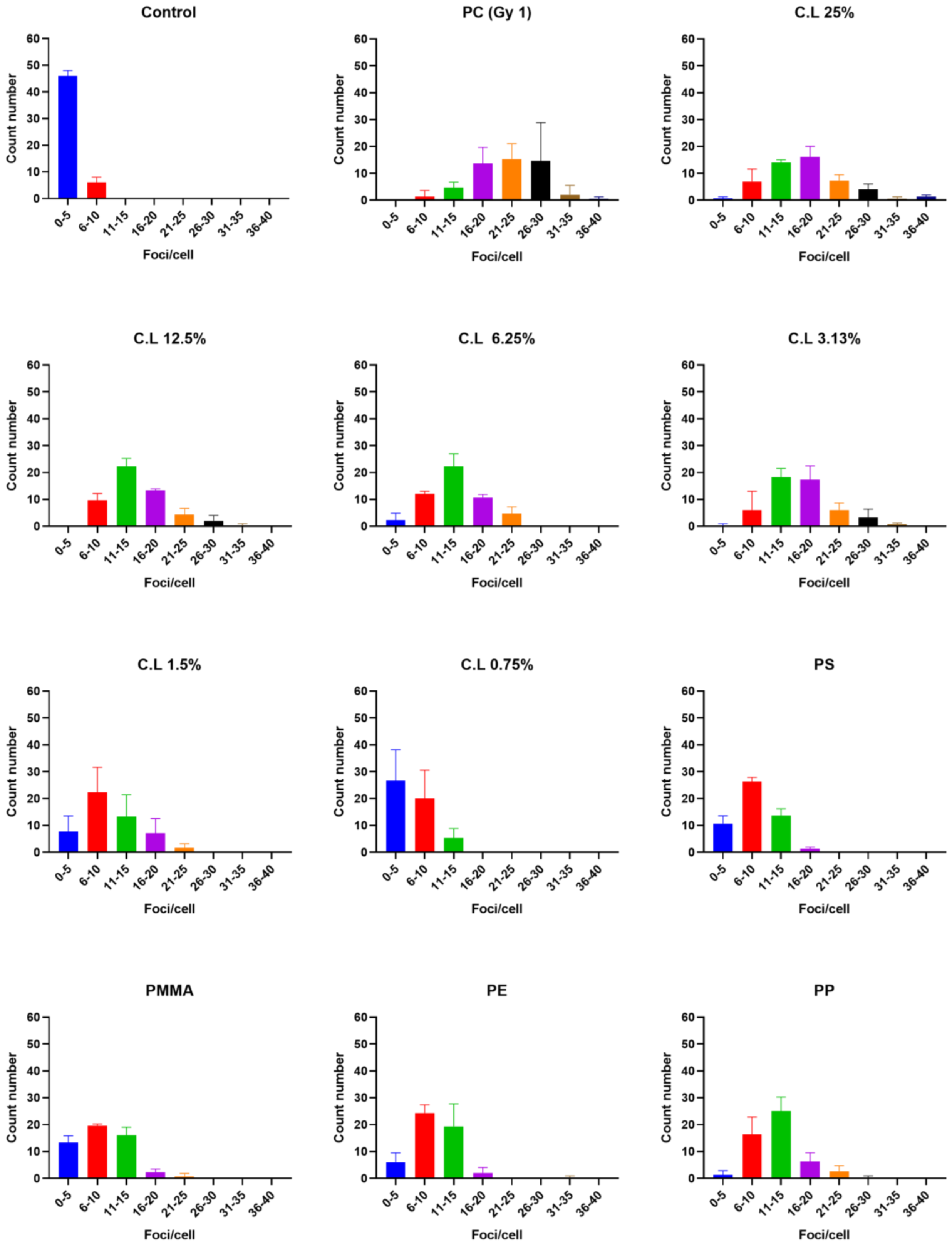

Figure 5.31: Histograms of DNA double strand breaks counts for different plastic NP treatments on MRC-5 cell line.

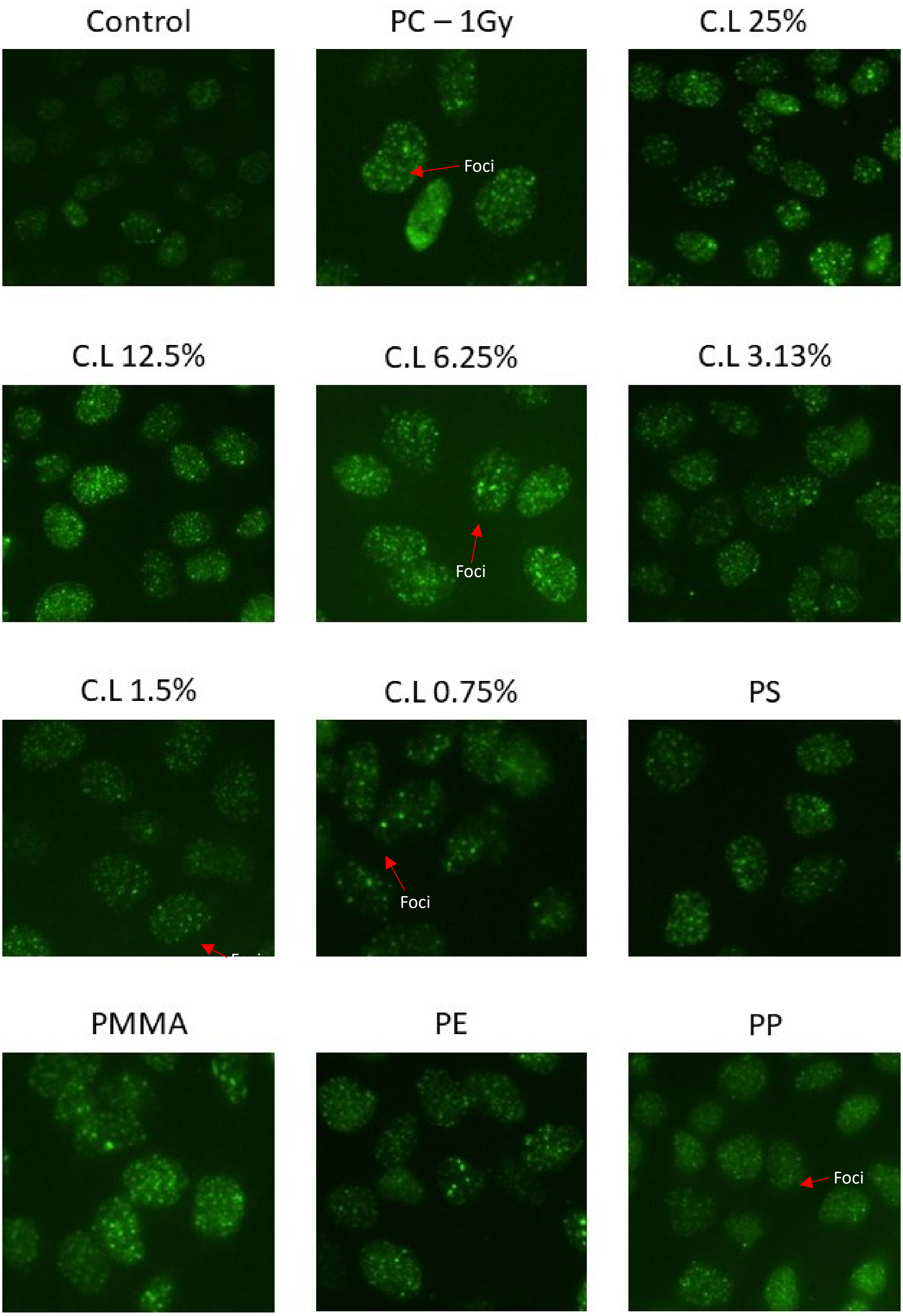

Control

PC – 1Gy

C.L 25%

C.L 12.5%

C.L 6.25%

C.L 3.13%

C.L 1.5%

C.L 0.75%

PS

PMMA

PE

PP

Figure 5.32: Microscope images at 20 x magnification to display possible DNA double strand breaks in MRC-5 cells from different plastic NP treatments. (Arrows used to indicate how the foci appears within a cell)

5.7 Conclusion

Overall, this chapter has covered a significant amount of detail and characterised the critical biological response parameters of the exposure to the NPs made from the raw PS in comparison to the PS coffee lid. It is well known that during the manufacturing of plastics, different types of additives are incorporated into the plastic to optimise and improve its properties for the desired use. For instance, phthalates or phthalic acid esters are often added to increase flexibility, making the plastic more suitable for its purpose *(Chen et al. 2021)*. TiO_2 has been used to increase the heat resistance and as a colourant to improve its properties in plastics *(Gojznikar et al. 2022)*.

Recently, there have been concerns about plastic pollution, the degradation of these plastics into micro and nanoparticles, and the damage caused to all organisms. However, the additives included within these plastics are of concern due to the high toxicity, which would also break down and contribute to pollution. A requirement for manufacturers to look for more bio-friendly additives that can still achieve the same performance as these toxic additives without the negative impact. This pushes towards the need for bioplastics, which will degrade much more rapidly in comparison to petroleum-based plastics.

Adding to the urgency of the situation, there has been a surprising lack of research into the potential effects of different types of plastic micro and nanoparticles on various relevant biological models. This is a critical area that requires immediate attention and further investigation. *Rubio et al. 2020* evaluated what 50 nm PS NPs did to Raji-B, TK6 and THP-1 cells and assessed cytotoxicity, cellular uptake, reactive oxygen species (ROS) production, and genotoxicity. But, an in-depth study has yet to evaluate a range of the most common plastic pollution and the damage caused.

In this case, it has been displayed that PS and PMMA NPs can be synthesised with narrow size distribution and uniform shape using a dissolution and precipitation process. There has been exciting preliminary cell biology testing with the PS coffee lid, which has caused significant damage and toxicity towards MRC-5 cells compared to raw PS, potentially due to the TiO_2 additive. It is unlikely that the $CaCO_3$, with a high content within the coffee lid, would cause any significant effect as the cells readily use $CO_{\underline{\underline{3}}}$ as a buffer. The cell viability for the coffee lid is less than 10 % compared to the raw polystyrene viability of just under 90 %. This is the case with the cryogenically milled coffee lid, which has a range of sizes from large microns to nanoparticles that also significantly affected cell viability. This shows that there is something within the plastic causing cell toxicity rather than a chemical byproduct from the synthesis. There is a drop in viability when PP was used as the treatment to 72 %. The foci experiment to look at DNA damage is of high concern as all plastic treatments showed an elevated amount of double strand breaks in comparison to the control suggesting that all plastics, no matter the toxicity, are internalised and cause damage and inhibition to the DNA.

An in-depth study is required to develop this research further to understand the mechanism and process of what occurs with the cells when encountering plastic NPs. Pulse field gel experiment to identify the DNA damage caused should be a focus of future research and whether other alterations within the cell are occurring. Whether it is double-strand breaks, single-strand breaks or interactions with the proteins within the DNA. It would be beneficial to carry out a long-term study on cells treated with plastic particles and the recovery/changes that occur to the cells over an extended period to identify long-term health effects.

To further understand the damage caused by cell viability, a seahorse experiment, which allows the monitoring of oxidative respiration in real time, to look at the oxygen consumption rate (OCR) and extracellular acidification rate (ECAR) would be interesting to see how the reactive oxygen species (ROS) increases with different plastic treatments. This could give more information and a further study to be carried out around the mitochondria and the mechanism of the cell, whether it is damage to the cell membrane or interactions within the cell between the organic plastic material and the cells. Another interesting study would entail exclusively using cryogenically milled samples to understand whether the size is the critical factor in the uptake of the particles and if the amorphous structure of the cryo-milled particles changes the cell viability and uptake rate.

References

Ackerman, S., & Horton, W. (2018). Effects of Environmental Factors on DNA : Damage and Mutations. In *Green Chemistry*. Elsevier Inc. https://doi.org/10.1016/B978-0-12-809270-5.00005-4

Ai, C., & Xie, Y. (2022). Quantitative Analysis and Study on the Maximum Bearing Capacity of Global Ecosystem to Disposable Plastic Products. *Iranian Journal of Science and Technology - Transactions of Civil Engineering*, *46*(3), 2369–2375. https://doi.org/10.1007/s40996-021-00638-3

Ali, S. S., Elsamahy, T., Koutra, E., Kornaros, M., El-Sheekh, M., Abdelkarim, E. A., Zhu, D., & Sun, J. (2021). Degradation of conventional plastic wastes in the environment: A review on current status of knowledge and future perspectives of disposal. *Science of the Total Environment*, *771*, 144719. https://doi.org/10.1016/j.scitotenv.2020.144719

Brandts, M. Cánovas, A. Tvarijonaviciute, M. Llorca, A. Vega, M. Farré, J. Pastor, N. Roher, M. T. (2022). Nanoplastics are bioaccumulated in fish liver and muscle and cause DNA damage after a chronic exposure. *Environmental Research*, *212*. https://www.sciencedirect.com/science/article/pii/S0013935122007605

Carpenter, E., & Smith, J. (1972). Plastics on the Sargasso Sea Surface. *Science*, *175*(4027), 1240–1241. https://doi.org/DOI: 10.1126/science.175.4027.1240

Carusillo, A., & Mussolino, C. (2020). DNA Damage: From Threat to Treatment. *Cells*, *9*(7), 1–20. https://doi.org/10.3390/cells9071665

Chen, Y., Kumar, A., Wei, F., Tan, Q., & Li, J. (2021). Science of the Total Environment Single-use plastics : Production , usage , disposal , and adverse impacts. *Science of the Total Environment*, *752*, 141772. https://doi.org/10.1016/j.scitotenv.2020.141772

Cohen, G. M. (1997). Caspases: The executioners of apoptosis. *Biochemical Journal*, *326*(1), 1–16. https://doi.org/10.1042/bj3260001

Fischer, K., Gawel, A., Rosen, D., Krause, M., Latif, A. A., Griebel, J., Prager, A., & Schulze, A. (2017). Low-temperature synthesis of anatase/rutile/brookite TiO2 nanoparticles on a polymer membrane for photocatalysis. *Catalysts*, *7*(7). https://doi.org/10.3390/catal7070209

Ghorbani, N., Yaghubi, R., Davoodi, J., & Pahlavan, S. (2023). How does caspases regulation play role in cell decisions? apoptosis and beyond. *Molecular and Cellular Biochemistry*, *479*(7), 1599–1613. https://doi.org/10.1007/s11010-023-04870-5

Gojznikar, J., Zdravkovi, B., Vidak, M., Leskošek, B., & Ferk, P. (2022). *TiO 2 Nanoparticles and Their Effects on Eukaryotic Cells : A Double-Edged Sword*.

Gosalvitr, P., Cuéllar-Franca, R. M., Smith, R., & Azapagic, A. (2023). An environmental and economic sustainability assessment of coffee production in the UK. *Chemical Engineering Journal*, *465*(March). https://doi.org/10.1016/j.cej.2023.142793

Guzmán, J. C. A., Bejtka, K., Fontana, M., Jones, E. V., Villezcas, A. M., Duhalt, R. V., & Hernández, A. G. R. (2022). Polyethylene terephthalate nanoparticles effect on RAW 264 . 7 macrophage cells. *Microplastics and Nanoplastics*, 1–15. https://doi.org/10.1186/s43591-022-00027-1

Koczoń, P., Bartyzel, B., Iuliano, A., Klensporf-Pawlik, D., Kowalska, D., Majewska, E., Tarnowska, K., Zieniuk, B., & Gruczyńska-Sękowska, E. (2022). Chemical Structures, Properties, and Applications of Selected Crude Oil-Based and Bio-Based Polymers. *Polymers*, *14*(24). https://doi.org/10.3390/polym14245551

Kumar, V., Sirohi, R., Ishfaq, M., Gautam, K., Sharma, P., Kumar, J., & Pandey, A. (2023).

Chemosphere A review on the effect of micro- and nano-plastics pollution on the emergence of antimicrobial resistance. *Chemosphere*, *311*(P1), 136877. https://doi.org/10.1016/j.chemosphere.2022.136877

Langlois, C., Benzo, P., Arenal, R., Benoit, M., Nicolai, J., Combe, N., Ponchet, A., & Casanove, M. J. (2015). Fully Crystalline Faceted Fe-Au Core-Shell Nanoparticles. *Nano Letters*, *15*(8), 5075–5080. https://doi.org/10.1021/acs.nanolett.5b02273

Leal-Esteban, L. C., & Fajas, L. (2020). Cell cycle regulators in cancer cell metabolism. *Biochimica et Biophysica Acta - Molecular Basis of Disease*, *1866*(5), 165715. https://doi.org/10.1016/j.bbadis.2020.165715

Liendo, F., Deorsola, F. A., Bensaid, S., & Giordani, S. (2020). Colloids and Surfaces B : Biointerfaces Toxicological pro fi le of calcium carbonate nanoparticles for industrial applications. *Colloids and Surfaces B: Biointerfaces*, *190*(March), 110947. https://doi.org/10.1016/j.colsurfb.2020.110947

MacLeod, M., Arp, H. P. H., Tekman, M. B., & Jahnke, A. (2021). The global threat from plastic pollution. *Science*, *373*(6550), 61–65. https://doi.org/10.1126/science.abg5433

Nachod, B., Keller, E., Hassanein, A., & Lansing, S. (2021). *Assessment of Petroleum-Based Plastic and Bioplastics Degradation Using Anaerobic Digestion*.

Nielsen, T. D., Hasselbalch, J., Holmberg, K., & Stripple, J. (2020). Politics and the plastic crisis: A review throughout the plastic life cycle. *Wiley Interdisciplinary Reviews: Energy and Environment*, *9*(1), 1–18. https://doi.org/10.1002/wene.360

Peng, L., Fu, D., Qi, H., Lan, C. Q., Yu, H., & Ge, C. (2020). Micro- and nano-plastics in marine environment: Source, distribution and threats — A review. *Science of the Total Environment*, *698*. https://doi.org/10.1016/j.scitotenv.2019.134254

Pérez-albaladejo, E., & Porte, C. (2020). ScienceDirect Toxicology Plastics and plastic additives as inducers of oxidative stress. *Current Opinion in Toxicology*, *20–21*, 69–76. https://doi.org/10.1016/j.cotox.2020.07.002

Plastics Europe. (2022). Plastics – the Facts 2022. *Plastics Europe*, *October*.

Prabhu, K. S., Kuttikrishnan, S., Ahmad, N., Habeeba, U., Mariyam, Z., Suleman, M., Bhat, A. A., & Uddin, S. (2024). Biomedicine & Pharmacotherapy H2AX : A key player in DNA damage response and a promising target for cancer therapy. *Biomedicine & Pharmacotherapy*, *175*(February), 116663. https://doi.org/10.1016/j.biopha.2024.116663

Reed, J. C. (2000). Warner-Lambert/Parke Davis award lecture: Mechanisms of apoptosis. *American Journal of Pathology*, *157*(5), 1415–1430. https://doi.org/10.1016/s0002-9440(10)64779-7

Roursgaard, M., Hezareh Rothmann, M., Schulte, J., Karadimou, I., Marinelli, E., & Møller, P. (2022). Genotoxicity of Particles From Grinded Plastic Items in Caco-2 and HepG2 Cells. *Frontiers in Public Health*, *10*(July). https://doi.org/10.3389/fpubh.2022.906430

Rubio, L., Barguilla, I., Domenech, J., Marcos, R., & Hernández, A. (2020). Biological effects, including oxidative stress and genotoxic damage, of polystyrene nanoparticles in different human hematopoietic cell lines. *Journal of Hazardous Materials*, *398*(May), 122900. https://doi.org/10.1016/j.jhazmat.2020.122900

Schafer, K. (1998). The Cell Cycle: A review. In *Veterinary Pathology* (pp. 461–478). https://doi.org/https://doi.org/10.1177/0300985898035006

Shen, M., Chen, X., Zhang, L., Wang, H., & Sun, W. (2021). Effects of AgTi3 intermetallic on suppression of Ag agglomeration: a theoretical study. *Molecular Simulation*, *47*(7), 586–593.

https://doi.org/10.1080/08927022.2021.1876232

Soo, J., Jung, Y., Hong, N., Hee, S., & Park, J. (2018). Toxicological e ff ects of irregularly shaped and spherical microplastics in a marine teleost , the sheepshead minnow (Cyprinodon variegatus). *Marine Pollution Bulletin*, *129*(1), 231–240. https://doi.org/10.1016/j.marpolbul.2018.02.039

Tang, X., Shen, C., Chen, L., Xiao, X., Wu, J., Khan, M. I., Dou, C., & Chen, Y. (2010). Inorganic and organic pollution in agricultural soil from an emerging e-waste recycling town in Taizhou area, China. *Journal of Soils and Sediments*, *10*(5), 895–906. https://doi.org/10.1007/s11368-010-0252-0

The Ocean Concervency. (2006). *Pocket Guide To Marine Debris*. https://www.mass.gov/files/documents/2016/08/pq/pocket-guide-2003.pdf

Ustun, I., Sungur, S., & Okur, R. (2015). *Determination of Phthalates Migrating from Plastic Containers into Beverages*. 222–228. https://doi.org/10.1007/s12161-014-9896-5

Voicu, S. N. P., Dinu, D., Sima, C., Hermenean, A., Ardelean, A., Codrici, E., Stan, M. S., Zărnescu, O., & Dinischiotu, A. (2015). Silica nanoparticles induce oxidative stress and autophagy but not apoptosis in the MRC-5 cell line. *International Journal of Molecular Sciences*, *16*(12), 29398–29416. https://doi.org/10.3390/ijms161226171

Wahyuningtyas, N., & Suryanto, H. (2017). Analysis of Biodegradation of Bioplastics Made of Cassava Starch. *Journal of Mechanical Engineering Science and Technology*, *1*(1), 24–31. https://doi.org/10.17977/um016v1i12017p024

Wang, W., Do, A. T. N., & Kwon, J. H. (2022). Ecotoxicological effects of micro- and nanoplastics on terrestrial food web from plants to human beings. In *Science of the Total Environment* (Vol. 834). https://doi.org/10.1016/j.scitotenv.2022.155333

Williams, G. H., & Stoeber, K. (2012). The cell cycle and cancer. *Journal of Pathology*, *226*(2), 352–364. https://doi.org/10.1002/path.3022

WWF. (2021). *THE LIFECYCLE OF PLASTICS*. https://wwf.org.au/blogs/the-lifecycle-of-plastics/

Yu, Y., & Flury, M. (2021). Current understanding of subsurface transport of micro- and nanoplastics in soil. *Vadose Zone Journal*, *20*(2), 1–14. https://doi.org/10.1002/vzj2.20108

Zarei, M. H., & Pourahmad, J. (2024). Toxicity of Dibutyl phthalate (DBP) toward isolated human blood lymphocytes: Apoptosis initiated from intracellular calcium enhancement and mitochondrial/lysosomal cross talk. *Toxicology Reports*, *13*(August), 101729. https://doi.org/10.1016/j.toxrep.2024.101729

Zhang, L., & Yu, J. (2013). Role of apoptosis in colon cancer biology, therapy, and prevention. *Current Colorectal Cancer Reports*, *9*(4), 331–340. https://doi.org/10.1007/s11888-013-0188-z

Chapter 6 – Conclusion and Future Work

6.1 Conclusion

Overall, this study covers two different topics centred around nanoparticles that can impact human health. Chapters 3 and 4 focuses on how nanoparticles can be used positively and synthesised for the treatment of radioresistant glioblastomas via the technique NCT. The research on this topic tries to bridge the gap by synthesising an effective nanoparticle that can be delivered effectively to the desired tumour. The research chapters try to develop the current synthesis techniques and improve boron incorporation significantly to increase the efficacy of the NPs for cancer treatment. Further research can be carried out to optimise the shell formation and begin biological testing. There is currently no published research that tries to synthesise a core-shell structure NP that contains a boron core and gold shell. This is likely due to the challenges faced during the synthesis to obtain the required structure. This research was required as upon diagnosis, patients expected to survive longer than one year is 17.7 %. By testing both aqueous and non-aqueous conditions, advancements were made on the synthesis of an enriched boron core and the key parameters for the synthesis of a gold shell around focusing around the temperature drop when adding the gold ion solution into the synthesised core.

The second part of this research focuses on the negative impact of NPs and the effect plastic NPs could have on living organisms. It was discussed the need to move away from single-use plastics, and the typical additives that have been found to be highly toxic towards cells. Many common waste plastics were tested on MRC-5 fibroblast cells, which could encounter these plastic NPs in the environment such as raw PS and processed PS, PE, PP and PMMA. Preliminary biological studies were carried out to examine the possible DNA damage and the cytotoxicity of common waste plastics towards MRC-5 cells. The research attempts to quantify the damage caused by the nanoplastics in the range of 50-100 nm that are small enough interact with DNA. It was found from the testing that the additives used in process plastics to improve the properties for the desired use may be more harmful than the plastic NPs. All the plastics which were trialled displayed that DNA damage was being caused even though not all plastics were inherently toxic to the cells.

Both sets of research try to bridge the gap of using NPs for a positive life changing cancer treatment and also how NPs can be very detrimental to the environment and human health. Research into NPs needs to continue to harness the power of NPs for positive effects to all industries. The work carried out in this thesis only scrapes the surface on what can be done and shows further advancements upon this research will lead to groundbreaking advancements in the field of nanoscience. This research needs to be continued to further develop the synthesis procedure for the core-shell NPs for glioblastomas and also further advanced biological experiments to understand the long term effect of the plastic NP pollution can have to human health.

6.1.1 Final remarks – Synthesis of Fe-B@Au via aqueous and non-aqueous techniques

In this thesis, two techniques were tested to synthesise core-shell nanoparticles composed of an iron-boron core and a gold shell. This research is pivotal as there is a gap in research to tackle glioblastomas. This very radioresistant cancerous cell, typical chemotherapy treatments are ineffective and causes more damage to healthy cells around the tumour than the cancerous cells themselves *(Ali et al. 2020)*. The advancement in treatments around NCT has not advanced and been at the forefront of research due to the challenges in synthesising the particles required for the treatment. This is necessary to combat the deadly disease that is currently a death sentence upon diagnosis. These trimetallic NPs have the potential to be developed into a very targeted cancer treatment using a targeting peptide to locate the glioblastoma and deliver the dose of boron that is needed to kill the cancerous cells.

Research has been carried out to synthesise Fe@Au core-shell NPs for various uses *(Iancu et al. 2020), (Kayal et al. 2010) (Li et al. 2019).* To turn this commonly used Fe@Au bimetallic nanoparticle into a particle that can be used for boron neutron capture therapy (BNCT) nanotherapeutic drug, ^{10}boron needs to be incorporated into the core. This specific elemental composition has several potential medical applications, the principal being a vehicle for targeted magnetic delivery of ^{10}boron to tumour cells for using a targeting peptide. The BNCT is a promising experimental radiotherapy technique for treating non-responsive tumours with inferior prognoses (e.g. glioblastomas). Nevertheless, a wider application of BNCT has been hampered by a lack of methodology for sufficiently loading tumour tissues with boron atoms - a critical prerequisite for a successful therapeutic outcome.

Within this research, we have attempted to tackle this problem and displayed how a vast amount of boron can be incorporated into the iron core during synthesis by using a borohydride source, such as sodium borohydride, as a reducing agent and source of boron. Many critical factors in using non-aqueous techniques and aqueous reverse micelle methods significantly influence the amount of boron incorporation. The critical factor found was the irons ionic state. When using $FeCl_3$ compared to $FeCl_2$, there was a boron/iron ratio of 0.91 compared to 0.32. This is due to the need for more borohydride ions to reduce the iron leading to the synthesis of more boron that can be incorporated into the core. The rate of addition of the reducing agent also plays a critical factor in the amount of incorporated boron with rapid addition leading to crystalline iron particles and slow addition leading to amorphous Fe-B particles. In both the research chapter 3, non-aqueous techniques, and chapter 4, aqueous techniques, the process variables were optimised to increase the amount of boron incorporated. However, the non-aqueous technique was incorporates a significant more boron than the aqueous technique with 0.91 B/Fe ratio in comparison to 0.34. This was due to absence of water in the non-aqueous technique, there was not the immediate reduction that occurs with the presence of water leading to a complex forming of $Fe(BH_4)_3$ that broke down and reduced the Fe upon heating.

This thesis also tried to tackle the challenges of seeding gold on top of the Fe-B core. Due to the significant difference in lattice structure, a major energy barrier exists to force gold shell formation. Two different techniques were trialled: Redox-transmetalation, less regularly reported in the literature, showed significant promise by using the iron core as the reducing agent for gold ions, causing the reduction of Au^{3+} to occur at the surface of the iron surface. As the Fe was not required for NCT, it was used as a sacrificial layer to reduce the gold and force the gold ions to seed at the surface of the core material to overcome the lattice mismatch. This research led to partial core-shell structures, which can be further developed into complete shells. Very interesting STEM analysis coupled with EDX showed core-shell structure formation but with gaps in the shell. The process was highly effective in forming a shell around the core when a rapid temperature drop was used by injecting rapidly a chilled gold solution at 4 °C into a heated core solution at 125 °C that produced gold nanoseeds but supressed homonucleation and promoted hetronucleation. The reverse micelle process, heavily reported in the literature for synthesising Fe@Au nanoparticles, did not show successful results. Many process variables were missing from the methodology so an attempt was made to try and establish the parameters of the process to have an in depth process that could be used to progress research further with. The method did not show any clear core-shell structure and predominately two separate distributions of gold and iron-boron NPs. However, when coupling the reverse micelle with redox-transmetalation led to more positive results where one experiment magnetic particles were present after acid washing suggesting some protection from the gold was present to avoid the core rapidly digesting in the acid solution. However, TEM, STEM and EDX analysis did not display any clear core-shell structures that would identify that the process was successful. It was challenging to identify whether there was core-shell structures from the STEM analysis as false positives were found in the HAADF analysis whereby a darker core and brighter shell was present which would usually indicate that core-shell structures with a lower Z number core, indicating Fe and B and a higher Z shell such as gold. However, EDX showed that these particles were just gold NPs.

6.1.2 Future work to be conducted.

This research has made significant advancements in boron incorporation and the formation of a gold shell around a Fe-B core. Out of the two methods tested, the redox-transmetalation process has shown more promising results. The future work should be focused on the seeding of the Au on the Fe-B core. While partial shells have been achieved, further research is needed to address key factors such as the rapid addition of Au solution to the Fe-B core solution and the temperature of both solutions upon addition to promote shell formation. These factors are crucial in achieving a specific temperature drop that inhibits homonucleation and promotes hetronucleation. Additional tests are required to use chilled gold solutions and measure the temperature drop to achieve the desired complete core-shell structure.

Upon this further research and the formation of the complete core-shell structure, cell biology can commence testing for cell toxicity, which should be low due to the gold shell around the core material, followed by neutron capture therapy experiments to see if the dose of radiation released matches what has been found in the literature. Once the proof of concept has been shown, the targeting peptide can be added to the particles to test whether the particles can find the necessary cells for the cancer treatment and if enough radiation is released to kill the cells.

In terms of further optimising around the chemistry, for the BNCT, a source of ^{10}B is required to deliver the toxic dose of radiation. ^{10}B is only 20 % of the abundance of naturally occurring B. In this case, optimisation around ^{10}B enrichment would be required to make the particles more effective for the desired use.

6.2.1 Final remarks – Synthesis of plastic nanoparticles and the damage caused to cells.

Some of the most common plastics were chemically synthesised into nanoparticles to test the toxicity and DNA damage on MRC-5 cells to mimic the damage that these plastics cause in the environment to different organisms. Through a comprehensive analytical study of raw polystyrene and a polystyrene coffee lid, there are further concerns with common plastic waste, and most significantly with single-use plastics. Additives are used within plastics to improve the properties of the plastic for the desired use. Phthalates or phthalic acid esters are often added to increase flexibility, making the plastic more suitable for its purpose. *(Chen et al. 2021)*. One of the additives found in the coffee lid was a small amount of TiO_2 that is toxic towards cells *(Podporska-Carroll et al. 2015)*. In most cases, TiO_2 is added to plastics to improve their thermal properties. However, in plastic degradation and contamination of the environment, it is not just the plastic micro and nanoparticles that need to be considered as the additives also break down and released into the environment.

It was found that the coffee lid was of significant concern. When compared to all other plastics, PMMA, raw PS, PE and PP, the coffee lid nanoparticles were highly toxic, and the cell viability of the cells was almost zero. To ensure no chemical waste was left over that was causing the damage, cryo milling was carried out to mechanical synthesise micro and nanoplastics that were also tested on cells, and the viability was also significantly low compared to the other plastics.

The characterisation suggested that the plastic particles contained TiO_2 which added to the low cell viability. The most intriguing and of high concern results was the possible DNA damage that could be caused to the cells from the plastic testing. Although not all plastics are cytotoxic from the foci experiment, indicated double strand breaks within the cells. This suggests that the plastics are entering the cells and causing damage within the nucleus of the cell. This is further indicated within the cell cycle analysis. After 6 hours of treatment, the cells appear to remain in the G2/M phase longer than the control indicating damage has been caused to the DNA, and the cells are repairing the damage before entering mitosis.

The data collected from this study underscores the need for a more in-depth investigation into the effects of plastic particles. This should be the impetus for a shift from single-use petroleum-based plastics to more environmentally friendly and biodegradable alternatives. Further research into less toxic additives for plastics is also warranted to provide a safer solution for both the environment and human health while maintaining the properties of the plastic.

6.2.2 Future work to be conducted.

With the findings in this chapter, a vast amount of research could be carried out depending on the target of the study to propose a mechanism for the damage being caused.

Initially, to find out where the particles aggregate within the cells, it would be beneficial and practical to fluorescently tag the particles so that when analysing via fluorescent microscope, it would be possible to see the distribution of the particles within the cell. This would indicate how the particles are up taken by the cell. It would be effective to analyse the cells on a time basis to understand how the particles move with time and how the damage increases with time.

There is a lot of promising data focusing on DNA damage, and the work carried out in Chapter 5 has laid the foundations for a more detailed and significant study in this area. Foci experiments are a surrogate measure for DNA damage. However, to conclusively determine the DNA damage, further tests are required with a pulse field gel experiment, which can identify the type of DNA damage caused, whether it is double strand breaks, single strand breaks or interactions with the bases of the DNA.

A more detailed study of the cell cycle analysis is required. As only one time point has been chosen, it only shows a small amount of detail around what the plastic nanoparticles cause to the cells. However, a study over a 24 - 48 hour time period is required to exactly see how the cells are cycling through the different phases. By doing it over a longer period, a comparison of which stage of the cell cycle the cells reside in and for what period after treatment. This would show how long the potential DNA damage takes to repair before moving into the next phase of the cell cycle.

For further studies not around DNA damage, there is a vast potential for new discoveries. Research could be carried out around the uptake of the particles across the mitochondria and what sort of damage is caused across this border. An investigation around Reactive Oxygen Species (ROS) and if, due to the treatment, there are elevated levels of ROS is a possible cause for the higher levels of apoptosis or simultaneously due to uptake but also the DNA damage. Work in this area could lead to exciting new findings and significantly advance our understanding of cellular biology and nanotechnology based around nanoplastics.

Repeating the experimentation with mechanically synthesised plastics to simulate further how organisms would come into contact with these particles in the environment would be beneficial. The plastics used for these tests have been synthesised chemically and formed spherical particles. However, the particles will undergo a series of mechanical processes in the environment, leading to amorphous-shaped plastics. This would make for an interesting study to see if the toxicity or DNA damage would change when the morphology of the particles changes and if this would affect the uptake of the particles by the cells.

References

Ali, M. Y., Oliva, C. R., Noman, A. S. M., Allen, B. G., Goswami, P. C., Zakharia, Y., Monga, V., Spitz, D. R., Buatti, J. M., & Griguer, C. E. (2020). Radioresistance in glioblastoma and the development of radiosensitizers. *Cancers*, *12*(9), 1–29. https://doi.org/10.3390/cancers12092511

Chen, Y., Kumar, A., Wei, F., Tan, Q., & Li, J. (2021). Science of the Total Environment Single-use plastics : Production , usage , disposal , and adverse impacts. *Science of the Total Environment*, *752*, 141772. https://doi.org/10.1016/j.scitotenv.2020.141772

Iancu, S. D., Albu, C., Chiriac, L., Moldovan, R., Stefancu, A., Moisoiu, V., Coman, V., Szabo, L., Leopold, N., & Bálint, Z. (2020). Assessment of gold-coated iron oxide nanoparticles as negative T2 contrast agent in small animal MRI studies. *International Journal of Nanomedicine*, *15*, 4811–4824. https://doi.org/10.2147/IJN.S253184

Kayal, S., & Ramanujan, R. V. (2010). *Anti-Cancer Drug Loaded Iron – Gold Core – Shell Nanoparticles (Fe @ Au) for Magnetic Drug Targeting*. *10*(9), 5527–5539. https://doi.org/10.1166/jnn.2010.2461

Li, Y., Dhawan, U., Wang, H., Liu, X., & Ku, H. (2019). *Theranostic Iron @ Gold Core – Shell Nanoparticles for Simultaneous Hyperthermia-Chemotherapy upon*. *1800419*, 1–14. https://doi.org/10.1002/ppsc.201800419

Podporska-Carroll, J., Panaitescu, E., Quilty, B., Wang, L., Menon, L., & Pillai, S. C. (2015). Antimicrobial properties of highly efficient photocatalytic TiO2 nanotubes. *Applied Catalysis B: Environmental*, *176–177*, 70–75. https://doi.org/10.1016/j.apcatb.2015.03.029